Universidade do Minho
I3Bs - Instituto de Investigação em Biomateriais,
Biodegradáveis e Biomiméticos

Ana Margarida Moura Pereira Ferreira Carvalho

NANOGLYCAN: Glycotools for elucidating molecular and cellular interactions of glycans *in vitro*

Abril de 2022

NANOGLYCAN: Glycotools for elucidating molecular and cellular interactions of glycans *in vitro*
Ana Margarida Moura Pereira Ferreira Carvalho
UMinho | 2022

REPÚBLICA PORTUGUESA | CIÊNCIA, TECNOLOGIA E ENSINO SUPERIOR
FCT Fundação para a Ciência e a Tecnologia
NORTE2020
UNIÃO EUROPEIA

Universidade do Minho

I3Bs - Instituto de Investigação em Biomateriais, Biodegradáveis e Biomiméticos

Ana Margarida Moura Pereira Ferreira Carvalho

NANOGLYCAN: Glycotools for elucidating molecular and cellular interactions of glycans *in vitro*

Tese de Doutoramento

Doutoramento em Engenharia de Tecidos, Medicina Regenerativa e Células Estaminais

Trabalho efetuado sob a orientação

Doutora Iva Pashkuleva

Professor Doutor Rui Luís Gonçalves dos Reis

Abril de 2022

DIREITOS DE AUTOR E CONDIÇÕES DE UTILIZAÇÃO DO TRABALHO POR TERCEIROS

Este é um trabalho académico que pode ser utilizado por terceiros desde que respeitadas as regras e boas práticas internacionalmente aceites, no que concerne aos direitos de autor e direitos conexos.

Assim, o presente trabalho pode ser utilizado nos termos previstos na licença abaixo indicada.

Caso o utilizador necessite de permissão para poder fazer um uso do trabalho em condições não previstas no licenciamento indicado, deverá contactar o autor, através do RepositóriUM da Universidade do Minho.

Licença concedida aos utilizadores deste trabalho

Atribuição

CC BY

https://creativecommons.org/licenses/by/4.0/

ACKNOWLEDGMENTS

Firstly, I would like to express my genuine gratitude to my supervisor, Dr. Iva Pashkuleva, whose expertise, insightful feedback, and guidance were invaluable during this path. Thank you for all the opportunities to learn and grow, for the support, motivation, and patience, for hearing me and challenging me at so many levels.

I would like to sincerely acknowledge my co-supervisor and director of 3B's Research Group, Prof. Dr. Rui L. Reis, for the continuous support of my Ph.D. degree and related research and for providing all the necessary means to carry out my work at 3B's.

I would also like to acknowledge Dr. Diana Soares da Costa and Dr. Ramón Novoa-Carballal for sharing their knowledge, helping me daily, and believing in the work developed. To Dr. Ricardo Pires, I would like to thank all the insightful discussions on the work, help, and availability. Finally, to the laboratory technicians, a special thanks for their devoted work, making ours easier every day.

This work would not be possible without funding. For that, I want to acknowledge the Portuguese Foundation for Science and Technology - FCT (SFRH/BD/114847/2016, PTDC/NAN-MAT/28468/2017, PTDC/QUI-POL/28117/2017, CEECIND/00814/2017, IF/00373/2014, IF/00032/2013 and CytoNanoHeal ENMed/001/2015) and European Commission (H2020-WIDESPREAD-FoReCaST-668983, H2020-TWIN-CHEM2NATURE-692333, and ComplexiTE ERC-2012-ADG 20120216-321266).

I am thankful to have and count on such amazing friends at work. Thank you, Diana, Luísa and Cristiana, for brightening my days and constantly reminding me that I matter.

Last but not least, I want to acknowledge the most important people in my life, my family. Thank you, mum and dad, for all your patience, support, and advice and for showing me how to be strong, resilient, and independent. You both are my role models. Thank you, João, for always being close and kind. Thank you, Edmundo, my best friend and love. Without you all, I could not do it.

STATEMENT OF INTEGRITY

I hereby declare having conducted this academic work with integrity. I confirm that I have not used plagiarism or any form of undue use of information or falsification of results along the process leading to its elaboration.

I further declare that I have fully acknowledged the Code of Ethical Conduct of the University of Minho.

NANOGLICANO: glicoferramentas para elucidar interações moleculares e celulares dos glicanos *in vitro*

Resumo: Os glicosaminoglicanos (GAGs) regulam processos biológicos vitais através da interação com recetores celulares, nas matrizes extracelular e pericelular. Estes apresentam diferentes bioatividades, tendo um papel fundamental em condições fisiológicas e patológicas. A diversidade de GAGs em estrutura e atividade tem motivado o desenvolvimento de plataformas destinadas ao estudo fundamental de mecanismos moleculares ativados por GAGs e de dispositivos que modulam o comportamento celular. Esta tese contribui para a ciência dos glicanos e para o estado de arte tecnológico com o desenvolvimento de diferentes glicoferramentas de 1D (Capítulo VI), 2D (Capítulos III, IV e V), e 3D (Capítulo VII) que demonstram a relevância da apresentação de GAGs na bioatividade, interação com recetores e potencial terapêutico. A tese explora a imobilização de GAGs pelo açúcar redutor, mimetizando a apresentação nativa e preservando a funcionalidade e movimento molecular. As glicoferramentas desenvolvidas foram usadas em estudos fundamentais na interação com células cancerígenas (Capítulos III, IV e V) e aplicados ao direcionamento terapêutico em cancro (Capítulos VI e VII). A tese é focada no GAG ácido hialurónico (HA) pelo seu envolvimento na iniciação e progressão do cancro. Os Capítulos III, IV e V são dedicados a estudos fundamentais, enquanto os Capítulos VI e VII são orientados a aplicações. No Capítulo III, mostramos que o HA solúvel e imobilizado interage de forma diferente com os recetores CD44 e RHAMM. Com base nestes resultados, os trabalhos seguintes foram planeados usando HA imobilizado. Nos Capítulos IV e V, desenvolvemos plataformas para testar a densidade do HA com gradientes unidirecionais de HA e gradientes duplos, de HA e grupos amina, mimetizando a apresentação do HA num ambiente complexo similar à matriz extracelular. Estas plataformas foram usadas para estudar o efeito da densidade do HA no comportamento de células do cancro da mama. Nos Capítulos VI e VII, são apresentadas nanoestruturas baseadas em GAGs com interação específica com o CD44. No Capítulo VI, sintetizamos um co-polímero ramificado com HA (polímeros longos de HA foram inseridos num polímero sintético central) com potencial de adjuvante no tratamento de cancro por interação competitiva com o CD44. No Capítulo VII, desenvolvemos veículos sensíveis a estímulos para transporte de fármacos hidrofóbicos e hidrofílicos em cancro. De uma forma geral, os resultados apresentados nesta tese demonstram a utilidade das glicoferramentas para compreender e modular mecanismos biológicos e patológicos.

Palavras-chave: cancro da mama; glicosaminoglicanos; gradientes de HA; imobilização pela extremidade; nanoestruturas

NANOGLYCAN: glycotools for elucidating molecular and cellular interaction of glycans *in vitro*

Abstract: Glycosaminoglycans (GAGs) regulate vital biological processes by interacting with cell receptors and other biomolecules at the extracellular and pericellular matrix. GAGs can display different bioactivities depending on the environment, and thus, they are key players in health and disease. Their diversity in terms of structure and activity has motivated the development of GAGs-based platforms towards fundamental studies of molecular mechanisms with GAGs involvement and devices that modulate the cell behavior. This thesis contributes to the glycoscience and technology state-of-the-art by developing different 1D (Chapter VI), 2D (Chapters III, IV, and V), and 3D (Chapter VII) glycotools that demonstrate the relevance of GAGs presentation on its bioactivity, receptors' interaction(s), and therapeutic potential. The thesis explores end-on immobilization of GAGs that mimics their native presentation and preserves their functionality and molecular freedom. The developed glycotools were used in fundamental biological studies on GAGs interactions with cancer cells (Chapter III, IV, and V) and for therapeutic targeting in cancer (Chapter VI and VII). The thesis focuses on the GAG hyaluronan (HA) due to its involvement in tumorigenesis, metastasis, and tumor progression: the altered synthesis and degradation of HA in cancer lead to activation of different pro-tumorigenic signaling pathways. Chapters III, IV, and V are devoted to fundamental studies, while Chapters VI and VII are application-oriented. In Chapter III, we show that soluble and immobilized HA interacts differently with CD44 and RHAMM receptors. Based on these results, we have designed the following works with end-on immobilized HA. In Chapters IV and V, we developed a screening platform for HA content, *i.e.*, a unidirectional HA gradient and a double gradient of HA and amino groups that mimic the presentation of HA in a complex ECM-like environment. We have used these platforms to study the effect of HA density on the behavior of breast cancer cells. In Chapters VI and VII, we present GAG-based nanostructures for targeting CD44, which is commonly overexpressed in cancer cells. In Chapter VI, we synthesize branched HA block co-polymer (long HA polymers grafted on a core synthetic polymer) with the potential to be an adjuvant in cancer treatment by competitive interactions with CD44. In Chapter VII, we develop stimuli-responsive vehicles for hydrophobic and hydrophilic drugs that are efficient for cancer targeting. Altogether, the results presented in this thesis highlight the utility of glycotools to understand and target biological and pathological mechanisms.

Keywords: breast cancer; end-on immobilization; glycosaminoglycans; HA gradients; nanostructures;

TABLE OF CONTENTS

LIST OF ABBREVIATIONS AND ACRONYMS

%EE	Encapsulation efficiency
1D	1 Dimension
1H NMR	Proton nuclear magnetic resonance spectroscopy
2D	2 Dimension
3D	3 Dimension
5-FU	Fluorouracil

A

Abs Mn	Absolute molecular weight
AcOH	Acetic acid
AcONa	Sodium acetate
AFAP-110	Actin filament-associated protein
AFM	Atomic force microscopy
AIBN	Azobisisobutyronitrile
AKT	Serine/threonine protein kinase B
ANOVA	Analysis of variance test
App Mn	Apparent molecular weight
APTES	(3-aminopropyl) triethoxysilane
ATCC	American type culture collection
AURKA	Aurora kinase A

B

BCA	Bicinchoninic acid
bFGFR	Basic fibroblast growth factor receptor
BS^3	Bis(sulfosuccinimidyl)suberate
BSA	Bovine serum albumin

C

CAF	Cancer-associated fibroblasts

CD168	Cluster of differentiation 168
CD44	Cluster of differentiation 44
CD44s	CD44 standard
CD44v	CD44 variants
Cdc42	Cell division control protein 42
cIAP-2	Cellular inhibitor of apoptosis 2
CMC	Critical micelle concentration
COL1A1	Collagen type I alpha 1 chain
COX-2	Cyclooxygenase-2
$cPLA_2\alpha$	Cytosolic phospholipase 2 alpha
CS	Chondroitin sulfate
CSC	Cancer stem cells
CSF-1	Macrophage-colony stimulating factor
CXCL1	C-X-C motif ligand 1
CXCL10	C-X-C motif chemokine ligand 10

D

DAMP	Damage-associated molecular pattern
DAPI	4′,6-diamidino-2-phenylindole
DC	Dendritic cells
Dh	Hydrodynamic diameter
ΔH_{app}	Apparent enthalpy
DLS	Dynamic light scattering
DMEM	Dulbecco modified Eagle medium
DMF	Dimethylformamide
DMSO	Dimethyl sulfoxide
DOT1L	DOT1-like histone H3K79 methyltransferase
DS	Degree of substitution
DTT	1,4-dithiothreitol

E

E	FRET efficiency
ECM	Extracellular matrix
EDTA	Ethylenediaminetetraacetic acid
EGFR	Epidermal growth factor receptor
ELK-1	ETS domain-containing protein Elk-1
ELS	Electrophoretic light scattering
EMT	Epithelial to mesenchymal transition
EPR	Enhanced permeability and retention
Eq.	Equivalents
ErbB2	Receptor tyrosine-protein kinase
ERK-1,2	Extracellular-signal-regulated kinase 1, 2
ERM	Ezrin/radixin/moesin
ERα	Estrogen receptor alpha
ETS	Erythroblast transformation specific

F

F-actin	Filamentous actin
FAK	Focal adhesion kinase
FBS	Fetal bovine serum
FGF-2	Fibroblast growth factor 2
FITC	Fluorescein-5-isothiocyanate
F	Fluorescence intensity
FRET	Förster resonance energy transfer

G

Gab1	GRB2-associated-binding protein 1
GAG	Glycosaminoglycan
GAPDH	Glyceraldehyde 3-phosphate dehydrogenase
GFP	Green fluorescent protein
GlcA	D-glucuronic acid

GlcNAc	N-acetyl-D-glucosamine
GPC	Gel permeation chromatography
Grb2	Growth factor receptor-bound protein 2
GSC	Glioblastoma stem cell
GSH	Glutathione
GSK-3β	Glycogen synthase kinase-3 beta

H

HA	Hyaluronan; hyaluronate; hyaluronic acid
HAbp	HA binding protein
HARE	Hyaluronan receptor for endocytosis
HAS	HA synthase
HEMA	2-hydrohyethylmethacrylate
HEPES	(4-(2-hydroxyethyl)-1-piperazineethanesulfonic acid)
HER2	Human epidermal growth factor receptor 2
HMMR	Hyaluronan-mediated motility receptor
HMW HA	High molecular weight, above 1 MDa HA
HOXD10	Homeobox D10
HPLC	High-performance liquid chromatography
HYAL	Hyaluronidase

I

IC_{50}	Half-maximal inhibitory concentration
IFN-γ	Interferon-gamma
IHABP	Intracellular hyaluronan receptor
IL	Interleukin
IP_3	Inositol trisphosphate
IRAK	IL-1 receptor-associated kinase 4
iRHAMM	Intracellular RHAMM
ITC	Isothermal titration calorimetry

J

JNK-1,2	Jun N-terminal kinase 1 and 2

K

k_{a1}	Association constants of the binding of the analyte
k_{a2}	Association constants of conformational adjustment of the formed complex
K_{CAT}	Turnover rate
k_{d1}	Dissociation constants of the binding of the analyte
k_{d2}	Dissociation constants of conformational adjustment of the formed complex
K_{EFF}	Catalytic efficiency
K_M	Michaelis constant
K_{SV}	Stern Volmer constant

L

Lgr5	Leucine-rich repeat-containing G protein-coupled
LMW HA	Low molecular weight HA, below 700 kDa
LS	Light scattering
LYVE-1	Lymphatic vessel endothelial hyaluronan receptor 1

M

MAPK	Mitogen-activated protein kinases
MDR1	Multidrug-resistant protein 1
MDSC	Myeloid-derived suppressor cells
MEK	Mitogen-activated protein kinase kinase
MIP	Major intrinsic protein
MMP	Metalloproteinase
Mn	Number-average molecular weight
mRNA	Messenger RNA
MT1-MMP	Membrane-type 1 matrix metalloproteinases
MTA3	Metastasis-associated 1 family member 3
mTOR	Mammalian target of rapamycin

MTS	3-(4,5-dimethylthiazol-2-yl)-5-(3-carboxymethoxyphenyl)-2- (4-sulphofenyl)-2H-tetrazolium
Mw	Weight average molecular weight
MyD88	Myeloid differentiation primary response 88

N

Nanog	Homeobox protein NANOG
NFE2L2	Nuclear factor erythroid 2-like 2
NF-κB	Nuclear factor-kappa light chain enhancer of activated B cells
NHE1	Na^+-H^+ exchanger-1
NHS	N-hydroxysuccinimide
NK	Natural killer cells
N-Pht	N-hydroxyphthalimide

P

p21	Cyclin-dependent kinase inhibitor 1
PAI-1	Plasminogen activator inhibitor-1
PAK1	P21-activated kinase 1
PAMP	Pathogen-associated molecular pattern molecules
PAR1b-MST	Partitioning-defective 1b-Macrophage Stimulating
PARP	Poly (ADP-ribose) polymerase
PBS	Phosphate-buffered saline
PDCD4	Program cell death 4
PDGF	Platelet-derived growth factor
PDGFR	Platelet-derived growth factor receptor
PDI	Polydispersity index
PDVF	Polyvinylidene fluoride
PE	Phycoerythrin
PI3K	Phosphoinositide 3-kinases
PKCα/βII	Protein kinase Calpha/betaII
PKCς	Protein kinase C sigma

PKCε	Protein kinase C epsilon
PMSF	Phenylmethylsulphonyl fluoride

R

Rac1	C3 botulinum toxin substrate 1
R_g	Radius of gyration
R_h	Hydrodynamic radius
RHAMM	Receptor for hyaluronic acid-mediated motility
Rho	Rhodamine
RhoA/ROK	Rhoa/Rho-associated protein kinase
RI	Refractive index
RIPA	Radioimmunoprecipitation assay buffer
RNS	Reactive nitrogen species
ROI	Region of interest
RON	Recepteur d'origine nantais
ROS	Reactive oxygen species
RT	Room temperature
RTK	Protein kinase receptor

S

SDS	Sodium dodecyl sulfate
SDS-PAGE	Sodium dodecyl sulfate-polyacrylamide gel electrophoresis
SEM	Scanning electron microscopy
SPR	Surface plasmon resonance
Src	Proto-oncogene tyrosine-protein kinase
Stab-2	Stabilin-2
STAT3	Signal transducer and activator of transcription 3

T

TAM	Tumor-associated macrophages
TBS-T	Tris-buffered saline-Tween 20

TCPS	Tissue culture polystyrene
TGF-β1	Transforming growth factor-beta 1
THF	Tetrahydrofuran
TLR2,4	Toll-like receptors 2 and 4
TLRs	Toll-like receptors
TME	Tumor microenvironment
TNF-α	Tumor necrosis factor-alpha
TPX2	TPX2 microtubule nucleation factor
TRAF6	TNF receptor-associated factor 6

U

uPa	Urokinase plasminogen activator

V

Vav2	Guanine nucleotide exchange factor Vav2
VEGF-C	Vascular endothelial growth factor C

W

WB	Western blotting
WGA	Wheat germ agglutinin

X

XIAP	X-linked inhibitor of apoptosis protein
XLKD1	Extracellular link domain containing 1

Y

YAP	Yes-associated protein

Z

ZEB1	Zinc finger E-box-binding homeobox 1

LIST OF EQUATIONS

LIST OF FIGURES

LIST OF SUPPLEMENTARY FIGURES

LIST OF SCHEMES

LIST OF SUPPLEMENTARY SCHEMES

LIST OF TABLES

LIST OF SUPPLEMENTARY TABLES

SHORT *CURRICULUM VITAE*

Ana Carvalho obtained a degree in Applied Biology in 2013 at the University of Minho with a bachelor's thesis entitled "Development of DODAP:MO liposomes for drug delivery" under the supervision of Prof. Dr. Elisabete Oliveira and Prof. Dr. Andreia Gomes from the School of Science at the University of Minho. In 2013, Ana enrolled the Master course in Biophysics and Bionanosystems at the University of Minho, which was concluded successfully in 2015. Her Master thesis entitled "Optimization of pharmacokinetic and pharmacodynamic profiles of anticancer drugs through its vesiculation in lipid-based nanosystems" was supervised by Dr. Marlene Lúcio and Prof. Dr. Andreia Gomes from the School of Science at the University of Minho, in collaboration with Prof. Dr. Elisabete Oliveira and Prof. Dr. Ana Preto. During her Master, Ana participated in a 6 month Master's Internship Programme at International Iberian Nanotechnology Laboratory (INL) under the supervision of Dr. Jana Nieder. In 2016, she worked for a year as a researcher under the projected ComplexiTE (ERC-2012-ADG 20120216-321266) under the supervision of Prof. Dr. Rui L. Reis at 3B's Research Group at the University of Minho. Since 2017, Ana has been a Ph.D. student in the Doctoral Programme on Tissue Engineering, Regenerative Medicine and Stem Cells, under the supervision of Dr. Iva Pashkuleva and Prof. Dr. Rui L. Reis and supported by an individual FCT fellowship (2017-2021).

So far, Ana has received two Awards: *Best Tissue Engineering Idea* awarded at Gene2Skin Winter School in 2017 and *Research Prize 2015* awarded by Students Association from the University of Minho (AAUM) and Microsoft. Ana is the author and co-author of 10 full-length papers published in international peer-reviewed scientific journals (8 published and 2 submitted), 2 review papers (1 published and 1 submitted), 9 oral communications and 19 poster presentations at national and international conferences.

LIST OF PUBLICATIONS

The work performed during the Ph.D. fellowship resulted in the publications listed below.

Papers in international scientific journals with peer-reviewing (as the first author)

Carvalho, Ana M.; Reis, Rui L.; Pashkuleva, Iva: "Hyaluronan receptors as mediators and modulators of the tumor microenvironment", submitted.

Carvalho, Ana M.; Soares da Costa, Diana; Reis, Rui L.; Pashkuleva, Iva: "RHAMM expression tunes the response of breast cancer cell lines to hyaluronan", submitted.

Carvalho, Ana M.; Valcarcel, Jesus; Gomes, Marisa; Vázquez, José António; Reis, Rui L.; Novoa-Carballal, Ramon; Pashkuleva, Iva: "Hyaluronan brush-like copolymers promote CD44 declustering in breast cancer cells", submitted.

Carvalho, Ana M.; Soares da Costa, Diana; Reis, Rui L.; Pashkuleva, Iva: "Influence of hyaluronan density on the behavior of breast cancer cells with different CD44 expression", Advanced Healthcare Materials, 2021, 2101309.

Carvalho, Ana M.; Soares da Costa, Diana; Paulo, Pedro M.R.; Reis, Rui L.; Pashkuleva, Iva: "Co-localization and crosstalk between CD44 and RHAMM depend on hyaluronan presentation" Acta Biomaterialia, 2021, 119, 114-124.

Carvalho, Ana M.; Teixeira, Raquel; Novoa-Carballal, Ramón; Pires, Ricardo A.; Reis, Rui L.; Pashkuleva, Iva: "Redox-Responsive Micellar Nanoparticles from Glycosaminoglycans for CD44 Targeted Drug Delivery" Biomacromolecules, 2018, 19, 7, 2991-2999.

Others - Papers published during the Ph.D. degree

Carvalho, Ana M., Fernandes, Eduarda; Gonçalves, Hugo; Giner-Casares, Juan J.; Bernstorff, Sigrid; Nieder, Jana B.; Oliveira, M. Elisabete C.D.R.; Lúcio, Marlene: "Prediction of paclitaxel pharmacokinetic based on in vitro studies: Interaction with membrane models and human serum albumin", International Journal of Pharmaceutics, 2020, 580, 119222.

Carvalho, Ana M., Marques, Alexandra P.; Silva, Tiago H.; Reis, Rui L.: "Evaluation of the Potential of Collagen from Codfish Skin as a Biomaterial for Biomedical Applications", Marine Drugs, 2018, 16, 495.

Papers in international scientific journals with peer-reviewing (as co-author)

Ribeiro, Sofia; **Carvalho, Ana M.**; Fernandes, Emanuel M.; Gomes, Manuela E.; Reis, Rui L.; Bayon, Yves; Zeugolis, Dimitrios I.: "Development and characterisation of cytocompatible polyester substrates with tunable mechanical properties and degradation rate" Acta Biomaterialia, 2021, 121, 303-315.

Domínguez-Arca, Vicente; Costa, Rui R.; **Carvalho, Ana M.**; Taboada, Pablo; Reis, Rui L.; Prieto, Gerardo; Pashkuleva, Iva: "Liposomes embedded in layer by layer constructs as simplistic extracellular vesicles transfer model" Materials Science and Engineering: C, 2021, 121, 111813.

Others - Papers published during the Ph.D. degree

Soares, Telma B.; Loureiro, Luís; **Carvalho, Ana M.**; Oliveira, M. Elisabete C.D.R.; Dias, Alberto; Sarmento, Bruno; Lúcio, Marlene: "Lipid nanocarriers loaded with natural compounds: Potential new therapies for age related neurodegenerative diseases?", Progress in Neurobiology, 2018, 168, 21-41.

Conference oral presentations (as first author speaker)

Carvalho, Ana M., Soares da Costa, Diana; Reis, Rui L.; Pashkuleva, Iva: "Hyaluronan presentation regulates RHAMM and CD44 expression in breast cancer cells", 2nd FORECAST Workshop, Porto (Portugal), July 2019

Carvalho, Ana M., Soares da Costa, Diana; Reis, Rui L.; Pashkuleva, Iva: "Hyaluronan presentation regulates RHAMM and CD44 expression and location in breast cancer cells", 2019 HA Conference, Cardiff (Whales), June 2019.

Carvalho, Ana M., Soares da Costa, Diana; Reis, Rui L.; Pashkuleva, Iva: "Hyaluronan gradients for cells separation and identification", 29th Annual Meeting of European Society for Biomaterials, Maastricht (Netherlands), September 2018.

Carvalho, Ana M.; Teixeira, Raquel; Novoa-Carballal, Ramón; Reis, Rui L.; Pashkuleva, Iva: "Glycosaminoglycans micelles for targeting drug delivery", 28th Annual Conference of the European Society for Biomaterials, Athenes (Greece), September 2017.

Carvalho, Ana M.; Teixeira, Raquel; Novoa-Carballal, Ramón; Reis, Rui L.; Pashkuleva, Iva: "Potential of thiol-amphiphile glycosaminoglycans as redox-sensitive nanoparticles", GLUPOR12 12ª Reunião do Grupo de Glúcidos, Aveiro (Portugal), September 2017.

Carvalho, Ana M.; Teixeira, Raquel; Novoa-Carballal, Ramón; Pires, Ricardo A.; Reis, Rui L.; Pashkuleva, Iva: "Redox-sensitive self-assembled glycosaminoglycans nanoparticles for targeted drug delivery", Chem2Nature Second School, Porto (Portugal), June 2017.

Conference posters (as first author)

Carvalho, Ana M.; Soares da Costa, Diana; Reis, Rui L.; Pashkuleva, Iva: "Hyaluronan degree of freedom determines its recognition and cell response in breast cancer cells", Second Achilles Conference, Braga (Portugal), November 2019.

Carvalho, Ana M.; Soares da Costa, Diana; Reis, Rui L.; Pashkuleva, Iva: "RHAMM/CD44 expression and co-localization in breast cancer cells depend on hyaluronan presentation", 1st Discoveries CTR Forum, Porto (Portugal), September 2019.

Carvalho, Ana M.; Soares da Costa, Diana; Reis, Rui L.; Pashkuleva, Iva: "Crosstalk between the main receptors of hyaluronan: a FRET-based study on CD44/RHAMM dynamics upon HA binding", Chem2Nature Final Conference, Guimarães (Portugal), October 2018.

Carvalho, Ana M.; Soares da Costa, Diana; Reis, Rui L.; Pashkuleva, Iva: "Hyaluronan gradients – nanoglycotools to understand the role of HA-CD44 interactions in cancer", Chem2Nature Summer School, Porto (Portugal), June 2018.

Carvalho, Ana M.; Soares da Costa, Diana; Reis, Rui L.; Pashkuleva, Iva: "High-throughput platform for the elucidation of cell-glycosaminoglycans interactions", International Symposium on Bioinspired Macromolecular Systems, Aveiro (Portugal), November 2017.

Carvalho, Ana M.; Soares da Costa, Diana; Reis, Rui L.; Pashkuleva, Iva: "Development of a glycan-based platform for the elucidation cell-glycosaminoglycans interactions", FoReCaST 1st Workshop, Porto (Portugal), November 2017.

Conference posters (as co-author)

Domínguez-Arca, Vicente; Costa, Rui R.; **Carvalho, Ana M.**; Taboada, Pablo, Reis, Rui L.; Prieto, Gerardo; Pashkuleva, Iva: "Layer-by-layer constructs containing liposomes as reductionist exosome transfer models", 1st Discoveries CTR Forum, Porto (Portugal), September 2019.

Domínguez-Arca, Vicente; Costa, Rui R.; **Carvalho, Ana M.**; Taboada, Pablo, Reis, Rui L.; Prieto, Gerardo; Pashkuleva, Iva: "Characterizing Biointerfaces formed by Supported Vesicle Layer (SVL) on Polyelectrolytes Multilayers (PEMs). Drug Release and Cell Interaction", 8th Iberian Meeting on Colloids and Interfaces (RICI8), Aveiro (Portugal), July 2019.

Domínguez-Arca, Vicente; Costa, Rui R.; **Carvalho, Ana M.**; Taboada, Pablo, Reis, Rui L.; Prieto, Gerardo; Pashkuleva, Iva: "Liposomes immobilization in ECM-like matrices for controlled drug delivery and cellular uptake", 2nd FORECAST Workshop, Porto (Portugal), July 2019.

Fernandes, Maria G.; Carvalho, Ana M.; Silva; Lucília P.; Pires, Ricardo A.; Reis, Rui L.; Marques, Alexandra P.: "Analysis of human skin mechanical properties by tensile and nanoindentation techniques" GENE2SKIN Final Conference, Guimarães (Portugal), October 2018.

Carvalho, Andreia F.; Ribeiro, Raquel S.; Gasperini, Luca; Silva, Lucília P.; **Carvalho, Ana M.**; Marques, Alexandra P.; Reis, Rui L.: "High-throughput screening of optimal osteogenic differentiation conditions in Gellan Gum hydrogel microfibers", 29th European Conference on Biomaterials, Maastricht (Netherlands), September 2018.

Ribeiro, Raquel S.; Carvalho, Andreia F.; Gasperini, Luca; **Carvalho, Ana M.**; Silva, Lucília P.; Marques, Alexandra P.; Reis, Rui L.: "Multiparametric Screening of Marine-Origin Biomaterials for Bone Tissue Engineering", Gene2Skin Winter School, Porto (Portugal), November 2017.

Awarded grants

Ph.D. scholarship awarded by Fundação para Ciência e Tecnologia (SFRH/BD/114847/2016).

"You can, you should, and if you're brave enough to start, you will."

Stephen King, On Writing: A Memoir of the Craft

SECTION 1

GENERAL INTRODUCTION

CHAPTER I

HYALURONAN RECEPTORS AS MEDIATORS AND MODULATORS OF THE TUMOR MICROENVIRONMENT

HYALURONAN RECEPTORS AS MEDIATORS AND MODULATORS OF THE TUMOR MICROENVIRONMENT

Abstract

The tumor microenvironment (TME) is a dynamic and complex matter shaped by heterogeneous cancer and cancer-associated cells present at the tumor site. Hyaluronan (HA) is a major TME component that plays pro-tumorigenic and carcinogenic functions. These functions are mediated by different hyaladherins expressed by cancer and tumor-associated cells triggering downstream signaling pathways that determine cells fate and contribute to TME progression towards a carcinogenic state.

Herein, we review the interaction of HA with several cell-surface hyaladherins - CD44, RHAMM, TLR2 and 4, LYVE-1, HARE and layilin. We discuss the signaling pathways activated by these interactions, the respective response of different cell populations within the TME, and the modulation of the TME. Potential cancer therapies *via* targeting these interactions are also briefly discussed.

This chapter is based on the following publications:

Carvalho, Ana M.; Reis, Rui L.; Pashkuleva, Iva: "Hyaluronan receptors as mediators and modulators of the tumor microenvironment", submitted.

I.1. Introduction

The tumor microenvironment (TME) is a complex and dynamic setting where tumorigenesis occurs. TME comprises multiple heterogeneous cellular populations, including cancer stem cells (CSC); tumor-infiltrating immune and inflammatory cells – T and B lymphocytes, tumor-associated macrophages (TAM), dendritic cells (DC), natural killer (NK) cells, neutrophils, and myeloid-derived suppressor cells (MDSC); stromal cells – cancer-associated fibroblasts (CAF), pericytes, mesenchymal stromal cells; blood and lymphatic vessels; and tissue-specific cell types (Fig. I.1). These cells participate in autocrine and paracrine signaling that modify the surrounding extracellular matrix (ECM) through the secretion and deposition of bioactive molecules. The introduced changes modulate the cell-cell and cell-ECM interactions, contributing to tumor cells proliferation, invasion, metastasis, and determining the therapeutic response, as explained in detail by several excellent recent reviews.[1-6]

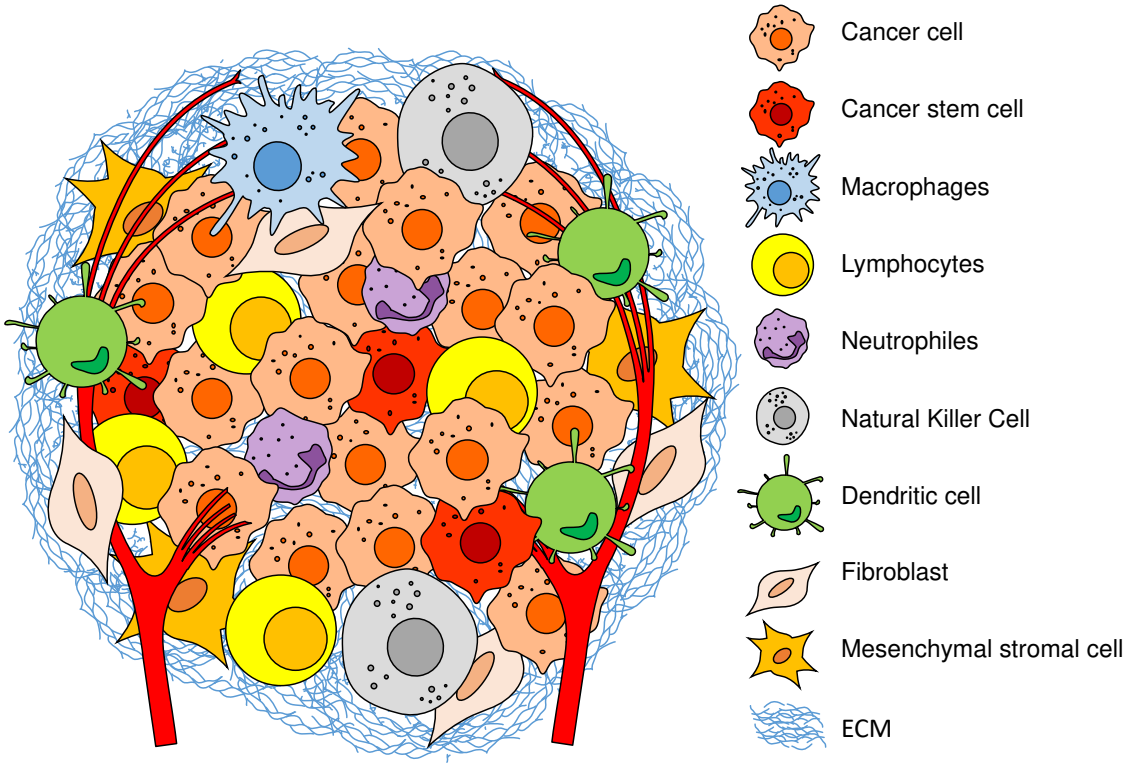

Figure I.1. Schematic presentation of the tumor microenvironment complexity arising from the heterogeneous cellular populations that constantly remodel the surrounding extracellular matrix (ECM).

Among different signaling molecules in TME, hyaluronan (HA) is a well-known multimodal player: it can regulate cell proliferation, apoptosis, multidrug resistance, and survival; induce cell invasion and metastases formation, and contribute to evading the immune response. HA homeostasis is altered since the early stages of tumorigenesis, and this alteration contributes to cancer initiation and progression (Fig. I.2).[7-11] HA is synthesized at the cell membrane by three hyaluronan synthases (HAS1-3) through the alternate conjugation of D-glucuronic acid (GlcA) and N-acetyl-D-glucosamine (GlcNAc) (Fig. I.2A).[12] The synthesized linear polymer with a size of 3 to 4 MDa is secreted into the ECM, where is degraded by hyaluronidases (HYALs) and reactive oxygen/nitrogen species (ROS/RNS) to shorter HA fragments and oligomers.[13] Both synthesis and degradation of HA are upregulated in most cancers, resulting in an accelerated turnover and accumulation of HA with different sizes in extra- and pericellular space (Fig. I.2B). Such HA accumulation is a hallmark of several cancers, *e.g.*, pancreatic carcinomas, lung, breast, prostate, and colorectal cancers, and head to neck tumors, and a marker of poor prognosis.[5, 14, 15]

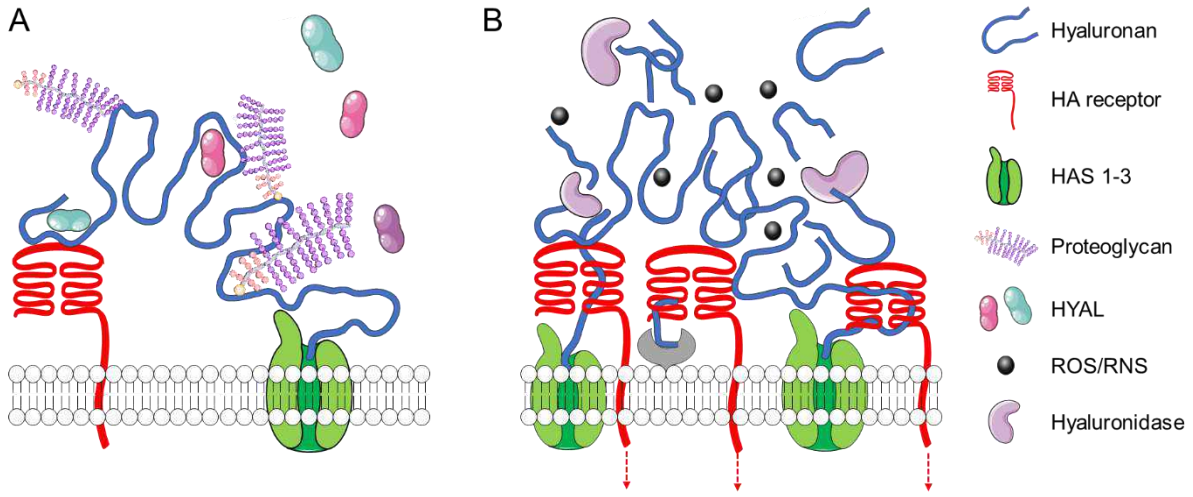

Figure I.2. Hyaluronan synthesis and degradation. (A) In healthy tissues, HA is synthesized at the cell membrane by HAS1-3 into a high molecular weight polymer. HA is secreted and deposited into the pericellular and extracellular matrix, where it interacts with cell receptors and other ECM components, including proteoglycans and hyaladherins. (B) In the tumor microenvironment, the increased expression and activity of HASs and HYALs, together with high redox potential and increased reactive oxygen/nitrogen species (ROS/RNS), lead to accelerated HA turnover and accumulation of HA fragments and oligomers.

The bioactivity of HA depends on its molecular weight: high molecular weight (above 1 MDa, HMW) and low molecular weight HA (up to 700 kDa, LMW) usually induce different and often opposite cell behavior (reviewed [16, 17]). This divergent cell response is due to the different interactions between the available extra- and pericellular HA and the specific cell receptors, namely cluster differentiation 44 (CD44), the receptor for hyaluronan-mediated motility (RHAMM), toll-like receptor 2 (TLR2), TLR4, lymphatic vessel endothelial hyaluronan receptor 1 (LYVE-1), hyaluronan receptor for endocytosis (HARE), and layilin, which regulate the TME interactome and thus, the cancer aggressiveness and metastatic potential (Table I.1).

In this review, we discuss the interactions of HA with these receptors and the respective downstream signaling pathways leading to tumorigenic behavior of different cell populations within TME. We also tackle the potential of targeting HA/receptors interactions as a therapeutic approach.

Table I.1: Cell response induced by HA interactions with its receptors in different models. Data from the last 5 years.

Receptor	Cell response	Model	Ref
CD44	Proliferation	Cholangiocarcinoma cell lines; Non-small cell lung cancer; Breast carcinoma cells; Colon cancer cells; Breast cancer stem cell-like cells; Ovarian cancer cells; Pancreatic cancer.	[18-24]
	Anti-apoptosis/Survival	Non-small cell lung cancer; Breast cancer cells; Colon cancer cells; Cancer stem cells of head and neck squamous cell carcinoma.	[19-21, 25, 26]
	Motility and Invasion	Cholangiocarcinoma cell lines; Breast carcinoma cells; Head and neck squamous cell carcinomas and its cancer stem cells; Ovarian cancer cells.	[18, 23, 26-28]
	Epithelial to mesenchymal transition	Head and neck squamous cell carcinomas; Breast cancer cells; Liver cancer cells.	[28-30]
	Stemness	Head and neck squamous cell carcinomas; Breast cancer stem cell-like cells; Liver cancer cells.	[22, 28, 30]
	Radio/Chemotherapy resistance	Head and neck squamous cell carcinomas; Colorectal cancer; Breast cancer stem cell-like cells.	[21, 22, 26, 28]

	Metastasis	Head and neck squamous cell carcinomas; Pancreatic cancer.	[24, 28]
RHAMM	Proliferation	Lung adenocarcinoma cells; Ovarian cancer cells; Prostate cancer cells; Breast carcinoma cells; Adenocarcinoma of the breast duct; Non-small cell lung cancer; Fibrosarcoma cells.	[19, 31-33]
	Survival	Ovarian cancer cells; Prostate cancer cells; Breast carcinoma cells; Adenocarcinoma of the breast duct; Non-small cell lung cancer.	[19, 32]
	Motility	Lung adenocarcinoma cells; choriocarcinoma cells.	[31, 34]
	Epithelial to mesenchymal transition; Chemotherapy resistance and stemness	Gastric cancer cells.	[35]
TLR2,4	Inflammation	Melanocytes.	[36]
	Proliferation	Colorectal cancer; Colorectal cancer cells; Glioblastoma stem-like cells.	[21, 37]
	Anti-apoptosis/Survival	Colorectal cancer; Colorectal cancer cells.	[21]
	Radiotherapy resistance	Colorectal cancer.	[21]
LYVE-1	(Lymph node) Metastasis	Breast cancer cells; Oral squamous cell carcinoma; Melanoma cells.	[38-40]
	Proliferation	Lymphatic endothelial cells.	[41]
	Motility	Breast cancer cells; Lymphatic endothelial cells.	[38]
	Adhesion/Docking and migration (to TME)	Dendritic cells.	[42]
	Lymphangiogenesis	Lymphatic endothelial cells.	[38, 41]
	Tight junctions disruption	Lymphatic vessels endothelium.	[40]
Soluble LYVE-1	Inhibits cell proliferation	Melanoma cells.	[43]
	Inhibits lymphangiogenesis	Corneal lymphangiogenic models in mice.	[44]
HARE	Proliferation, motility, and inflammation	Lymphatic endothelial cells.	[45]
Layilin	Immunomodulator	Immuno infiltrates in gastric and colon cancers; Infiltrating T cells in liver cancer;	[46, 47]
	Invasion	Glioma cells;	[48]

I.2. The Cluster of Differentiation 44 (CD44)

CD44 is the most studied HA receptor. It is involved in the normal homeostasis of different tissues and ubiquitously expressed on the surface of the cells of these tissues. It is overexpressed in several cancers and is a compelling marker of CSCs.[28] CD44 is a non-kinase transmembrane glycoprotein (P-glycoprotein 1) that interacts with HA through BX_7B motifs (where B is arginine or lysine residues and X_7 is a sequence of seven non-acidic amino acids) at the N-terminal region of the extracellular portion (Link domain, Fig. I.3).[49] CD44 mediates HA signaling and HA internalization and degradation, thus contributing to HA local turnover.[50] CD44 is coded by a single gene but has different variants (CD44v) due to alternative splicing and post-translational modifications, *e.g.*, glycosylation, which are often deregulated in cancer. Alternative splicing of *CD44* gene results in CD44 isoforms with variable exons - variant 2 to 10 (Fig. I.3), which provide new conformations and binding sites and have different/additional functions than standard CD44 (CD44s, 85-95 kDa), affecting tumor-initiating and metastatic potential (reviewed [51]). Altered *N*- or *O*- glycosylation of CD44 also affects HA-CD44 interactions and the metastatic potential of cancer cells.[52, 53] As an example, truncated *O*-glycosylation enhances the affinity of HA to CD44, thus, enhancing the tumorigenic signaling.[52]

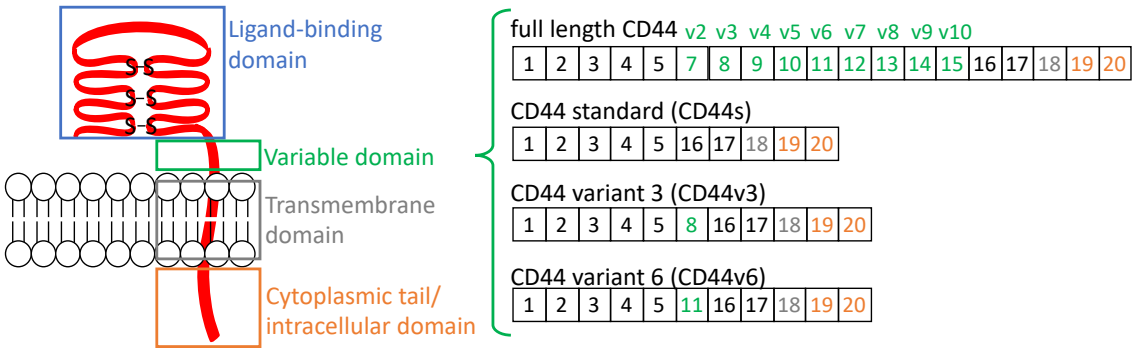

Figure I.3. CD44 structural diversity is due to variable exons (v) that are inserted in the extracellular region next to the cell membrane. Some of the cancer-associated variants are also shown.

I.2.1. CD44 as a signaling hub.

In TME, CD44 acts as a signaling hub because it can trigger different signaling cascades in a function of the environment, thus, eliciting various cellular responses. The high expression of CD44 alone is not an indicator of its (pro)tumorogenic behavior.[54] CD44 is usually activated upon HA binding, which elicits protein conformational changes. The adopted conformations favor the formation of multimolecular complexes by additional binding of adaptor molecules, such as molecular switchers (*e.g.*, Rho GTPase proteins RhoA, RhoC, Rac, and Cdc42) or cytoskeletal anchor proteins that trigger different downstream signaling.

There are also other mechanisms by which CD44 can affect the cell behavior in TME. One of these mechanisms implies the formation of clusters by multivalent interactions with HA, HAS, and other receptors (*e.g.*, Erbb2, Erbb3, EGFR, IGF1R-β, PDGFR, c-MET) within lipid rafts.[55-63] Another mechanism involves sequential cleavage of the CD44 that is frequently observed in human tumors and associated with increased metastatic potential.[55, 64-66] In this process, the ectodomain of CD44 is first cleaved by membrane-type 1 matrix metalloproteinases (MT1-MMP) and then presenilin-1/γ-secretase acts to release the CD44 intracellular domain. The released CD44 intracellular domain translocates to the nucleus where is involved in the regulation of the transcription of genes related to survival, inflammation, glycolysis, and tumor invasion

I.2.2. HA/CD44 mediates enhanced cell growth and survival via RhoA/ROK activation.

HA binding to CD44 can activate transforming protein RhoA/Rho-associated protein kinase (RhoA/ROK) downstream signaling *via* phosphorylation of proto-oncogene tyrosine-protein kinase (Src) (Fig. I.4A). [67, 68] The activation of this signaling cascade is associated with enhanced cell growth, survival, and invasion in different cancers, including head and neck, pancreatic, colon, ovarian, and breast. [19, 23, 24, 59, 65, 69, 70] The increased growth, survival and invasiveness of cancer cells result from the GRB2-associated-binding protein 1, phosphoinositide 3-kinases and protein kinase B pathway (Gab1-PI3K/AKT, Fig. I.4A1)[67, 68, 71] that triggers activation of the mammalian target of rapamycin (mTOR) transcriptor factor, downregulation of tumor suppressor proteins such as homeobox D10 (HOXD10) and cyclin-dependent kinase inhibitor 1 (p21), upregulation of survival proteins cellular inhibitor of apoptosis 2 (cIAP-2) and x-linked inhibitor of

apoptosis protein (XIAP), *i.e.*, different factors that contribute to a (pro)tumorogenic profile.[18, 26, 71-74] As an example, in human metastatic breast tumor cells, RhoA/ROK activates the adaptor protein Gab-1 linked to PI3K/Akt signaling, mediating cytokine macrophage-colony stimulating factor (CSF-1) production and enhancing cell growth, survival, and invasion.[71]

In addition, the activation of AKT signaling can lead to HAS2 overexpression and induce a feedback loop: an enhanced HA synthesis leads to CD44 overexpression and sustain PI3K/AKT signaling.[25]

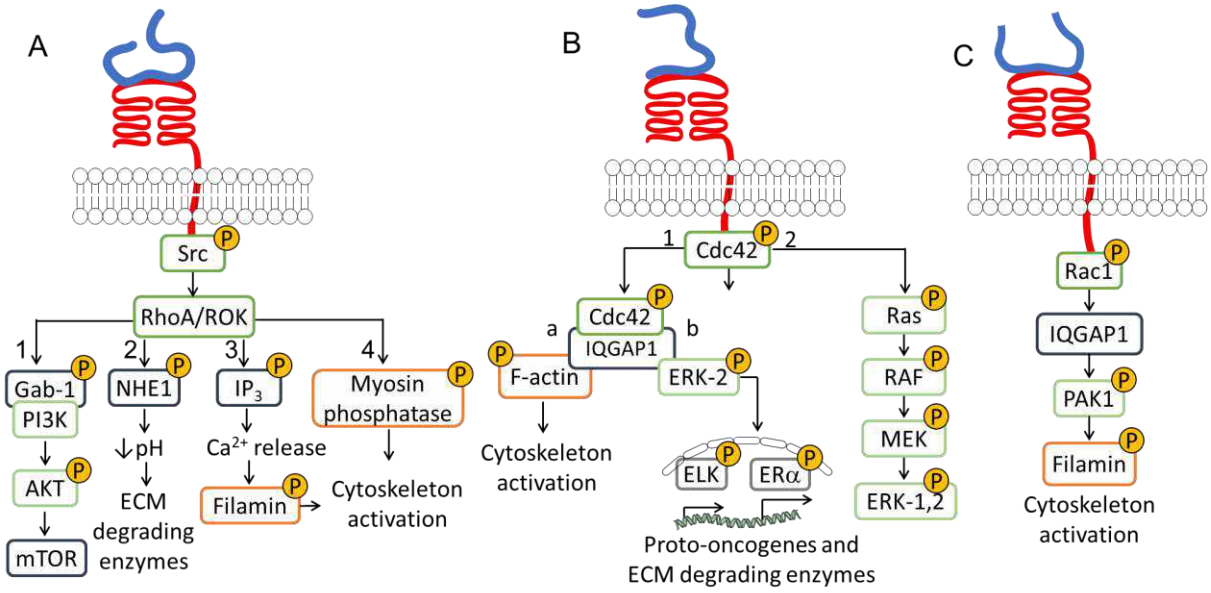

Figure I.4. HA/CD44-mediated RhoGTPase signaling pathways via (A) RhoA/ROK, (B) Cdc42, and (C) Rac1 that modulate cell proliferation, motility, and invasion.

The HA/CD44-mediated RhoA/ROK activation also affects the cytoskeletal function and cell motility of metastatic breast tumor cells and colon carcinoma cells (Figs. I.4A2-4).[75-77] RhoA/ROK activates Na^+-H^+ exchanger-1 (NHE1) (Fig. I4A2), resulting in ECM acidification and activation of ECM-degrading enzymes thus facilitating cell motility and invasion (Fig. I.4A2).[77] Another pathway involves RhoA/ROK triggered phosphorylation of inositol trisphosphate (IP_3) receptors that induce internal Ca^{2+} release and activation of Ca^{2+}-dependent signaling (Fig. I.4A3) such as phosphorylation of filamin, which activates the cytoskeleton and enhances cell motility.[76] In addition, RhoA/ROK activates myosin phosphatase that is a direct regulator of cytoskeletal contraction (Fig. I.4A4).[68, 75]

I.2.3. CD44 is involved in the cytoskeleton remodeling and enhances cell motility.

CD44 is involved in the formation and remodeling of the cell cytoskeleton *via* different signaling pathways. On one hand, structural and fundamental studies show that CD44 can interact directly with cytoskeleton proteins, such as ezrin/radixin/moesin (ERM), to facilitate microtubules and filamentous actin (F-actin) binding.[78-82] On the other hand, HA/CD44 binding can also trigger different signaling pathways that affect the cytoskeleton formation and the related cellular motility. The RhoA/ROK pathway mentioned above is one example but other members of the RhoGTPase family (Ras, Rac1, and Cdc42) can also be phosphorylated upon HA/CD44 interaction and evoke cytoskeleton remodeling and increased cell migration of ovarian and breast tumor cells, lymphomas, neuroblastomas, melanomas and carcinomas.[83-87] HA/CD44-dependent cell division control protein 42 (Cdc42) phosphorylation can activate the mitogen-activated protein kinases (MAPK)/ extracellular-signal-regulated kinase 1, 2 (ERK-1,2) signaling pathway (Fig. I.4B2), which is involved in actin remodeling and cytoskeletal organization.[83] In ovarian cancer cells, the phosphorylated Cdc42 forms complex with the cytoskeletal adaptor protein IQGAP1 that regulates the cytoskeletal function *via* F-actin (Fig. I.4B1a). Cdc42/IQGAP1 complex can be involved in the regulation of cell motility by association with ERK-2, leading to erythroblast transformation specific (ETS) domain-containing protein Elk-1 (ELK-1) and estrogen receptor-alpha (ERα) mediated transcriptional up-regulation and expression of proto-oncogenes and ECM-degrading enzymes (Fig. I.4B1b).[84]

HA/CD44-dependent c3 botulinum toxin substrate 1 (Rac1) activation provides a fast response to changes in the TME. In breast tumor cells and invasive lymphoma cells, signaling through Rac1 activates p21-activated kinase 1 (PAK1), IQGAP1, and filamin (Fig. I.4C), leading to actin assembly at membrane ruffling and pseudopod structures, mediating cell morphology alterations, adhesion, and motility.[85-87]

I.2.4. HA/CD44 induces epithelial to mesenchymal transition and stem-like phenotype.

HA/CD44 interaction induces epithelial to mesenchymal transition (EMT), which together with the HA-induced cell motility, supports tumor cell invasion and facilitates primary tumor extravasation.[88] In breast cancer, HA/CD44 interaction is associated with increased expression

and activity of the EMT marker zinc finger E-box-binding homeobox 1 (ZEB1).[29] ZEB1 is involved in a feedback signaling cascade resulting in overexpression of HAS2 and CD44.[29] This autocrine signaling mechanism supports EMT and promotes the formation of metastasis. In CD44-positive head and neck squamous cell carcinomas, the CD44-mediated activation of MAPK/ERK-1,2/Homeobox protein NANOG (Nanog) induces stem-like cells phenotypes (*e.g.*, increased phosphorylation of ERK-1,2 and jun N-terminal kinase 1,2 (JNK-1,2) and ability to colony and form spheroids).[28] These cells show increased growth, migration, and invasion, associated with EMT-characteristic markers and resistance to radiotherapy, which were reversed through Nanog knockdown.[28] CD44 also acts as a co-receptor mediating HA-dependent EMT (Table I.2). In liver cancer cells, HA interaction with CD44 associated with transforming growth factor-beta 1 (TGF-β1) signaling plays a central role in EMT.[30] SNU-368 hepatocarcinoma cells ($CD44^+$ and $TGF\text{-}\beta1^+$) express EMT markers (increased N-cadherin and decreased E-cadherin) regulated by AKT/glycogen synthase kinase-3β (GSK-3β)/β-catenin pathway. The activation of this signaling pathway is dependent on both CD44 and TGF-β1 and results in enhanced cell migration and ability to form spheres.

I.2.5. HA/CD44 dependent chemoresistance and survival.

HA/CD44 enhances cell survival by avoiding apoptosis and chemoresistance in several types of cancer. These events are regulated through CD44-mediated signaling with diverse downstream effectors. One of the reported mechanisms is *via* protein kinase C epsilon (PKCε) activation. In breast and ovarian tumor cells, PKCε phosphorylates the transcription factor Nanog that at nuclear level enhances the expression of anti-apoptotic proteins (IAPs) and multidrug-resistant protein 1 (MDR1) and decreases tumor suppressor proteins, *e.g.*, program cell death 4 (PDCD4) (Fig. I.5).[89-91] Nanog can also form complexes with signal transducer and activator of transcription 3 (STAT3) that have a similar effect.

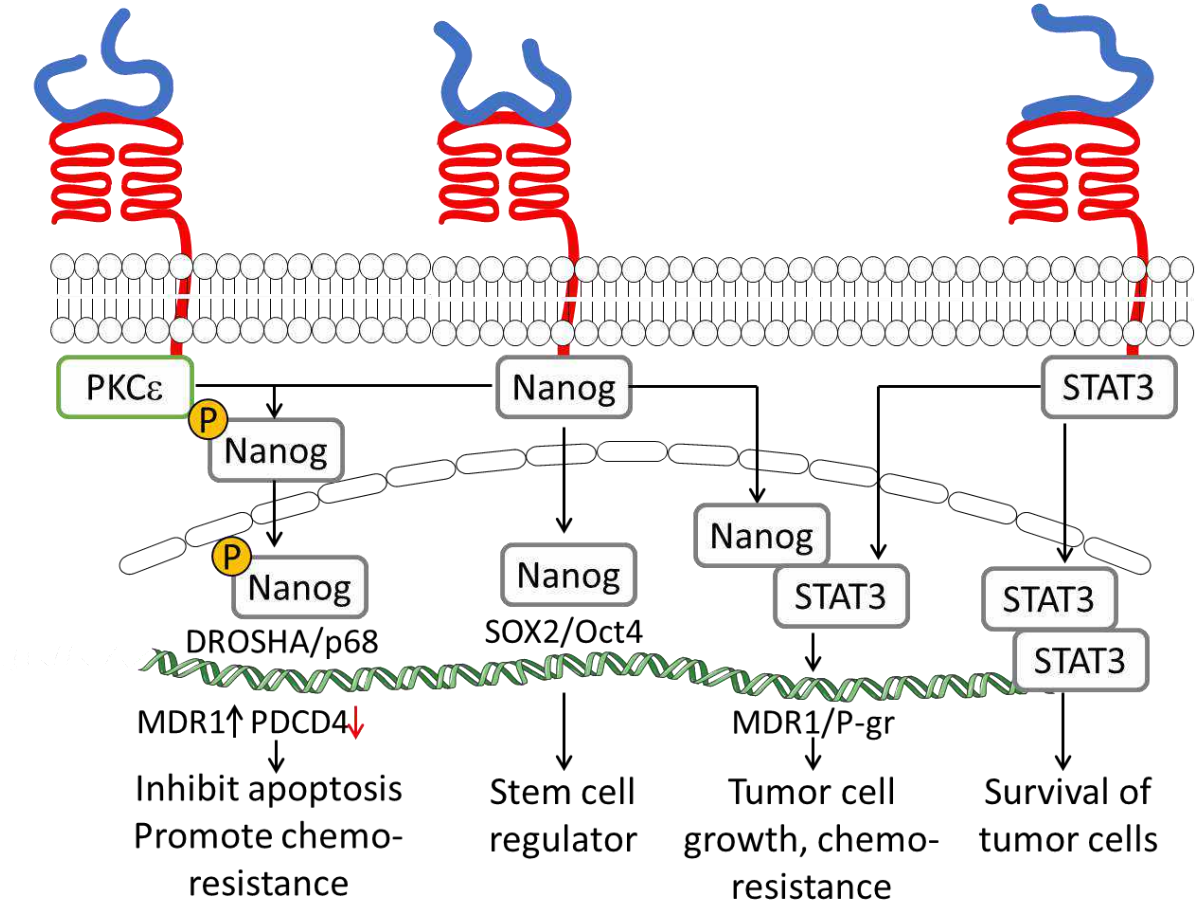

Figure I.5. HA/CD44 binding activates different signaling pathways that promote chemoresistance and inhibit the apoptosis of tumor cells.

In head and neck CSCs, HA/CD44 enhances cell survival and chemoresistance *via* DOT1-like histone H3K79 methyltransferase (DOT1L)/miR-10b-dependent activation of RhoGTPase pathway that leads to the expression of survival proteins, *e.g.*, cIAP-2 and XIAP.[26] HA/CD44 binding can also indirectly regulate cell survival and chemoresistance. In CSC, HA/CD44 activates the nuclear factor erythroid 2-like 2 (NFE2L2), a regulator of antioxidant genes, through p62 overexpression. As a result, CSC are protected from ROS-rich microenvironment, and the tumor aggressiveness, growth, and chemoresistance are enhanced.[22] Recently, the role of HA/CD44 as a regulator of the Hippo signaling pathway (modulates cell proliferation and apoptosis) was reported.[20] CD44 clusters sequester the Hippo signaling-inhibitor complex partitioning-defective 1b-macrophage stimulating (PAR1b-MST). Upon declustering, this pathway is inhibited through yes-associated

protein (YAP) nuclear translocation and the expression of pro-oncogenic and anti-apoptotic genes.[20, 92]

I.2.6. Co-association of CD44 with other receptors.

As mentioned above, CD44 can act as a co-receptor in signaling cascades, increasing pro-tumorigenic behavior (Table I.2). In colon and breast carcinoma cells, the formation of HA/CD44/receptor tyrosine-protein kinase (ErbB2) complex activates PI3K/AKT signaling pathway, increasing β-catenin transcription factor activity and, consequently, the transcription of proliferative (cyclooxygenase-2 (COX-2)) and multidrug resistance (MDR1) genes, leading to cancer cell growth, survival and chemoresistance (Fig. I.6A).[93, 94] In head and neck cancer cells, the HA/CD44/epidermal growth factor receptor (EGFR) complex increases cell growth, drug resistance, and motility through downstream MAPK/ERK-1,2 signaling.[62] HA/CD44/receptor for hyaluronan-mediated motility (RHAMM) forms a signaling complex with ERK-1,2 to sustain rapid basal motility of invasive breast cancer cell lines.[27, 95] In ovarian tumors, the association of HA/CD44 with growth factor receptor-bound protein 2 and human epidermal growth factor receptor 2 (Grb2-HER2) and guanine nucleotide exchange factor Vav2 (Vav2) protein activates Rac1 and Ras pathways, increasing cell growth and migration (Fig. I.6B).[69] HA/CD44 is also associated with the IP_3 receptor in lipid rafts, promoting HA-mediated Ca^{2+} signaling leading to nitric oxide generation and proliferation.[96]

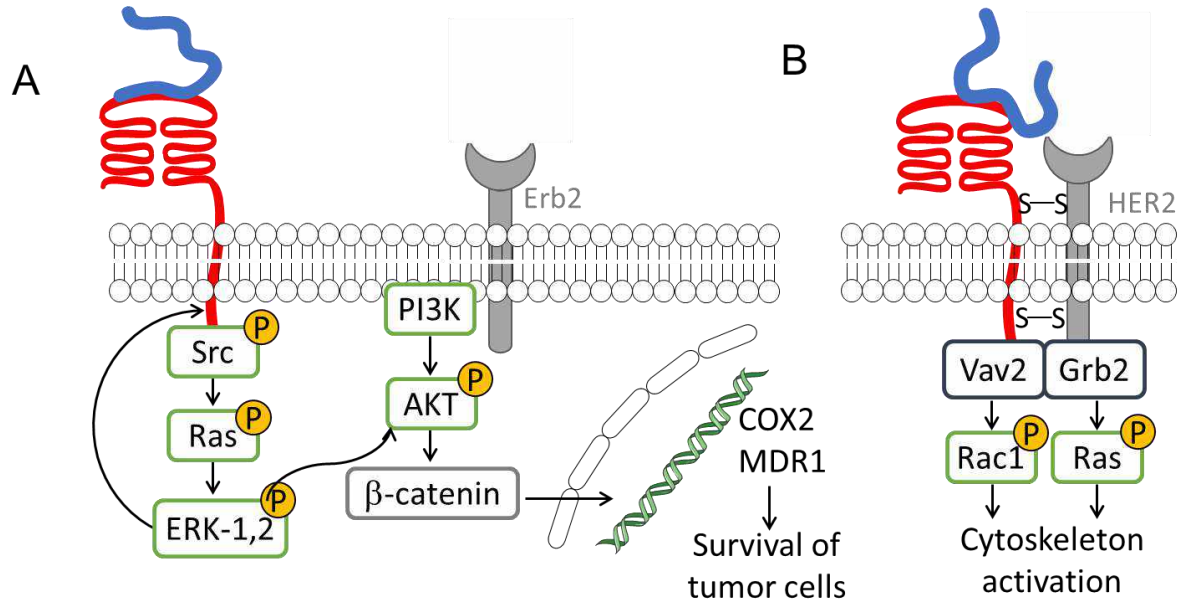

Figure I.6. Co-association of HA/CD44 signaling with (A) Erb2 and (B) HER2, supporting tumor cell survival and migration.

The supplementation of breast cancer cells with HA induces the association of CD44 and α5β1-integrin *via* talin.[88] This signaling complex activates Src and focal adhesion kinase (FAK), inducing phosphorylation of cortactin and paxillin that promote cell motility during cancer cell extravasation from TME and cell adhesion to endothelial cells and fibronectin-rich matrix of the metastatic environment.[88] Simultaneously, tumor cell motility and TME extravasation are facilitated through the upregulation and proteolytic activity of urokinase plasminogen activator (uPa), serin protease, collagen-degrading enzymes, metalloproteinases (MMPs), and cathepsin mediated by HA/CD44 interaction.[97-100]

The complex of HA, CD44 and toll-like receptors (TLRs) modulate cytokine/chemokine production in breast tumor cells (Table I.2).[101] Interaction of LMW HA with CD44 and TLR2,4 recruits actin filament-associated protein (AFAP-110) and myeloid differentiation primary response 88 (MyD88) into signaling complexes (Fig. I.9B). Active AFAP-110 binds to F-actin and activates the cytoskeleton, while MyD88 binds to nuclear factor kappa light chain enhancer of activated B cells (NF-κB) at the nuclear level and induces interleukin 1 beta (IL-1β) and interleukin 8 (IL-8)

expression. These signaling events lead to the stimulation of cell invasion and production of cytokine/chemokine in breast tumor cells.[101]

I.3. RECEPTOR FOR HYALURONAN MEDIATED MOTILITY (RHAMM)

RHAMM, also known as intracellular hyaluronan receptor (IHABP), hyaluronan-mediated motility receptor (HMMR), and the cluster of differentiation 168 (CD168) is not expressed in normal tissues. It is found transiently expressed during tissue repair[102, 103] and constitutively present in many carcinomas, *e.g.*, breast, prostate, gastrointestinal tract, and the aggressive forms of multiple myeloma, leukemias, and lymphomas.[104-106] RHAMM contains an HA-binding domain based on the BX_7B motif; however, it is structurally different from the CD44 HA-binding domain.[11, 107] Like CD44, RHAMM is coded by a single gene, *HMMR*, and different isoforms of RHAMM result from alternatively spliced transcript variants, alternate start codon, and post-translational processes (Fig. I.7).[108] RHAMM does not contain a membrane-spanning domain – it is soluble and, thus, can be localized in different cell compartments, including cytoplasm, nucleus, cell membrane, and/or in the ECM usually as a complex with two or more biomolecules.[109, 110] The different localizations of RHAMM contribute to the intra-/extracellular exchange of information – a phenomenon called dynamic reciprocity.[104, 111] Initially, intracellular RHAMM was identified (85 kDa in humans and 95 kDa in murine) and designated as RHAMMv5. It was associated with cell locomotion as indicated by its name. Currently, RHAMM is known as a multifunctional protein involved in different signaling processes at the cell surface and intracellularly. RHAMM variants have different functions in cancer. For example, overexpression of RHAMM isoform lacking N-terminal microtubule-binding domain[112] promotes pancreatic cancer in mouse and xenograft models. However, a recent study shows that RHAMM plays different roles in different cancer subtypes. While in malignant breast cancer, RHAMM overexpression correlates with aggressiveness and motility, overexpression of RHAMM on the luminal A subtype breast cancer inhibits cell migration via the AKT/GSK3β/Snail pathway.[113]

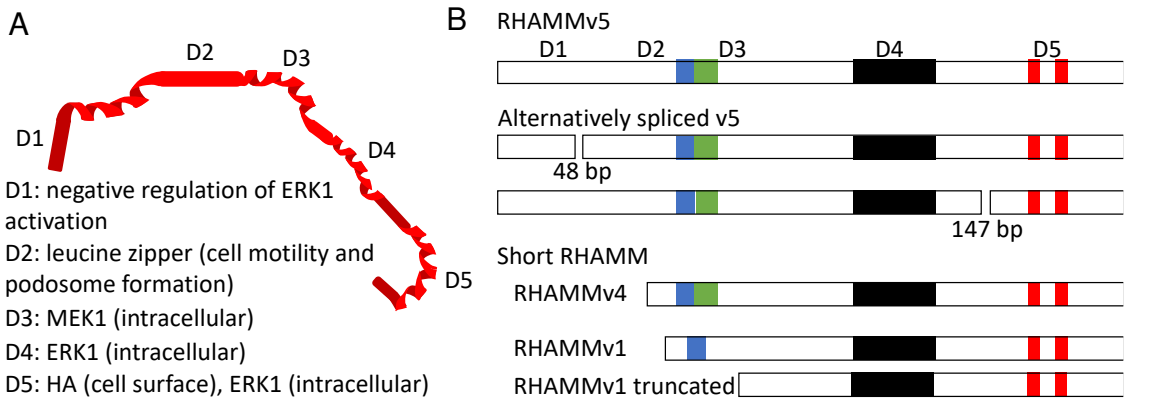

Figure I.7. (A) RHAMM exists as a coiled-coil protein containing short stretches and several functional domains (D1-D5). (B) Domain structure of RHAMM. The figure is adapted from [114]

I.3.1. Cell surface RHAMM.

Cell surface RHAMM/HA complexes usually include other proteins, *e.g.*, protein kinase receptors (RTKs) and non-RTKs, such as CD44[19, 27, 95, 115, 116], platelet-derived growth factor (PDGF)[117], TGFβ[35, 116] or Recepteur d'origine nantais (RON)[118]. The composition of these different complexes modulates the downstream signaling by activating alternative molecular switchers, *e.g.*, Src[119] and Ras[117, 119-122].

I.3.1.1. Cytoskeleton dynamics and cell motility.

The main cellular events arising from HA/RHAMM interaction are enhanced cell motility and invasion, which are regulated by different and complementary signaling pathways. HA/RHAMM interaction directly activates protein kinase C sigma (PKCς) and FAK, recruiting cortactin and paxillin to focal adhesions (Fig. I.8A1).[123]

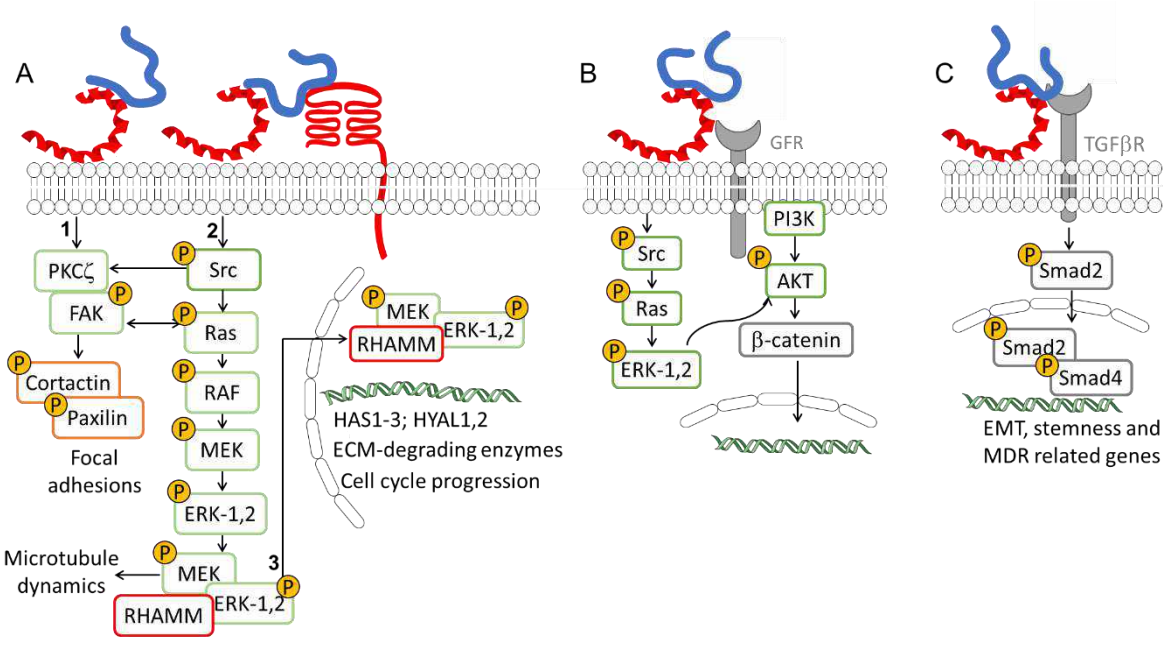

Figure I.8. The HA/RHAMM interactions at the cell surface activate different downstream signaling in cancer that can lead to (A) enhanced cell motility, (B) proliferation, and (C) epithelial to mesenchymal transition (EMT).

Alternative signaling involves the association of HA/RHAMM either with CD44 or GFR to transiently activate Src in cell lamellae, where it recruits and activates FAKs and cortactin, coordinating cell motility (Fig. I.8A2, Table I.2).[119] In c-H-ras oncogene transformed fibroblasts, the activation of Ras signaling pathway promotes a rapid assembly and disassembly (turnover) of focal adhesions at cell lamellae, promoting high random cell motility (Fig. I.8A2).[120, 121] In breast cancer cells, HA recognition by RHAMM activates Ras/MAPK pathway and requires both cell surface and intracellular RHAMM.[117] Cell surface RHAMM/HA complex, associated with CD44 and/or GFRs, activates Ras/MAPK, forming complexes between the intracellular RHAMM, mitogen-activated protein kinase kinase (MEK), and ERK-1,2 (Fig. I.8A2). This complex binds to microtubules and promotes cytoskeleton dynamics required for cell motility and cell cycle progression.[95, 115, 117, 124] RHAMM/MEK/ERK-1,2 complex displays different functions at the nuclear level, where it promotes the expression of plasminogen activator inhibitor-1 (PAI-1) and MMP-9 that are involved in cell invasion and inflammation (Fig. I.8A3).[106] In choriocarcinoma cells ($CD44^-/RHAMM^+$ phenotype), HA/RHAMM/GFR-induced motility results

from MEK/ERK-1,2 activation mediated by PI3K and evidence a crosstalk between PI3K/AKT and Ras/MAPK signaling pathways (Fig. I.8B, Table I.2).[34]

I.3.1.2. Cell proliferation.

Recently, cell proliferation has also been associated with HA/RHAMM interaction. [31, 35, 125] HT1080 fibrosarcoma cells treated with LMW HA showed RHAMM-dependent growth induced via Ras/MAPK interaction with the β-catenin pathway (Fig. I.8B).[125] This leads to β-catenin overexpression and complexation with ERK-1,2. The translocation of this complex to the nucleus upregulates c-Myc transcription and alters cell proliferation.[33, 126, 127] HA/RHAMM interaction promotes the association of TPX2 microtubule nucleation factor (TPX2) with RHAMM at the nucleus and the activation of aurora kinase A (AURKA), which directly regulates transcription of HAS1, HAS2 and HAS3, HYAL1 and HYAL2, cyclins and motility effectors, increasing cell proliferation, cell motility and enhancing tumorigenic HA signaling.[105, 128, 129] Other RHAMM-dependent pathways might be involved in enhancing cell proliferation as *HMMR* silencing decreases both mRNA and protein expression of Cdc2 and CyclinB1 related to cell cycle progression.[31] Blocking HA/RHAMM interactions, either by abolishing HA synthesis or RHAMM expression, decreases cancer cell proliferation and survival. Silencing of *HAS2* and *HAS3* in lung cancer cells has such effect. Blocking of HA synthesis downregulates CD44, RHAMM, EGFR, AKT, and ERK-1,2, and induces cleavage of caspase-3 and poly (ADP-ribose) polymerase (PARP), *i.e.*, an apoptotic effect, which is reversed upon supplementation with HA.[19] RHAMM blockage with specifically designed peptides also inhibits proliferation and compromises cell viability, as demonstrated for ovarian cancer, prostate cancer, breast carcinoma, and adenocarcinoma of the breast duct cells, but not in non-tumor fibroblasts and fibroblasts RHAMM$^{(-/-)}$.[32]

I.3.1.3. Epithelial to mesenchymal transition and multidrug resistance.

Multidrug resistance, EMT, and stem cell-like properties depend on RHAMM and Smad2 expression and activity (Fig. I.8C, Table I.2).[35] As an example, fluorouracil (5-FU) resistant gastric cancer cells upregulate *HMMR* and its knocking down recovers the drug sensitivity. On the other hand, ectopic expression of RHAMM in parental SGC7901 and BGC823 gastric cancer cell

lines resulted in 5-FU resistance.[35] This effect was observed together with EMT confirmed by a reduced E-cadherin expression and increased expression of vimentin, N-cadherin, fibronectin, and pluripotency-associated markers, including *SOX2*, *NANOG*, *OCT4*, and *BMI*, - a pattern that was reversed with *HMMR* silencing.[35]

I.3.2. Intracellular RHAMM.

Intracellularly, RHAMM is found in the cytoskeleton and nucleus. Because RHAMM interacts with several kinases, it has been suggested that the primary function of intracellular RHAMM (iRHAMM) is to connect the cytoskeleton to signaling complexes, similar to what happens at the cell membrane. Indeed, RHAMM can bind to different microstructures, like actin filaments, podosomes, centrosomes, microtubules, and mitotic spindle thus, affecting cell motility and proliferation.[109, 130, 131]

iRHAMM can transduce extracellular signaling activated upon interactions of cell surface RHAMM. Fundamental studies using fibroblast models show that iRHAMM binds and forms complexes with MEK1 and ERK-1,2 in the cytoskeleton or nucleus.[115, 132] These complexes regulate the cell's random motility, mitotic spindle integrity, cell cycle progression, and gene expression in breast cancer cells and fibroma cells. iRHAMM/ERK-1,2 complexes are required for microtubule nucleation and link to centrosomal proteins, *e.g.*, TPX2 and AURKA, thus, playing a fundamental role in centrosome function including dynamic turnover of interphase microtubules and mitotic spindles.[133-136] Additionally, iRHAMM interacts with the cortical proteins, such as supervillin, to coordinate myosin II contraction and activate ERK-1,2, required for cell migration and proliferation.[137-139]

Table I.2. Hyaladherins as co-receptors in TME signaling: activated pathways and cell response

Hyaladherin	Co-receptor	Model	Pathway	Cell response	Ref
CD44	ErbB2	Colon carcinoma cells	PI3K/AKT	Cell growth and survival	[93, 94]
	EGFR	Head and neck cancer cells	MAPK/ERK-1,2	Cell growth, multidrug resistance, and cell motility	[62]
	Grb2-HER2/Vav2	Ovarian tumor cells	Ras/Rac	Cell growth and migration	[69]
	β1-integrin	Breast cancer cells	Src/FAK – cortactin and paxillin phosphorylation	Cell motility	[88]
	TGFβ receptor	Liver cancer cells	AKT/GSK-3β/β-catenin	EMT, stemness and cell migration	[30]
	TLR-2,4	Breast tumor cells	AFAP-110; MyD88/NF-κB	Cell invasion and cytokine/chemokine production	[101]
RHAMM	CD44 and/or GFR	Breast cancer cells	Ras/MAPK→ MEK/ERK-1,2/RHAMM complex	Rapid basal motility and invasion, cell cycle progression and inflammation	[27, 95, 117, 124]
	GFR	Choriocarcinoma cells	PI3K/MEK1/Erl-1,2	Cell motility	[34]
	TGFβ receptor	Gastric cancer	TGFβ/Smad-2	EMT, stemness and multifrug resistance	[35]
LYVE-1	VEGF-C and FGF-2	Lymphatic endothelial cells	Not described	Cell proliferation and lymphangiogenesis	[41]

I.4. TOLL-LIKE RECEPTORS (TLRS) 2 AND 4

TLRs are type I transmembrane receptors (700-1100 amino acids) expressed by immune cells as macrophages and dendritic cells (Fig. I.9A). They have a crucial role in innate immunity and the induction of adaptive immune responses. TLRs contain extracellular leucine-rich sequences and a cytoplasmic domain (Fig. I.9A) that are responsible for the recognition of damage-associated

molecular patterns (PAMPs) and damage-associated molecular patterns (DAMPs), as HA fragments, causing inflammatory responses.[140] TLRs act as dimers that can be either homodimers or heterodimers (either with other members of the TLR family or with different proteins), thus increasing the ligand diversity.

In humans, ten TLRs have been identified (TLR1-10) and classified into two groups: cell-surface TLRs (TLR1, TLR2, TLR4, TLR5, and TLR6) that recognize bacterial cell-surface components, and endosomal TLRs (TLR3, TLR7, TLR8, and TLR9), which recognize microbial or viral nucleic acids. Among these TLRs, TLR2 and TLR4 can recognize and bind HA.[141] A minimal size of 4 monosaccharide units (4-mer) of HA is required to interact with TLR2 or TLR4[142] but only longer HA fragments (6-mer) can engage heterodimer association of TLR4 and CD44, thus, enhancing intracellular signaling.[143]

TLRs are expressed in different cancers, including hepatocellular carcinoma, melanoma, neuroblastoma, lung, colon, breast, ovarian, cervical, and prostate cancers.[144] In advanced stages of carcinogenesis, HA/TLR2,4 downstream signaling contributes to tumor cell invasion and expression of cytokines and chemokines, which are closely related to cancer progression. The specific effect of HA/TLR2,4 depends on the cell and tumor environment.

I.4.1. Effect of HA molecular weight on TLR signaling.

TLR/HA interactions and binding depend on HA molecular weight. The TLR complexes involving HMW HA and the respective downstream signaling in cancer are not well studied, and the reports on HMW HA/TLR2,4 involvement in inflammatory disorders are controversial. There is limited evidence that TLR2 and TLR4 binding to HMW HA attenuates inflammatory processes. [145-148] Recently, the interactions between HMW HA and TLRs were associated with the formation of a physical barrier that limits access to the receptors instead of direct binding.[149] This is, however, not a common mechanism, as TLR activation/signaling in cancer is complex and depends on the pericellular coat dynamics.

In breast cancer cells, HA oligomers (3-5 kDa) form a triple complex with CD44 and TLR2 or TLR4 that promotes the invasiveness and synthesis of IL-1β.[101] The formation of the triple complex LMW HA/TLR2,4/CD44 activates two downstream signaling pathways: AFAP-110 that binds to F-

actin is recruited and regulates cytoskeleton activation (Fig. I.9B1), increasing cell invasion; and downstream signaling *via* MyD88 (Fig. I.9B2) that promotes NF-κB activation and nuclear translocation leading to transcription and release of pro-inflammatory cytokines, including tumor necrosis factor-alpha (TNF-α), major intrinsic protein (MIP), IL-1β, IL-6, IL-8, and IL-12, essential for cell recruitment and inflammatory state of the tumor microenvironment.[101, 150-153] In human melanoma cells, the LMW HA/TLR4 also activates NF-κB that triggers the overexpression of MMP2 and IL-8, contributing to melanoma progression (Fig. I.9C1).[154] In UVB-exposed melanocytes, *in situ* degradation of endogenous hyaluronan, by HYAL treatment, induces expression of the inflammatory cytokines IL-6, IL-8, C-X-C motif ligand 1 (CXCL1), and C-X-C motif chemokine ligand 10 (CXCL10) and activation of AKT pathway *via* TLR4 binding (Fig. I.9C2) that lead to increased cell proliferation and survival.[36]

Several *in vivo* studies using specific animal models have shown that HA/TLR4 binding drives tumor growth and suppresses apoptosis. As an example, significant inhibition of tumor growth was found in TLR4 deficient *in vivo* models.[21] The inhibition of tumor growth was more pronounced than observed for the respective CD44 deficiency models. Moreover, the systemic administration of a specifically designed peptide, PEP1, which binds to endogenous HA and blocks HA/TLR4 interaction, reduced the number of adenocarcinomas and inhibited tumor growth.[21] Signaling through TLR4 was confirmed using the MyD88 deficient model, which had a similar effect as PEP1 treatment. HA/TLR4 binding also supports proliferation and prevents apoptosis of colon carcinoma CT26 tumor isografts in mice models. Molecular analysis showed that HA/TLR4 activates β-catenin through PI3K/AKT pathway leading to expression of proliferative proteins (leucine rich repeat containing G protein-coupled (Lgr5), cyclin D1, β-catenin, R-spondin) that increase the risk of carcinogenesis (Fig. I.9C3).[155] In addition, tumor survival was enhanced due to arrest to spontaneous apoptosis resulted from NF-κB activation.[156, 157]

I.4.2. TLR expression as a function of TME.

During tumor development, the expression of TLRs varies because of their different regulation by the cancer cell populations existing at each development stage. In glioblastoma stem cells (GSCs), the low expression of TLR4 receptors allow them to survive regardless of inflammatory signals in

the tumor microenvironment.[158] During GSCs differentiation into cancer cells, TLR4 is upregulated through endogenous HA synthesis and autocrine signaling.[37] TLR4 activation induces proliferation and inflammation *via* the NF-κB pathway while avoiding terminal differentiation and senescence, supporting tumor growth and recurrence.[37]

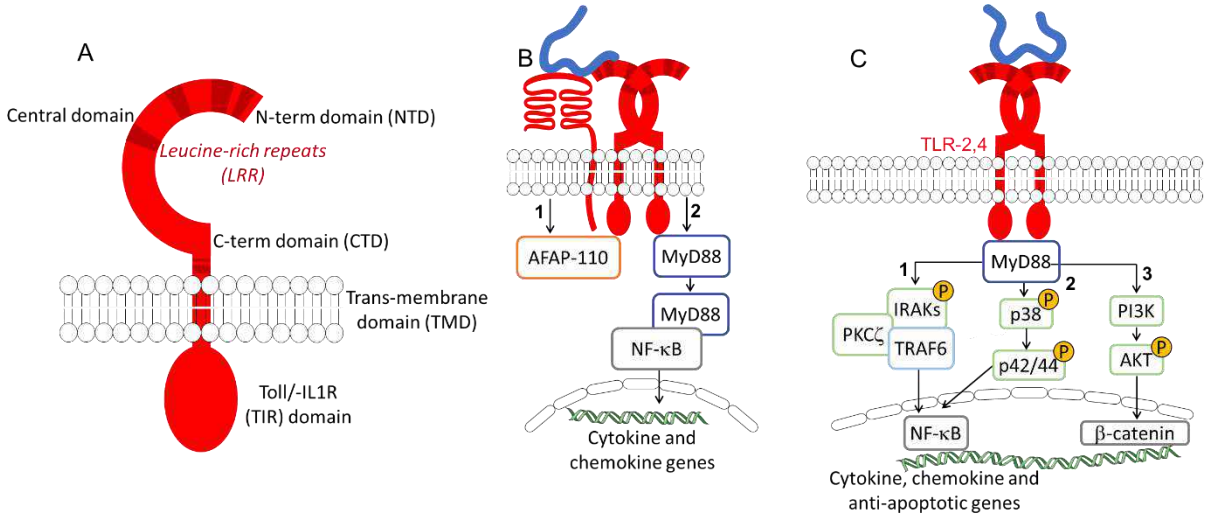

Figure I.9. (A) TLR structure and (B, C) signaling pathways activated upon (B) co-association of TLR4 with HA/CD44 and (C) homodimerization of TLR towards inflammation and cell survival in cancer.

The macrophages population in tumors is also tuned by the "cancerization" state of TME. After recruitment, monocytes differentiate to M2 immunosuppressive macrophages taking a pro-resolving role at the initial stages of cancer development.[159] At this point, the interaction of LMW HA, but not HMW, with CD44 and TLR4 inhibits the expression of pro-inflammatory cytokines (TNF-α and IL-12) and induces secretion of anti-inflammatory molecules (IL-10).[160, 161] Similar pro-resolving behavior is also observed in dendritic cells in the TME. HA fragments, but not native HA, interact with TLR4 in dendritic cells.[142] This interaction results in the activation of p38/p42/44 MAPK signaling pathway, nuclear translocation of NF-κB, and production of TNF-α that lead to dendritic cells maturation and immune-mediated anti-tumor response (Fig. I.9C2).[142]

With tumor progression, M0 macrophages and M2 macrophages are polarized into M1 pro-inflammatory macrophages and TLR signaling changes.[162] In human primary monocytes and murine macrophages, LMW HA engages TLR4 independently of other HA-receptors, through TLR4/MyD88/ERK-1,2/p38/JNK pathway resulting in the activation of cytosolic phospholipase 2 alpha ($cPLA_2\alpha$), responsible for the hydrolysis of arachnoid acid, which contributes to inflammation, proliferation, and metastasis.[162] Similar pro-inflammatory effects were observed as a consequence of the LMW HA/TLR2 interactions in macrophages. LMW HA/TLR2 activated NF-κB *via* MyD88/IL-1 receptor-associated kinase 4 (IRAK)/TNF receptor-associated factor 6 (TRAF6), and PKC-ζ pathway (Fig. I.9C1), stimulating the synthesis of pro-inflammatory cytokines (IL-2 and interferon-gamma (IFN-γ)). Supplementation of HMW HA inhibited this effect.[151]

I.5. LYMPHATIC VESSEL ENDOTHELIAL HYALURONAN RECEPTOR 1 (LYVE-1)

LYVE-1, also known as the extracellular link domain containing 1 (XLKD1), is a CD44 homolog encoded in humans by the *LYVE1* gene. This receptor is mainly expressed (but not limited to) by lymph vessels, and it is overexpressed in several cancers where it is considered an unfavorable prognostic marker. [38-40, 163, 164]

LYVE-1 binds to HA through the prototypic HA-binding domain (Fig. I.10A) conserved in the hyaladherins superfamily.[165] However, HA/LYVE-1 differs from HA/CD44 binding - while HA binding to CD44 is mediated by H-bonding and hydrophobic interaction, the HA/LYVE-1 interactions are mainly electrostatic and thus, sensitive to ionic strength (IC_{50} of 150 mM NaCl as compared with IC_{50}>2M NaCl for HA/CD44).[165] LYVE-1 binds either soluble LMW HA or HA immobilized within the pericellular coat.[42, 166] Mechanistically, LYVE-1 can act as a surface receptor,[42, 166] a signal transducer,[167] or a decoy for HA.[43] This receptor is also involved in HA uptake and degradation - it conveys HA for catabolism within lymphatic endothelial cells and also mediates HA transport into the lumen of afferent lymphatic vessels for subsequent re-uptake and degradation in lymph nodes.

The HA/LYVE-1 interactions are favored at high LYVE-1 density (focal clustering, Figs. I.10B, I.10C) or in the presence of HMW HA that increases the binding avidity (Fig. I.10D)[165, 166]. While the LYVE-1 binding domain is active as a monomer, its binding affinity to HA (K_d of 35.6

μM) is lower than the CD44 one (K_d of 65.7 μM),[165] and usually, LYVE-1 dimers bind HA with intermediate to high molecular weight and mediate its internalization.[168-170]

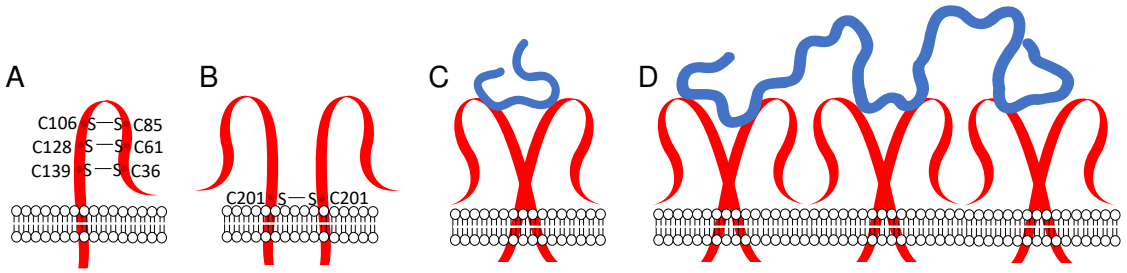

Figure I.10. (A) Schematic presentation of the structure of LYVE-1 receptor and (B) its homodimerization that occurs by formation of disulfide bond between the cysteines at C201 from the two receptors. (C) The conformation of LYVE-1 homodimers alters upon binding of low molecular weight HA. (D) In the presence of high molecular weight HA, the dimers can form clusters.

I.5.1. LYVE-1 role in lymph node metastasis.

The specific role of LYVE-1 in cancer development and progression is yet unclear, but some data suggest LYVE-1 involvement in lymphangiogenesis and lymph node metastasis formation. For example, LMW HA (generated in situ upon endogenous HA degradation) accumulates in interstitial tumor fluid (obtained from rat tumors and human colorectal tumors) and positively correlates with lymphatic invasion and lymph node metastasis.[164] LMW HA/LYVE-1 interaction in lymph node endothelial cells stimulates proliferation, migration, and tube formation of lymphatic endothelial cells *via* tyrosine phosphorylation of protein kinase Calpha/betaII (PKCα/βII) and ERK-1,2 (Fig. I.11A).[167] The LMW HA/LYVE-1 complexes can also engage vascular endothelial growth factor C (VEGF-C) and fibroblast growth factor 2 (FGF-2) to induce lymphatic endothelial cell proliferation and lymphangiogenesis (Table I.2).[41] Blocking the HA/LYVE-1 interactions with antibodies inhibits cell proliferation and migration, reduces the number of lymphatic vessels and volume of primary tumors, and inhibits lymph node metastasis formation in breast cancer cells implanted in mice. [38, 167] The process by which LMW HA potentiates the formation of lymph node metastasis is likely related to the altered permeability of lymph vessels.[40] LMW HA affects the

lymphatic lumen integrity due to alterations on VE-cadherin and β-catenin at membrane junctions upon interaction with LYVE-1 in human dermal lymphatic endothelial cells.

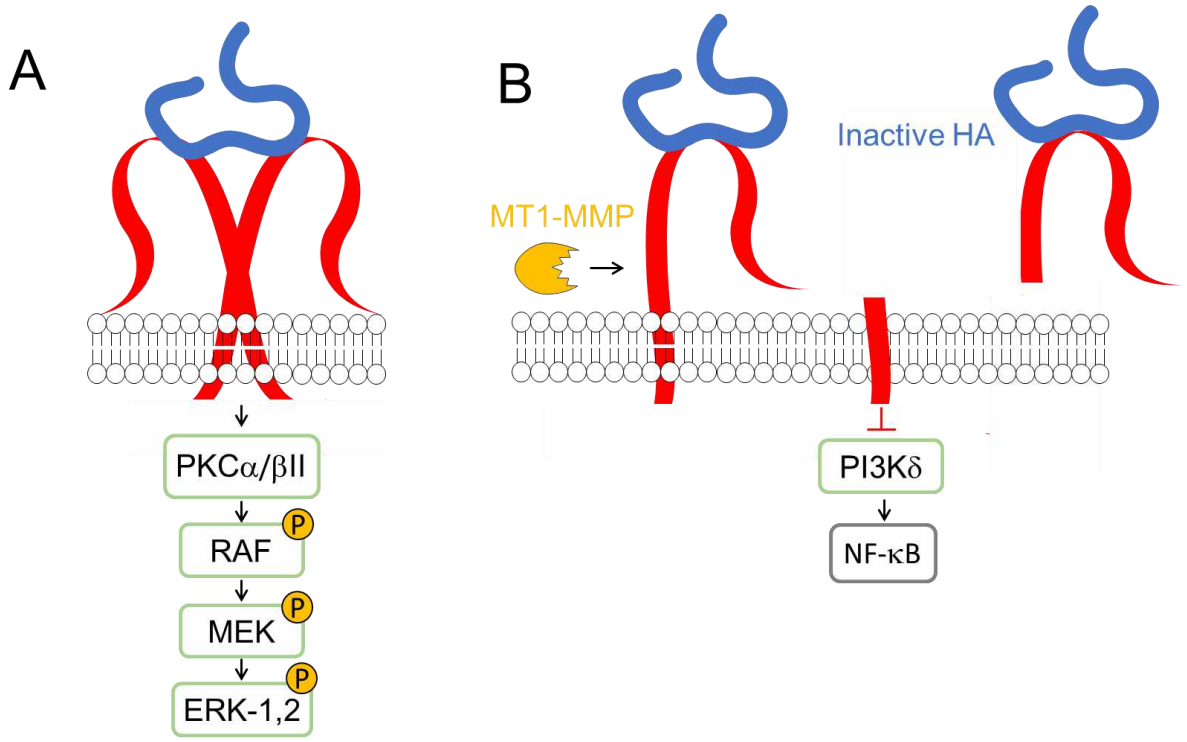

Figure I.11. (A) HA/LYVE-1-mediated intracellular signaling and (B) function as a decoy receptor.

I.5.2. LYVE-1 as a decoy for HA.

Contrary to the integral receptor, the shedded ectodomain of LYVE-1 acts as a decoy receptor of LMW HA fragments, inhibiting cell proliferation, migration, and lymphangiogenesis (Fig. 11B).[43] Soluble LYVE-1 (sLYVE-1) can be generated *in situ*, upon the action of MT1-MMP, and released into the tumor interstitium.[44] sLYVE-1 inhibits PI3Kδ signaling, as well NF-κB activation and synthesis of VEGF-C, and thus lymphangiogenesis (Fig. I.11B). On the other hand, sLYVE-1 derived from M2-like tumor-associated macrophages (present at initial stages of cancer), has pro-resolving functions *via* scavenging LMW HA from the TME. The generated sLYVE-1/LMW HA complexes inhibit the cell proliferation of human and murine melanomas in the early tumor growth phase, but not in advanced stages.[43]

I.6. HYALURONAN RECEPTOR FOR ENDOCYTOSIS (HARE)

HARE, also known as Stabilin-2 (Stab-2), is coded by the *STAB2* gene in humans (Fig. I.12A) and is mainly found in endocytic and recycling compartments of cells in lymph vessels and nodes, liver, and spleen.[171] HARE acts as a scavenger receptor for glycosaminoglycans, low-density lipoprotein particles, phosphatidylserine, and other bioentities resulting from matrix degradation.[172] HARE receptor binds to HA through the Link domain, present in other hyaladherins, and it mediates HA internalization via clathrin-mediated endocytosis, allowing a fast clearance of HA from biological fluids (Fig. I.12B).[173] HARE binding and endocytosis of HA with 40 to 400 kDa can activate MAPK, ERK-1,2 and NF-κB-mediated gene expression (Fig. I.12C).[174, 175] The exact downstream signaling(s) and its effect on cell behavior are yet unknown, but the sensitiveness to HA size might be related to ECM turnover.

In cancer, inhibition or knockout of this receptor prevents HA uptake and metastasis formation.[173, 176] Two possible mechanisms that drive toward this response have been proposed: (i) the resulting increase in HA fragments block or prevent the interaction of circulating cancer cells with surrounding tissues;[176] or (ii) possible actuation of HARE as an endothelial receptor for metastatic tumor cells with HA-rich pericellular coats that promotes tissue penetration of tumor cells.[173]

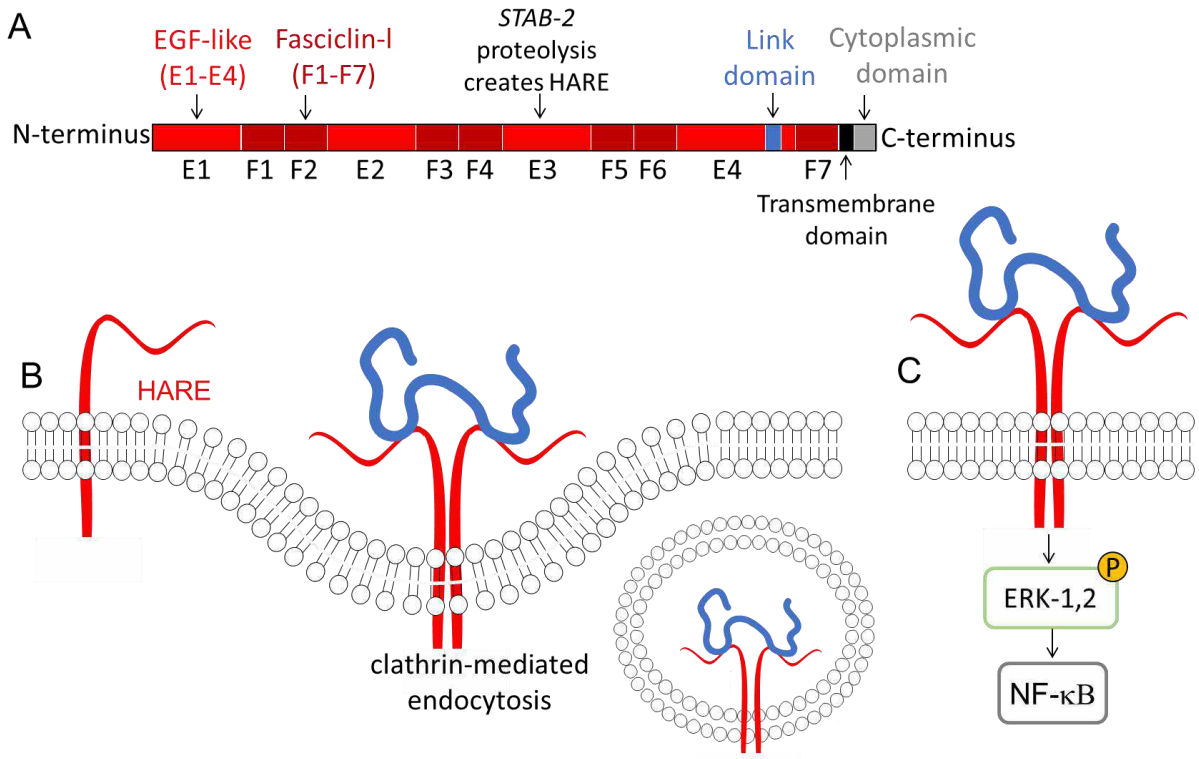

Figure I.12. (A) Human STAB2 domain organization and its involvement in tumor-associated (B) HA/HARE clathrin-mediated endocytosis and (C) HA/HARE signaling.

The involvement of HARE in the interactions between invasive breast cancer cells and lymphatic endothelial cells has been demonstrated in co-cultures.[45] Altered gene expression patterns in lymphatic endothelial cells were observed only when these cells were co-cultured with highly metastatic breast and prostate cancer cells. The expression pattern changes included upregulation of metastasis-related genes involved in the cell cycle (*CDC6*, *CLSPN*, kinases genes), cell adhesion, and motility (*BST2*, *SELE*, and *HMMR*), cytokines (*CCL7*, *CXCL6*, *CXCL1*, and *CSF1*), and factors of the complement system (*C1R*, *C3*, and *CFB*); which mediate lymphangiogenesis. Moreover, in these co-cultures, HARE was downregulated, which might prevent HA uptake from the tumor microenvironment (*via* the above described clathrin-mediated endocytosis), thus contributing to high levels of HA at TME.

I.7. LAYILIN

Layilin is a transmembrane homolog of C-type lectins coded by the *LAYN* gene, which recognizes LMW HA *via* the Link domain common to hyaladherins.[177-179] It participates in intracellular complexes with cytoskeletal-membrane linker proteins, including talin, merlin, and radixin (Fig. I.13A).[177, 180] Although negative regulatory functions over the immune system and cancer cell motility have been identified, layilin role in cancer is yet to be elucidated. Layilin is specifically and highly upregulated in tumor-infiltrating Treg and $CD8^+$ lymphocytes in human lung, colorectal, and hepatocellular carcinomas.[47, 181] Layilin overexpression inhibits IFN-γ production, a key cytokine in anti-tumor immune responses.[47] As the Treg cells become suppressive, tumor-infiltrating compromised $CD8^+$ T cells increase, contributing to tumor immune escape and poor prognosis. A correlation between high layilin expression and the presence of immune infiltrating cells in TME, including $CD8^+$ T cells, $CD4^+$ T cells, macrophages, neutrophils, and dendritic cells, has been identified in several types of cancer, and it is suggested as a prognostic biomarker for colon and gastric cancers.[46]

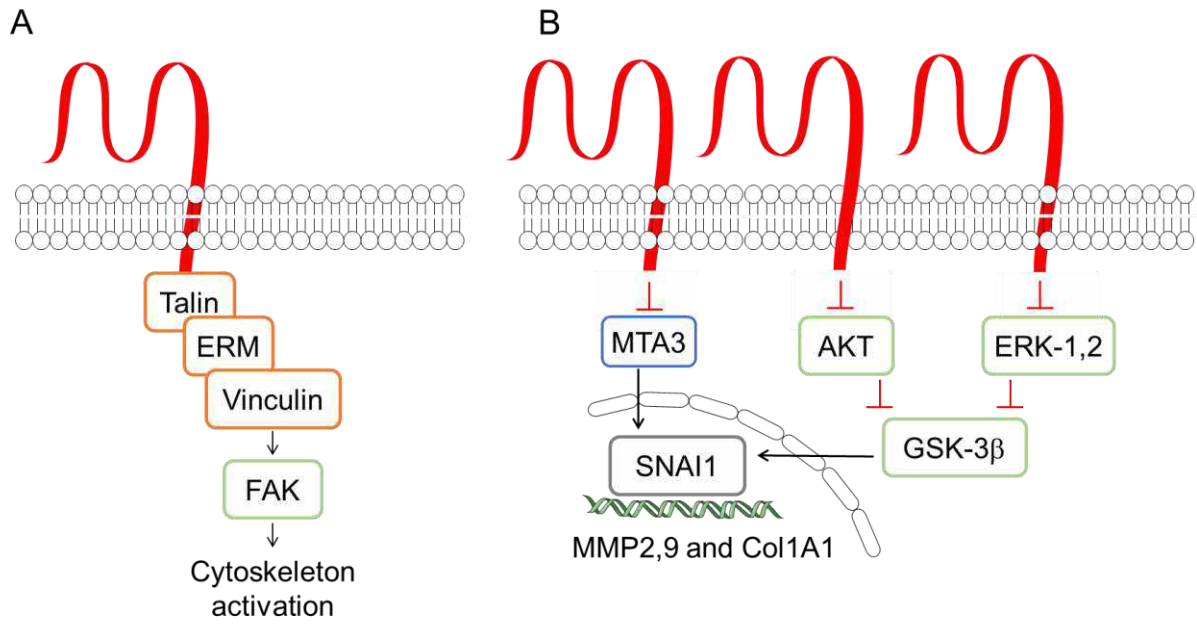

Figure I.13. HA/Laylin-mediated intracellular signaling towards motility and invasion.

Layilin ability to regulate cell motility was first observed in A549 human lung cancer cells. Knockdown of this HA receptor inhibited cell invasion and migration *in vitro* and lymphatic metastasis *in vivo* in the tumor-bearing mice model.[182] Recently, the role of layilin was investigated in highly invasive malignant glioma cells (Fig. I.13B).[48] Knockdown experiments showed that layilin upregulates SNAI1 transcription activity by suppressing metastasis-associated 1 family member 3 (MTA3, which is SNAI1 transcription repressor). At the nuclear level, SNAI1 causes overexpression of MMP2, MMP9, and collagen type I alpha 1 chain (COL1A1), potentiating the invasive ability of malignant glioma cells.[48]

Layilin might have other roles in cancer progression, including involvement in EMT. Previous studies have shown the importance of layilin in regulating intestinal epithelial tight junctions in inflammatory models [183, 184] as well as its role TNF-α induced EMT of renal tubular epithelial cells.[185]

I.8. Conclusions

In TME, HA homeostasis is altered by increased synthesis and degradation since the early stages of carcinogenesis. The HA receptors constitute a complex signaling hub that senses these changes and responds to them through clustering, formation of specific signaling complexes, and receptors cleavage. HA interaction with its receptors modulates several hallmarks of cancer, including proliferation (CD44, RHAMM, and TLR2,4), survival (CD44, RHAMM, and TLR2,4), invasion and metastasis (CD44, RHAMM, TLR2,4, LYVE-1, HARE, and Layilin), immune response (CD44, TLR2,4, and Layilin) and lymphangiogenesis (LYVE-1). In the TME, these interactions activate signaling cascades that affect different cell populations, including immune cells, fibroblasts, and vascular endothelial cells. HA and its receptors are also involved in the formation, protection, and sustained growth of stem cells niches and promote EMT of cancer cells, facilitating invasion and metastasis formation. HA receptors also participate in signaling cascades that lead to the upregulation and overexpression of several cytokines/chemokines and ECM-degrading enzymes, which modify the TME and enhance carcinogenesis.

HA signaling is thus a potential target for cancer therapy. At the molecular level, targeting HA signaling can be achieved with different approaches: HA synthesis inhibition with 4-MU or HASs silencing; HA inactivation with binding peptides; receptors inhibition with antibodies or specific

peptides; and receptors silencing, knockdown, or knockout. Another strategy includes the use of inhibitors specific to the most transversal HA-activated signaling pathways, as MAPK and PI3K/AKT pathways, blocking intracellular signaling. Nevertheless, given the role of HA and its signaling in normal tissue homeostasis, these strategies are not always applicable in a clinical scenario, and the development of specific systems for targeted and effective treatment remains a hot topic in the (bio)chemical, pharmaceutical, and medical sciences.

I.9 REFERENCES

1. Bejarano, L., M.J. Jordão, and J.A.J.C.D. Joyce, *Therapeutic Targeting of the Tumor Microenvironment.* 2021. **11**(4): p. 933-959.
2. Duan, Q., et al., *Turning cold into hot: firing up the tumor microenvironment.* 2020. **6**(7): p. 605-618.
3. McCarthy, J.B., D. El-Ashry, and E.A. Turley, *Hyaluronan, Cancer-Associated Fibroblasts and the Tumor Microenvironment in Malignant Progression.* 2018. **6**(48).
4. Roma-Rodrigues, C., et al., *Targeting Tumor Microenvironment for Cancer Therapy.* 2019. **20**(4): p. 840.
5. Nikitovic, D., et al., *Cancer microenvironment and inflammation: role of hyaluronan.* Frontiers in immunology, 2015. **6**: p. 169-169.
6. Brassart-Pasco, S., et al., *Tumor Microenvironment: Extracellular Matrix Alterations Influence Tumor Progression.* 2020. **10**(397).
7. Caon, I., et al., *Revisiting the hallmarks of cancer: The role of hyaluronan.* Seminars in Cancer Biology, 2020. **62**: p. 9-19.
8. Winkler, J., et al., *Concepts of extracellular matrix remodelling in tumour progression and metastasis.* Nature Communications, 2020. **11**(1): p. 5120.
9. Cox, T.R., *The matrix in cancer.* Nature Reviews Cancer, 2021. **21**(4): p. 217-238.
10. Toole, B.P., *Hyaluronan: from extracellular glue to pericellular cue.* Nat Rev Cancer, 2004. **4**(7): p. 528-39.
11. Turley, E.A., D.K. Wood, and J.B. McCarthy, *Carcinoma Cell Hyaluronan as a "Portable" Cancerized Prometastatic Microenvironment.* Cancer Res, 2016. **76**(9): p. 2507-12.
12. Passi, A., et al., *Dissecting the role of hyaluronan synthases in the tumor microenvironment.* Febs j, 2019. **286**(15): p. 2937-2949.
13. Nastase, M.V., et al., *Signaling at the Crossroads: Matrix-Derived Proteoglycan and Reactive Oxygen Species Signaling.* Antioxid Redox Signal, 2017. **27**(12): p. 855-873.
14. Henke, E., R. Nandigama, and S. Ergün, *Extracellular Matrix in the Tumor Microenvironment and Its Impact on Cancer Therapy.* Frontiers in molecular biosciences, 2020. **6**: p. 160-160.
15. Wu, M., et al., *A novel role of low molecular weight hyaluronan in breast cancer metastasis.* Faseb j, 2015. **29**(4): p. 1290-8.
16. Tavianatou, A.G., et al., *Hyaluronan: molecular size-dependent signaling and biological functions in inflammation and cancer.* 2019. **286**(15): p. 2883-2908.
17. Cyphert, J.M., C.S. Trempus, and S. Garantziotis, *Size Matters: Molecular Weight Specificity of Hyaluronan Effects in Cell Biology.* International Journal of Cell Biology, 2015. **2015**: p. 563818.
18. Thanee, M., et al., *CD44 modulates metabolic pathways and altered ROS-mediated Akt signal promoting cholangiocarcinoma progression.* 2021. **16**(3): p. e0245871.
19. Song, J.M., et al., *Hyaluronan-CD44/RHAMM interaction-dependent cell proliferation and survival in lung cancer cells.* 2019. **58**(3): p. 321-333.
20. Ooki, T., et al., *High-Molecular-Weight Hyaluronan Is a Hippo Pathway Ligand Directing Cell Density-Dependent Growth Inhibition via PAR1b.* Dev Cell, 2019. **49**(4): p. 590-604.e9.
21. Makkar, S., et al., *Hyaluronic acid binding to TLR4 promotes proliferation and blocks apoptosis in colon cancer.* 2019. **18**(12): p. 2446-2456.

22. Ryoo, I.G., et al., *High CD44 expression mediates p62-associated NFE2L2/NRF2 activation in breast cancer stem cell-like cells: Implications for cancer stem cell resistance.* Redox Biology, 2018. **17**: p. 246-258.
23. Mao, M., et al., *Effects of CD44 and E-cadherin overexpression on the proliferation, adhesion and invasion of ovarian cancer cells.* Experimental and therapeutic medicine, 2017. **14**(6): p. 5557-5563.
24. Matzke-Ogi, A., et al., *Inhibition of tumor growth and metastasis in pancreatic cancer models by interference with CD44v6 signaling.* Gastroenterology, 2016. **150**(2): p. 513-525. e10.
25. Liu, S. and C.J.C.r. Cheng, *Akt signaling is sustained by a CD44 splice isoform–mediated positive feedback loop.* 2017. **77**(14): p. 3791-3801.
26. Bourguignon, L.Y.W., G. Wong, and M. Shiina, *Up-regulation of Histone Methyltransferase, DOT1L, by Matrix Hyaluronan Promotes MicroRNA-10 Expression Leading to Tumor Cell Invasion and Chemoresistance in Cancer Stem Cells from Head and Neck Squamous Cell Carcinoma.* The Journal of biological chemistry, 2016. **291**(20): p. 10571-10585.
27. Carvalho, A.M., et al., *Co-localization and crosstalk between CD44 and RHAMM depend on hyaluronan presentation.* Acta Biomaterialia, 2021. **119**: p. 114-124.
28. Huang, C., et al., *ERK1/2-Nanog signaling pathway enhances CD44 (+) cancer stem-like cell phenotypes and epithelial-to-mesenchymal transition in head and neck squamous cell carcinomas.* 2020. **11**(4): p. 1-14.
29. Preca, B.-T., et al., *A novel ZEB1/HAS2 positive feedback loop promotes EMT in breast cancer.* Oncotarget, 2017. **8**(7): p. 11530-11543.
30. Park, N.R., et al., *Synergistic effects of CD44 and TGF-beta 1 through AKT/GSK-3 beta/beta-catenin signaling during epithelial-mesenchymal transition in liver cancer cells.* Biochemical and Biophysical Research Communications, 2016. **477**(4): p. 568-574.
31. Chen, F., et al., *RHAMM regulates the growth and migration of lung adenocarcinoma A549 cell line by regulating Cdc2/CyclinB1 and MMP9 genes Running title: RHAMM regulates the growth of lung adenocarcinoma cells.* Math Biosci Eng, 2020. **17**(3): p. 2150-2163.
32. Akentieva, N.P. and A.F. Topunov, *RHAMM-Target Peptides Inhibit Proliferation and Viability of Cancer Cells.* 2020.
33. Kouvidi, K., et al., *Receptor for hyaluronic acid- mediated motility (RHAMM) regulates HT1080 fibrosarcoma cell proliferation via a beta-catenin/c-myc signaling axis.* Biochimica Et Biophysica Acta-General Subjects, 2016. **1860**(4): p. 814-824.
34. Mascaro, M., et al., *Low molecular weight hyaluronan induces migration of human choriocarcinoma JEG-3 cells mediated by RHAMM as well as by PI3K and MAPK pathways.* Histochemistry and Cell Biology, 2017. **148**(2): p. 173-187.
35. Zhang, H.Z., et al., *Hyaluronan-mediated motility receptor confers resistance to chemotherapy via TGF/Smad2-induced epithelial-mesenchymal transition in gastric cancer.* Faseb Journal, 2019. **33**(5): p. 6365-6377.
36. Takabe, P., et al., *Melanocyte Hyaluronan Coat Fragmentation Enhances the UVB-Induced TLR-4 Receptor Signaling and Expression of Proinflammatory Mediators IL6, IL8, CXCL1, and CXCL10 via NF-κB Activation.* Journal of Investigative Dermatology, 2019. **139**(9): p. 1993-2003. e4.
37. Ferrandez, E., et al., *NFκB activation in differentiating glioblastoma stem-like cells is promoted by hyaluronic acid signaling through TLR4.* 2018. **8**(1): p. 1-10.
38. Hara, Y., et al., *Inhibition of tumor formation and metastasis by a monoclonal antibody against lymphatic vessel endothelial hyaluronan receptor 1.* 2018. **109**(10): p. 3171-3182.
39. Arimoto, S., et al., *Lymphangiogenesis and Lymph Node Metastasis in Oral Squamous Cell Carcinoma.* Anticancer Research, 2018. **38**(11): p. 6157-6162.
40. Du, Y., et al., *Low-molecular-weight hyaluronan (LMW-HA) accelerates lymph node metastasis of melanoma cells by inducing disruption of lymphatic intercellular adhesion.* OncoImmunology, 2016. **5**(11).
41. Bauer, J., et al., *TGFβ counteracts LYVE-1-mediated induction of lymphangiogenesis by small hyaluronan oligosaccharides.* 2018. **96**(2): p. 199-209.
42. Johnson, L.A., et al., *Dendritic cells enter lymph vessels by hyaluronan-mediated docking to the endothelial receptor LYVE-1.* 2017. **18**(7): p. 762.
43. Dollt, C., et al., *The shedded ectodomain of Lyve-1 expressed on M2-like tumor-associated macrophages inhibits melanoma cell proliferation.* Oncotarget, 2017. **8**(61): p. 103682-103692.

44. Wong, H.L.X., et al., *MT1-MMP sheds LYVE-1 on lymphatic endothelial cells and suppresses VEGF-C production to inhibit lymphangiogenesis.* Nature Communications, 2016. **7**.
45. Oliveira-Ferrer, L., et al., *Mechanisms of Tumor-Lymphatic Interactions in Invasive Breast and Prostate Carcinoma.* International Journal of Molecular Sciences, 2020. **21**(2).
46. Pan, J.H., et al., *LAYN Is a Prognostic Biomarker and Correlated With Immune Infiltrates in Gastric and Colon Cancers.* Frontiers in Immunology, 2019. **10**.
47. Zheng, C.H., et al., *Landscape of Infiltrating T Cells in Liver Cancer Revealed by Single-Cell Sequencing.* Cell, 2017. **169**(7): p. 1342-+.
48. Kaji, T., et al., *Layilin enhances the invasive ability of malignant glioma cells via SNAI1 signaling.* Brain Research, 2019. **1719**: p. 140-147.
49. Liao, H.X., et al., *N-terminal and central regions of the human CD44 extracellular domain participate in cell surface hyaluronan binding.* J Immunol, 1995. **155**(8): p. 3938-45.
50. Knudson, W., G. Chow, and C.B. Knudson, *CD44-mediated uptake and degradation of hyaluronan.* Matrix Biology, 2002. **21**(1): p. 15-23.
51. Prochazka, L., R. Tesarik, and J. Turanek, *Regulation of alternative splicing of CD44 in cancer.* Cellular Signalling, 2014. **26**(10): p. 2234-2239.
52. Mereiter, S., et al., *O-glycan truncation enhances cancer-related functions of CD44 in gastric cancer.* 2019. **593**(13): p. 1675-1689.
53. Azevedo, R., et al., *CD44 glycoprotein in cancer: a molecular conundrum hampering clinical applications.* Clinical Proteomics, 2018. **15**(1): p. 22.
54. Lesley, J., P.W. Kincade, and R. Hyman, *Antibody-induced activation of the hyaluronan receptor function of CD44 requires multivalent binding by antibody.* Eur J Immunol, 1993. **23**(8): p. 1902-9.
55. Yang, C., et al., *The high and low molecular weight forms of hyaluronan have distinct effects on CD44 clustering.* 2012. **287**(51): p. 43094-43107.
56. Misra, S., et al., *Delivery of CD44 shRNA/nanoparticles within cancer cells: perturbation of hyaluronan/CD44v6 interactions and reduction in adenoma growth in Apc Min/+ MICE.* 2009. **284**(18): p. 12432-12446.
57. Misra, S., S. Ghatak, and B.P.J.J.o.B.C. Toole, *Regulation of MDR1 expression and drug resistance by a positive feedback loop involving hyaluronan, phosphoinositide 3-kinase, and ErbB2.* 2005. **280**(21): p. 20310-20315.
58. Ghatak, S., S. Misra, and B.P.J.J.o.B.C. Toole, *Hyaluronan constitutively regulates ErbB2 phosphorylation and signaling complex formation in carcinoma cells.* 2005. **280**(10): p. 8875-8883.
59. Wang, S.J. and L.Y.W. Bourguignon, *Hyaluronan and the Interaction Between CD44 and Epidermal Growth Factor Receptor in Oncogenic Signaling and Chemotherapy Resistance in Head and Neck Cancer.* Archives of Otolaryngology–Head & Neck Surgery, 2006. **132**(7): p. 771-778.
60. Sherman, L.S., et al., *CD44 enhances neuregulin signaling by Schwann cells.* 2000. **150**(5): p. 1071-1084.
61. Misra, S., B.P. Toole, and S.J.J.o.B.C. Ghatak, *Hyaluronan constitutively regulates activation of multiple receptor tyrosine kinases in epithelial and carcinoma cells.* 2006. **281**(46): p. 34936-34941.
62. Wang, S.J. and L.Y. Bourguignon, *Hyaluronan and the interaction between CD44 and epidermal growth factor receptor in oncogenic signaling and chemotherapy resistance in head and neck cancer.* Arch Otolaryngol Head Neck Surg, 2006. **132**(7): p. 771-8.
63. Meran, S., et al., *Hyaluronan facilitates transforming growth factor-β 1-dependent proliferation via CD44 and epidermal growth factor receptor interaction.* 2011. **286**(20): p. 17618-17630.
64. Okamoto, I., et al., *CD44 cleavage induced by a membrane-associated metalloprotease plays a critical role in tumor cell migration.* 1999. **18**(7): p. 1435-1446.
65. Subramaniam, V., H. Gardner, and S. Jothy, *Soluble CD44 secretion contributes to the acquisition of aggressive tumor phenotype in human colon cancer cells.* Experimental and Molecular Pathology, 2007. **83**(3): p. 341-346.
66. Senbanjo, L.T. and M.A. Chellaiah, *CD44: A Multifunctional Cell Surface Adhesion Receptor Is a Regulator of Progression and Metastasis of Cancer Cells.* Frontiers in cell and developmental biology, 2017. **5**: p. 18-18.
67. Bourguignon, L.Y.W., et al., *Hyaluronan-CD44 interaction promotes c-Src-mediated twist signaling, microRNA-10b expression, and RhoA/RhoC up-regulation, leading to Rho-kinase-associated cytoskeleton activation and breast tumor cell invasion.* The Journal of biological chemistry, 2010. **285**(47): p. 36721-36735.

68. Bourguignon, L.Y.W., *Hyaluronan-CD44 interaction promotes microRNA signaling and RhoGTPase activation leading to tumor progression.* Small GTPases, 2012. **3**(1): p. 53-59.
69. Bourguignon, L.Y., et al., *Hyaluronan promotes CD44v3-Vav2 interaction with Grb2-p185HER2 and induces Rac1 and Ras signaling during ovarian tumor cell migration and growth.* 2001. **276**(52): p. 48679-48692.
70. Li, L., et al., *Transforming growth factor-β 1 induces EMT by the transactivation of epidermal growth factor signaling through HA/CD44 in lung and breast cancer cells.* International journal of molecular medicine, 2015. **36**(1): p. 113-122.
71. Bourguignon, L.Y., et al., *Hyaluronan-mediated CD44 interaction with RhoGEF and Rho kinase promotes Grb2-associated binder-1 phosphorylation and phosphatidylinositol 3-kinase signaling leading to cytokine (macrophage-colony stimulating factor) production and breast tumor progression.* 2003. **278**(32): p. 29420-29434.
72. Manning, B.D. and A.J.C. Toker, *AKT/PKB signaling: navigating the network.* 2017. **169**(3): p. 381-405.
73. Bourguignon, L.Y., *Hyaluronan-mediated CD44 activation of RhoGTPase signaling and cytoskeleton function promotes tumor progression.* Semin Cancer Biol, 2008. **18**(4): p. 251-9.
74. Faes, S. and O. Dormond, *PI3K and AKT: Unfaithful Partners in Cancer.* Int J Mol Sci, 2015. **16**(9): p. 21138-52.
75. Amano, M., et al., *Phosphorylation and activation of myosin by Rho-associated kinase (Rho-kinase).* 1996. **271**(34): p. 20246-20249.
76. Bourguignon, L.Y. *Hyaluronan-mediated CD44 activation of RhoGTPase signaling and cytoskeleton function promotes tumor progression*. in *Seminars in cancer biology*. 2008. Elsevier.
77. Bourguignon, L.Y., et al., *CD44 interaction with Na+-H+ exchanger (NHE1) creates acidic microenvironments leading to hyaluronidase-2 and cathepsin B activation and breast tumor cell invasion.* 2004. **279**(26): p. 26991-27007.
78. Mori, T., et al., *Structural basis for CD44 recognition by ERM proteins.* 2008. **283**(43): p. 29602-29612.
79. Duterme, C., et al., *Two novel functions of hyaluronidase-2 (Hyal2) are formation of the glycocalyx and control of CD44-ERM interactions.* 2009. **284**(48): p. 33495-33508.
80. Solinet, S., et al., *The actin-binding ERM protein Moesin binds to and stabilizes microtubules at the cell cortex.* 2013. **202**(2): p. 251-260.
81. Lokeshwar, V.B., N. Fregien, and L.Y. Bourguignon, *Ankyrin-binding domain of CD44(GP85) is required for the expression of hyaluronic acid-mediated adhesion function.* J Cell Biol, 1994. **126**(4): p. 1099-109.
82. Mori, T., et al., *Structural basis for CD44 recognition by ERM proteins.* The Journal of biological chemistry, 2008. **283**(43): p. 29602-29612.
83. Vigetti, D., et al., *Hyaluronan-CD44-ERK1/2 regulate human aortic smooth muscle cell motility during aging.* 2008. **283**(7): p. 4448-4458.
84. Bourguignon, L.Y., et al., *Hyaluronan-CD44 interaction with IQGAP1 promotes Cdc42 and ERK signaling, leading to actin binding, Elk-1/estrogen receptor transcriptional activation, and ovarian cancer progression.* 2005. **280**(12): p. 11961-11972.
85. Ridley, A.J., et al., *The small GTP-binding protein rac regulates growth factor-induced membrane ruffling.* 1992. **70**(3): p. 401-410.
86. Habets, G., et al., *Sequence of the human invasion-inducing TIAM1 gene, its conservation in evolution and its expression in tumor cell lines of different tissue origin.* 1995. **10**(7): p. 1371-1376.
87. Stam, J., et al., *Invasion of T-lymphoma cells: cooperation between Rho family GTPases and lysophospholipid receptor signaling.* 1998. **17**(14): p. 4066-4074.
88. McFarlane, S., et al., *CD44-mediated activation of α 5 β 1-integrin, cortactin and paxillin signaling underpins adhesion of basal-like breast cancer cells to endothelium and fibronectin-enriched matrices.* Oncotarget, 2015. **6**(34): p. 36762-36773.
89. Bourguignon, L.Y., et al., *Hyaluronan-CD44 interaction with protein kinase Cε promotes oncogenic signaling by the stem cell marker Nanog and the production of microRNA-21, leading to down-regulation of the tumor suppressor protein PDCD4, anti-apoptosis, and chemotherapy resistance in breast tumor cells.* 2009. **284**(39): p. 26533-26546.

90. Bourguignon, L.Y.W., et al., *Hyaluronan-CD44 interaction activates stem cell marker Nanog, Stat-3-mediated MDR1 gene expression, and ankyrin-regulated multidrug efflux in breast and ovarian tumor cells.* The Journal of biological chemistry, 2008. **283**(25): p. 17635-17651.
91. Bourguignon, L.Y., et al., *Hyaluronan-CD44 interaction with protein kinase C(epsilon) promotes oncogenic signaling by the stem cell marker Nanog and the Production of microRNA-21, leading to down-regulation of the tumor suppressor protein PDCD4, anti-apoptosis, and chemotherapy resistance in breast tumor cells.* J Biol Chem, 2009. **284**(39): p. 26533-46.
92. Ooki, T. and M.J.B. Hatakeyama, *Hyaluronan Degradation Promotes Cancer via Hippo-YAP Signaling: An Intervention Point for Cancer Therapy.* 2020. **42**(7): p. 2000005.
93. Misra, S., et al., *Hyaluronan Constitutively Regulates Activation of COX-2-mediated Cell Survival Activity in Intestinal Epithelial and Colon Carcinoma Cells.* Journal of Biological Chemistry, 2008. **283**(21): p. 14335-14344.
94. Misra, S., et al., *Hyaluronan, CD44, and cyclooxygenase-2 in colon cancer.* Connect Tissue Res, 2008. **49**(3): p. 219-24.
95. Hamilton, S.R., et al., *The Hyaluronan Receptors CD44 and Rhamm (CD168) Form Complexes with ERK1,2 That Sustain High Basal Motility in Breast Cancer Cells*.* Journal of Biological Chemistry, 2007. **282**(22): p. 16667-16680.
96. Singleton, P.A. and L.Y. Bourguignon, *CD44 interaction with ankyrin and IP3 receptor in lipid rafts promotes hyaluronan-mediated Ca2+ signaling leading to nitric oxide production and endothelial cell adhesion and proliferation.* Exp Cell Res, 2004. **295**(1): p. 102-18.
97. Montgomery, N., et al., *CD44 enhances invasion of basal-like breast cancer cells by upregulating serine protease and collagen-degrading enzymatic expression and activity.* Breast Cancer Res, 2012. **14**(3): p. R84.
98. Montgomery, N., et al., *CD44 enhances invasion of basal-like breast cancer cells by upregulating serine protease and collagen-degrading enzymatic expression and activity.* Breast cancer research : BCR, 2012. **14**(3): p. R84-R84.
99. Fieber, C., et al., *Hyaluronan-oligosaccharide-induced transcription of metalloproteases.* Journal of Cell Science, 2004. **117**(2): p. 359-367.
100. Kung, C.-I., et al., *Enhanced membrane-type 1 matrix metalloproteinase expression by hyaluronan oligosaccharides in breast cancer cells facilitates CD44 cleavage and tumor cell migration.* Oncol Rep, 2012. **28**(5): p. 1808-1814.
101. Bourguignon, L.Y., et al., *Interaction of low molecular weight hyaluronan with CD44 and toll-like receptors promotes the actin filament-associated protein 110-actin binding and MyD88-NF κ B signaling leading to proinflammatory cytokine/chemokine production and breast tumor invasion.* Cytoskeleton (Hoboken), 2011. **68**(12): p. 671-93.
102. Savani, R.C. *Modulators of inflammation in bronchopulmonary dysplasia*. in *Seminars in perinatology*. 2018. Elsevier.
103. Garantziotis, S. and R.C.J.M.B. Savani, *Hyaluronan biology: A complex balancing act of structure, function, location and context.* 2019. **78**: p. 1-10.
104. Telmer, P.G., et al., *How does a protein with dual mitotic spindle and extracellular matrix receptor functions affect tumor susceptibility and progression?* 2011. **4**(2): p. 182-185.
105. Misra, S., et al., *Interactions between Hyaluronan and Its Receptors (CD44, RHAMM) Regulate the Activities of Inflammation and Cancer.* Frontiers in immunology, 2015. **6**: p. 201-201.
106. Tolg, C., et al., *Hyaluronan and RHAMM in wound repair and the "cancerization" of stromal tissues.* 2014. **2014**.
107. Day, A.J. and G.D. Prestwich, *Hyaluronan-binding Proteins: Tying Up the Giant *.* Journal of Biological Chemistry, 2002. **277**(7): p. 4585-4588.
108. Crainie, M., et al., *Overexpression of the receptor for hyaluronan-mediated motility (RHAMM) characterizes the malignant clone in multiple myeloma: identification of three distinct RHAMM variants.* 1999. **93**(5): p. 1684-1696.
109. Assmann, V., et al., *The human hyaluronan receptor RHAMM is expressed as an intracellular protein in breast cancer cells.* J Cell Sci, 1998. **111 (Pt 12)**: p. 1685-94.

110. Entwistle, J., C.L. Hall, and E.A. Turley, *HA receptors: regulators of signalling to the cytoskeleton.* J Cell Biochem, 1996. **61**(4): p. 569-77.
111. Xu, R., et al., *Tissue architecture and function: dynamic reciprocity via extra-and intra-cellular matrices.* 2009. **28**(1): p. 167-176.
112. Choi, S., et al., *Function and clinical relevance of RHAMM isoforms in pancreatic tumor progression.* 2019. **18**(1): p. 1-7.
113. Wang, J., et al., *RHAMM inhibits cell migration via the AKT/GSK3β/Snail axis in luminal A subtype breast cancer.* 2020. **303**(9): p. 2344-2356.
114. Turley, E. and R.J.S.o.h.t.h.w.g.g.j.s.h.H.H.E.h. Harrison, *RHAMM, a member of the hyaladherins.* 1999.
115. Tolg, C., et al., *Rhamm-/- fibroblasts are defective in CD44-mediated ERK1,2 motogenic signaling, leading to defective skin wound repair.* J Cell Biol, 2006. **175**(6): p. 1017-28.
116. Park, D., et al., *Hyaluronic acid promotes angiogenesis by inducing RHAMM-TGFβ receptor interaction via CD44-PKCδ.* 2012. **33**(6): p. 563-574.
117. Zhang, S., et al., *The Hyaluronan Receptor RHAMM Regulates Extracellular-regulated Kinase*.* Journal of Biological Chemistry, 1998. **273**(18): p. 11342-11348.
118. Manzanares, D., et al., *Apical oxidative hyaluronan degradation stimulates airway ciliary beating via RHAMM and RON.* 2007. **37**(2): p. 160-168.
119. Hall, C.L., et al., *pp60(c-src) is required for cell locomotion regulated by the hyaluronanreceptor RHAMM.* Oncogene, 1996. **13**(10): p. 2213-2224.
120. Hall, C.L., et al., *Hyaluronan and the hyaluronan receptor RHAMM promote focal adhesion turnover and transient tyrosine kinase activity.* The Journal of cell biology, 1994. **126**(2): p. 575-588.
121. Hall, C.L., et al., *Overexpression of the hyaluronan receptor RHAMM is transforming and is also required for H-ras transformation.* 1995. **82**(1): p. 19-28.
122. Wang, C., et al., *The overexpression of RHAMM, a hyaluronan-binding protein that regulates ras signaling, correlates with overexpression of mitogen-activated protein kinase and is a significant parameter in breast cancer progression.* 1998. **4**(3): p. 567-576.
123. Hall, C.L., et al., *Fibroblasts require protein kinase C activation to respond to hyaluronan with increased locomotion.* Matrix Biol, 2001. **20**(3): p. 183-92.
124. Mohapatra, S., et al., *Soluble hyaluronan receptor RHAMM induces mitotic arrest by suppressing Cdc2 and cyclin B1 expression.* 1996. **183**(4): p. 1663-1668.
125. Kouvidi, K., et al., *Receptor for hyaluronic acid- mediated motility (RHAMM) regulates HT1080 fibrosarcoma cell proliferation via a β-catenin/c-myc signaling axis.* Biochimica et Biophysica Acta (BBA) - General Subjects, 2016. **1860**(4): p. 814-824.
126. Nelson, W.J. and R. Nusse, *Convergence of Wnt, ß-Catenin, and Cadherin Pathways.* 2004. **303**(5663): p. 1483-1487.
127. Juan, J., et al., *Diminished WNT→ β-catenin→ c-MYC signaling is a barrier for malignant progression of BRAFV600E-induced lung tumors.* 2014. **28**(6): p. 561-575.
128. Kouvidi, K., et al., *Hyaluronan/RHAMM interactions in mesenchymal tumor pathogenesis: role of growth factors.* 2014. **123**: p. 319-349.
129. Maxwell, C.A., J. McCarthy, and E. Turley, *Cell-surface and mitotic-spindle RHAMM: moonlighting or dual oncogenic functions?* Journal of Cell Science, 2008. **121**(7): p. 925-932.
130. Maxwell, C.A., et al., *Receptor for hyaluronan-mediated motility correlates with centrosome abnormalities in multiple myeloma and maintains mitotic integrity.* Cancer Res, 2005. **65**(3): p. 850-60.
131. Assmann, V., et al., *The intracellular hyaluronan receptor RHAMM/IHABP interacts with microtubules and actin filaments.* Journal of Cell Science, 1999. **112**(22): p. 3943-3954.
132. Tolg, C., et al., *RHAMM promotes interphase microtubule instability and mitotic spindle integrity through MEK1/ERK1/2 activity.* J Biol Chem, 2010. **285**(34): p. 26461-74.
133. Maxwell, C.A., et al., *Interplay between BRCA1 and RHAMM regulates epithelial apicobasal polarization and may influence risk of breast cancer.* 2011. **9**(11): p. e1001199.
134. Hatano, H., et al., *RHAMM/ERK interaction induces proliferative activities of cementifying fibroma cells through a mechanism based on the CD44–EGFR.* 2011. **91**(3): p. 379-391.

135. Chen, H., et al., *Spatial regulation of Aurora A activity during mitotic spindle assembly requires RHAMM to correctly localize TPX2.* 2014. **13**(14): p. 2248-2261.
136. Blanco, I., et al., *Assessing associations between the AURKA-HMMR-TPX2-TUBG1 functional module and breast cancer risk in BRCA1/2 mutation carriers.* 2015. **10**(4): p. e0120020.
137. Smith, T.C., et al., *Supervillin binding to myosin II and synergism with anillin are required for cytokinesis.* 2013. **24**(23): p. 3603-3619.
138. Hasegawa, H., et al., *The role of PLK1-phosphorylated SVIL in myosin II activation and cytokinetic furrowing.* 2013. **126**(16): p. 3627-3637.
139. Gangopadhyay, S.S., et al., *Smooth muscle archvillin: a novel regulator of signaling and contractility in vascular smooth muscle.* 2004. **117**(21): p. 5043-5057.
140. Jang, G.-Y., et al., *Interactions between tumor-derived proteins and Toll-like receptors.* 2020: p. 1-10.
141. Beutler, B.A., *TLRs and innate immunity.* Blood, 2009. **113**(7): p. 1399-1407.
142. Termeer, C., et al., *Oligosaccharides of Hyaluronan activate dendritic cells via toll-like receptor 4.* 2002. **195**(1): p. 99-111.
143. Campo, G.M., et al., *Small hyaluronan oligosaccharides induce inflammation by engaging both toll-like-4 and CD44 receptors in human chondrocytes.* Biochem Pharmacol, 2010. **80**(4): p. 480-90.
144. Dajon, M., K. Iribarren, and I. Cremer, *Toll-like receptor stimulation in cancer: A pro- and anti-tumor double-edged sword.* Immunobiology, 2017. **222**(1): p. 89-100.
145. Zheng, L., T.E. Riehl, and W.F. Stenson, *Regulation of colonic epithelial repair in mice by Toll-like receptors and hyaluronic acid.* Gastroenterology, 2009. **137**(6): p. 2041-2051.
146. Jiang, D., et al., *Regulation of lung injury and repair by Toll-like receptors and hyaluronan.* Nat Med, 2005. **11**(11): p. 1173-9.
147. Nakamura, K., et al., *High, but not low, molecular weight hyaluronan prevents T-cell-mediated liver injury by reducing proinflammatory cytokines in mice.* J Gastroenterol, 2004. **39**(4): p. 346-54.
148. Li, F., et al., *Effects of 4-methylumbelliferone and high molecular weight hyaluronic acid on the inflammation of corneal stromal cells induced by LPS.* Graefes Arch Clin Exp Ophthalmol, 2017. **255**(3): p. 559-566.
149. Ebid, R., J. Lichtnekert, and H.-J.J.I.S.R.N. Anders, *Hyaluronan is not a ligand but a regulator of toll-like receptor signaling in mesangial cells: role of extracellular matrix in innate immunity.* 2014. **2014**.
150. Taylor, K.R., et al., *Recognition of hyaluronan released in sterile injury involves a unique receptor complex dependent on Toll-like receptor 4, CD44, and MD-2.* J Biol Chem, 2007. **282**(25): p. 18265-18275.
151. Scheibner, K.A., et al., *Hyaluronan fragments act as an endogenous danger signal by engaging TLR2.* 2006. **177**(2): p. 1272-1281.
152. Taylor, K.R., et al., *Hyaluronan fragments stimulate endothelial recognition of injury through TLR4.* J Biol Chem, 2004. **279**(17): p. 17079-84.
153. Kawasaki, T. and T.J.F.i.i. Kawai, *Toll-like receptor signaling pathways.* 2014. **5**: p. 461.
154. Voelcker, V., et al., *Hyaluronan fragments induce cytokine and metalloprotease upregulation in human melanoma cells in part by signalling via TLR4.* 2008. **17**(2): p. 100-107.
155. Santaolalla, R., et al., *TLR4 activates the β-catenin pathway to cause intestinal neoplasia.* PLoS One, 2013. **8**(5): p. e63298.
156. Rakoff-Nahoum, S. and R. Medzhitov, *Toll-like receptors and cancer.* Nature Reviews Cancer, 2009. **9**(1): p. 57-63.
157. Mantovani, A., et al., *Cancer-related inflammation.* Nature, 2008. **454**(7203): p. 436-444.
158. Alvarado, A.G., et al., *Glioblastoma Cancer Stem Cells Evade Innate Immune Suppression of Self-Renewal through Reduced TLR4 Expression.* Cell Stem Cell, 2017. **20**(4): p. 450-+.
159. Duan, Z. and Y. Luo, *Targeting macrophages in cancer immunotherapy.* Signal Transduction and Targeted Therapy, 2021. **6**(1): p. 127.
160. Del Fresno, C., et al., *Tumor cells deactivate human monocytes by up-regulating IL-1 receptor associated kinase-M expression via CD44 and TLR4.* 2005. **174**(5): p. 3032-3040.
161. Kuang, D.-M., et al., *Tumor-derived hyaluronan induces formation of immunosuppressive macrophages through transient early activation of monocytes.* 2007. **110**(2): p. 587-595.

162. Sokolowska, M., et al., *Low molecular weight hyaluronan activates cytosolic phospholipase A2 α and eicosanoid production in monocytes and macrophages.* 2014. **289**(7): p. 4470-4488.
163. Banerji, S., et al., *LYVE-1, a new homologue of the CD44 glycoprotein, is a lymph-specific receptor for hyaluronan.* The Journal of cell biology, 1999. **144**(4): p. 789-801.
164. Schmaus, A., et al., *Accumulation of small hyaluronan oligosaccharides in tumour interstitial fluid correlates with lymphatic invasion and lymph node metastasis.* British journal of cancer, 2014. **111**(3): p. 559-567.
165. Banerji, S., et al., *Distinctive properties of the hyaluronan-binding domain in the lymphatic endothelial receptor Lyve-1 and their implications for receptor function.* J Biol Chem, 2010. **285**(14): p. 10724-35.
166. Lawrance, W., et al., *Binding of hyaluronan to the native lymphatic vessel endothelial receptor LYVE-1 is critically dependent on receptor clustering and hyaluronan organization.* 2016. **291**(15): p. 8014-8030.
167. Wu, M., et al., *Low molecular weight hyaluronan induces lymphangiogenesis through LYVE-1-mediated signaling pathways.* 2014. **9**(3): p. e92857.
168. Banerji, S., et al., *Homodimerization of the lymph vessel endothelial receptor LYVE-1 through a redox-labile disulfide is critical for hyaluronan binding in lymphatic endothelium.* 2016. **291**(48): p. 25004-25018.
169. Prevo, R., et al., *Mouse LYVE-1 Is an Endocytic Receptor for Hyaluronan in Lymphatic Endothelium *.* Journal of Biological Chemistry, 2001. **276**(22): p. 19420-19430.
170. Johnson, L.A., et al., *Inflammation-induced Uptake and Degradation of the Lymphatic Endothelial Hyaluronan Receptor LYVE-1.* Journal of Biological Chemistry, 2007. **282**(46): p. 33671-33680.
171. Harris, E.N. and E.J.I.J.o.M.S. Baker, *Role of the Hyaluronan Receptor, Stabilin-2/HARE, in Health and Disease.* 2020. **21**(10): p. 3504.
172. Park, S., et al., *Rapid cell corpse clearance by stabilin-2, a membrane phosphatidylserine receptor.* 2008. **15**(1): p. 192-201.
173. Simpson, M.A., J.A. Weigel, and P.H. Weigel, *Systemic blockade of the hyaluronan receptor for endocytosis prevents lymph node metastasis of prostate cancer.* International Journal of Cancer, 2012. **131**(5): p. E836-E840.
174. Pandey, M.S. and P.H. Weigel, *A Hyaluronan Receptor for Endocytosis (HARE) Link Domain N-Glycan Is Required for Extracellular Signal-regulated Kinase (ERK) and Nuclear Factor-kappa B (NF-kappa B) Signaling in Response to the Uptake of Hyaluronan but Not Heparin, Dermatan Sulfate, or Acetylated Low Density Lipoprotein (LDL).* Journal of Biological Chemistry, 2014. **289**(32): p. 21807-21817.
175. Pandey, M.S., et al., *The Hyaluronan Receptor for Endocytosis (HARE) Activates NF-kappa B-mediated Gene Expression in Response to 40-400-kDa, but Not Smaller or Larger, Hyaluronans.* Journal of Biological Chemistry, 2013. **288**(20): p. 14068-14079.
176. Hirose, Y., et al., *Inhibition of Stabilin-2 elevates circulating hyaluronic acid levels and prevents tumor metastasis.* Proceedings of the National Academy of Sciences of the United States of America, 2012. **109**(11): p. 4263-4268.
177. Borowsky, M.L. and R.O. Hynes, *Layilin, a novel talin-binding transmembrane protein homologous with C-type lectins, is localized in membrane ruffles.* The Journal of cell biology, 1998. **143**(2): p. 429-442.
178. Bono, P., et al., *Layilin, a novel integral membrane protein, is a hyaluronan receptor.* Molecular Biology of the Cell, 2001. **12**(4): p. 891-900.
179. Forteza, R.M., et al., *Hyaluronan and Layilin Mediate Loss of Airway Epithelial Barrier Function Induced by Cigarette Smoke by Decreasing E-cadherin.* Journal of Biological Chemistry, 2012. **287**(50): p. 42288-42298.
180. Bono, P., et al., *Layilin, a cell surface hyaluronan receptor, interacts with merlin and radixin.* Experimental Cell Research, 2005. **308**(1): p. 177-187.
181. De Simone, M., et al., *Transcriptional landscape of human tissue lymphocytes unveils uniqueness of tumor-infiltrating T regulatory cells.* 2016. **45**(5): p. 1135-1147.
182. Chen, Z.T., et al., *Down-regulation of layilin, a novel hyaluronan receptor, via RNA interference, inhibits invasion and lymphatic metastasis of human lung A549 cells.* Biotechnology and Applied Biochemistry, 2008. **50**: p. 89-96.
183. Bellos, D.A., et al., *Specifically Sized Hyaluronan (35 kDa) Prevents Ethanol-Induced Disruption of Epithelial Tight Junctions Through a layilin-Dependent Mechanism in Caco-2 Cells.* Alcoholism-Clinical and Experimental Research, 2019. **43**(9): p. 1848-1858.

184. Kim, Y., et al., *Layilin is critical for mediating hyaluronan 35 kDa-induced intestinal epithelial tight junction protein ZO-1 in vitro and in vivo.* Matrix Biology, 2018. **66**: p. 93-109.
185. Adachi, T., et al., *Roles of layilin in TNF-α-induced epithelial-mesenchymal transformation of renal tubular epithelial cells.* Biochem Biophys Res Commun, 2015. **467**(1): p. 63-9.

SECTION 2

EXPERIMENTAL DESIGN

CHAPTER II

MATERIALS & METHODS

MATERIALS AND METHODS

Overview

The Chapter II: Materials and Methods aims to describe and explain the experimental procedures and designs used in the thesis. The principles behind the used instrumental techniques are also presented. Each Chapter of Section III has a dedicated section of materials and methods regarding specific and detailed methodologies used for that work.

II.1 End-on modification of hyaluronan

Studies elucidating HA bioactivity are usually based on supplementation of exogenous HA in solution or immobilized either in a coating or in a hydrogel where HA is commonly functionalized at the -COOH group, *i.e.,* in a side-on fashion. These presentations are different from the native HA immobilization in the ECM or at the cell surface (Scheme II.1A) and impact HA bioactivity.[1-3] In this thesis, we have used end-on immobilization of HA (Schemes II.1B-E), *i.e.,* immobilization at the reducing end. This strategy to present HA has several advantages: (i) it copycats HA orientation at the cell surface (Scheme II.1A); (ii) it increases the local HA concentration that differs from the HA supplementation in a solution; (iii) it does not compromise HA bioactivity, since no functional groups, *e.g.*, COOH, are modified; (iv) it guarantees partial molecular mobility that allows conformational adjustments upon receptors binding, thus, mimicking the physiological contextualization of HA. We applied oxime condensation for end-on modification. Previous studies have demonstrated that this reaction generates products with preserved bioactivity and enhanced stability under physiological conditions compared with other methods, *e.g.,* hydrazone ligation.[4, 5]

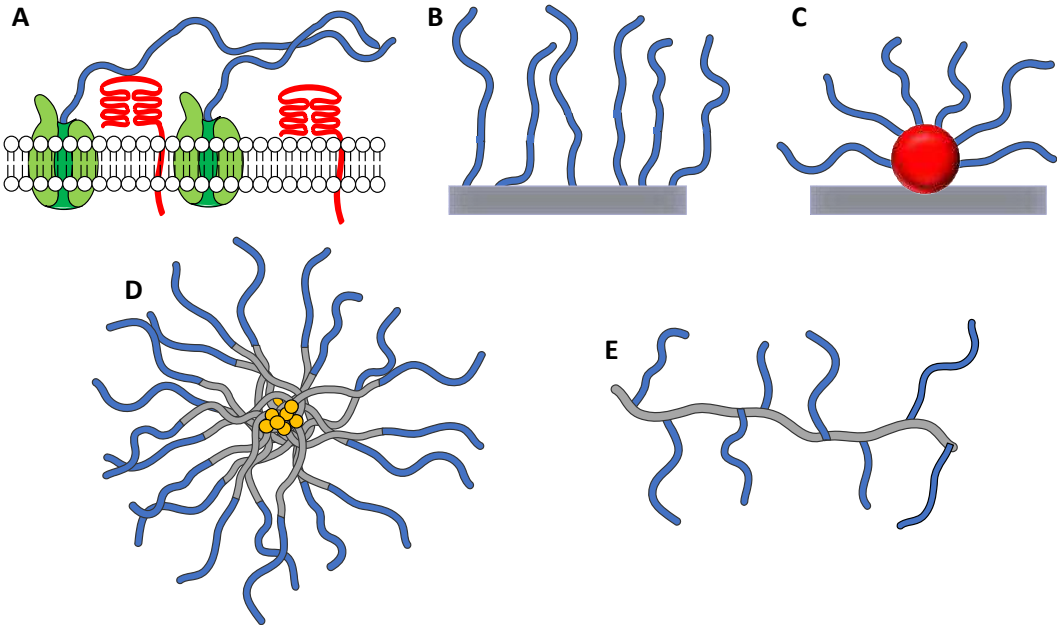

Scheme II.1. Schematic overview of HA presentation at the surface of (A) cells where it is immobilized by HA synthases and receptors; (B) gold-coated plane substrates (Chapter III); (C) gold nanoparticles (Chapters IV and V); (D) self-assembled micellar nanoparticles (Chapter VII); and (E) brush-like copolymer (Chapter VI).

II.1.1 End-on thiolated hyaluronan and chondroitin sulfate.

All commercial reagents were used without purification. The used solvents were analytical or HPLC grade.

II.1.1.1 Synthesis and purification of 11-(aminooxy)-1-undecanethiol.

11-(Aminooxy)-1-undecanethiol was obtained from 11-bromo-1-undecene as previously described (Scheme II.2).[6, 7] A solution of N-hydroxyphthalimide (2.44 g, 1.5 mol eq., Sigma) and sodium bicarbonate (1.388 g, Sigma) in dimethylformamide (DMF, 50 mL) was stirred at 60 °C under argon for 1h. 11-bromo-1-undecene (2.3 mL, 1 mol eq., Sigma) was then added, and the reaction was carried overnight: indicators for the successful synthesis of the product (**1**) are the color change (from orange to dark orange) and the product precipitation. The product was isolated by liquid-liquid extraction (water and chloroform).

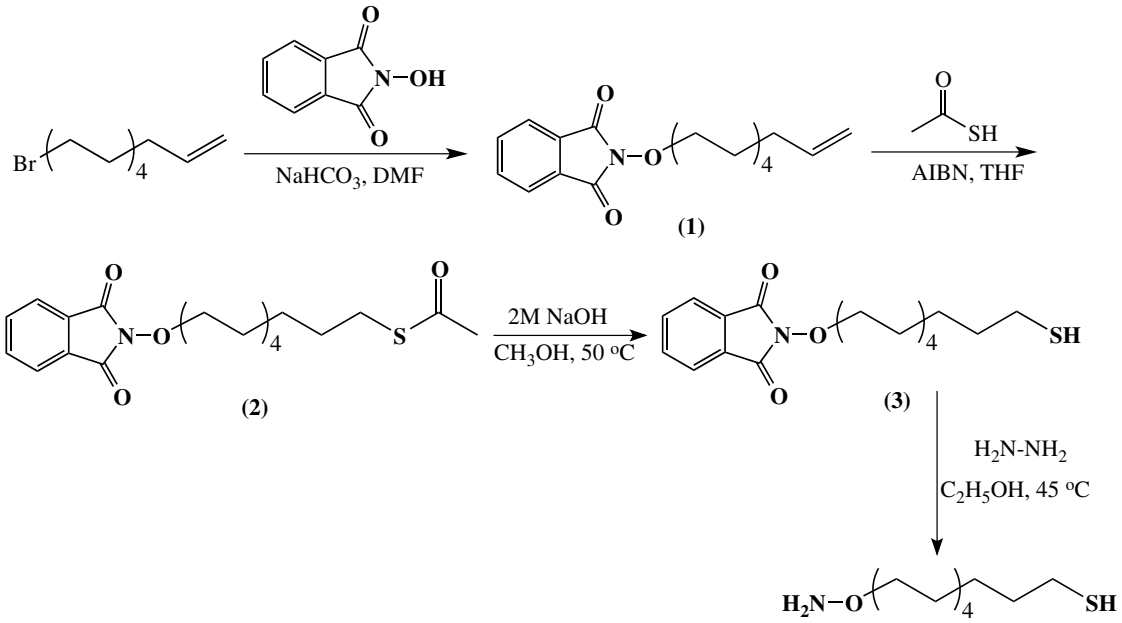

Scheme II.2. Schematic presentation of the synthetic route used to obtain 11-(aminooxy)-1-undecanethiol

2 g of **1** were dissolved in degassed tetrahydrofuran (THF, 80 mL). Azobisisobutyronitrile (AIBN, 100 mg, Sigma) and thioacetic acid (2 mL, Sigma) were added to this solution. The reaction mixture was stirred at room temperature under reflux for 3 days. After this period, toluene (50 mL) was added, and the solvents were evaporated. This procedure was repeated (3x). The product (**2**) was purified by

recrystallization in chloroform/hexane mixture (1:30) at 4°C. The final product was obtained by solvent evaporation.

Deprotection of **2** (950 mg; 2.43 mmol) was carried out in methanol (50 mL) at 50 °C by adding 2M NaOH (1.5 mL, 3 mol excess to **2**, Panreac AppliChem). The reaction was carried for 3h under an inert argon atmosphere. The product (**3**) was isolated by precipitation with 2M HCl (Sigma). Purification was carried out by dissolving the obtained powder in ethanol, filtering the solution, concentrating it, and finally, the pure product was obtained by freeze-drying with dioxane.

3 was dissolved in ethanol (10 mL), and then hydrazine (100 μL) was added to the solution. The reaction was carried at 45 °C for 1h. Next, unreacted hydrazine and solvent were removed by evaporation (30 mBar at 45 °C). The obtained 11-(aminooxy)-1-undecanethiol was used immediately to react with hyaluronan or chondroitin sulfate. Of note, the obtained product is unstable.

II.1.1.2 End-on modification of hyaluronan and chondroitin sulfate with 11-(aminooxy)-1-undecanethiol.

The synthesized alkanethiol was used for oxime condensation at the reducing end of the glycosaminoglycan (GAG, hyaluronan, or chondroitin sulfate) (Scheme II.3). 11-(Aminooxy)-1-undecanethiol (3 mol excess to GAG) was dissolved in 5 mL ethanol (for the synthesis of end-on thiolated HA - **4**) or 5 mL dimethyl sulfoxide (in case of end-on thiolated CS - **5**), followed by the addition of 200 mg of HA or CS dissolved in 5 mL acetate buffer (AcOH /AcONa (0.078 M AcOH/0.0625 AcONa; pH 4.5). The reaction mixture was magnetically stirred at 45 °C for 24 h. Unreacted reagents were removed by dialysis against ethanol (Mw cut off 14 kDa). The product was obtained by ethanol evaporation followed by freeze-drying. Compound **4** was used in Chapters III, IV, V, and VII, while compound **5** was used only in Chapter VII.

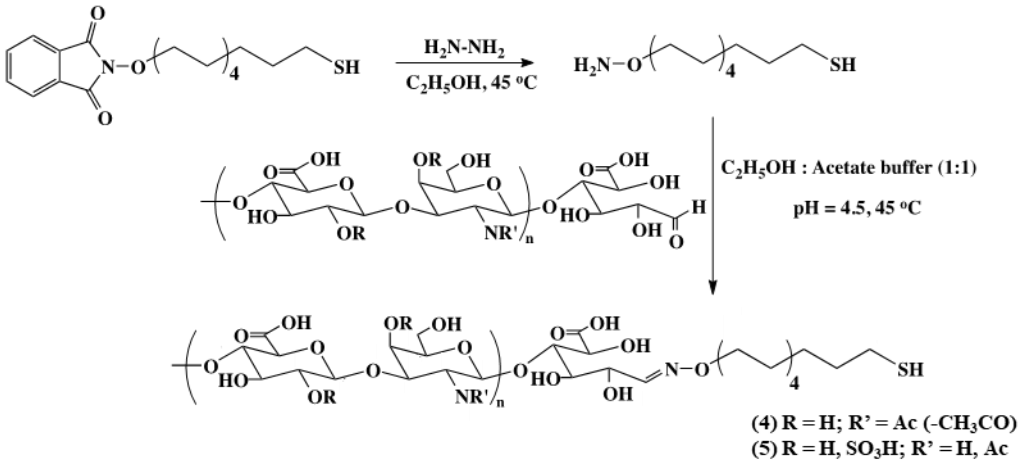

Scheme II.3. Schematic presentation of the oxime condensation used to modify HA (4) and CS (5).

II.1.1.3 Characterization of the obtained compounds.

The structure and purity of the intermediate were confirmed by proton Nuclear Magnetic Resonance spectroscopy (^{1}H NMR). Spectra were recorded on Bruker Avance III spectrometer (Bruker, Germany) at 25 °C in chloroform-d (Sigma). The chemical shifts are reported in ppm (δ units) downfield to the solvent signal. The final products, **4** and **5**, were characterized by ^{1}H NMR (60 °C, D_2O or DMSO-d_6) and Gel Permeation Chromatography (GPC). GPC measurements were performed with a Malvern Viscotek TDA 305 with a refractometer (RI-Detector 8110, Bischoff), right-angle light scattering (LS), and viscometer detectors on a set of four columns: precolumn Suprema 5 μm 8 × 50 S/N 3111265, Suprema 30 Å 5 μm 8 × 300 S/N 3112751, Suprema 1000 Å 5 μm 8 × 300 S/N 3112851 PL, and Aquagel-OH MIXED 8 μm 7.5 × 300 S/N 8M-AOHMIX-46-51. The system was kept at 30 °C. We used 0.1 M NaN_3, 0.01 M NaH_2PO_4 (pH 6.6) as an eluent at a flow rate of 1 mL/min. The molecular weight of the GAGs was determined by GPC with a conventional (RI *vs.* elution time) and multidetector calibration (RI+LS+Viscosity) using the software Omnisec 4.6.1 (ViskoteK).

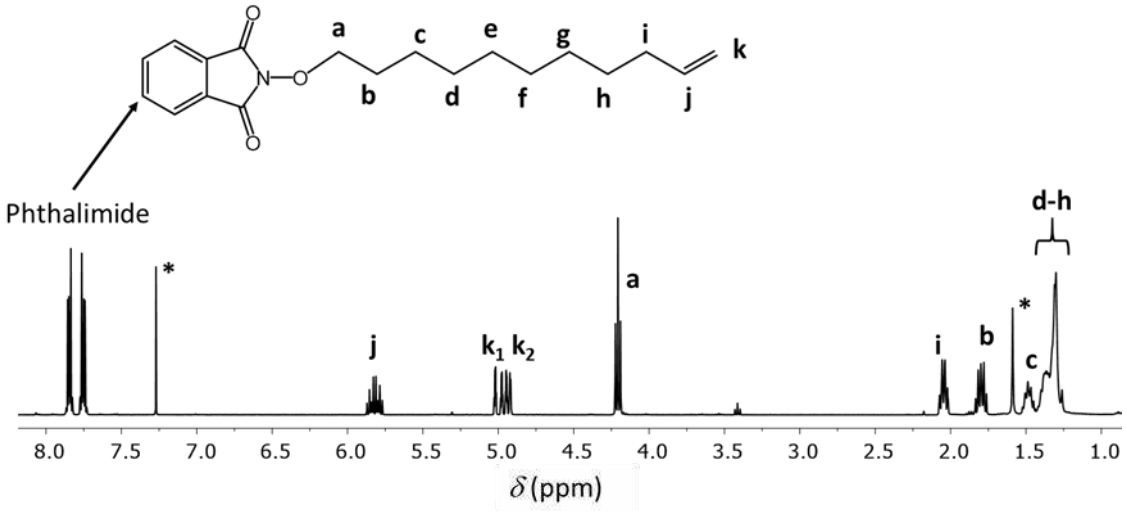

Figure II.1. ^{1}H NMR spectrum (400 MHz, 25 ºC, $CDCl_3$) of compound (1): δ 7.89 – 7.80 (m, 2H), 7.80 – 7.70 (m, 2H), 5.82 (ddt, J = 16.9, 10.2, 6.7 Hz, 1H), 5.00 (ddt, J = 17.1, 2.1, 1.6 Hz, 1H), 4.96 – 4.90 (m, 1H), 4.21 (t, J = 6.8 Hz, 2H), 2.05 (dtd, J = 8.0, 6.6, 6.0, 1.4 Hz, 2H), 1.85 – 1.73 (m, 2H), 1.49 (ddt, J = 9.4, 5.5, 3.5 Hz, 2H), 1.44 – 1.24 (m, 10H). * solvent

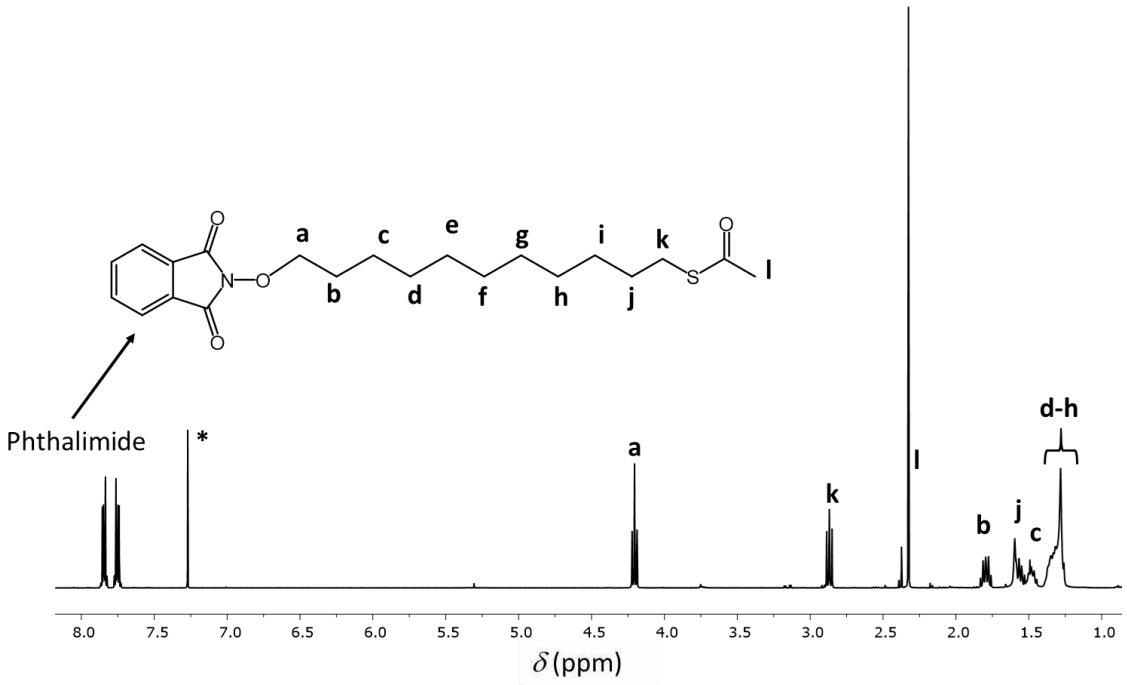

Figure II.2. ^{1}H NMR spectrum (400 MHz, 25 ºC, $CDCl_3$) of compound (2): δ 7.88 – 7.81 (m, 2H), 7.79 – 7.72 (m, 2H), 4.20 (t, J = 6.8 Hz, 2H), 2.89 – 2.83 (t, J = 7.4 Hz, 2H), 2.33 (s, 3H), 1.86 – 1.73 (m, 2H), 1.59– 1.53 (m, 2H), 1.53 – 1.42 (m, 1H), 1.41 – 1.19 (m, 4H). * solvent

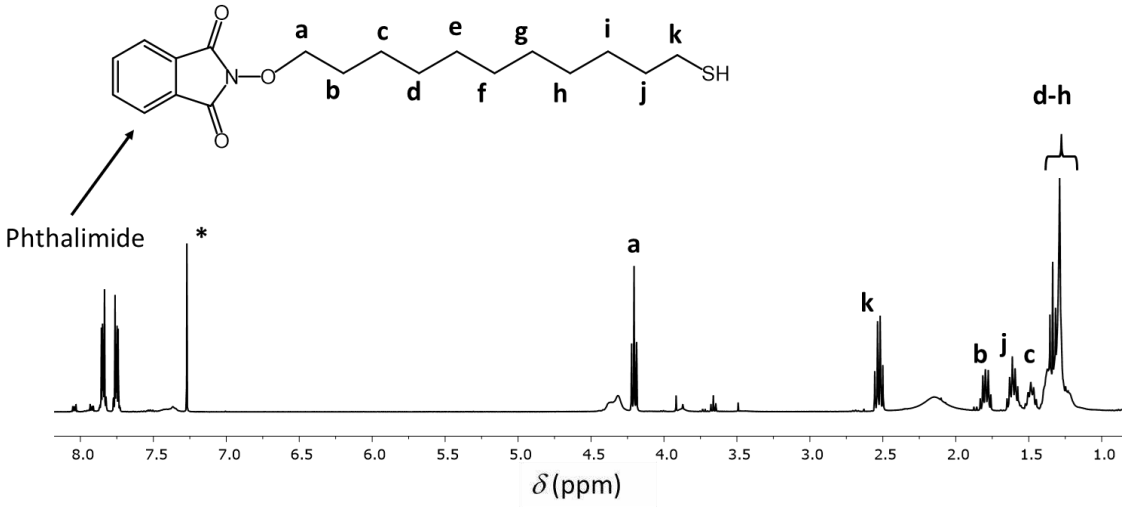

Figure II.3. ^{1}H NMR spectrum (400 MHz, 25 ºC, $CDCl_3$) of compound (3): δ 7.88 – 7.81 (m, 2H), 7.79 – 7.72 (m, 2H), 4.21 (t, J = 6.8 Hz, 3H), 2.53 (qd, J = 7.6, 1.9 Hz, 4H), 1.79 (dq, J = 8.6, 6.8 Hz, 2H), 1.69 – 1.54 (m, 2H), 1.49 (s, 2H), 1.43 – 1.16 (m, 10H). * solvent

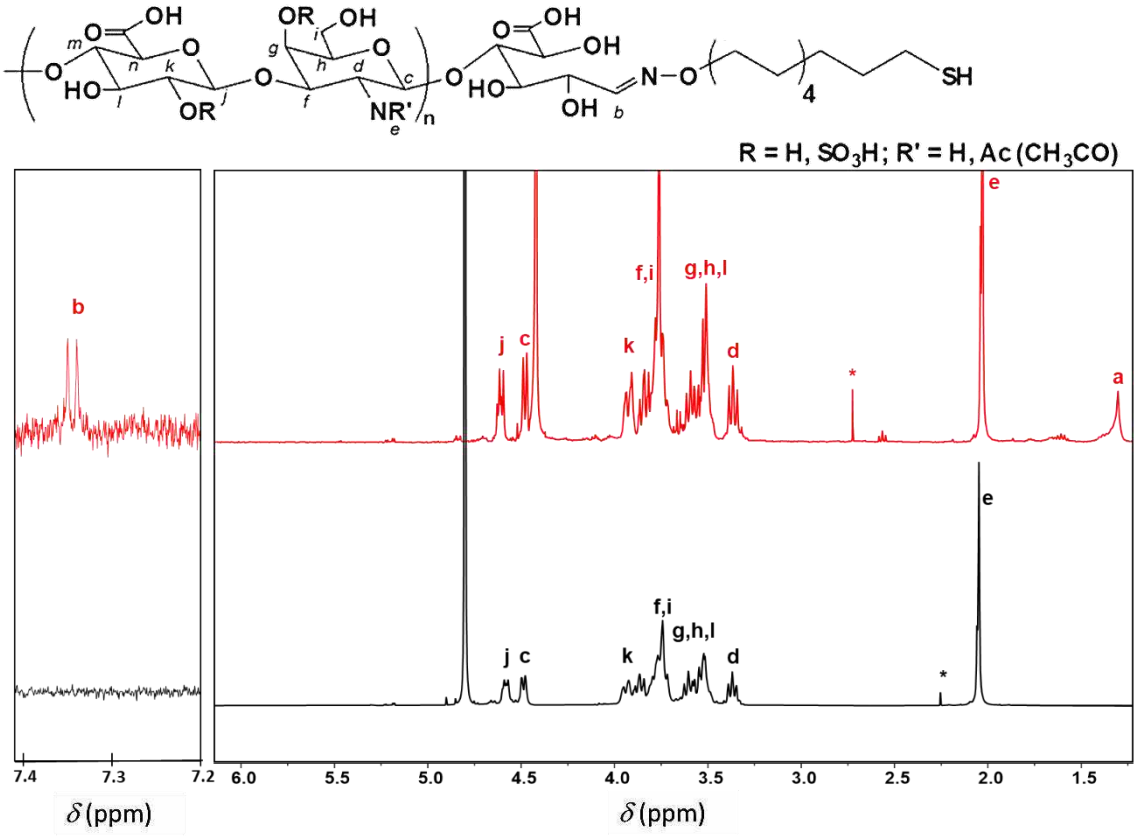

Figure II.4. Structure and ^{1}H NMR (400 MHz, 60 ºC, D_2O) spectrum (red) of end-on thiolated HA (4). The ^{1}H NMR spectrum of unmodified HA (black) is shown for comparative purposes. The signal at 7.35 confirms the oxime condensation (b, left box). Signals marked with (*) correspond to impurities from the solvent.

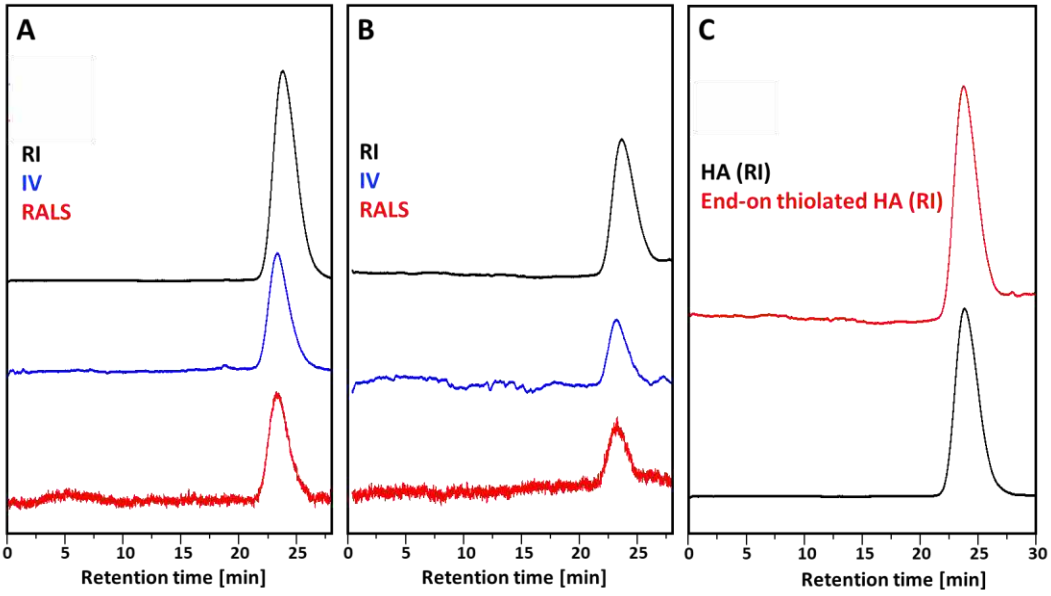

Figure II.5. GPC profiles of (A) HA, (B) end-on thiolated HA (4), and (C) comparison between the elugrams of unmodified and modified HA.

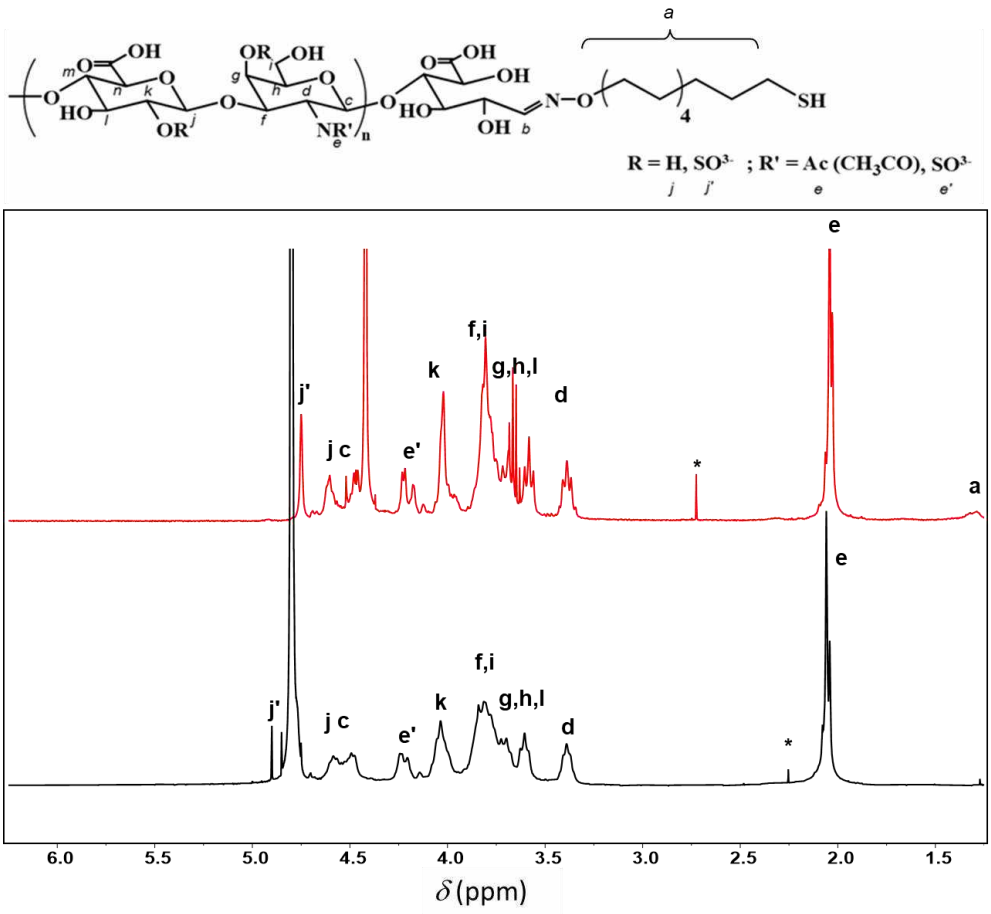

Figure II.6. Structure and ^{1}H NMR (400 MHz, 60 ºC, D_2O) spectrum (red) of end-on thiolated CS (5). ^{1}H NMR spectrum of unmodified CS (black) is shown for comparative purposes. Signals marked with (*) correspond to impurities from the solvent.

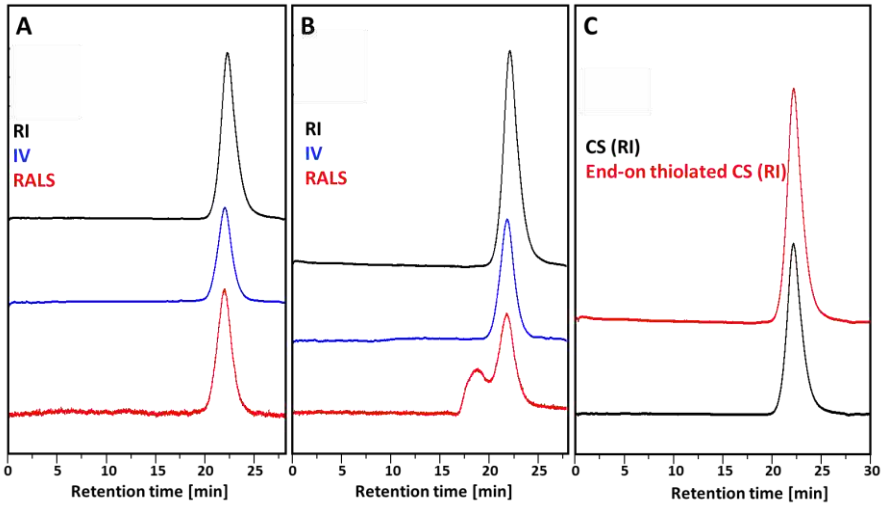

Figure II.7. GPC profiles of (A) CS, (B) end-on thiolated CS (5), and (C) comparison between the elugrams of unmodified and modified CS.

II.1.2 Synthesis of HEMA-*g*-HA copolymer.

All commercial reagents were used without purification unless noticed. The solvents used were analytical or HPLC grade.

II.1.2.1 Polymerization of 2-hydroxyethylmethacrylate (HEMA).

We used atom transfer radical polymerization with an alkyl bromoinitiator and CuBr/ 2,2´-bipyridine as a catalyst.[8] HEMA (99%, Aldrich) was passed through a plastic syringe filled with basic alumina to remove the inhibitor. A round bottom flask was charged with 2-bromo-2-methylpropionic acid (0.12 g, 1 mol eq.), HEMA (20 g, 220 eq.), 2,2´-bipyridine (1.1 g, 10 mol eq.), and 5 mL of methanol. The mixture was degassed with N_2 stream, and CuBr (0.5 g, 5 mol eq.) was added into the reaction system under N_2. Next, the polymerization was performed at 40 °C for 24 h under magnetic stirring. The reaction flask was opened and bubbled with air to stop the polymerization. The crude reaction product was dissolved in methylene chloride; the solution passed through a column with neutral aluminum oxide to remove the copper catalyst and dialyzed (Mw cut off 12 kDa, cellulose) against ethanol to remove the excess of the monomer. After 7 days of dialysis, water was added, ethanol evaporated under vacuum, the polymer (**6**) was recovered by lyophilization and analyzed by NMR and GPC

II.1.2.2 Synthesis of HEMA-ONH_2.

Poly-HEMA (**6**, 1 Eq), N-hydroxyphthalimide (N-Pht, from 0.5 to 1.2 eq. in respect to OH of HEMA to obtain different degrees of substitution), and triphenylphosphine (same eq. as N-Pht) were mixed in dried DMF (ca 20 g/L mL of HEMA) under N_2 atmosphere. To this mixture, diisopropyl azodicarboxylate (same eq. as N-Pht) was added dropwise (color change to red). The reaction was stirred at room temperature (RT) for 24 h. The product (**7**) was purified by ultrafiltration (Mw cut off 5 kDa) in DMF, and then an excess of water was added, and freeze-drying was performed. The obtained products were analyzed by NMR. The degree of substitution was determined by integration of the peaks corresponding to the phthalimide substituted -OH groups and was found to be 10, 25, 50, 60, 80, and 100 %. The phthalimide group was cleaved by adding hydrazine hydrate (3 eq. per phthalimide group) in DMF. After 2 h, the product was diluted in water and freeze-dried under a vacuum. The cleavage was confirmed by NMR. The

crude product was ultra-filtered with cellulose membrane YM3 (Mw cut off 5 kDa) in DMF before being used in the next step.

II.1.2.3 Synthesis of HEMA-*g*-HA.

The crude HEMA-ONH_2 (25 % degree of substitution) and 15 mol excess of HA (with respect to moles of the full HEMA chain) were added in a mixture of an acetate buffer (0.078 M AcOH/0.0625 AcONa; pH 4.5) and DMSO (1:2 volume ratio). The reaction mixture was stirred at 60 °C. Then 10 mol excess of aniline (with respect to the HA) was added to the mixture. Aliquots were taken every 24 h along 7 days and analyzed by GPC. Finally, the product (**8**) was freeze-dried and ultra-filtered with a cellulose membrane (Mw cut off 30 kDa).

II.1.2.4 Characterization of the obtained polymers.

The structure and purity of the intermediate were confirmed by ^{1}H NMR and GPC. ^{1}H NMR spectra were recorded on Bruker AVANCE 400 and Varian Inova 750 spectrometers. D_2O, DMSO-d_4, or $CDCl_3$ were used as solvents. Chemical shifts are reported in ppm (δ units) downfield from internal tetramethylsilane when $CDCl_3$ was used as a solvent or 3-(trimethylsilyl)-propionic acid-d_4 when the spectra were recorded in D_2O. GPC characterization of HEMA homopolymer was performed on an LC system consisting of Agilent-SECcurity-Pump and an Agilent-SECcurity Autosampler connected to a refractive index (PSS-SECcurity DRI) and multi-angle static light scattering (PSS SLD 7100 MALLS) detectors. Samples separation was achieved using 4 columns (PSS, Mainz, Germany): PSS GRAM (Guard, 10 µm, 8x50mm), PSS GRAM (10 µm, 8x300mm, 100 Å), 2x PSS GRAM (10 µm, 8x300mm, 3000 Å). Column and detectors were kept at 70 °C. Samples were eluted with 57 mM LiBr in N,N-dimethylformamide at a constant rate of 1 mL/min. The light scattering detector was calibrated with a narrow polystyrene standard (PSS, Mainz, Germany) of Mw 87600 kDa and polydispersity index (PDI) 1.08. The dn/dc was set to 0.065 according to the literature.[9, 10] GPC characterization of HA and HA-*g*-HEMA was performed with a Malvern Viscotek TDA 305 with refractometer (RI-Detector 8110, Bischoff), right and low angle light scattering (RALS and LALS), and viscometer detectors on a set of four columns: pre-column Suprema, 5 µm, 8x50, Suprema 30 Å, 5 µm, 8x300, and 2x Suprema 1000 Å, 5 µm 8x300. The system was kept at 30 °C. We have used phosphate-buffered saline (0.01 M phosphate buffer, 0.0027 M potassium

chloride and 0.137 M sodium chloride, pH 7.4, at 25 °C) and 0.05% w/v NaN_3 as eluent that was pumped at the rate of 1 mL/min. The absolute molecular weight was determined by a calibration of the RI, LS, and Viscosity detectors using the software Omnisec 5.12 (ViskoteK) and pullulan (number average molecular weight (Mn) 48.8 kDa and PDI 1.07) as a standard. The dn/dc of HA (0.15 mL/g) was taken from the literature.[11] For HEMA-*g*-HA copolymers, the dn/dc was determined on-line or estimated from the mass percentage of HA and HEMA calculated from NMR. A conventional calibration was also performed with a commercial polysaccharide set from Polymer standard Service GmbH that contains 10 Pullulans with narrow polydispersity and Mp (molecular mass at the peak maximum) ranging from 180 Da to 708 kDa. Data are presented in Chapter VI.

II.1.3 Fluorescence labeled HA polymers.

II.1.3.1 Synthesis of Rhodamine labeled HA polymers.

HA polymer (15 mg of HA with a weight average molecular weight (Mw) of 1.35 MDa (HMW HA), or 45 mg of HA with Mw 4.8 kDa (LMW HA), or 10 mg of HA-*g*-HEMA with 8 HA chains) was dissolved in water (0.25 mL). A solution of rhodamine (Rho) isothiocyanate in DMSO was then added to the reaction and stirred for 24 h. Different amounts of Rho were used to modify the HA polymers to not compromise the solubility of the final product - we observed that a high degree of LMW HA modification results in a precipitation of the labeled polymer in aqueous media. Thus, we used 4 mol % (per disaccharide) of Rho in the case of HMW HA and HEMA-*g*-HA and 1 mol % in the case of LMW HA. The product was purified by ultrafiltration with a cellulose membrane (Mw cut off 1 kDa). The solution was concentrated and then purified by ultrafiltration against 200 mM NaCl (4x), water (4x), and finally freeze-dried. All procedures were performed under light protection. The Rho-modified HA polymers were characterized by GPC, and we did not observe any difference in the retention times of unmodified and respective Rho-labeled polymers.

II.1.3.2 Characterization of Rho-labeled HA polymers.

The degree of modification was assessed by spectrophotometry and fluorescence spectroscopy. For spectrophotometry, standard solutions of Rhodamine B were prepared at concentrations between 4 μM

and 300 μM in MilliQ water. Rho-labeled HA polymers were dissolved in MilliQ water (1 mg/mL). The absorption spectrum of standards and Rho-labeled HA polymers was acquired at the wavelengths λ= 450 nm and 600 nm in Synergy HT microplate reader (Bio-Tek Instruments, USA). Rhodamine concentration was determined at the maximum absorbance peak (λmax = 562 nm). For fluorescence spectroscopy, standard solutions of Rhodamine B were prepared between 85 nM and 200 nM in MilliQ water, and Rho-labeled HA polymers were diluted to 50 μg/mL in MilliQ water. Rhodamine B was excited at λex 520 nm and fluorescence spectrum acquired between 550 nm and 650 nm in FP-8500 Spectrofluorometer (Jasco Corporation, Japan). Rhodamine B concentration was determined according to the peak area. The degree of modification was determined by the molar ratio between Rhodamine B and HA disaccharides (Table II.1).

Table II.1 Degree of HA modification with rhodamine determined by spectrophotometry and fluorescence spectroscopy.

HA or HEMA-*g*HA	Degree of modification (%)	
	Absorbance	Fluorescence
LMW HA	1.42 ± 0.11	1.22 ± 0.24
HMW HA	0.35 ± 0.01	0.24 ± 0.05
HEMA-*g*HA	2.39 ± 0.71	2.07 ± 0.09

II.2 DEVELOPMENT OF GLYCOTOOLS FOR ELUCIDATING AND TARGETING MOLECULAR AND CELLULAR INTERACTIONS OF GLYCANS *IN VITRO*

The studies in this thesis are set in two parts: the first one aims to understand the significance of the HA presentation on its bioactivity, and the second one is to translate this understanding into the development of biofunctional devices. We, therefore, designed different platforms (Scheme II.4) to address the relevant questions about the bioactivity of immobilized *vs.* soluble HA (Chapter IV) and the importance of the HA density (Chapters V and VI) and translated the findings in the development of molecular tools for an active targeting towards cancer therapy.

II.2.1 Immobilization of HA on plane substrates.

In the first part of this thesis (Chapters III, IV, and V), we used the high affinity of the thiol to gold for surface immobilization.[12] To generate surfaces with homogeneously immobilized HA, gold-coated substrates were simply immersed in a solution of HA end-on modified with alkanethiol (0.5 mg/mL MilliQ water) overnight at room temperature (RT) with orbital shaking. The substrates were then removed, washed with PBS, and dried with a nitrogen stream.

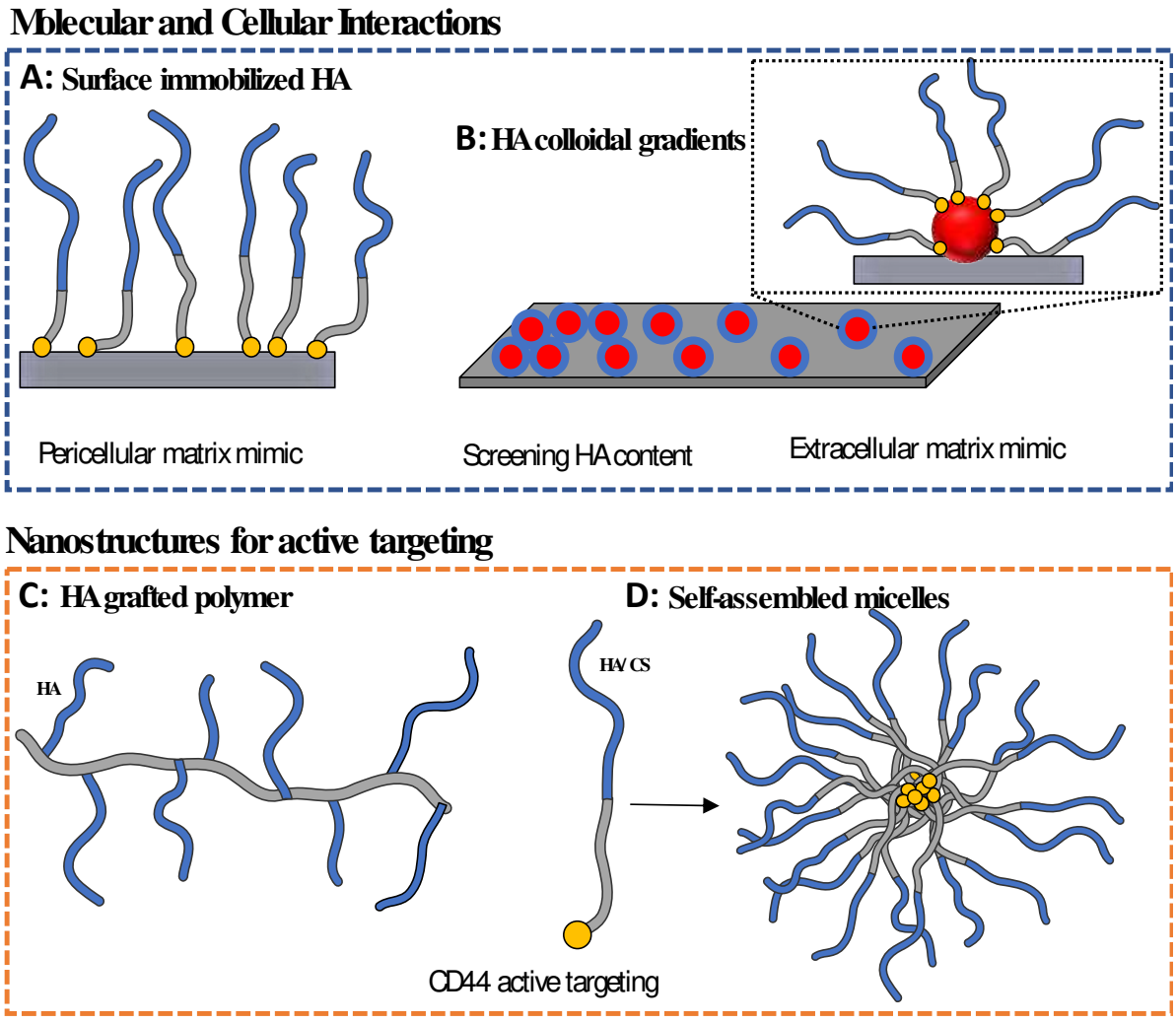

Scheme II.4. Different types of platforms developed in the thesis: HA and CS are presented in blue, the thiol groups in yellow, and the synthetic portion (HEMA in C or undecan in D) of the polymer in grey.

II.2.2 Colloidal gradients.

We generated gradients by diffusional deposition of colloidal gold nanoparticles (negatively charged) on aminated glass coverslip (positively charged). The continuous injection of colloidal gold nanoparticles to a vertically fixed aminated glass results in different interaction times between the substrate and the nanoparticles (Scheme II.5): short interaction times result in a lower density of immobilized gold nanoparticles, while higher density can be obtained by prolongation of the contact time, thus, offering a method to develop a gradient by controlling the time of the immobilization. Using this methodology, we obtained reproducible gradients of gold nanoparticles that allow further functionalization with end-on thiolated HA (Chapters IV and V).

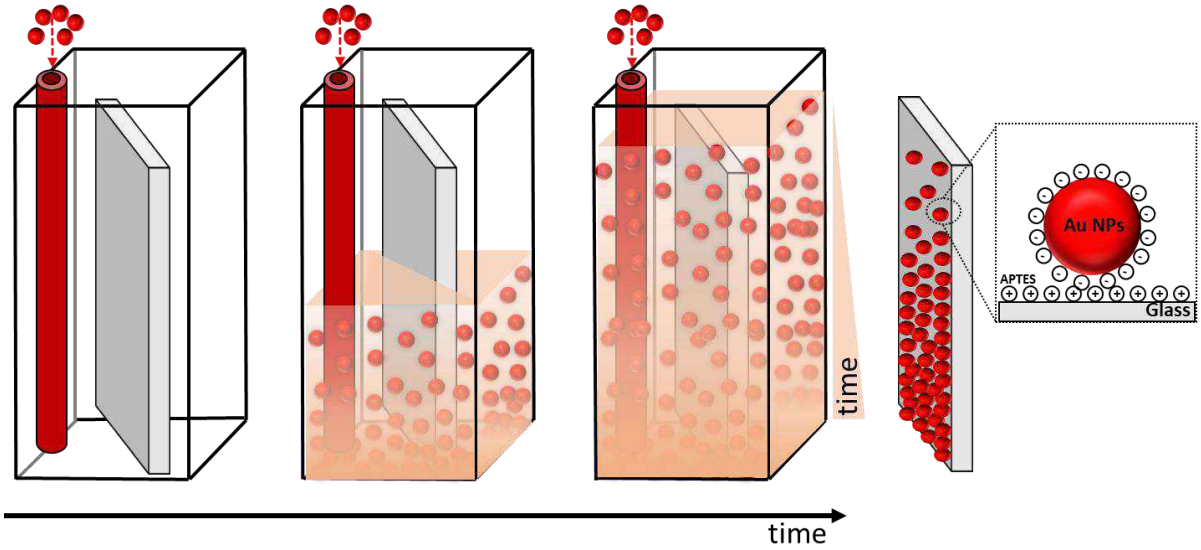

Scheme II.5. Schematic representation on the preparation of colloidal gold nanoparticles gradient by diffusional deposition.

II.2.3 HA-grafted brush-like polymers.

In this thesis, we used a new HA copolymer design: grafting of long HA chains on a synthetic polymer (Scheme II.4C). The grafting was achieved *via* an oxime ligation at the reducing end of HA (see II.1.2 above) and allowed a controlled HA density at a molecular level (Chapter VI).

II.2.4 Self-assembly of HA micelles.

The introduction of an alkanethiol at the GAG (HA and CS) reducing end confers amphiphilic properties to the polymer, *i.e.,* the polymer is composed of lipophilic (alkanethiol) and hydrophilic (GAG) portions. Amphiphilic polymers can self-organize above a critical concentration and form aggregates with different structures, *e.g.*, micelles (Scheme II.4D). The stability of these aggregates depends on supramolecular forces, including hydrogen bonding, hydrophobic effects, electrostatic interactions, and van der Waals forces.[13] In our molecular design, the spontaneous organization of GAG amphiphile (alkanethiol at the core and GAG at the surface) also favors the formation of disulfide bonds that confer additional redox-sensibility to the micelles. In all cases, the modified GAG was dissolved in MilliQ water above the critical micellar concentration (3 mg/mL) and homogenized with a vortex (Chapter VII).

II.3 CHARACTERIZATION OF THE DEVELOPED GLYCOTOOLS

II.3.1 Contact angle measurement.

The contact angle is a quantitative measure of wetting of a solid by a liquid. It is defined as the angle formed by a liquid at the three-phase boundary where a liquid, gas (usually air), and solid intersect (Scheme II.6). It is a straightforward, fast, and cost-effective approach to determine wettability quantitatively. Water contact angles were measured on OCA15+ goniometer (Dataphysics) using the sessile drop method with Milli-Q water (3 μL). Measurements were performed in triplicate on 3 different substrates at RT. We used contact angle measurements to evaluate glass amination before gradients preparation in Chapters IV and V.

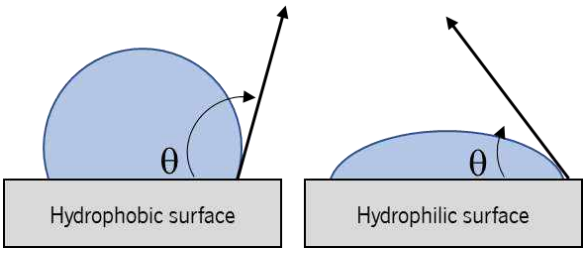

Scheme II.6. Schematic representation of a contact angle (θ) between the water droplet and hydrophobic or hydrophilic substrate.

II.3.2 Atomic Force Microscopy (AFM).

AFM is a scanning probe microscopy with a high resolution, which can be applied to analyze *in situ* dry or hydrated samples without any sample manipulation or treatment. It gives information about the sample topography and morphology. In AFM, a nanoscale tip attached to a spring-like cantilever raster screens the sample surface. Atomic forces are used to map the tip-surface interactions, and thus, the resolution of the AFM is very high (angstrom scale). Analysis can be performed either by contact or non-contact mode. A laser beam is used to detect cantilever deflections, *i.e.*, any changes on cantilever deflection result in changes in the direction of the reflected beam and ultimately build a topographical and force image. This technique was used to determine the size of gold nanoparticles (dry) in Chapters IV and V and characterize GAGs micelles in Chapter VII.

Sample preparation: A drop of gold nanoparticles or micelles suspension was deposited on a freshly cleaved mica functionalized with amine groups using 50 μL of (3-aminopropyl) triethoxysilane (APTES) for 30 min in a desiccator at RT. In the case of gold nanoparticles, the mica sheet was washed and dried before imaging. All AFM images were acquired with a JPK Nanowizard 3 in quantitative imaging mode using silicon cantilevers (ACSTA, AppNano, USA) with a typical resonance frequency of 150 kHz and a spring constant of about 7.8 N m^{-1} at RT.

II.3.3 Scanning Electron Microscopy (SEM).

SEM uses a focused electron beam as the illumination source. The emitted electrons scatter from the scanned sample surface, thus generating information about the sample morphology with a resolution of 20 nm. This technique was used to characterize either the morphology of the used glycotools or the morphology of the cells in contact with these tools (Chapters IV and V).

Sample preparation: Dry samples do not require any manipulation. Wet samples (*e.g.*, substrates with cells) were thoroughly washed with PBS, fixed with glutaraldehyde (1 h, 4 °C), dehydrated with ethanol with increasing concentration (50 %, 70 %, 90 %, and 100 %), and dried overnight at RT. The dry samples were mounted on holders with carbon tape and sputter-coated with gold (1 nm) using a Leica ACE600 sputter coater. After coating, samples were imaged using a high-resolution field emission scanning electron microscope AIRIGA® (Zeiss).

II.3.4 Dynamic Light Scattering (DLS).

DLS is used for measuring the size of particles in suspension within the submicron range. It uses light (laser beam) scattering to scan macromolecules or nanoparticles in Brownian motion. The light scattered by particles contains information on the diffusion speed (smaller particles move faster while larger ones move slower) and thus on the size distribution. This methodology was used in Chapters IV, V, and VII.

Sample preparation: For size determination, GAGs micelles were prepared as described above (II.2.4) and measured in a Nano ZS (Malvern Instruments, Malvern). The scattered light was detected at a back-scatter angle (173º), providing the sensitivity required to measure particles at low concentrations. Measurements were carried using a polystyrene cell at 25 °C. The CONTIN algorithm (intensity weighted) was applied to obtain the size distribution.

II.3.4.1 Electrophoretic Light Scattering (ELS) - Zeta (ζ) Potential.

Electrophoretic Light Scattering combines the application of a current field and light scattering to determine particles' charge. Zeta potential is the difference in the electrokinetic potential between a dispersion medium and the stationary layer (Stern layer) of a fluid attached to a charged particle (Scheme II.7). By applying a current field, particles in suspension move towards the opposite charge. In ELS, particles' electrophoretic mobility is determined, and ζ potential is yielded. This methodology was used to determine the surface charge of GAGs micelles in Chapter VII.

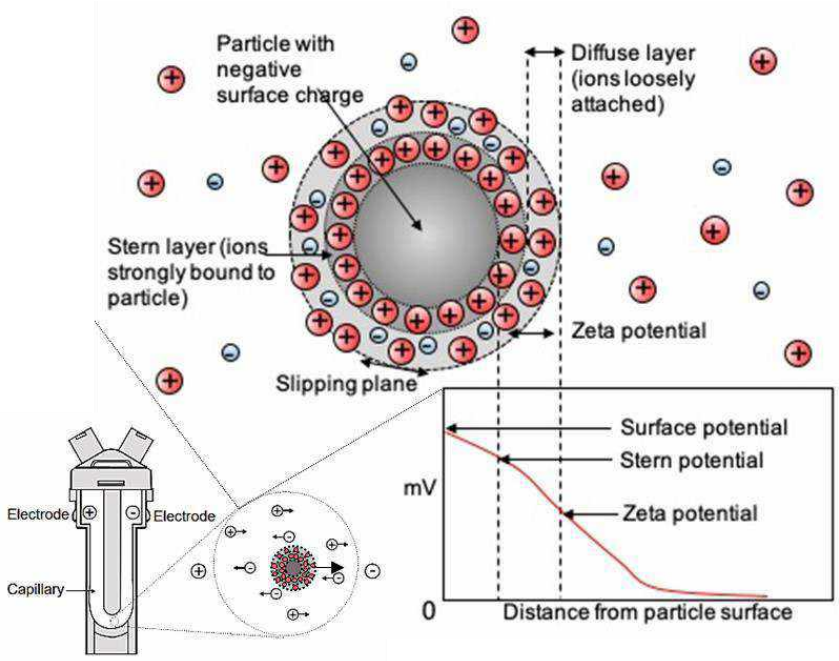

Scheme II.7. Schematic representation of the surface potential, Stern layer, and zeta potential as a function of distance from a charged particle in suspension and representation of ELS fundamentals. Adapted from [14].

II.3.5 UV-Vis Spectrophotometry.

This spectrophotometry measures the light absorption in the UV-Vis range by chemical entities in the solution. The light absorption is proportional to the concentration of the chemical and is therefore used for quantitative analysis. We have used it to determine the degree of modification of Rho-labeled polymers (Chapter VI) and protein concentration with BCA assay (Chapters III and VI). For quantitative analysis, a calibration curve is first obtained by analyzing standard solutions with known concentrations at the wavelength with a maximum absorption peak. The absorption spectrum of samples is then measured at the same conditions, and the concentration is determined by interpolating absorption intensity from the calibration curve drawn from the standards. Qualitative analysis with UV-Vis spectrophotometry was also used in the case of MTS assay (Chapter VI). In this case, all samples and controls are analyzed automatically, and the absorption values are normalized to the controls. In this thesis, solutions were transferred to a transparent microplate (100 μL in triplicate), and absorption spectra were measured in a microplate reader SYNERGY HT (BioTek).

II.3.6 Fluorescence emission spectroscopy.

Fluorescence emission is observed when a fluorophore in an excited state (induced by light absorption) returns to the fundamental state through light emission – fluorescence. This spectroscopy is quantitative and more sensitive than spectrophotometry. Herein, we use Rhodamine fluorescence to determine the degree of modification of Rho-labeled HA polymers (Chapter VII). Moreover, fluorescence can be combined with the fluorophore inherent properties to render different information. For example, the Nile Red emission spectrum is greatly affected by the medium polarity: in polar mediums (*e.g.,* water), the fluorescence emission is low, and in nonpolar mediums (*e.g.,* in the lipophilic portion of GAGs amphiphiles) it is observed a red-shift in the spectrum together with an increase of fluorescence emission (Scheme II.8). Thus, Nile Red is suitable for critical micellar concentration (CMC) determination and evaluation of micelles stability under redox environments (Chapter VII).

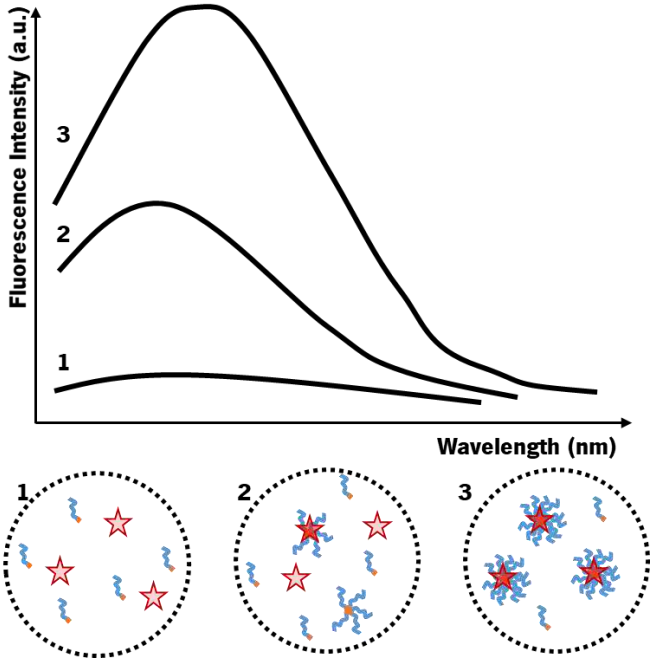

Scheme II.8. Schematic representation of Nile Red spectral properties in determining CMC and micelles stability

II.3.7 Surface Plasmon Resonance (SPR).

SPR is a sensitive spectroscopic technique to study molecular interaction *in situ* and without the requirement of labels. SPR is used to detect mass change at the surface of a gold chip in real-time by

measuring the light absorption of a material deposited on the chip. It is relevant for the characterization of biochemical processes: a ligand of interest is immobilized on the chip, and a solution of the analyte then flows in contact with the chip placed in a microfluidic chamber. The real-time monitoring of the mass change can be used to determine the kinetics and affinity of the ligand-analyte interactions (Scheme II.9). In this thesis, SPR was used to determine the affinity of HA and HA-grafted polymers to CD44 in Chapter VI. CD44 was immobilized through avidin-biotin ligation on the surface of a dextran-gold chip (Sensor chip SA). Solutions of HA or HEMA-*g*-HA (25 – 200 ng/mL) prepared in running buffer were then injected on the chip surface in single cycle injection (successive injection of a sample with increasing concentration), and association and dissociation phases were monitored. Kinetic constants were determined using BIAevaluation 2.0.2 software.

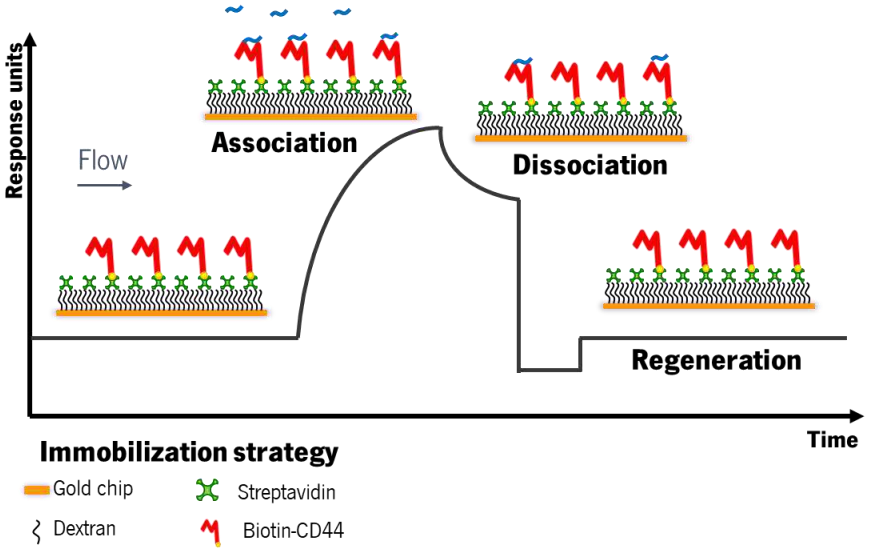

Scheme II.9. Schematic representation of analyte-ligand (HA-CD44) interaction measured in SPR

II.3.8 Isothermal titration calorimetry (ITC).

ITC is a free-label, quantitative technique used to study biomolecular interactions by measuring the heat released or absorbed in real-time, thus determining the thermodynamic parameters of binding reactions (Scheme II.10). In this thesis, we used ITC in Chapter VI to analyze the enzymatic degradation of HA and HA-grafted polymers by hyaluronidase (HYAL). Briefly, HA polymer (1 mg/mL in PBS) was injected (single injection experiment) in a HYAL solution (1.5 mg/mL in PBS), and the generated heat was measured until the equilibrium was reached. Apparent enthalpy of the reaction, heat rate (dQ/dt), and Michaelis–Menten plots were obtained using MicroCal PEAQ-ITC Analysis Software (Malvern).

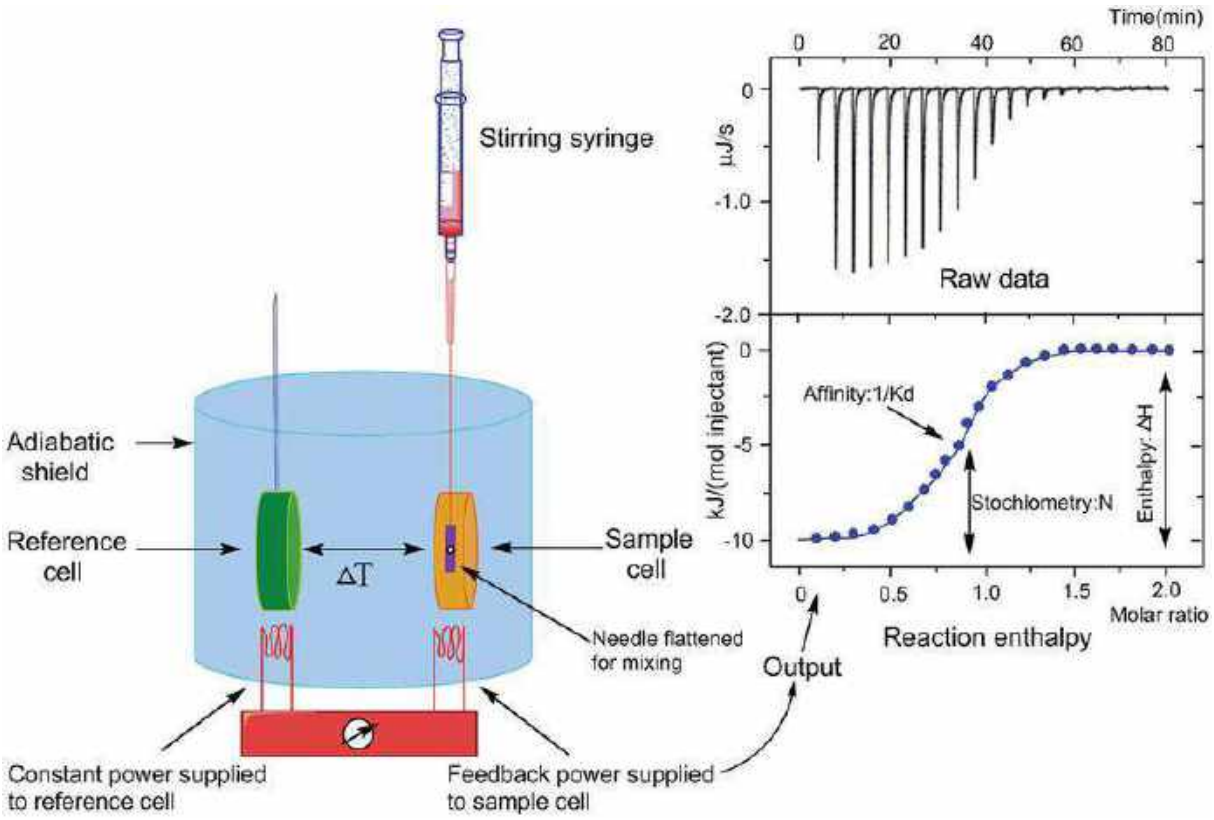

Scheme II.10. Schematic representation of ITC principles and general determination of affinity and parameter.[15]

II.4 BIOLOGICAL ASSESSMENT OF GLYCOTOOLS

II.4.1 *In vitro* cell culture.

Breast cancer cell lines MDA-MB-231, MDA-MB-468, and Sk-Br-3 were purchased from American Type Culture Collection (ATCC) and were used in Chapters III, IV, V, VI, and VII. Cells were cultured at 37 °C in a humidified 5% CO_2 atmosphere using Dulbecco's modified Eagle's medium (DMEM) high glucose (Sigma) supplemented with 10 % fetal bovine serum (FBS, Gibco, UK) and 1 % antibiotic/antimycotic (Gibco, UK) solution containing 100 U/mL penicillin G sodium, 100 μg/mL streptomycin sulfate, and 250 ng/mL amphotericin B.

II.4.2 Sk-Br-3 transfection and vector expression.

Transfected Sk-Br-3 cell line was used in Chapter VI. Sk-Br-3 cells were transfected with GFP-tagged CD44 (human, transcript variant 7, NM_001202556, Origene, 25 ng) using Lipofectamine 3000 (Invitrogen) according to manufacture instructions. Briefly, DNA-lipid complexes were formed by incubating DNA with Lipofectamine for 15 min at RT in Opti-MEM medium and added to previously seeded cells (5 x 10^5 in 24-well plate) and kept in culture with Opti-MEM medium. After 48 h incubation, cells were observed under a fluorescence microscope to confirm the expression of GFP-tagged CD44. Selection and culture of transformed cells were performed in a growth medium (II.4.1) supplemented with 1 μg/mL of geneticin. Transformed cells were cryopreserved in FBS with 10 % DMSO and thaw before each assay. Transfected cells were used up to passage number 3.

II.4.3 Glycan-cells interactions.

Cells were studied in direct contact with the developed glycotools: they were either seeded on plane substrates with immobilized HA (Chapters III, IV, and V) or incubated with HA copolymers (Chapter VI) or with HA micelles (Chapter VII). Upon confluence, cells were detached from the culture flask, seeded at a predetermined density on the HA-immobilized substrate, and let to adhere/interact for a specific time according to the experimental design. At the end of the culture period, the medium was removed, cells were washed and treated according to the following characterization. For the incubation with micelles or HA polymers, stock solutions were mixed with the growth medium and added to adhered cells. After incubation, the medium was removed, cells were washed with PBS, and the cells were then processed according to the following characterization. The exact conditions, such as cell detachment method, cell seeding density, incubation temperature, and time for each experimental design, are described in the respective chapter.

II.4.3.1 Viability assessment.

The assay is based on the ability of mitochondrial dehydrogenase enzymes from the viable cells to convert the 3-(4,5-dimethylthiazol-2-yl)-5-(3-carboxymethoxyphenyl)-2-(4-sulphofenyl)-2H-tetrazolium (MTS) compound into a brown formazan product that is soluble in a culture medium. MTS assay was used to

determine the cell viability after incubation with HA polymers following the supplier's instructions (Chapter VI). First, cells adhered to tissue culture polystyrene were supplemented with HA polymers (HMW HA, LMW HA, or HEMA-*g*-HA) at different concentrations (25 to 100 μg/mL) and incubated for 2 h and 24 h. Next, the culture medium was removed, cells were gently washed with PBS, and MTS medium was added (DMEM low glucose without phenol red supplemented with 1% antibiotic/antimycotic and 5:1 volume ratio of culture medium to CellTiter 96®AQueous One Solution) and incubated for 3 h at humidified 37 °C and 5 % CO_2 atmosphere. Then, the MTS medium was transferred to a transparent 96-well plate, and the absorbance was read at 490 nm on a multiwell microplate reader (Synergy HT, BioTek Instruments). The measured absorbance was compared to a control (cells cultured in the absence of the tested compounds) and used to determine the cytotoxicity.

II.4.3.2 Protein expression.

The expression of specific proteins can be characterized using different characterization techniques. In this thesis, we used immunocytochemistry, flow cytometry, and Western blotting (WB). Despite having a common molecular basis (specific antibody interaction with a protein of interest), these techniques have specific features. For instance, WB is a destructive technique that gives information from a pool of cells, while immunocytochemistry and flow cytometry can be used for individual cell characterization.

II.4.3.2.1 Immunostaining.

The principle of immunostaining is the use of antibodies to target specific proteins or antigens in cells. This methodology comprises fixation, permeabilization (in the case of intracellular proteins), and labeling steps, which are interchangeable according to the experimental design and detection technique.

Fluorescence Microscopy: Cells were fixed with 10 % buffered formalin. An additional permeabilization step with 0.2% Triton X-100 in PBS (15 min at RT) is needed if the target protein is intracellular, and sample blocking with 3% Bovine serum albumin (BSA) in PBS (30 min at RT) is required to avoid unspecific antibody binding. The labeling consisted of incubation with a primary antibody, diluted according to each antibody's specifications, in 1 % Bovine serum albumin in PBS overnight at 4 °C. This step is followed by washing with PBS and incubation with fluorochrome-conjugated secondary antibody in 1 % BSA in PBS (if the initial antibody is fluorescent-labeled, there is no need for this step) 1 h at RT. Finally, cells were

washed and mounted in a glass slide with Vectashield (Vector, USA) and then imaged under an inverted laser scanning confocal microscope (TCS SP8, Leica). This technique allows acquiring images at different focal planes rendering high spatial resolution of the signal in x, y, and z planes. Additionally, we can acquire tile images for the whole sample using an automated platform, which is relevant for the surface gradients (Chapter IV and V). This technique was used in Chapters IV, V, VI, and VII.

Flow cytometry: Flow cytometry allows a fast analysis of a significant cell number at a single-cell level. It is based on the detection of fluorescence emitted by labeled cells, which can render different information according to the experimental design, *e.g.*, cell viability, particles internalization, protein expression, and can be used to characterize either live cells or fixed cells. In this thesis, we used flow cytometry to analyze receptors' (CD44, CD24, RHAMM) expression. Briefly, cells were detached from the substrate by incubation with 4 mM EDTA in PBS (pH 8, 15 min at 37 °C). Cells in suspension ($5x10^5$ cells in 100 μL of PBS) were immunolabeled using a fluorescent antibody (30 min at RT) or indirect cell labeling with primary and secondary antibodies (1 h at 4 °C, then 30 min at RT) with or without permeabilization (0.2 % Triton X-100 in PBS for 15 min at RT) for total and surface-expressed quantification. Then, cells were fixed with 1% formalin in PBS and analyzed in the flow cytometer BD FACSCalibur (BD Bioscience). This methodology was used in Chapters II, IV, and V.

II.4.3.2.2 Western Blotting (WB).

In WB, a mixture of proteins is separated based on their molecular weight by gel electrophoresis. The separated proteins are transferred to a hydrophobic membrane, and proteins of interest can be detected using immunostaining. WB was used to determine the protein expression by cells supplemented with HA polymers. After treatment at different conditions (described in II.4.3), proteins were extracted from a pool of cells (control or treated) using Radioimmunoprecipitation assay (RIPA) buffer supplemented with protease and phosphatase inhibitors. The total protein concentration in the extract was determined by bicinchoninic acid (BCA) protein assay following the manufacturer's instructions. Next, samples with a defined protein concentration were prepared in sample buffer (Laemli or LDS buffer) containing a reducing agent and denatured (10 min, at 90 °C). The proteins were separated based on molecular weight (Mw) through gel electrophoresis in Bis-Tris gels (8% or 12%) at 50-100V in Bolt MES SDS running buffer and transferred to nitrocellulose or polyvinylidene fluoride (PDVF) membranes (iBlot2 system). Membranes were treated with a blocking solution (5 % skimmed milk, 1 % BSA, and 0.5% Tween 20 in Tris-buffered

saline-Tween 20 (TBS-T) or 5 % BSA in TBS-T) to inhibit unspecific antibody binding. Next, membranes were incubated with specific antibodies against receptors of interest (antibody diluted in 3 % BSA in TBS-T solution overnight at 4 °C) and with secondary fluorescent antibodies (IRDyes in TBS-T, 1h at RT). After immunostaining, the signal of the protein of interest was imaged using Odyssey Fc Imaging System and quantified relative to internal control, *e.g.*, glyceraldehyde 3-phosphate dehydrogenase (GAPDH). Specific details and modifications on this general methodology can be found in each chapter. This methodology was used to determine CD44 and RHAMM expression in Chapters III and VI.

II.4.3.3 Live-cell optical microscopy.

We used optical microscopy coupled with an automatic station and an incubation chamber (37 °C and humidified 5% CO_2 atmosphere) to perform time-lapse imaging of live cells. Briefly, conditioned cells, *e.g.*, seeded on HA gradients, were imaged in an inverted microscope Axio Observer (Zeiss, Germany) for 16 h with a 5 min lapse between image acquisition. This technique was used in Chapter V.

II.4.4 Glycan-receptor interactions.

We used several methods to study the interactions of RHAMM and CD44 upon supplementation of HA polymers: Förster resonance energy transfer (FRET) microscopy and co-immunoprecipitation were used to study CD44/RHAMM co-localization upon recognition of HA in Chapter III (Scheme II.11). FRET microscopy was also used to assess the co-localization of HA and HEMA-*g*-HA to CD44 in Chapter VI. Finally, receptors chemical crosslinking was used to evaluate CD44 clustering at cells membrane in Chapter VI.

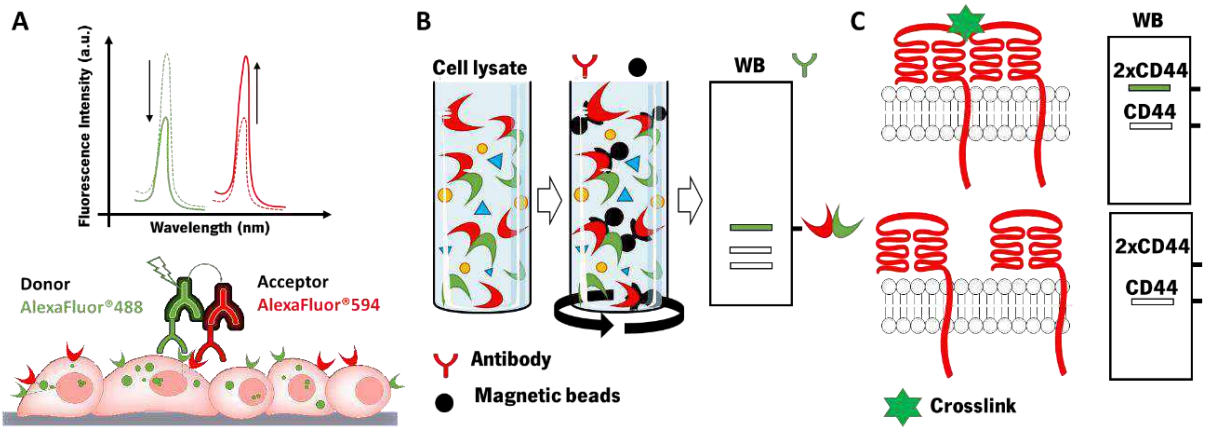

Scheme II.11. Schematic presentation of methodologies used to determine biomacromolecules co-localization. A) FRET microscopy. B) Co-immunoprecipitation. C) Chemical crosslinking.

II.4.4.1 Glycan-receptor co-localization.

II.4.4.1.1 FRET microscopy.

FRET is a physical phenomenon that occurs between two fluorochromes, a donor and an acceptor (FRET pairs), with overlapping spectral properties, *i.e.*, the donor's emission spectrum must overlap with the acceptor's excitation spectrum. The emission spectrum of both fluorochromes shouldn't overlap to avoid signal bleedthrough. FRET only occurs if the donor/acceptor pair is at a close distance - a maximum of 10 nm apart. At these conditions, it is observed an increase of fluorescence intensity emitted by the acceptor upon excitation of the donor due to energy transfer (Scheme II.11A). This technique overcomes the inherent microscopy resolution as a positive FRET signal ensures a co-location of fluorochromes under 10 nm range. In this thesis, FRET microscopy was used to assess CD44 and RHAMM co-localization by indirect staining with antibodies in Chapter III and to assess Rho-labeled HA and HEMA-g-HA binding to CD44-GFP in Chapter VI.

II.4.4.1.2 Co-immunoprecipitation.

Co-immunoprecipitation is an extraction method that allows the identification of interacting proteins. In this technique, a specific antibody is used to precipitate a target protein alone or in a complex with other

proteins as in cells. By analyzing the proteins that form the complex, we can obtain information on cellular interactome and signaling pathways. We used co-immunoprecipitation to evaluate CD44/RHAMM interactions in response to HA supplementation (Chapter III). Briefly, whole proteins extract (Scheme II.11B) was incubated with the antibody for one of the target proteins (CD44 or RHAMM). The protein/protein complexes were then recovered using magnetic beads and analyzed by WB to identify the complex's proteins (Scheme II.11B). In this methodology, we have used either CD44 or RHAMM as the target protein.

II.4.4.2 Receptor blocking.

To study receptor-specific interactions, we have used antibodies against the receptor's active portion to block its activity. To this end, cells were treated with blocking antibodies in suspension (100 µL and a maximum of 2 x 10^5 cells) for 30 min at 37 °C. Next, cells were washed with PBS, resuspended in a growth medium, and seeded according to the steps mentioned above (II.4.3).

II.4.4.3 Receptors crosslinking.

Chemical crosslink of surface proteins was performed with bis(sulfosuccinimidyl)suberate (BS^3). BS^3 is a homobifunctional crosslink containing N-hydroxysuccinimide ester (NHS ester) at each extremity that efficiently reacts with the primary amines of the proteins. This crosslinker is water-soluble, membrane-impermeable, and compatible with biological studies. Briefly, live cells were incubated with a freshly prepared BS^3 solution in PBS and incubated at 4 °C for crosslinking for 30 minutes. After crosslinking quenching by 1M Tris HCl (pH 7.5, 15 minutes at RT), proteins were extracted and separated based on their molecular weight (II.4.3.2.2). Then, WB was performed to identify the protein crosslinking by increasing the molecular weight (Scheme II.11C).

II.5 References

1. Herrera-Gayol, A. and S. Jothy, *Effects of hyaluronan on the invasive properties of human breast cancer cells in vitro.* International journal of experimental pathology, 2001. **82**(3): p. 193-200.
2. Amorim, S., et al., *Molecular weight of surface immobilized hyaluronic acid influences CD44-mediated binding of gastric cancer cells.* Scientific Reports, 2018. **8**(1): p. 16058.

3. Pang, X., et al., *Hyaluronan (HA) Immobilized on Surfaces via Self-Assembled Monolayers of HA-Binding Peptide Modulates Endothelial Cell Spreading and Migration through Focal Adhesion.* ACS Applied Materials & Interfaces, 2021. **13**(22): p. 25792-25804.
4. Thakar, D., et al., *A quartz crystal microbalance method to study the terminal functionalization of glycosaminoglycans.* 2014. **50**(96): p. 15148-15151.
5. Silva, C., et al., *Design of protein delivery systems by mimicking extracellular mechanisms for protection of growth factors.* Acta Biomaterialia, 2017. **63**: p. 283-293.
6. Carvalho, A.M., et al., *Redox-responsive micellar nanoparticles from glycosaminoglycans for CD44 targeted drug delivery.* Biomacromolecules, 2018. **19**(7): p. 2991-2999.
7. Chan, E.W.L. and L. Yu, *Chemoselective Immobilization of Gold Nanoparticles onto Self-Assembled Monolayers.* Langmuir, 2002. **18**(2): p. 311-313.
8. Beers, K.L., et al., *Atom Transfer Radical Polymerization of 2-Hydroxyethyl Methacrylate.* Macromolecules, 1999. **32**(18): p. 5772-5776.
9. Adharis, A., et al., *Synthesis and Self-Assembly of Double-Hydrophilic and Amphiphilic Block Glycopolymers.* Biomacromolecules, 2019. **20**(3): p. 1325-1333. Altohught the dn/dc is not included in the article the value was provided by the auhtors.
10. Gallow, K.C., et al., *Influence of gradient strength and composition profile on the onset of the cloud point transition in hydroxyethyl methacrylate/dimethylaminoethyl methacrylate gradient copolymers.* Polymer, 2012. **53**(5): p. 1131-1137.
11. Han, Y., et al., *Impact of refractive index increment on the determination of molecular weight of hyaluronic acid by muti-angle laser light-scattering technique.* Scientific Reports, 2020. **10**(1): p. 1858.
12. Frasconi, M., et al., *Protein immobilization at gold–thiol surfaces and potential for biosensing.* 2010. **398**(4): p. 1545-1564.
13. Lombardo, D., et al., *Amphiphiles Self-Assembly: Basic Concepts and Future Perspectives of Supramolecular Approaches.* Advances in Condensed Matter Physics, 2015. **2015**: p. 151683.
14. Manual, Z.N.S.U.J.W., UK, *Malvern instruments.* 2004.
15. Takacs, M. *Adapting Proteins for Clinical and Industrial Use*. 2018.

SECTION 3

EXPERIMENTAL STUDIES

CHAPTER III

CO-LOCALIZATION AND CROSSTALK BETWEEN CD44 AND RHAMM DEPEND ON HYALURONAN PRESENTATION

CO-LOCALIZATION AND CROSSTALK BETWEEN CD44 AND RHAMM DEPEND ON HYALURONAN PRESENTATION

Abstract

CD44 and the receptor for hyaluronic acid-mediated motility (RHAMM) are the main hyaluronan (HA) receptors. They are commonly overexpressed in different cancers activating signaling pathways related to tumor progression, metastasis, and chemoresistance. Besides their involvement in signal transduction *via* interaction with HA, currently, there is little information about the possible crosstalk between CD44 and RHAMM and the role of HA in this process. In the present work, we used immunocytochemistry combined with Förster resonance energy transfer (FRET) microscopy and co-immunoprecipitation to elucidate the involvement of HA in CD44 and RHAMM expression, co-localization and crosstalk. We studied breast cancer cells lines with different degrees of invasiveness and expression of these receptors in the absence of exogenous HA and compared the data with the results obtained for cultures supplemented with either soluble HA or seeded on substrates with end-on immobilized HA. Our results demonstrated that cells response depends on the HA presentation: CD44/RHAMM complexation was upregulated in all cell lines upon interaction with immobilized HA, but not with its soluble form. Moreover, the results showed that the expression of both CD44 and RHAMM is regulated via interactions with HA indicating cell-specific feedback loop(s) in the signaling cascade.

This chapter is based on the publication:

Carvalho, Ana M.; Soares da Costa, Diana; Paulo, Pedro M.R.; Reis, Rui L.; Pashkuleva, Iva: "Co-localization and crosstalk between CD44 and RHAMM depend on hyaluronan presentation", Acta Biomaterialia, 2021, 119, 114-124.

III.1. INTRODUCTION

Hyaluronan (HA) is a linear non-sulfated glycosaminoglycan synthesized at the cell surface and secreted into the extracellular environment. Once secreted, HA assembles with different components of the extracellular matrix (ECM) and interacts with cell receptors, thus, mediating both ECM-cell and cell-cell crosstalk.[1-5] HA is critical in various physiological processes and its amount is tightly controlled and regulated by several HA synthetases (HAS) and hyaluronidases (HYAL).[6-9] The expression of these enzymes is altered in different pathological states, *e.g.,* cancers and inflammation, causing specific HA turnover profiles.[6, 9-13] Overexpression of HAS (mainly HAS2 but also HAS1 and HAS3) is a hallmark of several malignancies and related to poor prognosis: it results in accumulation of HA both in tumor parenchyma and in the surrounding stroma.[14-18] The molecular size of the accumulated HA is also altered: the proportion of short fragments is greater due to the HYALs and reactive oxygen species (ROS), which are overexpressed in the tumor microenvironment.[6, 9, 19] These HA changes trigger different cell behavior (*e.g.,* increased cell survival, drug resistance, proliferation, migration/motility, invasion, and metastasis) by the formation of immunoprotective pericellular coats and through interactions of the generated HA fragments with the cellular receptors.[18-22]

There are two main HA receptors – the transmembrane glycoprotein CD44 and the receptor for HA-mediated motility (RHAMM). The standard form of CD44 (CD44s) is widely expressed in cells of different healthy tissues. Inflammation and several types of cancer are associated with upregulation and structural changes of the extracellular domain of CD44, giving rise to so-called variants (CD44v) that promote tumor progression and metastasis.[23-25] CD44 binds HA via an amino-terminal link domain leading to ligand-induced clustering of CD44.[26, 27] Of note, CD44 also binds other ECM components and is a co-receptor for different proteins, thus it is very sensitive to its environment and involved in the activation of several signaling pathways (*e.g.* Erk1/2, AKT, and FAK).[1, 28-31] The minimal size of HA fragments that CD44 can bind is six monosaccharide units, *i.e.,* the fragments generated by overexpressed HYAL in tumors still can bind to CD44, but clustering occurs only upon binding of oligosaccharides that are larger than 20 residues.[32-34] The interactions of HA with CD44 promote cell survival, motility, and invasion.[20, 23, 25, 35]

RHAMM (also known as CD168 and hyaluronan-mediated motility receptor, HMMR) is a soluble protein with low or no expression in homeostatic tissues.[36, 37] It is an unusual protein: structurally, RHAMM is a typical cytoplasmic protein as it lacks a membrane-spanning domain and signal peptides needed for export via the Golgi/endoplasmic reticulum pathway.[38-40] Indeed, RHAMM is identified in the cytoplasm but also in the cytoskeleton, nucleus, and cell surface, where it is transported in response to specific stimuli by unconventional mechanisms. Upregulation of RHAMM is observed during tissue remodeling (*e.g.,* after injury or during tumorigenesis) and affects different cell functions as motility, migration, invasion, and ECM remodeling.[41-45] Unlike CD44, RHAMM has no HA-binding module domain. Instead, it uses a BX_7B motif (B is either Lys or Arg and X_7 contains no acidic residues) on its COOH terminus to bind HA.[46, 47]

There is a significant body of evidence that supports the formation of a triple complex between CD44, RHAMM, and HA on the cell surface during tumorigenesis. In this complex, the role of RHAMM is to enhance the CD44 surface localization, stabilize the CD44-HA interaction and thus, contribute to the activation of Erk1/2 signaling.[42-44] Besides this role, the presence of RHAMM in different cellular compartments and at the cell surface suggests that it might contribute to the signal transmission across the cell membrane.[38] However, the association dynamics between CD44 and RHAMM upon HA binding and the feedback responses are not completely understood. In this study, we used Förster resonance energy transfer (FRET) and co-immunoprecipitation to follow the dynamics in CD44 and RHAMM expression and clustering in response to exogenously supplemented HA (Fig. III.1).

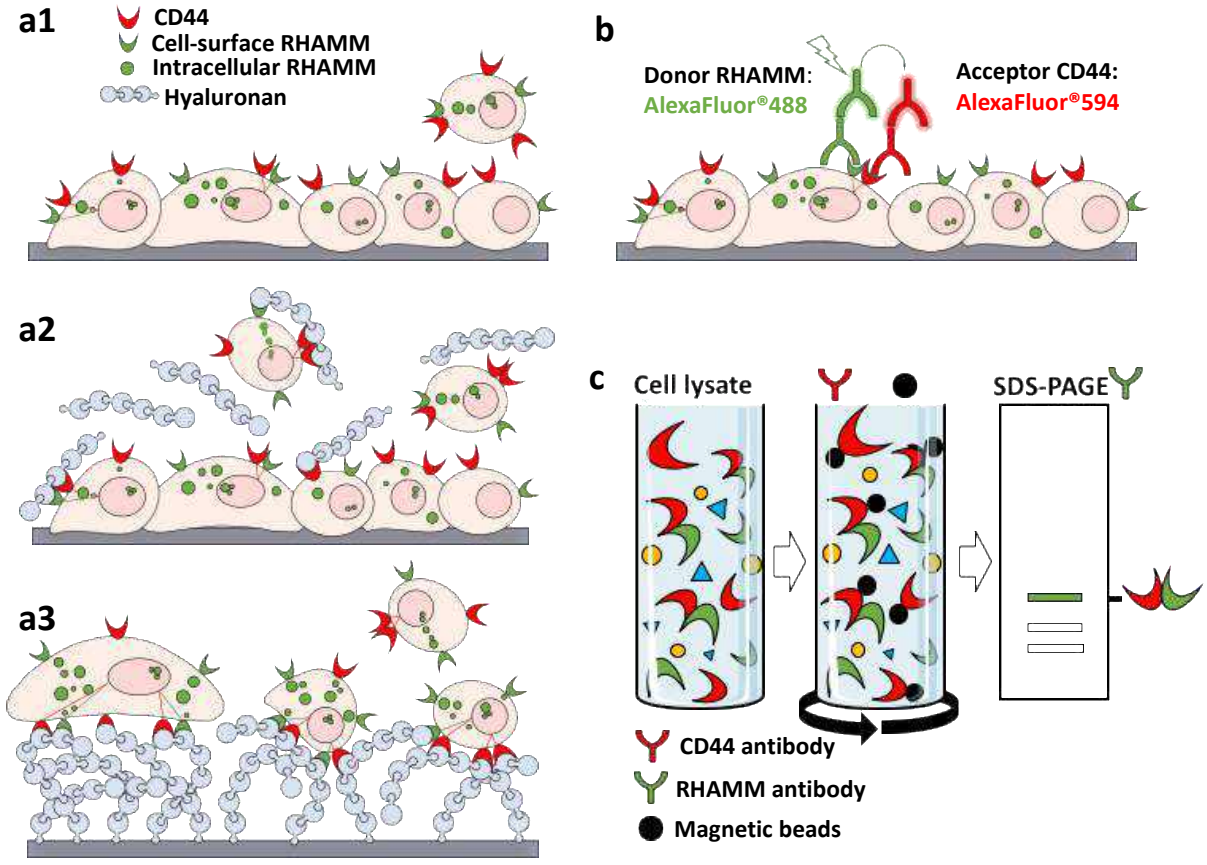

Figure III.1. Schematic presentation of the experimental setup. (a) Cells culture conditions used: (a1) cells cultured on tissue culture polystyrene (TCPS) in the absence of exogenous hyaluronan (controls); (a2) cultures supplemented with hyaluronan dissolved in the media; and (a3) cells seeded on substrates with end-on immobilized hyaluronan. (b) Determination of the proximity of CD44 and RHAMM using immunocytochemistry combined with Förster resonance energy transfer (FRET). (c) Characterization of RHAMM/CD44 co-localization by co-immunoprecipitation.

III.2. Materials and Methods

III.2.1. Materials

Sodium hyaluronate (HA, average molecular weight of 4.8 kDa, polydispersity of 1.18 was obtained from Lifecore (USA). The antibodies used in this study were: human anti-CD44 PE (BD Pharmingen), RHAMM (H-8) (Santa Cruz Biotechnology), anti-CD168 antibody [EPR4055] (Abcam), anti-CD44 antibody [KM201] (abcam) monoclonal antibody to CD44 – Ascites (Acris),

monoclonal antibody phospho-p44/42 MAPK (Erk1/2) (Thr202/Tyr204) (Cell Signaling), mouse IgG1, clone MOPC-21 (StemCell Technologies), AlexaFluor® 594 donkey anti-mouse IgG1 (H+L) and AlexaFluor® 488 donkey anti-rabbit IgG (H+L) (Molecular Probes).

III.2.2. Cell cultures.

We studied MDA-MB-231 and Sk-Br-3 breast cancer cell lines. Cells were seeded on tissue culture polystyrene (TCPS) at 37 °C in Dulbecco Modified Eagle Medium (DMEM) high glucose with phenol red (Sigma-Aldrich) supplemented with 3.7 mg/mL sodium bicarbonate (Sigma-Aldrich), 10 % fetal bovine serum (FBS, Invitrogen) and 1 % antibiotic/antimycotic (Invitrogen). Upon confluence, the cells were detached with TrypLE Express™ (Invitrogen) and used in the following experiments at a cell density of $5x10^5$ cells/mL.

III.2.3. Hyaluronan-supplemented cell cultures.

Cells were seeded on TCPS coverslips (Fig. III.1a) and after 24 h were supplemented with 0.5 mg/mL of HA (soluble HA, Fig. III.1b) and kept for an additional 24 h in contact with the HA. The substrates with immobilized HA were obtained by overnight incubation of a gold-coated glass with end-on modified HA (details are provided in the III.6). Cells were directly seeded on these substrates for 24 h (Fig. III.1c). At the end of each experiment, cells were washed with PBS and fixed with 10 % formalin (Thermo Scientific) for further processing. Cells seeded on TCPS coverslips for 24 h were used as controls.

III.2.4. Pericellular hyaluronan coat.

Cells were cultured on TCPS as described above. After 24 h and 48 h of culture, cells were fixed with 10 % formalin (1 h, 4 °C). Samples were stained with biotinylated HA binding protein (HAbp) from bovine nasal cartilage (1 μg/mL, 1 h at room temperature, Millipore) followed by incubation with streptavidin-AlexaFluor® 488 conjugate (1 μg/mL, 10 minutes room temperature, Molecular Probes). Images were acquired using an Inverted Confocal Microscope (TCS SP8, Leica).

III.2.5. Expression of hyaluronan receptors RHAMM and CD44 at the cell surface (flow cytometry).

Cells were cultured as described above. Upon confluence, they were detached with 4 mM ethylenediaminetetraacetic acid (EDTA) in phosphate-buffered saline (PBS pH 8, Sigma-Aldrich), and membrane expression of CD44 and RHAMM was characterized. Direct labeling of cells with anti-human CD44-PE was performed at room temperature for 20 min (0.2 μg/mL of the antibody for $5x10^5$ cells in 100 μL PBS). RHAMM tagging was performed in two steps: cells were incubated with mouse anti-human RHAMM (H-8) at 4 °C for 40 min (0.3 μg/mL of the antibody for $5x10^5$ cells in 100 μL PBS), followed by washing step and incubation with 0.1 μg/mL of secondary antibody AlexaFluor® 488 donkey anti-mouse IgG (H+L) (100 μL PBS, 40 min, 4 °C). Cells were fixed with 1 % formalin/PBS (1 h at 4 °C). Fluorescence was measured in BD FACSCaliburflow cytometer (BD Biosciences), and data was analyzed with Flowing software.

III.2.6. Total expression of RHAMM and CD44 (immunocytochemistry).

Cells were fixed with 10 % formalin and permeabilized with 0.2 % of triton-X-100/PBS (15 min, room temperature). Unspecific interactions were blocked with 3% BSA/PBS (1 h, room temperature). Incubation with primary antibody was performed in 1% BSA/PBS for 1 h at room temperature. Anti-CD168 antibody (dilution 1:300) was used for RHAMM and CD44 were tagged with monoclonal antibody to CD44 (dilution 1:400). IgG1 (dilution 1:400) was used as isotype control. After thorough washing with PBS (3x 5 min), a secondary antibody (AlexaFluor® 488 (dilution 1:600) for RHAMM and AlexaFluor® 594 (dilution 1:600) for CD44 was added in 1% BSA/PBS (1 h at room temperature), together with DAPI (1 μg/mL) for nucleus counterstaining. Microscope slides were prepared with VectaShield mounting medium (Vector Laboratories, USA). Images were acquired by an Inverted Confocal Microscope (TCS SP8, Leica). At least 30 cells were analyzed per condition.

III.2.7. Förster resonance energy transfer (FRET) measurements.

FRET-based immunocytochemistry was performed with AlexaFluor® 488 (RHAMM, dilution 1:600) and AlexaFluor® 594 (CD44, dilution 1:600) as donor/acceptor (RHAMM/CD44) FRET pair. For double immunostaining, a blocking step with 3% BSA/PBS (overnight, 4 °C) was performed between procedures. FRET images were acquired on a confocal laser scanning microscope (TCS SP8, Leica) using a 63x immersion objective. For sensitized fluorescence emission measurement, images were acquired sequentially through DAPI, AlexaFluor® 488, FRET and AlexaFluor® 594. The microscopy sets used were: DAPI λex = 405 nm and λem = 415 – 485 nm; AlexaFluor® 488 λex = 488 nm and λem = 494 – 576 nm; AlexaFluor® 594 λex = 461 nm and λem = 587 – 709 nm; and FRET λex = 488 nm and λem = 587 – 709 nm.

ImageJ was used to determine the mean grey intensity within cells pixel-by-pixel. Images were saved in TIFF format (LAS X, Leica) and processed by ImageJ 1.52p. Images were imported in a virtual stack and converted to 8-bit images. After the sum projection of Z stacks, the threshold was determined for each cell using Moments Method, and the grey value was measured for the studied conditions. Corrected FRET was determined by subtracting the spectral bleedthrough of AlexaFluor® 488 signal to AlexaFluor® 594 channel. Bleed-through of AlexaFluor® 488 into AlexaFluor® 594 channel was determined at each condition and cell line used. Corrected FRET ($FRET_{corr}$) signal was calculated by equation 1 (Equation III.1):

Equation III.1: $$FRET_{corr} = FRET_{total} - (a\ x\ donor)$$

where $FRET_{total}$ is the total FRET signal measured, α is the fraction of bleedthrough of AlexaFluor® 488 to acceptor channel (Table III.S1) and the donor is the Alexa Fluor® 488 signal measured. At least 30 cells were analyzed per condition.

III.2.8. Acceptor photobleaching-based FRET measurements.

To determine FRET efficiency (E), photobleaching assays were performed. The photobleached area was manually selected and defined as a region of interest (ROI). Photobleaching experiments were performed using a confocal laser scanning microscope (TCS SP8, Leica). A pulse of high-intensity laser (561 nm) was applied for 30 s to locally bleach the signal of the acceptor

(AlexaFluor® 594) in the ROI. Pre-bleaching and post-bleaching images were acquired (AlexaFluor® 488 channel) as described above for FRET imaging. We verified the acceptor's emission (CD44-tagged cells) at the donor excitation wavelength and determined negligible crosstalk at all studied conditions. The FRET efficiency (E) was calculated by Equation III.2:

Equation III.2: $$E = \frac{(F_{pos} - F_{pre})}{F_{pos}} \times 100$$

where F_{pre} and F_{pos} are the fluorescence intensity of the donor (Alexa Fluor® 488 channel) before and after acceptor photobleaching, respectively.[48] At least 3 assays were made per condition.

III.2.9. Co-immunoprecipitation assay.

All materials and reagents were ice-cooled; cells and cell lysates were kept over ice. Co-immunoprecipitation was performed following a previously described protocol.[42] Briefly, cells were seeded at a density of $4x10^4$ cells/cm^2 and maintained in culture for 24 h (control) or exposed to exogenous HA (soluble or immobilized) for 24 h as described in section III.2.3. Cells were washed with PBS and lysed with freshly supplemented RIPA buffer (25 mM Tris-HCl, pH 7.2, 0.1 % SDS, 1 % Triton-X-100, 1 % sodium deoxycholate, 150 mM NaCl, 1 mM EDTA and 50 nM HEPES pH 7.3) containing the proteases inhibitor cocktail (1:50) (Sigma-Aldrich), phenylmethylsulphonyl fluoride (PMSF, 2 mM), 3,4-dichloroisocoumarin (200 mM), sodium orthovanadate (1 mM), and sodium fluoride (NaF, 1 mM). The obtained cell lysate was passed 10x through a 1 mL syringe equipped with a 27 G needle, cooled down (20 min on ice), and centrifuged (13 000 g, 20 min, 4 °C). Protein concentration in the supernatant was determined with Micro BCA™ Protein assay kit (ThermoFisher Scientific). Co-immunoprecipitation was performed using 200 μg of protein from each cell lysate. We performed two sets of experiments: in the first one, the lysates were mixed with primary antibody for RHAMM precipitation, namely anti-CD168 (6 μL), while in the second one, a monoclonal antibody to CD44 (6 μL) was used to precipitate CD44. Immunoprecipitation with IgG1 (6 μL) was used as a control. Incubation of the lysate with the respective antibodies was performed at 4 °C for 12 h in a tube rotator. Next, 12 μL of a suspension of functionalized magnetic beads (Protein G Mag Sepharose™, GE Healthcare) was added and the samples were mixed for 6 h at 4 °C. The beads were separated from the supernatant with a magnetic rack and washed 3x with 0.5 % Triton-X-10/PBS. Bound proteins

were released from the beads by boiling the samples in 25 μL of 1X Laemmli buffer for 10 min. Recovered protein from each cell lysate was loaded and separated by electrophoresis on a 12 % SDS-PAGE together with PageRuler™ Plus pre-stained protein ladder (Thermo Scientific). Proteins were then transferred to Amersham™ Protan® blotting membranes (Merk) with Bjerrum Schafer-Nielsen Buffer (48 mM Tris-HCl, 98 mM glycine, 20 % methanol, and 1.3 mM SDS) by the semi-dry method in a Pierce Power Station (Thermo Scientific). Protein binding sites on the membrane were blocked by incubation with 5 % skimmed milk, 1 % BSA, and 0.5 % Tween-20/TBS-T (50 mM Tris base pH 7.6, 150 mM NaCl, 0.1 % Tween-20) for 30 min at room temperature. The membranes were incubated with primary antibodies in 1% BSA/TBS-T overnight at 4 °C: anti-CD168 (diluted 1:4000) was used in the case of immunoprecipitated CD44, and monoclonal antibody to CD44 (diluted 1:10000) was used for immunoprecipitated RHAMM. The membranes were washed 3x 15 min with TBS-T. Immunodetection was performed using anti-rabbit or anti-mouse IRDye (diluted 1:10000, Li-Cor) in 1 % BSA/TBST for 1 h at room temperature followed by washing with TBS-T (3x 5 min) and TBS. Blotting was visualized using Odyssey® Fc Imaging System (Li-Cor).

III.2.10. Erk1/2 activation.

Erk1/2 activation was evaluated through immunocytochemistry. Immunocytochemistry was performed as described above using monoclonal antibody phospho-p44/42 MAPK (Erk1/2) (dilution 1:200) and secondary antibody anti-rabbit AlexaFluor® 488 (dilution 1:600). Images were acquired in an Inverted Confocal Microscope (TCS SP8, Leica), and at least 30 cells were used for image analysis.

III.2.11. Statistical analysis.

All experiments were repeated at least two times, and at least three images were acquired with the same parameters. The results are presented as mean ± standard deviation. Statistical differences among data with homogeneous variance were assessed by analysis of variance (ANOVA), followed by Tuckey posthoc test. Data that did not follow normal distribution were analyzed with the Kruskal-Wallis test. All tests were performed with a 95% significance.

III.3. Results and Discussion

III.3.1. Characterization of selected breast cancer cells.

We selected two breast cancer cell lines, MDA-MB-231 and Sk-Br-3, based on previous reports describing different invasive properties and expression of HA receptors for these cells.[35, 42, 49-52] MDA-MB-231 cells are invasive and have a motile phenotype, while Sk-Br-3 cells are described as non-invasive.[51, 52] We characterized these cell lines in terms of HA deposition in the pericellular space and surface expression of main HA receptors (Fig. III.2 and Table S2) and, indeed, observed different profiles.

MDA-MB-231 cells presented an HA-rich coat while less HA is visible around Sk-Br-3, and this difference increases with the culture time (Figs. III.2a and III.S3). These results suggest that MDA-MB-231 and Sk-Br-3 have different HA metabolism. The HA recognition apparatus is also distinct: flow cytometry data of non-permeabilized MDA-MB-231 cells showed that they are CD44 positive and contain a small population (about 5%) of RHAMM positive cells (Fig. III.2b, Table III.S2). On the contrary, a bigger population of RHAMM positive cells and a few cells that express CD44 on the surface were presented in the Sk-Br-3 cells culture. Total expression (membrane and cytoplasmic) of CD44 followed the same trend (Figs. III.2c and III.S4): higher CD44 expression is visible for MDA-MB-231 whereas Sk-Br-3 cells have a weak CD44 signal. The total expression of RHAMM was similar for both cell lines. Localization of RHAMM and CD44 is critical for their function(s) and contribution to cancer cell aggressiveness.[18, 36, 39] CD44 is co-localized with the endogenous HA in MDA-MB-231 cells but not in SkBr-3 cells where mainly cytoplasmic CD44 is expressed (Figs. III.2d and III.S4). RHAMM is mostly located in the cytoplasm for both cell lines, although higher surface expression was observed in Sk-Br-3 cells as compared with MDA-MB-231 cells. Intracellular RHAMM affects cytoskeleton dynamics, cell proliferation, and genomic instability, contributing to tumor cell susceptibility and aggressiveness.[36, 38, 44, 53-55] Cell-surface RHAMM, on the other hand, can bind to HA and associate with other proteins, e.g., CD44. Mechanistically, it has similar functions to CD44, *i.e.*, increases invasiveness in breast cancer.[39, 56]

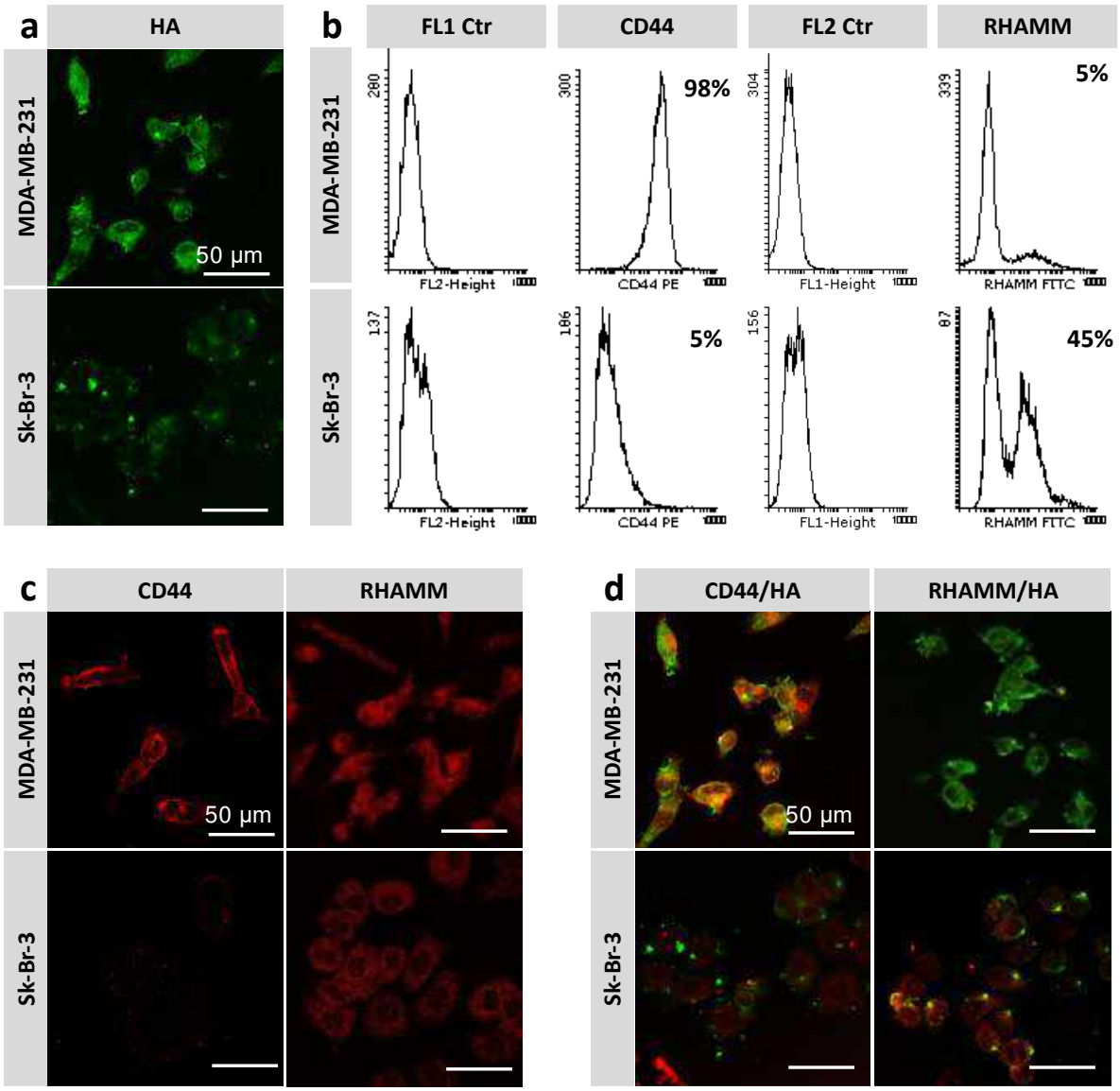

Figure III.2. Characterization of breast cancer cell lines MDA-MB-231 and Sk-Br-3: (a) Confocal microscopy images showing the endogenous hyaluronan secreted by MDA-MB-231 and Sk-Br-3; (b) Flow cytometry analysis showing unstained (FL1 and FL2 control) and immuno-tagged CD44 and RHAMM at the surface of the studied cell lines; (c) Total expression of CD44 and RHAMM visualized by confocal microscopy of immunostained and permeabilized cells; (d) Confocal microscopy images showing secreted hyaluronan (green) and its receptors (red) CD44 and RHAMM. Cells were cultured on TCPS for 24 h. Supplementary information (III.5) about the flow cytometry analysis of permeabilized and non-permeabilized cells are reported in Fig. III.S4 and Table III.S2.

III.3.2. HA induces feedback on CD44 and RHAMM expression.

The effect of HA on cancer cells is mainly studied upon supplementation of culture media with soluble HA or its oligomers (Fig. III.1a2). Such presentation differs from the one observed in the ECM and pericellular space where HA spatial freedom is confined by its interactions with other biomolecules resulting in the formation of concentration gradients and spatial definition of its binding sites.[1, 20] Thus, in addition to supplementation with soluble HA, we also studied cultures on substrates with end-on immobilized HA (Figs. III.S1 and III.S2). Such immobilization does not affect HA structure and does not compromise its bioactivity but allows limited HA spatial freedom and increased local concentration, *i.e.* it mimics the HA-rich pericellular coats.[20, 22, 57, 58]

Soluble HA did not induce any significant changes in the studied cultures (Fig. III.3). On the other hand, immobilized HA affected both cell lines. RHAMM expression was significantly increased in MDA-MB-231 and SkBr-3 cells (Figs. III.3c and III.3d). This result is in agreement with previous studies showing that HA–RHAMM interaction can activate a signal transduction pathway resulting in both mRNA production and protein overexpression and RHAMM mobilization to the cell surface.[38] RHAMM overexpression was concomitant with decreased CD44 expression in MDA-MB-231 cells, *i.e.*, CD44 positive cells (Figs. III.3a and III.3c). Such compensatory effect between CD44 and RHAMM has been previously described, and it is consistent with the concept of molecular redundancy.[41, 56]

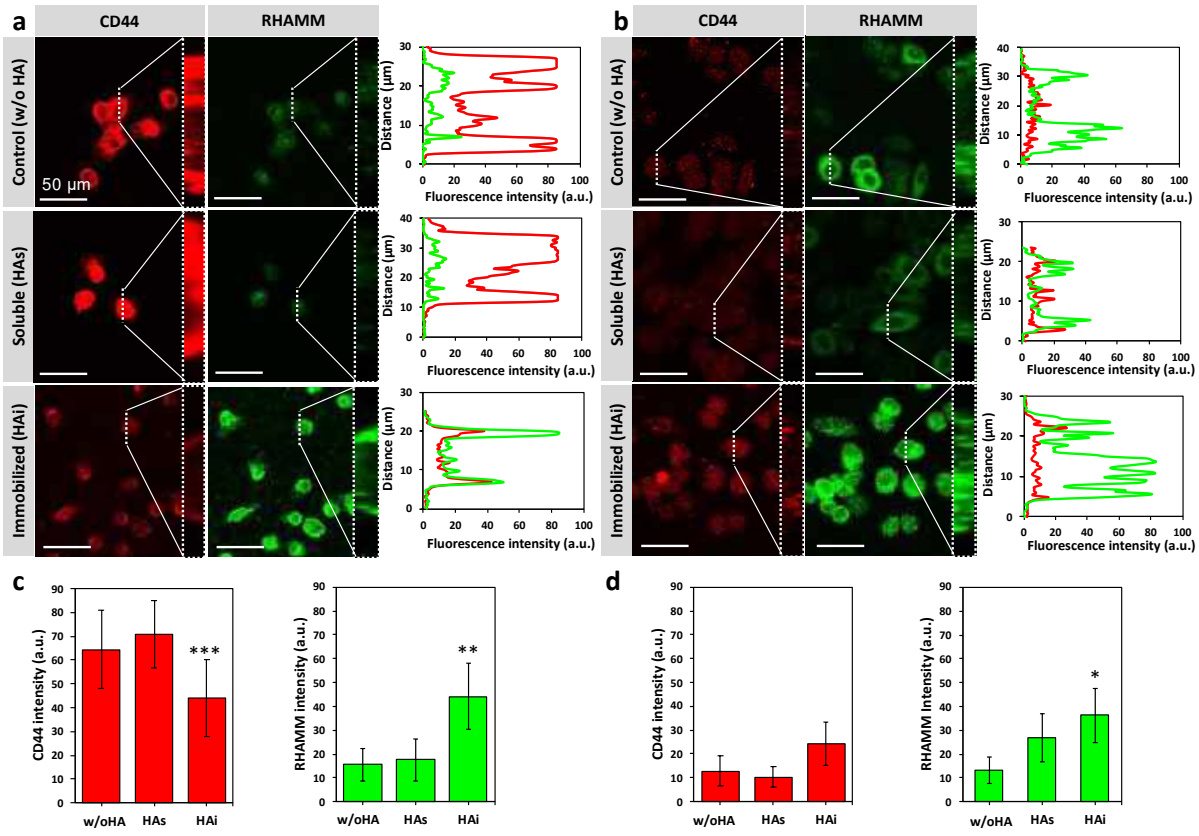

Figure III.3. Expression of CD44 (red) and RHAMM (green) by (a, c) MDA-MB-231 and (b, d) Sk-Br-3 cells cultured at the studied conditions. Maximum projections (z-stacks) and orthogonal YZ (lateral inserts) confocal microscopy images of (a) MDA-MB-231 and (b) Sk-Br-3 cultures. The images show the total expression of CD44 (red) and RHAMM (green) and the respective distribution of these proteins across the cells (lateral images inserts and graphs). Non-immune IgG1 was used as isotype control (Fig. III.S5). Average fluorescence intensity showing the relative total expression of CD44 and RHAMM in (c) MDA-MB-231 and (d) Sk-Br-3 cells cultured at the studied conditions. Statistical differences between HA cultures and control: *$p \leq 0.05$; **$p < 0.005$ and ***$p < 0.001$.

The recognition and binding to HA via CD44 activate different signaling cascades, including HA endocytosis.[3, 59] When MDA-MB-231 cells are cultured on immobilized HA, CD44 recognizes and binds HA, but its endocytosis is hampered.[59]_ENREF_58 As a result, the expression of CD44 is reduced (as it is "blocked"), and RHAMM is overexpressed to compensate it. The magnitude of these changes is proportional to the initial level of CD44 expression, *i.e.,* more dramatic changes are observed for cells with higher expression of CD44. Immunostaining showed that the overexpressed RHAMM is also localized in the cytoplasm (Fig. III.3a), suggesting its

involvement in the intracellular signaling upon HA binding. In Sk-Br-3 cells, both RHAMM and CD44 are expressed (Fig. III.2b), but the competition between them for HA binding is different as more RHAMM is expressed on the cell surface. Upon exposure to immobilized HA, these cells overexpressed both receptors, but the induced changes in RHAMM expression are greater as compared with CD44 (Fig. III.3d).

III.3.3. Immobilized HA induces CD44/RHAMM complexation.

We used FRET to study the possible co-localization of CD44 and RHAMM (Fig. III.1b) upon HA exposure.[60] Herein, we took advantage of the secondary antibodies used to detect RHAMM (AlexaFluor® 488, donor) and CD44 (AlexaFluor® 594, acceptor). These secondary antibodies were specifically chosen to maximize the energy transfer: there is a 96% overlapping between AlexaFluor® 594 excitation spectrum with the emission spectrum of AlexaFluor® 488 and only 10% of the emission spectrum of AlexaFluor® 488 matches with the emission spectra of AlexaFluor® 594, thus avoiding signal bleedthrough (Fig. III.S7). While using the antibodies for FRET measurements can compromise the resolution, this approach can be very useful in a clinical scenario and as a fast pre-screening method. Moreover, FRET is more reliable than the conventional signal overlap of confocal micrographs/channels often applied to show the co-localization of immunolabelled proteins.[61, 62]

We detected FRET for both studied cell lines, but the signal had different intensities (Fig. III.4, controls): the most intense signal is visible for the invasive MDA-MB-231 cell line (Fig. III.4c *vs.* Fig. III.4d). Of note, FRET was detected both intracellular and on the surface of these cells, indicating co-localization of RHAMM and CD44 at these locations. However, the intracellular signal was weaker, showing predominant co-localization of RHAMM and CD44 at the cell surface. The low intensity of the FRET signal of Sk-Br-3 cells (Figs. III.4b and III.4d, controls) suggests that RHAMM on the cell surface is not co-localized with CD44. Previous studies have shown that once translocated to the cell surface, RHAMM can complex not only with CD44 but also with other receptors such as PDGFR, TGFβ Receptor-1, bFGFR, and RON, among others.[41, 43, 44, 63-68]

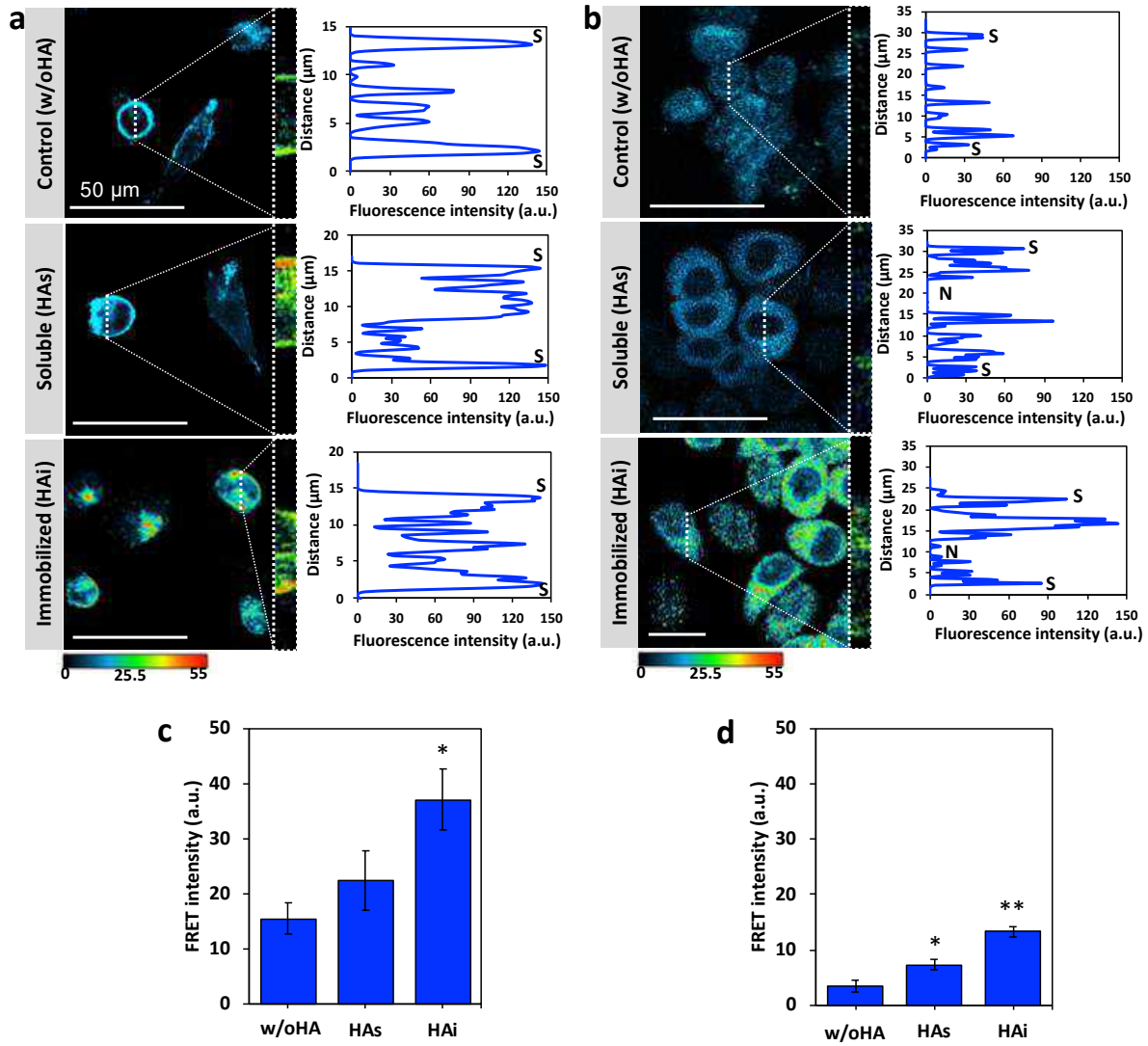

Figure III.4. FRET-based immunocytochemistry of (a, c) MDA-MB-231 and (b, d) Sk-Br-3 cultured in the absence of exogenous HA (controls, w/oHA) or conditioned with soluble HA (HAs) or immobilized HA (HAi). (a, b) The images show maximum and orthogonal (lateral inserts) projections obtained by confocal microscopy together with the respective distribution of signal intensity across the cells (S: surface, N: nucleus). FRET signals were acquired at the 594 nm channel after excitation at 488 nm in both RHAMM and CD44 immunostained cells. (c, d) Graphical presentation of average FRET intensity after correction for bleedthrough for (c) MDA-MB-231 and (d) Sk-Br-3 cells. Controls showing unspecific binding of secondary antibodies are presented in Fig. III.S5. Lower resolution images and bleedthrough signals are shown in Fig. III.S7. Statistical differences between HA supplemented cultures and control: *$p \leq 0.05$ and **$p < 0.005$.

The obtained data indicated that the main HA receptors in the studied cell lines have not only different expression but might also be engaged in different cell-surface interactions and thus,

anticipated different cellular responses upon HA supplementation. FRET signal did not show any substantial changes in RHAMM/CD44 complexes upon supplementation of MDA-MB-231 with soluble HA, while an increased co-localization of these receptors was observed for Sk-Br-3 cells at these conditions. On the other hand, a significant increase of the FRET signal intensity was obtained for cells seeded on immobilized HA (Fig. III.4). This change suggests that the interaction with immobilized HA results in RHAMM overexpression and co-localization with CD44.

FRET/RHAMM signal ratio is proportional to FRET efficiency, which depends on receptors proximity (Fig. III.S8).[33] The FRET/RHAMM signal ratio was constant and close to 1 for MDA-MB-231 at all studied conditions. In Sk-Br-3 cells, this ratio was 0.2 when cells were seeded on TCPS or supplemented with soluble HA. These results show close localization of RHAMM and CD44 in MDA-MB-231 but not in Sk-Br-3 cells and indicate that CD44 and RHAMM can participate in different protein complexes in the studied cell lines. However, when Sk-Br-3 cells were cultured on immobilized HA, FRET/RHAMM signal ratio increased significantly to about 0.8, evidencing possible complexation between RHAMM and CD44 at these conditions. Acceptor photobleaching at a selected region of interest (ROI) was performed for cells seeded over immobilized HA to determine FRET efficiency. Photobleaching of CD44 (acceptor) leads to a decrease of the FRET signal and an increase in the average intensity of RHAMM (donor) signal (Fig. III.5 and III.S9). The average energy transfer efficiency for cells seeded on immobilized HA was calculated, and we obtained FRET efficiency of 28.49 ± 8.2 % for MDA-MB-231 cells and 3.75 ± 3.2 % for Sk-Br-3 cells. These results suggest co-localization of CD44 and RHAMM in MDA-MB-231 cells seeded on immobilized HA but are not conclusive for Sk-Br-3 cells. We, therefore, studied the possible complexation of CD44 and RHAMM by co-immunoprecipitation (Fig. III.6).

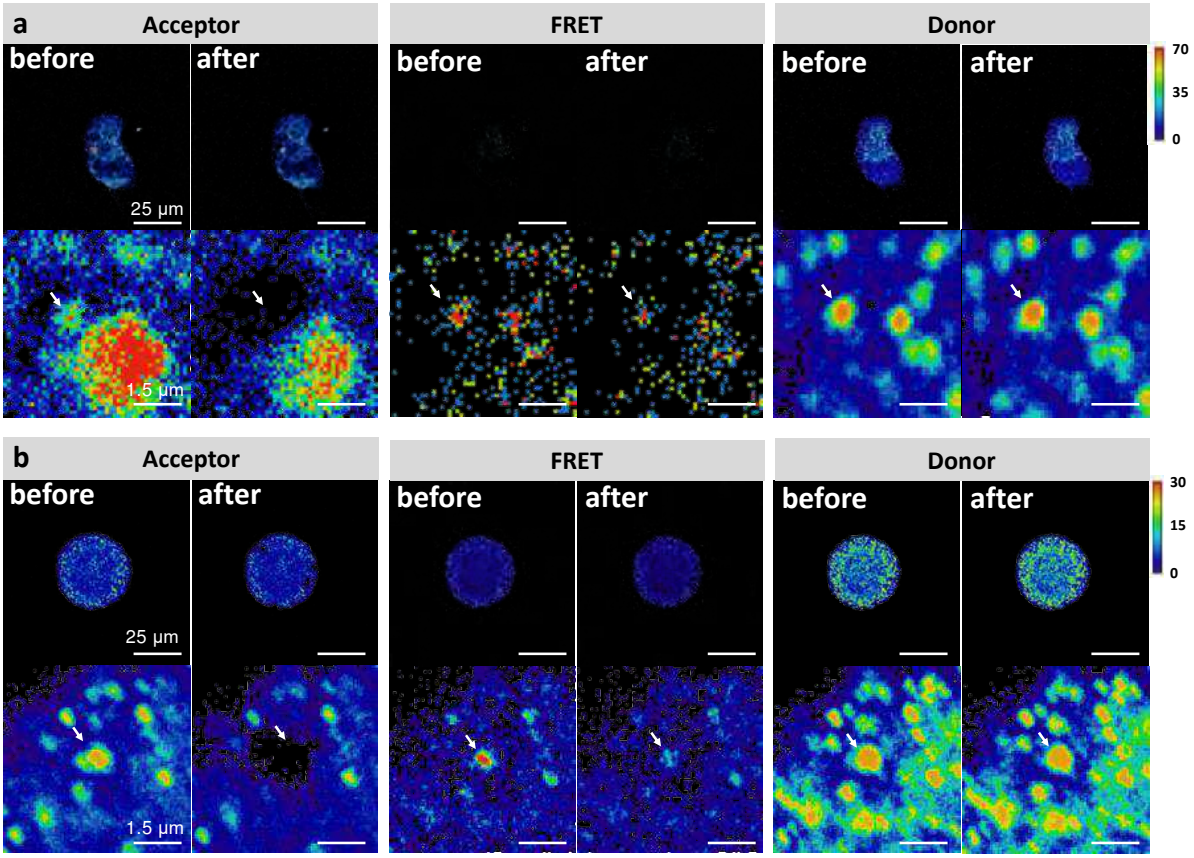

Figure III.5. Representative photobleaching FRET data showing RHAMM/CD44 complexation in (a) MDA-MB-231 and (b) Sk-Br-3 cells. Local photobleaching of the acceptor results in FRET signal decreasing and donor signal increasing (indicated with arrows).

In control samples (without exogenous HA supplementation), anti-CD168 antibodies co-immunoprecipitated two CD44 isoforms in the case of MDA-MB-231 cells (50 and 77 kDa, Fig. III.6a) and three CD44 isoforms in Sk-Br-3 cells (50, 70 and 85 kDa, Fig. III.6b). These sizes correspond to the standard CD44 (85 kDa) and truncated forms of CD44.[42, 69] In reciprocal immunoprecipitation assay (anti-CD44 antibodies co-immunoprecipitated RHAMM; Figs. III.6c and III.6d), we detected two RHAMM isoforms (43 and 70 kDa).[42, 70] Supplementation with HA induced an increase of RHAMM/CD44 co-localization in MDA-MB-231 cells that were more pronounced (2.5-fold) in the case of immobilized HA (Fig. III.4c). The trend was the same for Sk-Br-3 cells (RHAMM is the main surface HA-receptor), but the magnitude was bigger: we observed 6-fold higher co-localization for cells seeded on immobilized HA when compared to the control (Fig. III.6d).

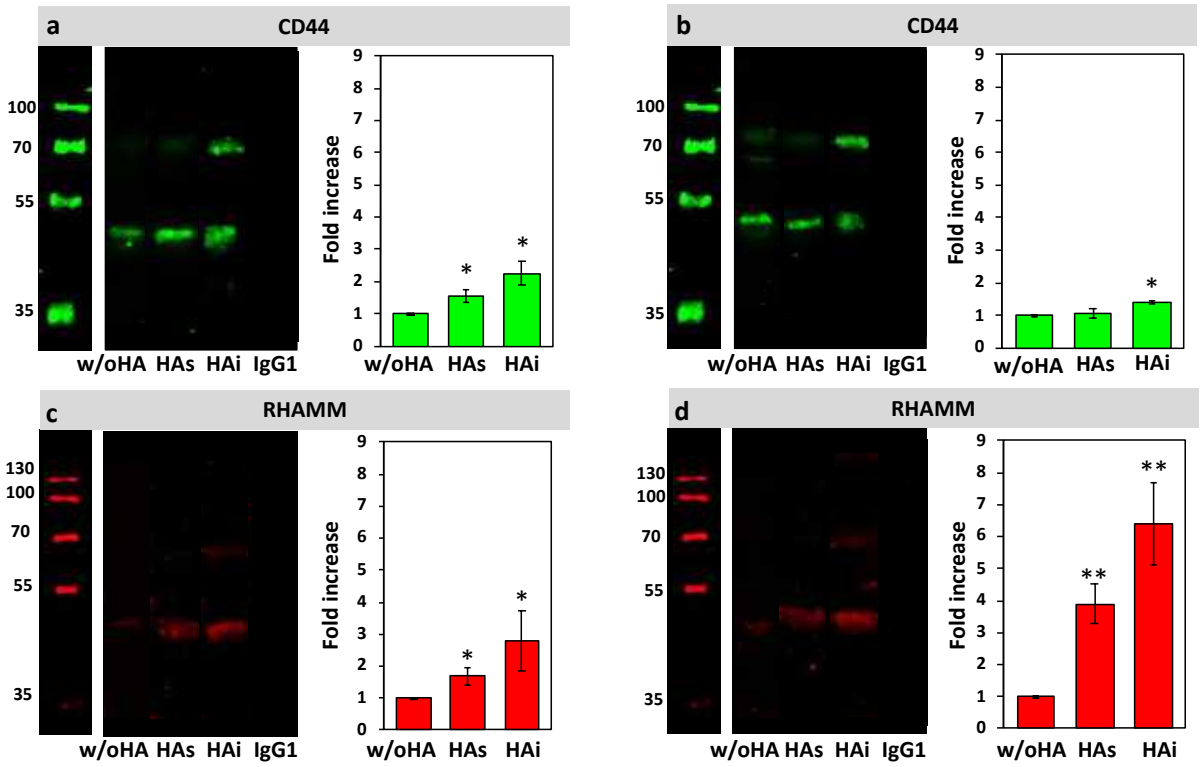

Figure III.6. Western blot of (a, b) RHAMM immunoprecipitated with CD44 detection (green) and (c, d) CD44 immunoprecipitate with RHAMM detection (red) together with the respective densitometry quantification (fold increase as compared to the control without HA) for (a, c) MDA-MB-231 and (b, d) Sk-Br-3 cells cultured at the studied conditions. Non-immune IgG1 was used for immunoprecipitation control. HAs: soluble hyaluronate; HAi: immobilized hyaluronate.

Western blot analysis of non-immunoprecipitated proteins showed that not all CD44 co-localizes with RHAMM in MDA-MB-231 cells at the studied conditions (Fig. III.S10a, green). This result is expected, keeping in mind the high expression of CD44 by these cells. On the other hand, non-immunoprecipitated CD44 was not detected for Sk-Br-3 cells, *i.e.,* for these cells, all CD44 is engaged with RHAMM (Fig. III.S10c). The results for non-immunoprecipitated RHAMM confirmed that HA supplementation (either soluble or immobilized) promotes CD44/RHAMM co-localization (Figs. III.S10b and III.S10d). Of note, in the case of Sk-Br-3 cells cultured on immobilized HA, we did not observe any non-immunoprecipitated CD44 and RHAMM indicating an optimal co-localization of the two proteins at these conditions. Altogether, these results confirmed FRET data and showed that RHAMM/CD44 co-localization depends on HA presentation and on the expressed cell surface receptor(s).

III.3.4. Erk1/2 activation.

Interaction of HA with CD44 and RHAMM can activate different signaling pathways towards cell survival, proliferation, and migration/motility.[66] Among these, Erk1/2 is known to be HA-dependent and to regulate cell migration in invasive breast cancers.[42] We evaluated the activation of Erk1/2 in the studied cell lines by immunocytochemistry (Fig. III.7). We found that MDA-MB-231 and Sk-Br-3 cells have similar basal levels of active Erk1/2. A slight increase of Erk1/2 activation was found in MDA-MB-231 cells seeded on immobilized HA while supplemented soluble HA did not affect this pathway. On the other hand, a significant increment of Erk1/2 activation was found for Sk-Br-3 cells at both studied conditions. These results show an effect of HA presentation beyond cell surface receptors co-localization. The increased RHAMM expression and co-localization were observed for the same conditions (immobilized HA for both cell lines and soluble HA for Sk-Br-3) and are indicative of RHAMM involvement in the regulation of Erk1/2 pathway and contribution to aggressive tumorigenic phenotype as previously proposed by other studies.[42, 71]

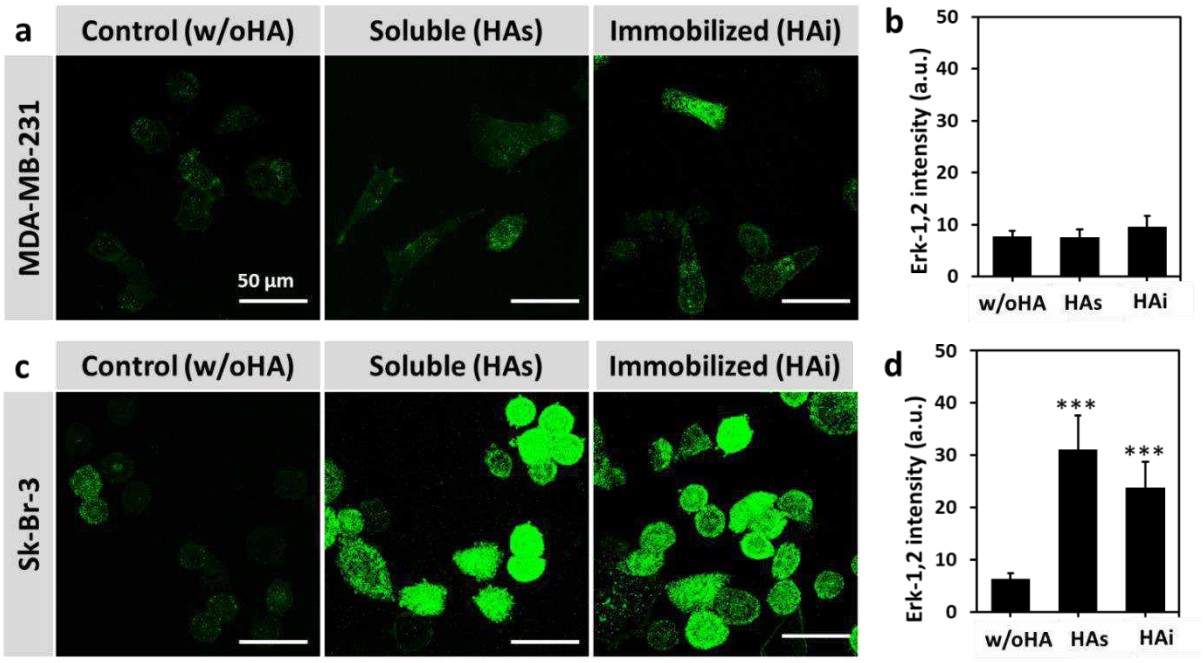

Figure III.7. (a, c) Representative confocal images showing the activation of Erk-1,2 pathway (green) in (a) MDA-MB-231 and (c) Sk-Br-3 cells cultured in the absence (w/o HA) and presence of HA (soluble and immobilized); and (b, d) the respective graphical representation of active Erk-1,2 fluorescence intensity. Statistical differences between HA cultures and control are marked ***$p < 0.001$.

III.4. Conclusions

Our results suggested a link between HA presentation, CD44/RHAMM co-localization and cancer aggressiveness. Supplementation with exogenous, immobilized HA can enhance CD44/RHAMM co-localization and contribute towards an aggressive and invasive phenotype. In this process, RHAMM has manifold functions: to compensate CD44, to transduce the feedback response upon HA binding, and to regulate signaling pathways.

III.5. Supplementary Information

HA end-on modification.

Hyaluronan was modified at its reducing end with an alkanethiol as previously described.[49] Briefly, 11-(Aminooxy)-1-undecanethiol (3 mol excess to HA) was dissolved in 5 mL followed by the addition of 200 mg of HA 5 mL acetate buffer (78 mM acetic acid and 62.5 mM sodium acetate, pH 4.5). The reaction mixture was magnetically stirred at 45 °C for 24 h. Unreacted reagents were removed by dialysis against ethanol (cut-off 14 kDa). The product was obtained by ethanol evaporation followed by freeze-drying.

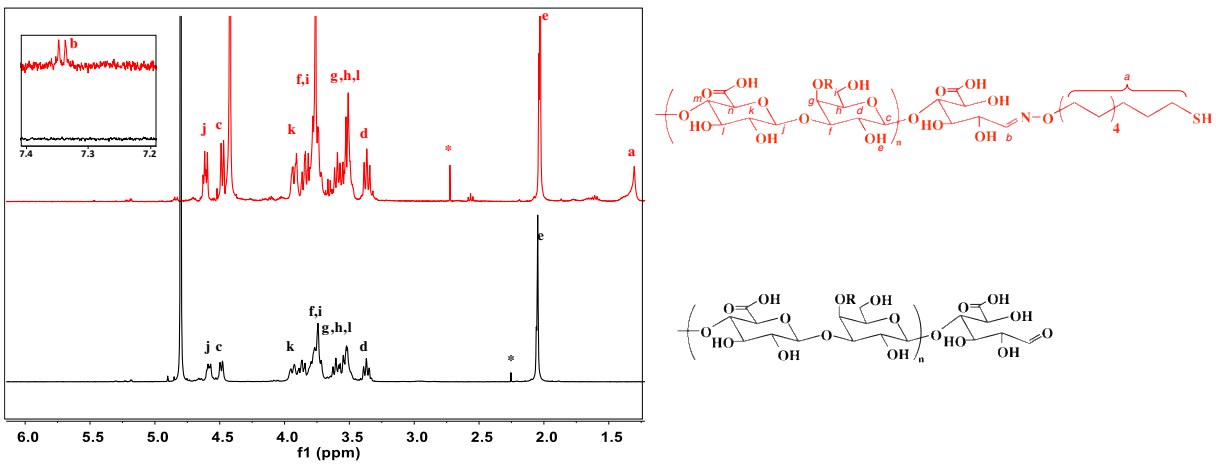

Figure III.S1. ^{1}H-NMR spectra of unmodified hyaluronan (black) and the obtained end-on modified derivative (red).

HA end-on immobilization on gold substrates.

Gold substrates were thoroughly washed and incubated with end-on modified HA (0.5 mg/mL in ultrapure water) overnight under orbital shaking (100 rpm, room temperature). The surfaces were washed (150 mM NaCl, 3x double distilled water), dried, and sterilized under UV prior to cell culture. Hyaluronic acid binding protein (HAbp, Millipore) was used to confirm HA immobilization on gold surfaces. Gold and HA-gold substrates were incubated with biotinylated HAbp (1 μg/mL in PBS) for 1 h at room temperature and then with streptavidin-Alexa Fluor 488 (2 μg/mL in PBS, 10 min at room temperature). Images were acquired using an Inverted Confocal Microscope (TCS SP8, Leica).

Table III.S1. Determined α values for FRET signal correction.

Conditions	MDA-MB-231	Sk-Br-3
Control (w/o HA)	0.35 ± 0.25	0.30 ± 0.25
Soluble HA	0.58 ± 0.26	0.38 ± 0.16
Immobilized HA	0.25 ± 0.14	0.29 ± 0.07

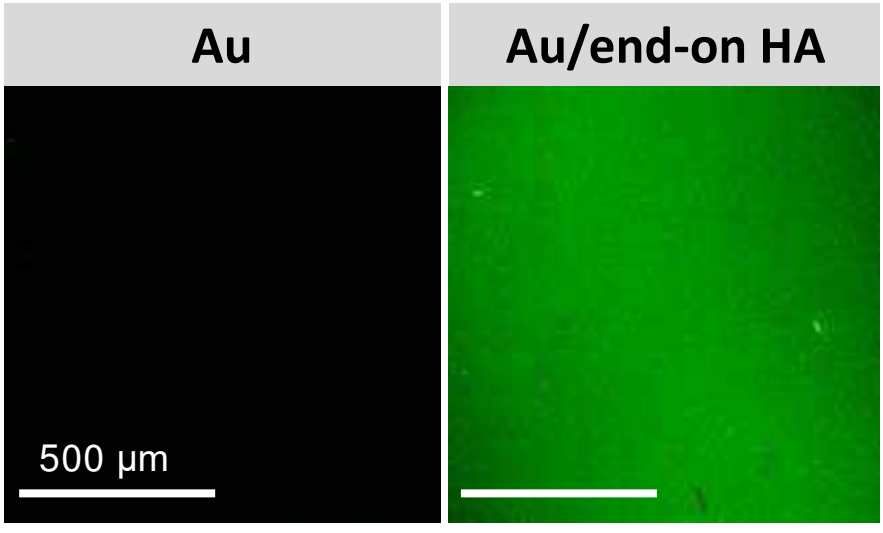

Figure III.S2. Fluorescence microscopy images of gold (Au) slides prior (Au) and after coating with end-on modified hyaluronan: substrates were incubated with biotinylated hyaluronan binding protein and then with streptavidin-Alexa Fluor 488.

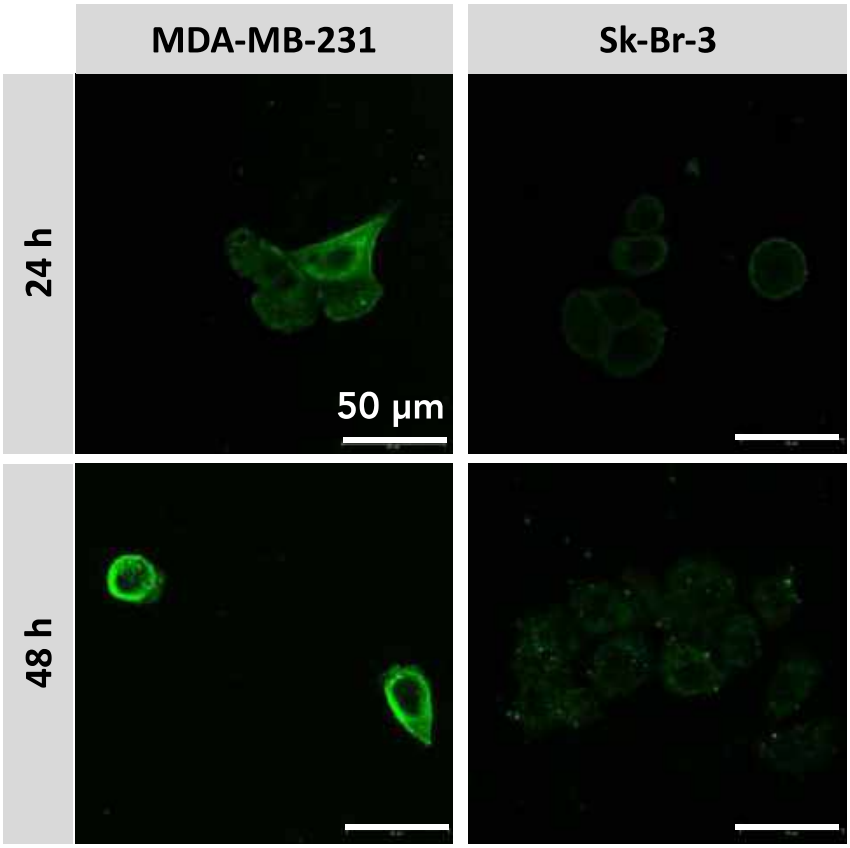

Figure III.S3. Confocal microscope images of MDA-MB-231 and Sk-Br-3 cells seeded in TCPS for 24h and 48h. Endogenous hyaluronan (green) was stained with streptavidin-AlexaFLuor® 488 after incubation with biotinylated hyaluronan binding protein.

Table III.S2. Cell-surface expression of hyaluronan receptors CD44 and RHAMM in MDA-MB-231 and Sk-Br-3. The quantification was performed by flow cytometry after 72 h of cell culture on tissue culture polystyrene. The presented data are average values of at least three experiments.

	MDA-MB-231		Sk-Br-3	
	Population* [%]	MFI** [a.u.]	Population [%]	MFI (a.u.)
CD44(+)	99.5 ± 0.5	232.6 ± 28.0	10.3 ± 15.1	24.0 ± 7.3
RHAMM(+)	5.5 ± 0.9	44.8 ± 8.9	28.7 ± 10.9	91.1 ± 75.2

*The results are presented as the percentage of positive cells from the total cell population

**MFI is the abbreviation for Mean Fluorescence Intensity and indicates the quantity of the expressed receptor per cell.

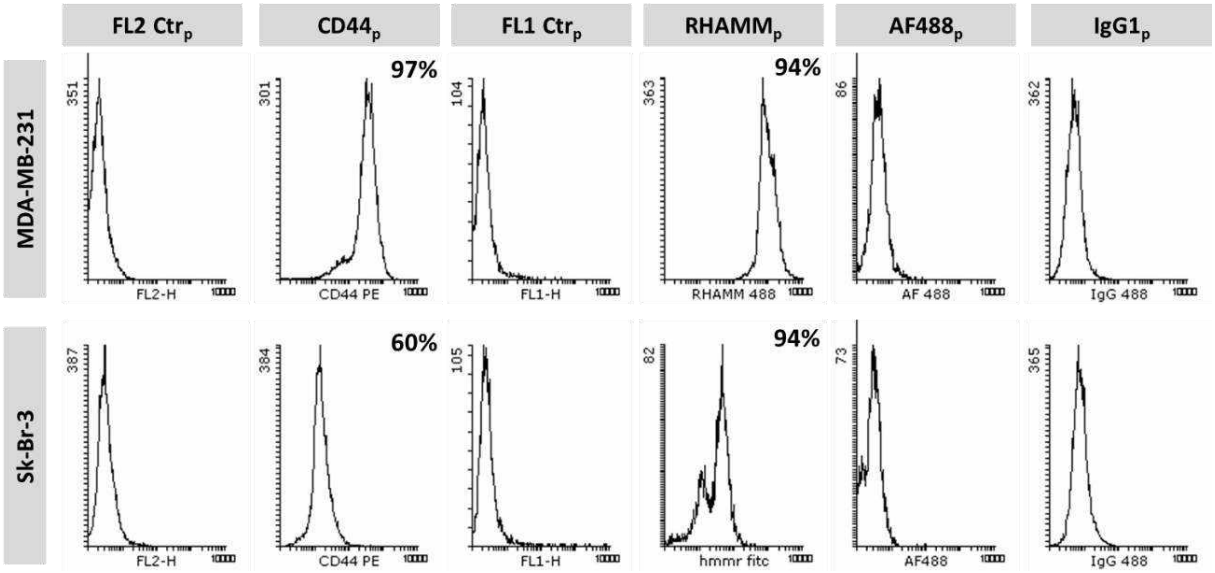

Figure III.S4. Flow cytometry analysis of permeabilized MDA-MB-231 and Sk-Br-3 cells: unstained (FL1 and FL2 control), immuno-tagged for CD44 (CD44p) and RHAMM (RHAMMp), and controls of secondary antibody AlexaFluor® 488 (AF488) and IgG1.

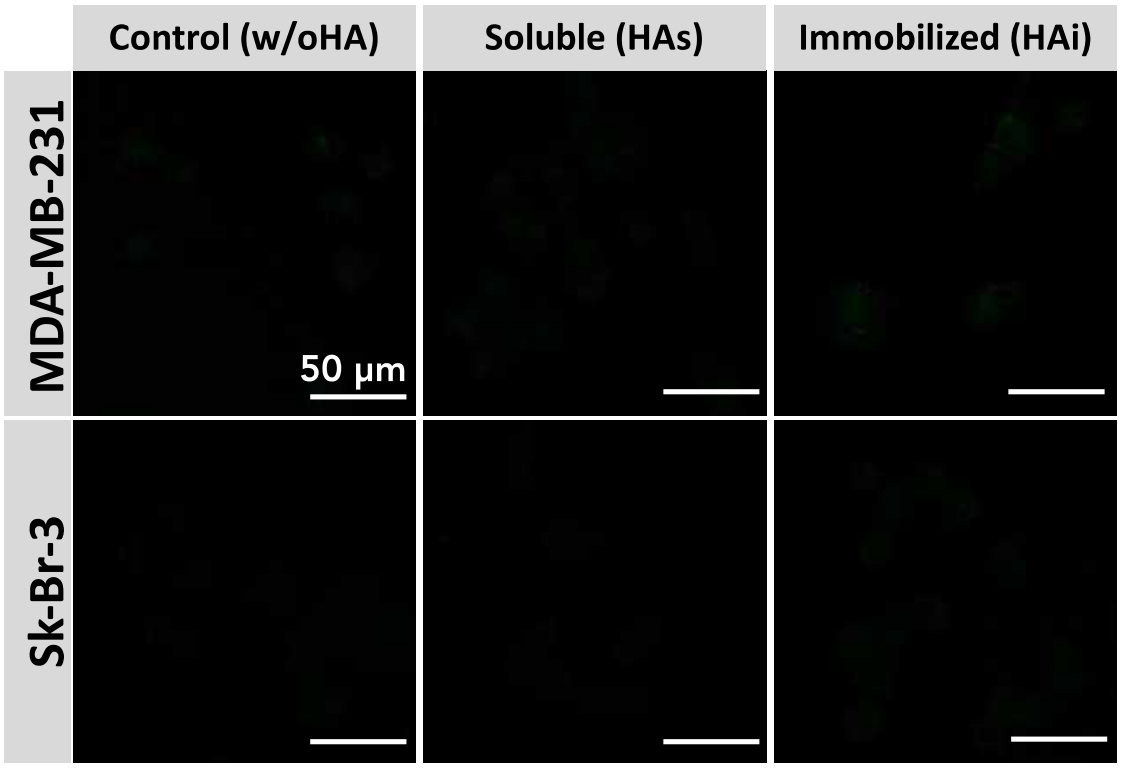

Figure III.S5. Confocal microscopy images of MDA-MB-231 and Sk-Br-3 cells supplemented with hyaluronan (soluble) or cultured on hyaluronan functionalized substrates (immobilized). The images show control experiments for the data presented in Fig. III.3 of the main manuscript, in which non-immune IgG1 is used as an isotype control.

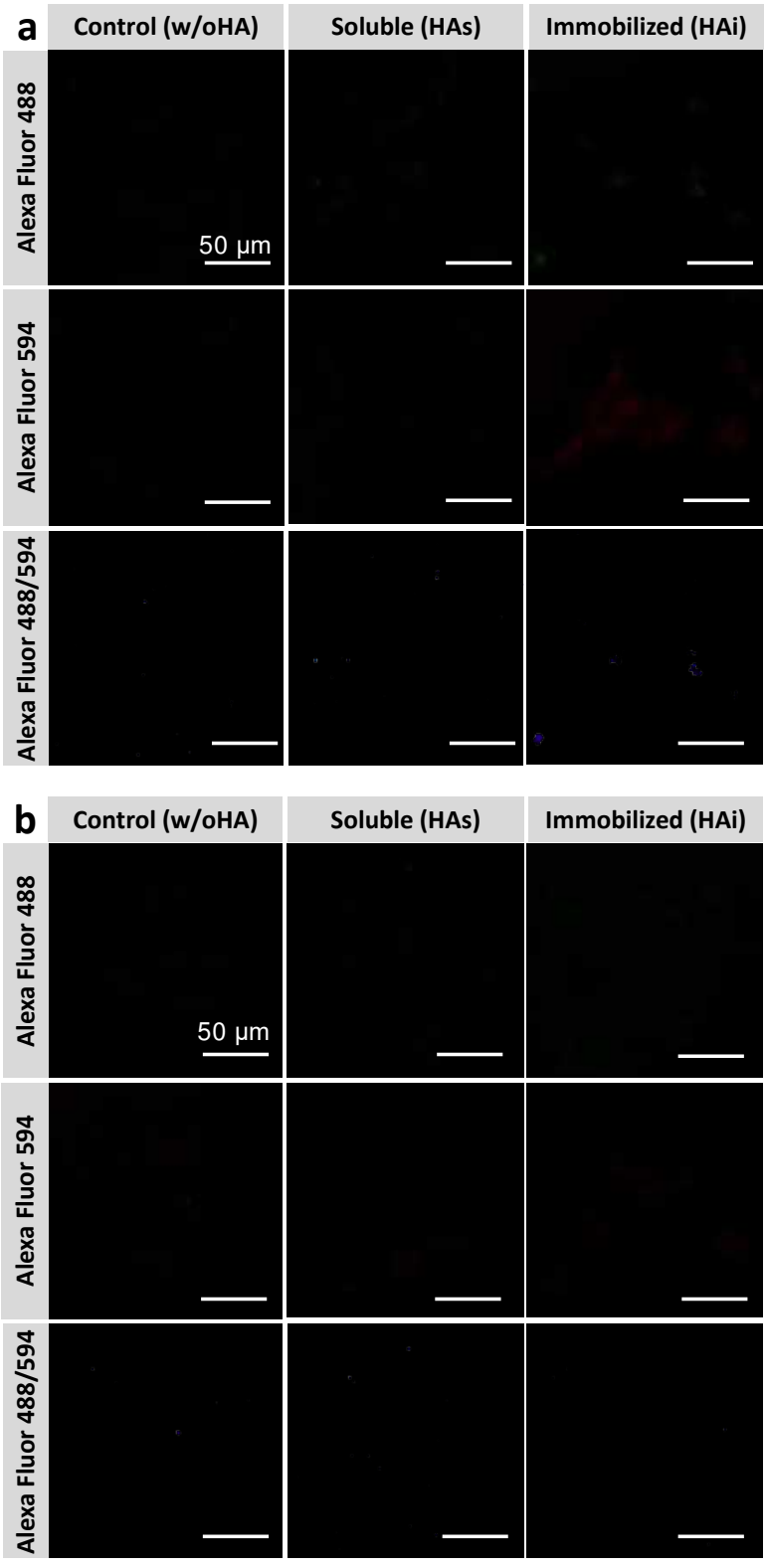

Figure III.S6. Immunocytochemistry controls for unspecific binding of secondary antibodies – sample without primary antibody. Representative images of (a) MDA-MB-231 and (b) Sk-Br-3 incubated with AlexaFluor® 488 and AlexaFluor® 594.

FRET-based immunocytochemistry. During FRET, donor fluorochrome transfers energy to the acceptor. This process can be monitored either by increasing acceptor fluorescence intensity or by decreasing the fluorescence intensity of the donor both upon donor excitation. We monitored the fluorescence intensity of RHAMM (donor) in FRET samples (RHAMM and RHAMM/CD44 immuno-tagged cells) (Fig. III.6). RHAMM fluorescence intensity decreased in cells seeded in immobilized HA, but not in cells seeded in TCPS or cells supplemented with soluble HA. The fluorescence ratio between acceptor and donor upon donor excitation indicates the transferred energy from AlexaFluor® 488 to AlexaFluor® 594 (Fig. III.S7). MDA-MB-231 cells have similar ratio values (around 1) in all three conditions studied and, therefore, similar FRET efficiency. In Sk-Br-3 cells, the ratio between FRET/RHAMM signal in cells seeded in TCPS is 0.3, and similar values were obtained in cells supplemented with soluble HA. Higher values were obtained for cells seeded in immobilized HA (0.7), indicating higher FRET efficiency and closer proximity between CD44 and RHAMM.

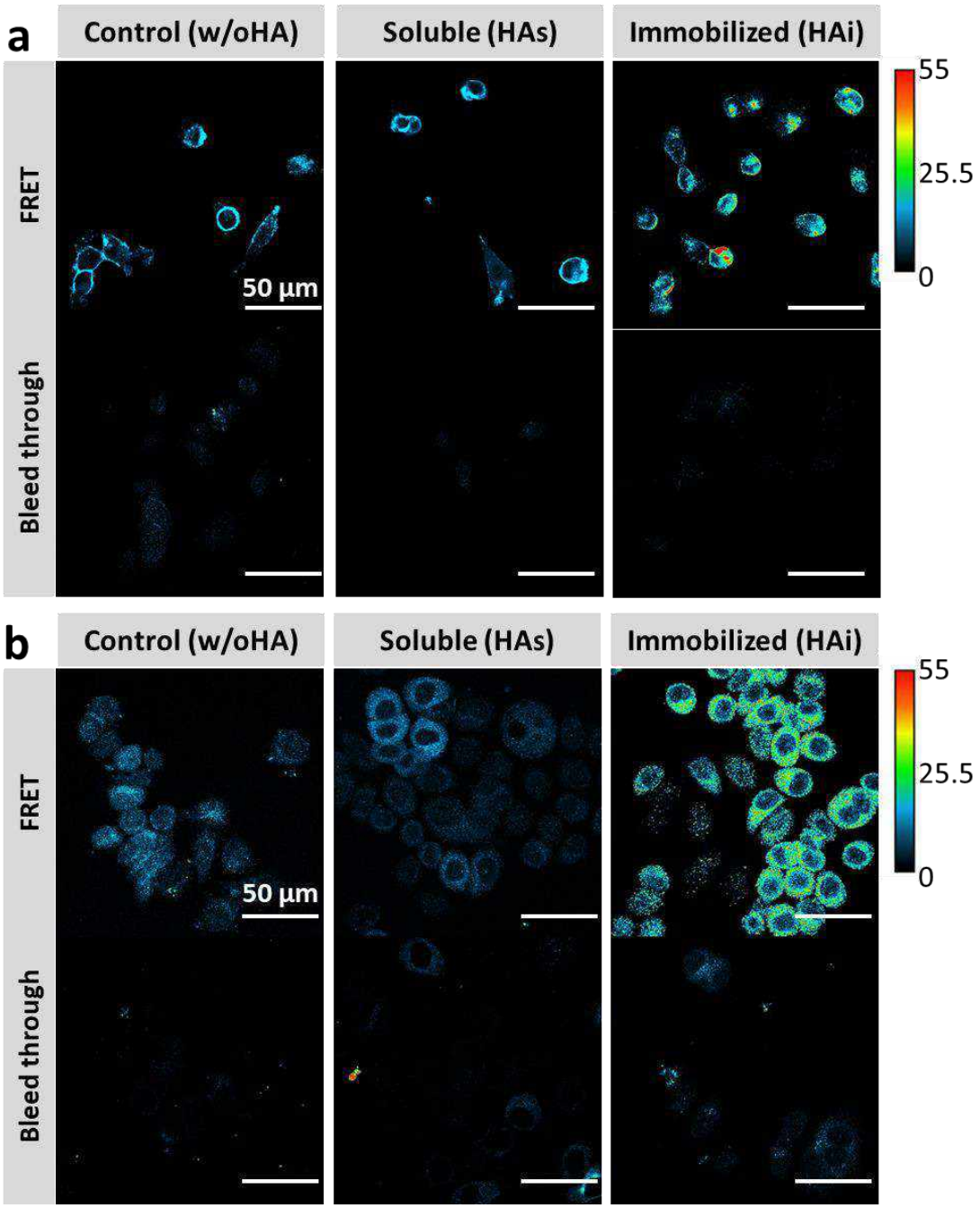

Figure III.S7. FRET-based immunocytochemistry and bleedthrough signals of (a) MDA-MB-231 and (b) Sk-Br-3 cultured in the absence of exogenous HA (controls, w/oHA), supplemented with soluble HA (HAs) or on substrates with immobilized HA (HAi). Images were acquired at 594 nm channel after excitation at 488 nm in both RHAMM and CD44 immunostained cells and RHAMM immunostained cells (no acceptor), respectively.

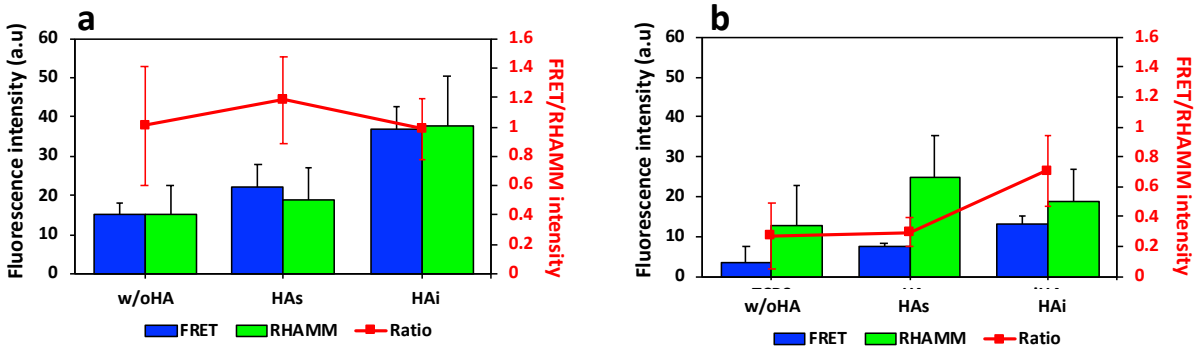

Figure III.S8. Graphical presentation of corrected FRET and RHAMM fluorescence intensity in double immunostained cells and FRET efficiency between donor and acceptor (ratio) in (a) MDA-MB-231 and (b) Sk-Br-3 cells seeded in the absence (w/oHA) or supplemented with hyaluronan (HAs: soluble or HAi: immobilized).

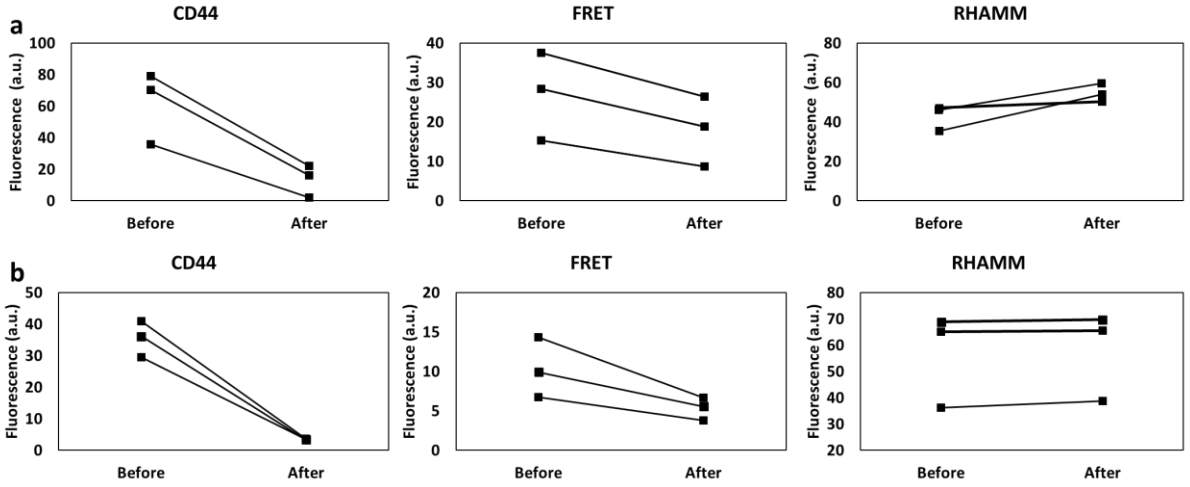

Figure III.S9. Graphical presentation of photobleaching data: the photobleaching of the CD44 signal (acceptor) is associated with a decrease of the FRET intensity and an increase of the intensity of the RHAMM signal (donor).

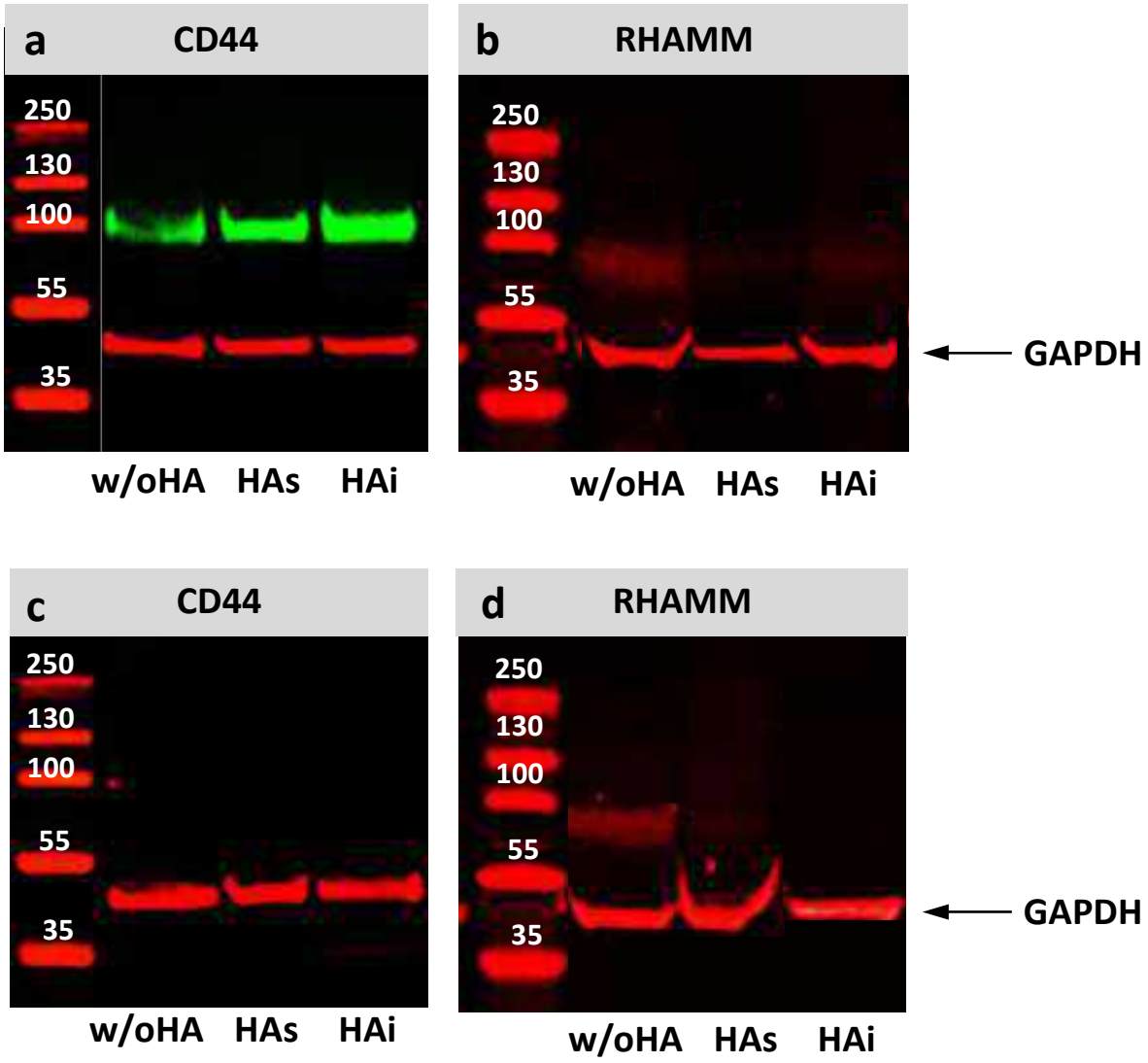

Figure III.S10. Western blot of non-immunoprecipitated proteins (a, c) CD44 (green) and (b, d) RHAMM (red) of (a, b) MDA-MB-231 and (c, d) Sk-Br-3 cells cultured at the studied conditions. GAPDH (~40kDa) was used as the loading control. w/oHA: control without HA supplementation; HAs: soluble hyaluronate; HAi: immobilized hyaluronate.

III.6. REFERENCES

1. Toole, B.P., *Hyaluronan: From extracellular glue to pericellular cue.* Nature Reviews Cancer, 2004. **4**(7): p. 528-539.
2. Vigetti, D., et al., *Hyaluronan: Biosynthesis and signaling.* Biochimica Et Biophysica Acta-General Subjects, 2014. **1840**(8): p. 2452-2459.
3. Knudson, W., G. Chow, and C.B. Knudson, *CD44-mediated uptake and degradation of hyaluronan.* Matrix Biology, 2002. **21**(1): p. 15-23.

4. Knudson, W., E. Bartnik, and C.B. Knudson, *Assembly of Pericellular Matrices by Cos-7 Cells Transfected with Cd44 Lymphocyte-Homing Receptor Genes.* Proceedings of the National Academy of Sciences of the United States of America, 1993. **90**(9): p. 4003-4007.
5. Misra, S., et al., *Hyaluronan constitutively regulates activation of COX-2-mediated cell survival activity in intestinal epithelial and colon carcinoma cells.* Journal of Biological Chemistry, 2008. **283**(21): p. 14335-14344.
6. McAtee, C.O., J.J. Barycki, and M.A. Simpson, *Emerging Roles for Hyaluronidase in Cancer Metastasis and Therapy*, in *Hyaluronan Signaling and Turnover*, M.A. Simpson and P. Heldin, Editors. 2014. p. 1-34.
7. Weigel, P.H. and P.L. DeAngelis, *Hyaluronan synthases: A decade-plus of novel glycosyltransferases.* Journal of Biological Chemistry, 2007. **282**(51): p. 36777-36781.
8. Jacobson, A., et al., *Expression of human hyaluronan synthases in response to external stimuli.* Biochemical Journal, 2000. **348**: p. 29-35.
9. Stern, R., *Hyaluronidases in cancer biology.* Seminars in Cancer Biology, 2008. **18**(4): p. 275-280.
10. Heldin, P., et al., *Deregulation of hyaluronan synthesis, degradation and binding promotes breast cancer.* Journal of Biochemistry, 2013. **154**(5): p. 395-408.
11. Chanmee, T., P. Ontong, and N. Itano, *Hyaluronan: A modulator of the tumor microenvironment.* Cancer Letters, 2016. **375**(1): p. 20-30.
12. Schwertfeger, K.L., et al., *Hyaluronan, inflammation, and breast cancer progression.* Frontiers in Immunology, 2015. **6**: p. 1-12.
13. Auvinen, P., et al., *Hyaluronan in peritumoral stroma and malignant cells associates with breast cancer spreading and predicts survival.* American Journal of Pathology, 2000. **156**(2): p. 529-536.
14. Tolg, C., et al., *Hyaluronan and RHAMM in Wound Repair and the "Cancerization" of Stromal Tissues.* Biomed Research International, 2014.
15. Porsch, H., et al., *Efficient TGF beta-induced epithelial-mesenchymal transition depends on hyaluronan synthase HAS2.* Oncogene, 2013. **32**(37): p. 4355-4365.
16. Li, P., et al., *Hyaluronan synthase 2 overexpression is correlated with the tumorigenesis and metastasis of human breast cancer.* International Journal of Clinical and Experimental Pathology, 2015. **8**(10): p. 12101-12114.
17. Liu, N.F., et al., *Hyaluronan synthase 3 overexpression promotes the growth of TSU prostate cancer cells.* Cancer Research, 2001. **61**(13): p. 5207-5214.
18. Turley, E.A., D.K. Wood, and J.B. McCarthy, *Carcinoma Cell Hyaluronan as a "Portable" Cancerized Prometastatic Microenvironment.* Cancer Research, 2016. **76**(9): p. 2507-2512.
19. Scheibner, K.A., et al., *Hyaluronan fragments act as an endogenous danger signal by engaging TLR2.* Journal of Immunology, 2006. **177**(2): p. 1272-1281.
20. Amorim, S., et al., *Molecular weight of surface immobilized hyaluronic acid influences CD44-mediated binding of gastric cancer cells.* Scientific Reports, 2018. **8**.
21. Yang, C.X., et al., *The High and Low Molecular Weight Forms of Hyaluronan Have Distinct Effects on CD44 Clustering.* Journal of Biological Chemistry, 2012. **287**(51): p. 43094-43107.
22. Wolny, P.M., et al., *Analysis of CD44-Hyaluronan Interactions in an Artificial Membrane System INSIGHTS INTO THE DISTINCT BINDING PROPERTIES OF HIGH AND LOW MOLECULAR WEIGHT HYALURONAN.* Journal of Biological Chemistry, 2010. **285**(39): p. 30170-30180.
23. Ponta, H., L. Sherman, and P.A. Herrlich, *CD44: From adhesion molecules to signalling regulators.* Nature Reviews Molecular Cell Biology, 2003. **4**(1): p. 33-45.
24. Misra, S., et al., *Interactions between hyaluronan and its receptors (CD44, RHAMM) regulate the activities of inflammation and cancer.* Frontiers in Immunology, 2015. **6**.
25. Afify, A., P. Purnell, and L. Nguyen, *Role of CD44s and CD44v6 on human breast cancer cell adhesion, migration, and invasion.* Experimental and Molecular Pathology, 2009. **86**(2): p. 95-100.
26. Peach, R.J., et al., *Identification of Hyaluronic-Acid Binding-Sites in the Extracellular Domain of Cd44.* Journal of Cell Biology, 1993. **122**(1): p. 257-264.
27. Banerji, S., et al., *Characterization of a functional hyaluronan-binding domain from the human CD44 molecule expressed in Escherichia coli.* Protein Expression and Purification, 1998. **14**(3): p. 371-381.

28. Orian-Rousseau, V. and J. Sleeman, *CD44 is a Multidomain Signaling Platform that Integrates Extracellular Matrix Cues with Growth Factor and Cytokine Signals*, in *Hyaluronan Signaling and Turnover*, M.A. Simpson and P. Heldin, Editors. 2014. p. 231-254.
29. Sohara, Y., et al., *Hyaluronan activates cell motility of v-Src-transformed cells via Ras-mitogen-activated protein kinase and phosphoinositide 3-kinase-Akt in a tumor-specific manner.* Molecular biology of the cell, 2001. **12**(6): p. 1859-1868.
30. Fujita, Y., et al., *CD44 signaling through focal adhesion kinase and its anti-apoptotic effect.* FEBS Letters, 2002. **528**(1-3): p. 101-108.
31. Bourguignon, L.Y.W., E. Gilad, and K. Peyrollier, *Heregulin-mediated ErbB2-ERK signaling activates hyaluronan synthases leading to CD44-dependent ovarian tumor cell growth and migration.* Journal of Biological Chemistry, 2007. **282**(27): p. 19426-19441.
32. Lesley, J., et al., *Hyaluronan binding by cell surface CD44.* Journal of Biological Chemistry, 2000. **275**(35): p. 26967-26975.
33. Yang, C., et al., *The High and Low Molecular Weight Forms of Hyaluronan Have Distinct Effects on CD44 Clustering.* The Journal of Biological Chemistry, 2012. **287**(51): p. 43094-43107.
34. Jiang, L., et al., *Molecular weight impact on the mechanical forces between hyaluronan and its receptor.* Carbohydrate Polymers, 2018. **197**: p. 326-336.
35. Sheridan, C., et al., *CD44(+)/CD24(-) breast cancer cells exhibit enhanced invasive properties: an early step necessary for metastasis.* Breast Cancer Research, 2006. **8**(5).
36. Telmer, P.G., et al., *How does a protein with dual mitotic spindle and extracellular matrix receptor functions affect tumor susceptibility and progression?* Communicative & integrative biology, 2011. **4**(2): p. 182-185.
37. Turley, E.A., *PURIFICATION OF A HYALURONATE-BINDING PROTEIN-FRACTION THAT MODIFIES CELL SOCIAL-BEHAVIOR.* Biochemical and Biophysical Research Communications, 1982. **108**(3): p. 1016-1024.
38. Turley, E.A., P.W. Noble, and L.Y.W. Bourguignon, *Signaling properties of hyaluronan receptors.* Journal of Biological Chemistry, 2002. **277**(7): p. 4589-4592.
39. Maxwell, C.A., J. McCarthy, and E. Turley, *Cell-surface and mitotic-spindle RHAMM: moonlighting or dual oncogenic functions?* Journal of Cell Science, 2008. **121**(7): p. 925-932.
40. Prudovsky, I., et al., *Secretion without Golgi.* Journal of cellular biochemistry, 2008. **103**(5): p. 1327-1343.
41. Tolg, C., et al., *Rhamm(-/-) fibroblasts are defective in CD44-mediated ERK1,2 motogenic signaling, leading to defective skin wound repair.* Journal of Cell Biology, 2006. **175**(6): p. 1017-1028.
42. Hamilton, S.R., et al., *The hyaluronan receptors CD44 and Rhamm (CD168) form complexes with ERK1,2 that sustain high basal motility in breast cancer cells.* Journal of Biological Chemistry, 2007. **282**(22): p. 16667-16680.
43. Hatano, H., et al., *RHAMM/ERK interaction induces proliferative activities of cementifying fibroma cells through a mechanism based on the CD44-EGFR.* Laboratory Investigation, 2011. **91**(3): p. 379-391.
44. Tolg, C., et al., *RHAMM Promotes Interphase Microtubule Instability and Mitotic Spindle Integrity through MEK1/ERK1/2 Activity.* Journal of Biological Chemistry, 2010. **285**(34): p. 26461-26474.
45. Veiseh, M., et al., *Cellular heterogeneity profiling by hyaluronan probes reveals an invasive but slow-growing breast tumor subset.* Proceedings of the National Academy of Sciences of the United States of America, 2014. **111**(17): p. E1731-E1739.
46. Zhao, J.S., et al., *Characterization of a motif for specific binding to hyaluronan in chicken SPACR.* Journal of Neurochemistry, 2008. **106**(3): p. 1117-1124.
47. Yang, B.H., et al., *Identification of a Common Hyaluronan-Binding Motif in the Hyaluronan-Binding Proteins Rhamm, Cd44 and Link Protein.* Embo Journal, 1994. **13**(2): p. 286-296.
48. Zal, T. and N.R. Gascoigne, *Photobleaching-corrected FRET efficiency imaging of live cells.* Biophysical journal, 2004. **86**(6): p. 3923-3939.
49. Carvalho, A.M., et al., *Redox-Responsive Micellar Nanoparticles from Glycosaminoglycans for CD44 Targeted Drug Delivery.* Biomacromolecules, 2018. **19**(7): p. 2991-2999.
50. Chen, L.Q. and L.Y.W. Bourguignon, *Hyaluronan-CD44 interaction promotes c-Jun signaling and miRNA21 expression leading to Bcl-2 expression and chemoresistance in breast cancer cells.* Molecular Cancer, 2014. **13**.
51. Sun, N., et al., *Potential Indexing of the Invasiveness of Breast Cancer Cells by Mitochondrial Redox Ratios.* Advances in experimental medicine and biology, 2016. **923**: p. 121-127.

52. Thompson, E.W., et al., *Association of increased basement-membrane invasiveness with absence of estrogen-receptor and expression of vimentin in human breast-cancer cell-lines.* Journal of Cellular Physiology, 1992. **150**(3): p. 534-544.
53. Assmann, V., et al., *The human hyaluronan receptor RHAMM is expressed as an intracellular protein in breast cancer cells.* Journal of Cell Science, 1998. **111**: p. 1685-1694.
54. Maxwell, C.A., et al., *Receptor for hyaluronan-mediated motility correlates with centrosome abnormalities in multiple myeloma and maintains mitotic integrity.* Cancer Research, 2005. **65**(3): p. 850-860.
55. Sohr, S. and K. Engeland, *RHAMM is differentially expressed in the cell cycle and downregulated by the tumor suppressor p53.* Cell Cycle, 2008. **7**(21): p. 3448-3460.
56. Nedvetzki, S., et al., *RHAMM, a receptor for hyaluronan-mediated motility, compensates for CD44 in inflamed CD44-knockout mice: A different interpretation of redundancy.* Proceedings of the National Academy of Sciences of the United States of America, 2004. **101**(52): p. 18081-18086.
57. Novoa-Carballal, R., et al., *Tunable nano-carriers from clicked glycosaminoglycan block copolymers.* Journal of Materials Chemistry B, 2014. **2**(26): p. 4177-4184.
58. Altgarde, N., et al., *Probing the biofunctionality of biotinylated hyaluronan and chondroitin sulfate by hyaluronidase degradation and aggrecan interaction.* Acta Biomaterialia, 2013. **9**(9): p. 8158-8166.
59. Aguiar, D.J., W. Knudson, and C.B. Knudson, *Internalization of the hyaluronan receptor CD44 by chondrocytes.* Experimental Cell Research, 1999. **252**(2): p. 292-302.
60. Sekar, R.B. and A. Periasamy, *Fluorescence resonance energy transfer (FRET) microscopy imaging of live cell protein localizations.* Journal of Cell Biology, 2003. **160**(5): p. 629-633.
61. Hamilton, S.R., et al., *The hyaluronan receptors CD44 and Rhamm (CD168) form complexes with ERK1,2 that sustain high basal motility in breast cancer cells.* The Journal of biological chemistry, 2007. **282**(22): p. 16667-16680.
62. Yang, C., et al., *Inducible formation of leader cells driven by CD44 switching gives rise to collective invasion and metastases in luminal breast carcinomas.* Oncogene, 2019. **38**(46): p. 7113-7132.
63. Zhang, S.W., et al., *The hyaluronan receptor RHAMM regulates extracellular-regulated kinase.* Journal of Biological Chemistry, 1998. **273**(18): p. 11342-11348.
64. Park, D., et al., *Hyaluronic acid promotes angiogenesis by inducing RHAMM-TGF beta receptor interaction via CD44-PKC delta.* Molecules and Cells, 2012. **33**(6): p. 563-574.
65. Nikitovic, D., et al., *The Roles of Hyaluronan/RHAMM/CD44 and Their Respective Interactions along the Insidious Pathways of Fibrosarcoma Progression.* Biomed Research International, 2013.
66. Du, Y.C.N., et al., *Receptor for hyaluronan-mediated motility isoform B promotes liver metastasis in a mouse model of multistep tumorigenesis and a tail vein assay for metastasis.* Proceedings of the National Academy of Sciences of the United States of America, 2011. **108**(40): p. 16753-16758.
67. Savani, R.C., et al., *Differential involvement of the hyaluronan (HA) receptors CD44 and receptor for HA-mediated motility in endothelial cell function and angiogenesis.* Journal of Biological Chemistry, 2001. **276**(39): p. 36770-36778.
68. Manzanares, D., et al., *Apical oxidative hyaluronan degradation stimulates airway ciliary beating via RHAMM and RON.* American Journal of Respiratory Cell and Molecular Biology, 2007. **37**(2): p. 160-168.
69. Okamoto, I., et al., *CD44 cleavage induced by a membrane-associated metalloprotease plays a critical role in tumor cell migration.* Oncogene, 1999. **18**(7): p. 1435-1446.
70. Gurski, L.A., et al., *Hyaluronan (HA) Interacting Proteins RHAMM and Hyaluronidase Impact Prostate Cancer Cell Behavior and Invadopodia Formation in 3D HA-Based Hydrogels.* Plos One, 2012. **7**(11).
71. Lynn, B.D., et al., *Sequence, protein expression and extracellular-regulated kinase association of the hyaladherin RHAMM (receptor for hyaluronan mediated motility) in PC12 cells.* Neuroscience Letters, 2001. **306**(1-2): p. 49-52.

CHAPTER IV

RHAMM EXPRESSION TUNES THE RESPONSE OF BREAST CANCER CELL LINES TO HYALURONAN

RHAMM EXPRESSION TUNES THE RESPONSE OF BREAST CANCER CELL LINES TO HYALURONAN

Abstract

Hyaluronan (HA) synthesis and degradation are altered during carcinogenesis leading to an increased HA content in the tumor microenvironment, which correlates with poor prognosis and treatment outcomes. The main HA receptors, CD44 and RHAMM, are also overexpressed in tumors where they activate anti-apoptotic, proliferative, invasive, and migration signaling pathways.

Herein, we used a unidirectional HA gradient to investigate in a high-throughput fashion the bi-directional communication between HA and breast cancer cell lines with different surface expression of CD44 and RHAMM. We found that the expression of CD44 and RHAMM depends on the HA density: the expression of these receptors is promoted at higher HA density and RHAMM is more sensitive to these changes when compared to CD44. Blocking either CD44 or RHAMM revealed different functions on binding and recognizing HA and a compensatory expression between these two receptors that maintains protumorigenic effectors such as cortactin.

This chapter is based on the following publication:

Carvalho, Ana M.; Soares da Costa, Diana; Reis, Rui L.; Pashkuleva, Iva: "RHAMM expression tunes the response of breast cancer cell lines to hyaluronan", submitted.

IV.1. INTRODUCTION

Breast cancer development and progression are correlated with a constant remodeling of the extracellular matrix (ECM). Among different ECM components, hyaluronan (HA) has been associated with several tumorigenesis processes.[1] Overexpression of hyaluronan synthases (HAS), particularly HAS2, leads to an accumulation of HA at the tumor site.[2-4] The increased content of HA is a poor prognosis marker of most invasive breast cancer cells because in the tumor microenvironment HA activates anti-apoptotic, pro-invasion, and pro-migration signaling pathways and regulates multidrug resistance, tumor growth, and progression.[5-11]

In breast cancer, HA bioactivity is transduced by its main receptors, cluster of differentiation 44 (CD44) and the receptor for hyaluronan mediated motility (RHAMM). CD44 is a type I transmembrane protein that interacts with HA via an amino-terminal link domain present at the protein ectodomain and common to other hyaladherins.[12, 13] This receptor is ubiquitously expressed at the cell surface, and it is involved in cell-cell and cell-ECM communication.[1] CD44 receptor is overexpressed in several cancers, including breast, and correlates with an aggressive behavior and poor prognosis.[14, 15] RHAMM binds HA through an HA-binding region that structurally differs from the CD44 one.[16] RHAMM has different cellular functions according to its localization in the cell: it can take part of the cell in-out signal transduction when is expressed at the cell surface, and/or act as an intracellular effector and regulator of motile and proliferative pathways.[17-21] This HA receptor is not detected in most tissues; however, it is expressed during wound repair and in several cancers.[22] In breast cancer, RHAMM overexpression is linked to poor clinical outcomes.[23] Despite their structural differences, CD44 and RHAMM have some overlapping functions in HA signaling, and both compensatory and cooperative mechanisms between these receptors have been proposed.[5, 24-26] Herein, we developed molecular gradients to study the relationship between HA content and CD44 and RHAMM expression and function.

IV.2. Materials and Methods

IV.2.1. Materials.

Sodium hyaluronate (HA, weight average molecular weight (MW), 4.8 kDa, MW dispersity of 1.2) was acquired from Lifecore (USA). End-on-thiolated HA was synthesized by coupling a short (C_{11}) alkanethiol at HA reducing end using an oxime reaction, as previously described (details provided in the SI).[5, 27] The antibodies used in this study were monoclonal antibody to CD44 – Ascites (Acris), anti-CD44 antibody [KM201] (Abcam), anti-CD168 antibody [EPR4055] (Abcam), RHAMM antibody (H-8) (Santa Cruz Biotechnology), anti-CD44-PE (BD Biosciences), and AlexaFluor® 594 donkey anti-mouse IgG1 (H+L) (ThermoFisher Scientific). We used 4′,6-diamidino-2-phenylindole (DAPI, Biotium), and fluorescein isothiocyanate labeled phalloidin (phalloidin-FITC, Sigma) for nucleus and cytoskeleton staining, respectively.

IV.2.2. Preparation of HA gradients.

Glass coverslips (2 x 2 cm^2) were cleaned in piranha solution and amino-functionalized using 3-(aminopropyl)triethoxysilane (APTES) (1% v/v in acetone, 30 min, room temperature (RT)). Substrates were washed with acetone in an ultrasonic bath and cured (110 °C for 1 h under vacuum).[28, 29] Gold nanoparticles were synthesized by the Turkevich method[30] (details provided in the SI) and immobilized on the amino-functionalized coverslips by diffusional deposition. Briefly, a dispersion of gold nanoparticles (5 mL of the obtained gold nanoparticles colloidal suspension in 95 mL of Milli-Q water) was pumped (100 mL/min for 2 h) at the bottom of a container with the vertically positioned substrate. The generated gold nanoparticles gradients were washed with Milli-Q water, dried under nitrogen flow, and stored or further functionalized by immobilization of end-on-thiolated HA (0.5 mg/mL in Milli-Q water, overnight incubation, RT). The HA-functionalized substrates were washed with phosphate-buffered saline (PBS) and passivated with bovine serum albumin (BSA 3 % w/v in PBS for 30 min at RT). Wheat germ agglutinin (WGA) Alexa Fluor® 488 conjugate (1.25 μg/mL in PBS, 10 min, RT, Molecular Probes) was used to confirm the presence and bioactivity of the immobilized HA. Gold nanoparticles gradients passivated with BSA were used as a control substrate.

IV.2.3. Breast cancer cells culture and interaction with HA gradients.

The obtained HA gradients were sterilized with UV light (30 min) before cells seeding. We used two breast cancer cell lines, namely MDA-MB-231 and Sk-Br-3 (American Type Culture Collection, ATCC). Cells were kept in culture on tissue culture polystyrene in Dulbecco Modified Eagle Medium high glucose (4500 mg/L) containing phenol red (Sigma-Aldrich) and supplemented with 3.7 mg/mL sodium bicarbonate (Sigma-Aldrich), 10 % fetal bovine serum (FBS, Gibco) and 1 % antibiotic/antimycotic (10000 units/mL penicillin G sodium, 10000 μg/mL streptomycin sulfate, and 25 μg/mL amphotericin B in 0.85% saline; Gibco) at 37 °C with 5% CO_2 humidified atmosphere. At 80 % confluence, cells were detached with TrypLE Express (Gibco), centrifuged (300*g* for 5 min), and subcultured.

To study the interaction with gradients (HA or gold), cells were seeded at a density of 10^5 cells/cm^2. For blocking CD44 or RHAMM receptors, cells (2 x 10^5 cells) were suspended in 100 μL of complete growth medium containing anti-CD44 antibody (1 μg, KM201 Abcam) or anti-CD168 antibody (400 ng, EPR4055 Abcam), respectively for 30 min at 37 °C in 5 % CO_2 humidified atmosphere. After washing with PBS, cells were seeded on gradients at a density of 10^5 cells/cm^2. Receptors' expression was evaluated 24 h after the seeding by immunocytochemistry.

IV.2.4. Flow cytometry.

Upon 70 % of confluence, cells were detached by incubation with 4 mM ethylenediaminetetraacetic acid (EDTA, Sigma-Aldrich) in PBS pH 8 (Sigma-Aldrich) for 10 min at 37 °C in 5% CO_2 humidified atmosphere. Cells were characterized by flow cytometry using the following antibodies: human anti-CD44 PE (BD Pharmingen) and RHAMM antibody (H-8) (Santa Cruz Biotechnology). The expression of surface receptors CD44 was quantified by incubating the cells with anti-CD44-PE (2 μg for 5 x 10^5 cells in 100 μL of PBS) for 30 min at RT. In the case of RHAMM, cells were first incubated with the RHAMM antibody (H-8) (2 μg for 5 x 10^5 cells in 100 μL of PBS) for 30 min at 4 °C. After washing, a second incubation was performed with donkey anti-mouse Alexa Fluor® 488 (1 μg, ThermoFisher). Cells were washed with PBS, centrifuged for

5 min at 300*g*, and suspended in acquisition buffer (1 % formalin in PBS) for flow cytometry analysis (BD FACSCalibur).

IV.2.5. Immunocytochemistry.

Substrates with the cultured cells were washed with PBS, fixed with 10 % formalin (1 h at 4 °C), and cells were permeabilized with 0.2 % triton-X-100/PBS (15 min at RT). Incubation with monoclonal CD44 antibody (dilution 1:400 in 1% BSA/PBS) or with anti-CD168 antibody (1:200 in 1% BSA/PBS) was performed overnight at 4 °C. After washing with PBS, secondary antibody Alexa Fluor® 488 or Alexa Fluor® 647 (dilution 1:750) was added together with DAPI (1 μg/mL) and phalloidin (50 ng/mL) for nucleus and actin counterstaining (1 h at RT). Microscope slides were mounted with VectaShield mounting medium (Vector Laboratories), and fluorescent tiled images were acquired edge-to-edge of the gradient on an inverted confocal microscope (TCS SP8, Leica Microsystems). Image post-processing was performed by ImageJ 1.53c. Tiled images were projected to the sum and sectioned in 10 positions along the gradient. To quantify the mean grey value of CD44 and RHAMM, a region of interest (cell body, ROI) was first selected using the phalloidin signal. The ROI was then used to measure the mean grey value of the receptors signal. The number of adhesion cells was determined by nucleus counting.

IV.2.6. Scanning Electron Microscopy (SEM).

Substrates with cultured cells were washed with PBS, fixed with 2.5 % glutaraldehyde in PBS (1 h, 4 °C), incubated with a series of ethanol solutions with increasing concentration (50 %, 70 %, 90 %, and 100 %) for dehydration, and dried overnight at RT. The dried substrates were mounted on the SEM pins, sputter-coated with gold (1 nm) and analyzed in a high-resolution field emission scanning electron microscope AIRIGA® (Zeiss).

IV.2.7. Statistics.

All reported data were obtained from three independent experiments (n=3) with gradients duplicates. To facilitate the analysis and data presentation, the gradients were divided into 10 equisized areas defined as positions 1-10. At least 3 regions were analyzed per each area. Data

failed Levene's test for equality of variances at $p < 0.05$. The non-parametric Kruskal-Wallis test was used to determine statistical differences between the studied conditions (gold, HA, CD44 block, and RHAMM block) with a 95% confidence level. Multi-comparisons were tested using Benjamini and Hochberg *p*-adjusting method. Data processing, graphical representation, and statistical analysis were performed using RStudio (Version 1.2.5042).

IV.3. Results and Discussion

Molecular gradients are commonly observed in biological systems. As an example, cells create gradients by secreting biomolecules that diffuse in the ECM. These gradients are temporally and spatially controlled and determine the cellular identity and fate.[31] They are critical for different physiological and pathological processes, including inflammation, wound healing, and cancer.[31] HA is a main component of the ECM that supports the normal cellular function. [1] However, in breast cancer, HA homeostasis is altered, resulting in its accumulation of low molecular weight HA and formation of local gradients that play an important role in cancer.[32, 33] Thus, studies of cellular response to HA gradients are of utmost interest for revealing mechanistic insights in HA-associated carcinogenesis and identifying possible molecular targets. Previous studies have demonstrated that soluble low molecular weight HA has a chemoattractant effect (Dunn chamber assay) and promotes the directional migration of MDA-MB-231 and MDA-MB-486 cells.[34] However, either at the cell membrane or in the ECM, HA is partially immobilized by interactions with hyaluronan synthases (HAS), and other ECM components. To better mimic this scenario, hydrogel HA gradients have been developed to screen the cell behavior.[35-37] In this model, the gradient in HA content is concomitant with alterations in hydrogel mechanical properties, and it is not clear whether the cell response is triggered by HA-activated signaling pathways or mechanosensing. Recently, we have developed continuous HA gradients by surface immobilization of end-on thiolated HA (4.8 kDa) on gold gradients formed via diffusional deposition of colloidal nanoparticles (Fig. IV.1A1-3).[38]

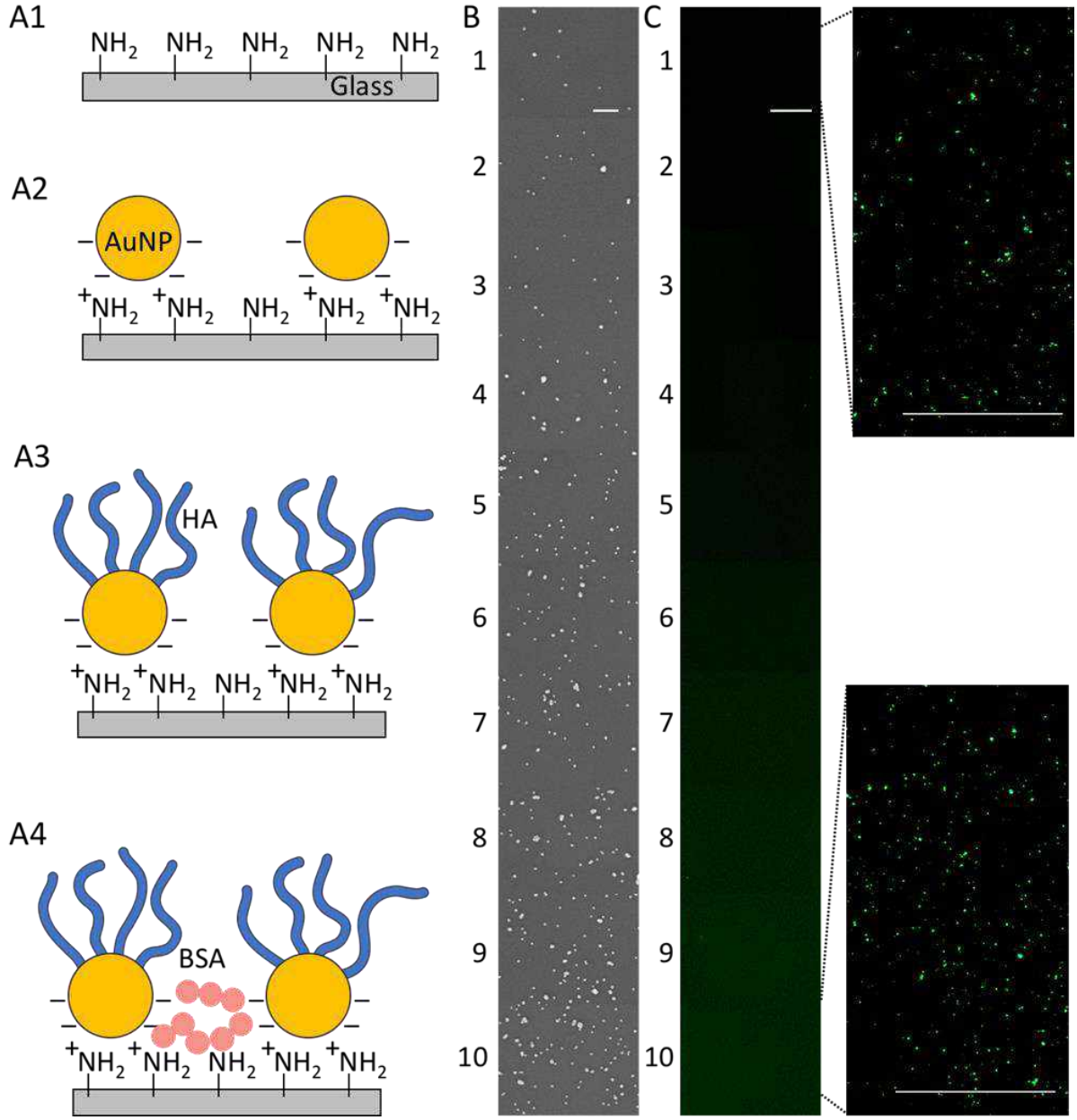

Figure IV. 1. Preparation of hyaluronan gradients. (A) Schematic presentation of different experimental steps in the preparation of the gradients: (A1) amination of the substrates, (A2) electrostatic deposition of gold nanoparticles (AuNP), (A3) functionalization of the gold nanoparticles with thiolated hyluronan (HA), and (A4) passivation of unfunctionalized surface with bovine serum albumin (BSA); (B) Representative scannining electron microscopy images of subsrate surface along the gradient showing different density of the deposited gold nanoparticles, scale bar = 200 nm; (C) Representative fluorescence microscopy images showing the gradients used in this study after staining with Wheat germ agglutinin (WGA) Alexa Fluor® 488 conjugate, scale bar = 100 μm for the gradient and 500 μm for the magnified individual images at position 1 and 10. The respective quantification of the fluorescent intensity along the gradient is provided in Fig. IV.S2 (SI).

This approach allows a relevant biofunctional presentation of HA since its main chain and functional groups are preserved. Herein, we used the same procedure to prepare HA gradients but after the HA deposition, the substrates were passivated with bovine serum albumin – a protein that does not bind HA and prevents cell adhesion (Fig. IV.1A4).[39, 40] As a result, we obtained gradients that have only one surface-exposed component for interaction with cells, *i.e.* HA whose bioactivity is preserved as demonstrated by binding with fluorescent-labeled wheat germ agglutinin (Figs. IV.1C, IV.S1).[41]

IV.3.1. CD44 and RHAMM expression by breast cancer cell lines.

CD44 and RHAMM interactions play a critical role in invasive breast cancer cells.[42] We used two breast cancer cell lines MDA-MB-231 (basal mesenchymal, triple-negative) and Sk-Br-3 (HER2-OE) [43, 44] with different aggressiveness and expression of CD44 and RHAMM.[5, 38, 45] The expression of these receptors was confirmed by immunocytochemistry (total expression) and flow cytometry (expression at the cell surface). The immunostaining showed that the two cell lines have similar expression of RHAMM but differ by the CD44 expression: MDA-MB-231 cells have a high CD44 expression, while Sk-Br-3 cells express less CD44 as shown by the faint staining (Fig. IV.2A). Because the recognition of extracellular HA occurs in the pericellular space, the expression of RHAMM and CD44 at the cell surface is consequential for cells/HA interactions. The results from the flow cytometry (Fig. IV.2B, characterization was performed without cell permeabilization) showed that the MDA-MB-231 cells are CD44 positive, while Sk-Br-3 cells are CD44 negative with only 10% of these cells exhibiting a basal CD44 expression at the cell surface. An opposite trend was observed for RHAMM expression – 40% of the Sk-Br-3 cells were positive for cell-surface RHAMM, while only 5% of the MDA-MB-231 cells were RHAMM positive but this population express RHAMM at high levels. Therefore, the selected cell models have distinct phenotypes with MDA-MB-231 being CD44++/RHAMM+ and Sk-Br-3 CD44-/RHAMM++.

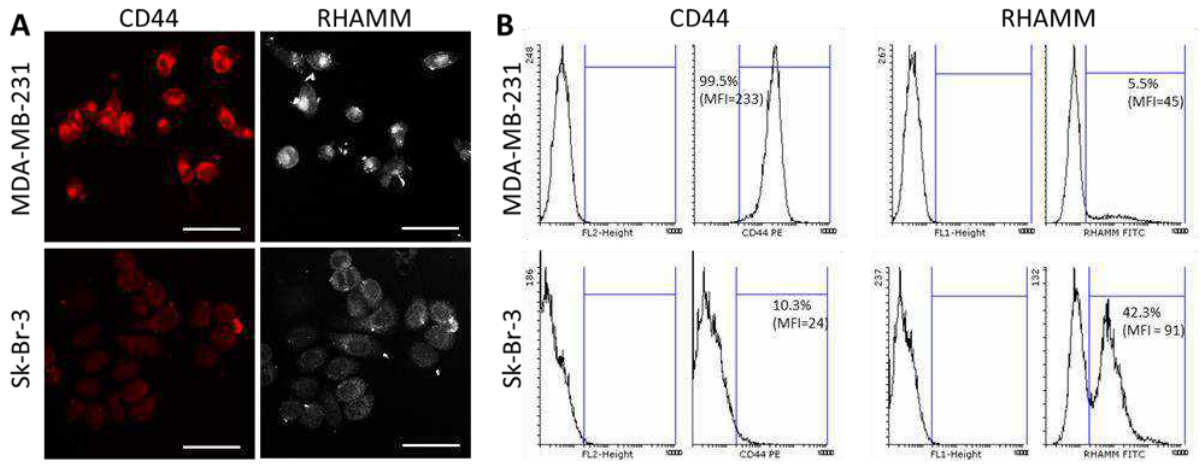

Figure IV. 2. CD44 and RHAMM expression in MDA-MB-231 and Sk-Br-3 cells. (A) Confocal microscopy images of immunostained cells displaying the total expression of CD44 (red) and RHAMM (white) by the studied cells, scale bar = 50 μm; (B) Characterization of non-permeabilized cells by flow cytometry showing quantitative data for the CD44 and RHAMM expressed on the cells surface.

IV.3.2. HA affects the adhesion of breast cancer cells

The morphology of the cells adherent to HA gradients was evaluated by scanning electron microscopy (SEM, Figs. IV.3B and IV.S3). On the passivated gold gradients, we observed spherical cells with numerous transient filopodia pointing in all directions consistent with the substrate exploring function of these protrusions. Cells on HA gradients were spread and with different morphology: Sk-Br-3 cells were round-shaped, while a spindle-like morphology was observed for MDA-MB-231 cells. These shapes were preserved along the HA gradient (Fig. IV.S3) but we observed differences in the formed protrusions. In Sk-Br-3 cells the transient filopodia disappear completely in favor of lamellipodia, while MDA-MB-231 cells were polarized with parallel filipodia at the front edge (Figs. IV.3B and IV.S3), *i.e.* a morphology typical for migrating cells. Of note, more and longer filopodia are visible for the MDA-MB-231 cells at higher HA density (Fig. IV.S3). This result agrees with recent data that correlates an increased secretion of HA to the pericellular space of breast cancer cells with filopodial growth.[38, 48]

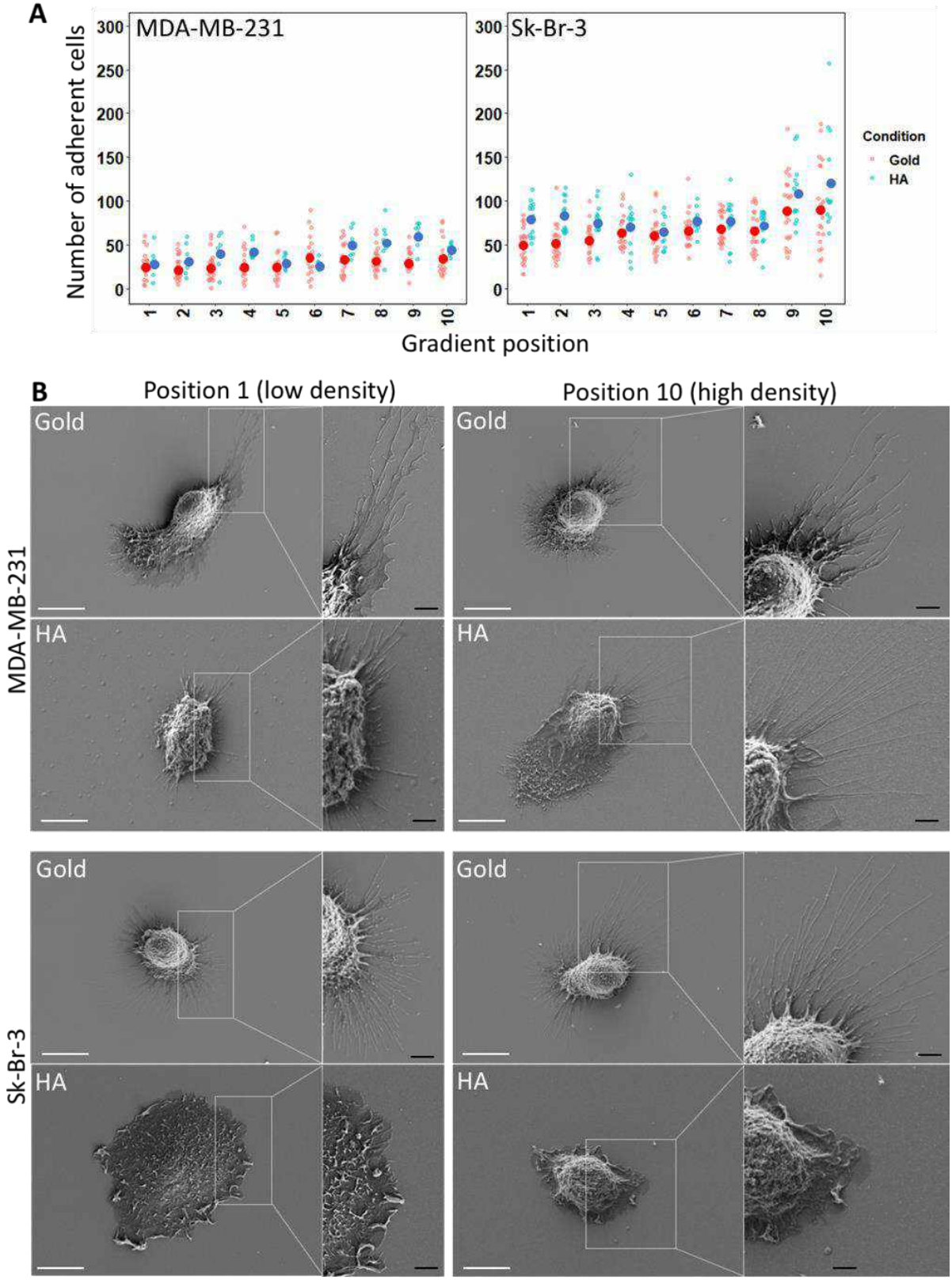

Figure IV.3. Adhesion of MDA-MB-231 and Sk-Br-3 cells to gold and HA gradients. (A) Number of adherent cells on gold (control) and HA gradients. Data for individual cells are presented as small points

and big circles correspond to the mean values. Data sets for HA gradients are statistically significant from the control gradients (p<0.005, n=3). (B) Representative scanning electron microscopy images of breast cancer cells adherent to low- and high-density regions of HA gradients. White scale bar = 10 μm, black scale bar = 2.5 μm. The gradient density increases from position 1 to 10. Supplementary images are provided in Fig. IV.S3 (SI).

IV.3.3. HA gradient modulates the expression of CD44 and RHAMM of breast cancer cells.

The bidirectional communication between cancer cells and their ECM results in a dynamic remodeling of the local cell environment, which in turn favors cancer progression.[49] Herein, we investigated the impact of the HA density on the behavior of breast cancer cells. The primary HA receptors, CD44 and RHAMM, are expected to be responsive towards changes in HA content. Indeed, we observed a significant (p<0.005) increase of the CD44 expression for MDA-MB-231 cells (CD44++) adherent on HA gradients when compared to the control. Additionally, the CD44 expression was dependent on the HA density: higher HA density promoted CD44 expression by the MDA-MB-231 cells (Fig. IV.4A).

Moreover, colocalization of CD44 and actin was observed (Fig. IV.4B) confirming the well-known involvement of HA/CD44 signaling in the cytoskeleton remodeling. Interesting results were obtained for the CD44 expression in Sk-Br-3 cells: we observed an increased CD44 expression along the gold gradient, indicating that these cells are sensitive to changes in the nanotopography introduced by the gold nanoparticles (Fig. IV.4A). The functionalization of the gold gradients with HA abolished this response and similar averaged CD44 expression was determined along the HA gradient. This result is indicative that the roughness introduced by the deposition of the gold nanoparticles is hidden after functionalization with HA and does not influence the cell response. Of note, the used method/platform allowed the distinction of Sk-Br-3 populations with different CD44 expression: one population that has the same average expression of this protein along the whole gradient (Fig. IV.4A, Sk-Br-3, filled blue circles) and a second population that is responsive to HA density (Fig. IV.4A, Sk-Br-3, contoured blue circles) and has low CD44 expression at low HA density (positions 1-6 of the HA gradient), which gradually increases upon augmentation of the HA density (positions 7-10). This result shows that besides the low CD44 expression, Sk-Br-3 cells use CD44 signaling to respond to HA density, although the activated pathway(s) might be different from the one(s) of MDA-MB-231 cells. The dispersal pattern of CD44 in the cytoplasm

(Fig. IV.4B) supports such difference – in MDA-MB-231, CD44 is mainly observed around the nucleus while in Sk-Br-3 its distribution is even through all cytoplasm.

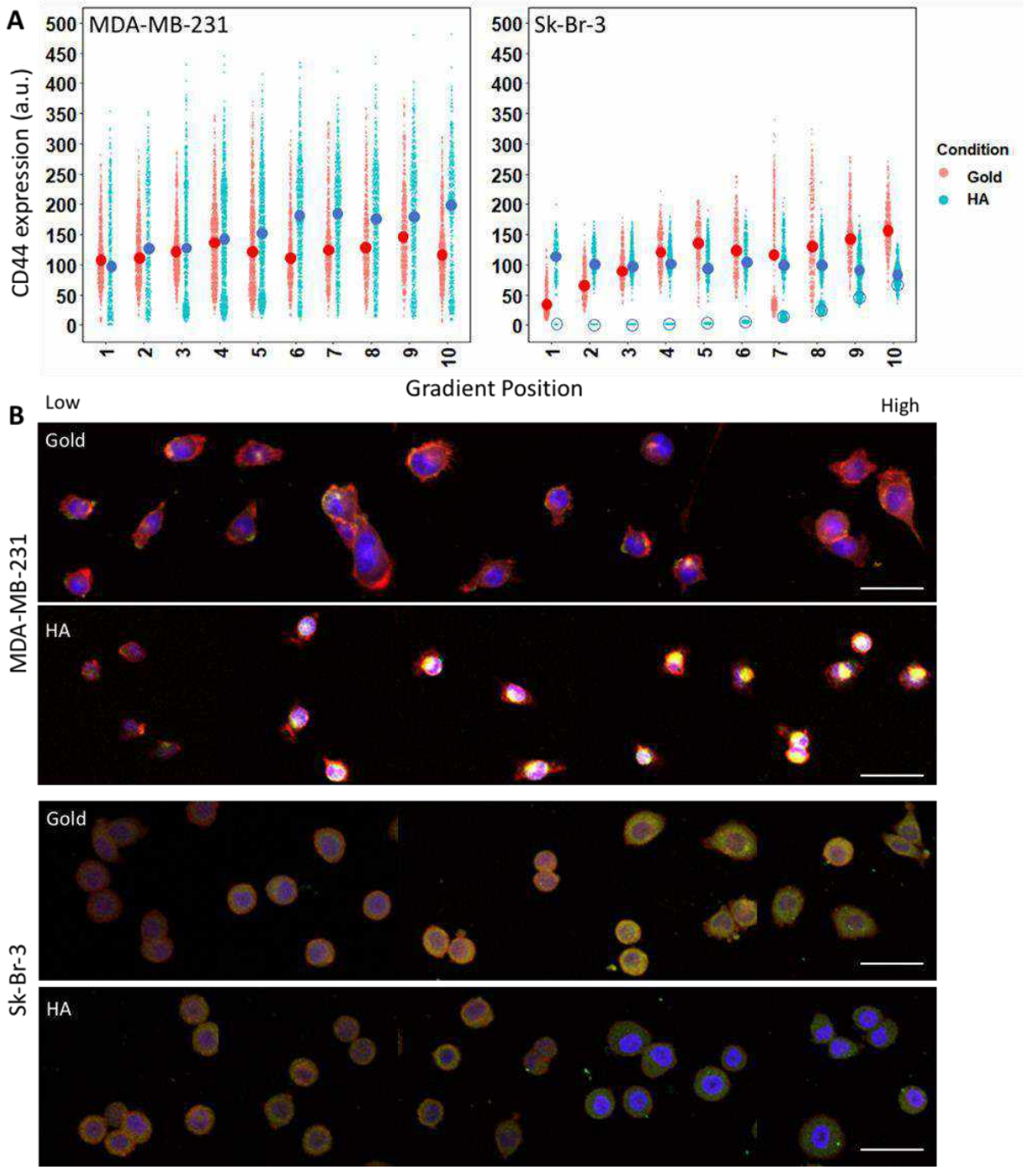

Figure IV.4. Expression of CD44 in response to HA density. (A) Graphical representation of CD44 expression by MDA-MB-231 and Sk-Br-3 cells seeded on gold and HA gradient (24 h of culture). Data for individual cells are presented as small points and big circles show the mean values. Trends for HA gradients are statistically significant from the control gradients (p<0.005, n=3). (B) Representative

fluorescence microscopy images of breast cancer cells seeded on gold and HA gradient. Color code: CD44 (green), actin is stained with phalloidin (red), and the nucleus was counterstained with DAPI (blue), scale bar = 50 μm. Gradient density increases from position 1 to position 10.

The effect of HA density was more pronounced for RHAMM expression (Fig. IV.5). When seeded on gold gradients, a higher average expression of RHAMM was observed for MDA-MB-231 cells than for Sk-Br-3 cells and no significant changes were determined along the gradient. Significantly higher (p<0.005) RHAMM expression was measured for cells seeded on HA gradients (Fig. IV.5A).

Moreover, this increase was in a function of HA density, *i.e.* MDA-MB-231 and Sk-Br-3 cells adherent to gradient areas with higher HA density expressed more RHAMM. Despite different expression of HA receptors at the surface, MDA-MB-231 and Sk-Br-3 cells have a similar response to HA gradient. The expression of HA receptors by these cell lines changes upon interaction with HA gradients and both become CD44+/RHAMM++ (Fig. IV.4 and Fig. IV.5). This result demonstrates the importance of the tumor environment in potentiating pro-tumorigenic phenotypes. It agrees with previous reports about possible mechanisms inducing such response that can be RHAMM-mediated in the case of RHAMM++ cells (*e.g.* Sk-Br-3, mesenchymal progenitor cells)[5, 24] for which RHAMM can either act as a major receptor for HA binding (this is the case of non-adherent and newly attached cells) or function in synergism with CD44.[24] Our results showed major overexpression of RHAMM rather than CD44 for both cell lines, suggesting that RHAMM is a central receptor mediating the changes in HA content in the cell microenvironment. The central role of RHAMM in mediating pericellular HA changes has already been reported for RHAMM+ cancer subpopulations that were found to establish a migration front and promote peripheral and lymphatic invasion and metastasis in aggressive breast and colorectal cancers.[50, 51]

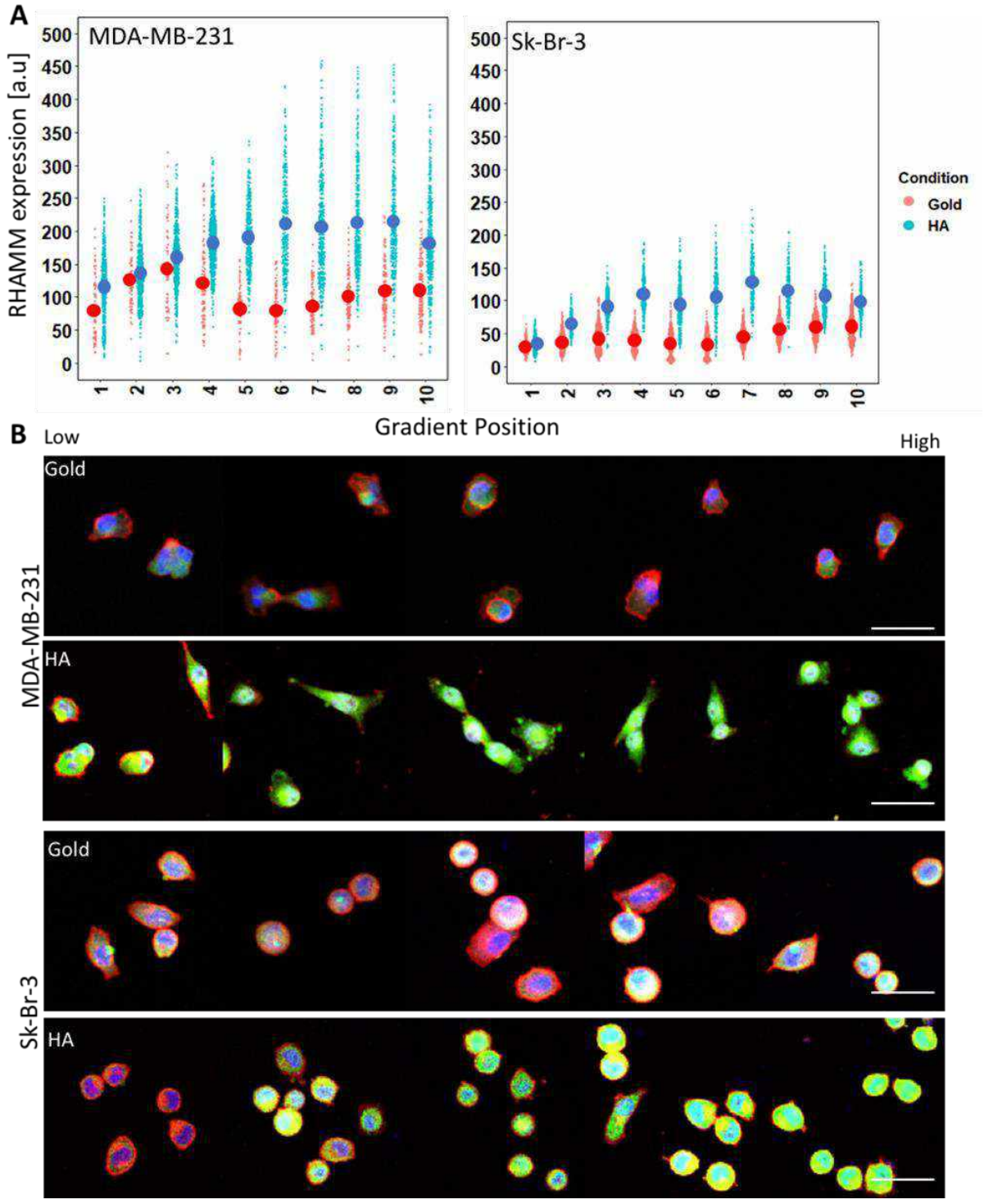

Figure IV.5. Expression of RHAMM by MDA-MB-231 and Sk-Br-3 breast cancer cells on gold and HA gradients. (A) Graphical representation of RHAMM expression by breast cancer cells along the gradients, small dots correspond to data for individual cells and the big dots are the mean values; trends for HA gradients are significantly different from the respective controls (p<0.005, n=3). (B) Representative fluorescence microscopy images of breast cancer cells interacting with gold and HA

gradients. RHAMM is shown in green; actin and nucleus were counterstained with phalloidin (red) and DAPI (blue), respectively, scale bar = 50 μm. HA density increases from position 1 to position 10.

IV.3.4 CD44 and RHAMM redundancy on HA recognition

To confirm the CD44 and RHAMM involvement in HA recognition, we performed activity blocking experiments (using neutralization antibodies) for MDA-MB-231 cells that have a more pronounced response to HA density. CD44 blocking resulted in a significant decrease in the expression of this receptor (p<0.005, Fig. IV.6A green) and upregulation of RHAMM (p<0.005, Fig. IV.6B green).

When RHAMM was blocked instead, we observed RHAMM downregulation (p<0.005, Fig. IV.6B blue) and CD44 upregulation (p<0.005, Fig. IV.6A blue), which depends on the HA density. These results clearly demonstrate the redundancy of CD44 and RHAMM previously reported by us (*in vitro*, [5]) and others (*in vivo* by knocking-out and knocking-down the CD44 gene [52-54]) and agree with the previously proposed compensatory mechanism between CD44 and RHAMM. Furthermore, we found a significantly higher number of adhered MDA-MB-231 cells after treatment with CD44 blocking antibody (p<0.005) but not for cells treated with RHAMM blocking antibody (Fig. IV.6C), *i.e.* the higher number of adherent cells correlates with the increase of RHAMM expression, confirming again that this receptor plays a fundamental role on HA binding.

We further investigated the impact of this compensatory mechanism on HA-induced protumorigenic signaling by evaluating the cortactin expression - a downstream effector common to CD44 and RHAMM mediated signaling.[55-61] Cortactin is a cytoskeletal protein involved in the formation of invadopodia and cell migration.[62, 63] It is a well-known transcriptional target of HA signaling transduced by interaction with CD44.[63, 64] We observed relatively high cortactin expression for the MDA-MB-231 cells seeded on HA gradients (Fig. IV.6D red). This expression increases along the gradient, indicating an HA-mediated response. The CD44 blocking did not significantly affect the cortactin expression by MDA-MB-231 cells (Fig. IV.6D green *vs.* red). On the other hand, the RHAMM blocking resulted in a significant increase of cortactin along the gradient (p<0.005, Fig. IV.6D blue *vs.* red) and the tendency was very similar to the observed for CD44 expression (Fig. IV.6A), suggesting a mechanism in which RHAMM is indirectly involved in the cortactin regulation via CD44.

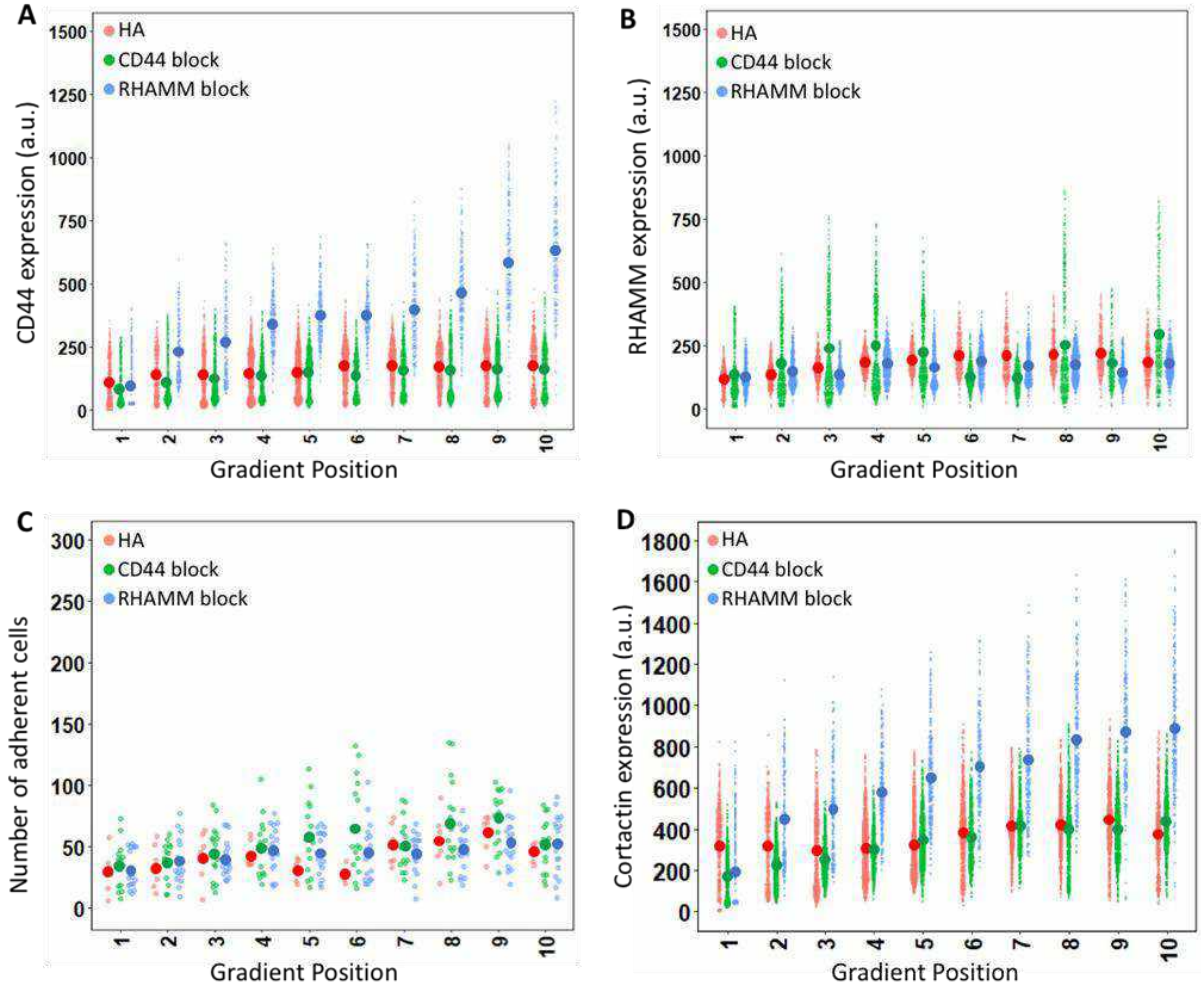

Figure IV.6. Characterization of MDA-MB-231 cells treated with blocking activity antibodies. (A) CD44 and (B) RHAMM expression by MDA-MB-231 cells seeded on HA gradients (controls) and treated with a blocking activity antibody against CD44 or RHAMM; trend for control is significantly different from RHAMM block (p<0.005, n=3). (C) Number of adherent cells on HA gradients before (controls) and after treatment with blocking activity antibody against CD44 and RHAMM. (D) Cortactin expression by MDA-MB-231 cells seeded on HA gradients and treated with an antibody against CD44 or RHAMM: trend for control is significantly different (p<0.005, n=3) from RHAMM and CD44 block; representative fluorescent microscopy images for cortactin expression are provided in Fig. IV.S4 (SI). Small dots represent data for individual cells and the big dots are the mean values. HA density increases from position 1 to position 10.

IV.4. Conclusions

During the last years, significant efforts have been devoted to HA-CD44 targeting in the context of cancer treatment. Such efforts include the use of anti-CD44 antibodies, inhibitory peptides, and siRNA/shRNA methodologies and are limited to CD44 without providing data for RHAMM.[65-75] Herein, we have analyzed thousands of cells in a high-throughput manner and show a major role of RHAMM in HA recognition, *i.e.* in tunning the cell sensitivity towards its microenvironment. Our results demonstrate that cells with high surface expression of RHAMM are more sensitive to HA density. Such RHAMM overexpression can be phenotypic (native) or acquired upon CD44 blocking – conditions at which RHAMM is recruited to compensate CD44 in protumoregnic signaling. We also demonstrate that upon increasing of HA, both CD44 and RHAMM are recruited and protrusions are formed - these are essential steps in forming migration fronts.

IV.5. Supplementary Information

Modification of Hyaluronan. Sodium hyaluronate (HA, average molecular weight 4.8 kDa, polydispersity of 1.181) was obtained from Lifecore (USA). HA was modified at the reducing end by oxime reaction with an alkanethiol as previously described.[76, 77] Briefly, HA (200 mg in 5 mL of acetate buffer, pH 4.5) was added to 11-(Aminooxy)-1-undecanethiol (3 mol excess to HA, in 5 mL of ethanol). Aniline (100 μL) was used as a catalyst. The reaction was performed under stirring at 45 °C for 24 h. The product was precipitated with ethanol and extensively dialyzed (cut-off 14 kDa, ethanol 96%). Solvent was evaporated (40 mBar, 50 °C), and the final product was freeze-dryed. The degree of modification was determined from the ^{1}H NMR (60 °C in D_2O, Bruker Avance 400 MHz) using the peaks corresponding to the aliphatic protons (δ 1.25 ppm) and the protons of the glucuronic acid unit (δ 3.4 ppm) and calculated to be 98 %.

Glass coverslips cleaning. Glass coverslips (2x2 cm^2) were first immersed in piranha solution (30 min) followed by several cycles of sonication in chloroform and Milli-Q water. The cleaned coverslips were dried under a nitrogen stream. Surface amination was performed right after coverslips cleaning.

Synthesis of gold nanoparticles. Gold nanoparticles were synthesized by the Turkevich method.[78] Gold (III) chloride trihydrate (95 mL, MiliQ water) was heated to 95 °C, and sodium citrate dihydrate (5 mL, MiliQ water) was added under vigorous magnetic stirring for 15 min (final concentration of gold was 1 mM and of sodium citrate - 3.8 mM). The solution was cooled down to room temperature and stored at 4 °C (stock dispersion). The size of the nanoparticles (Ø 35 nm) was determined by atomic force microscopy.

Glass coverslip passivation. Two methodologies were tested in the formation of the unidirectional HA gradient. In the first approach, we performed passivation of the surface before immobilization of HA, while in the second one, we first immobilized HA and then performed BSA passivation. Staining with WGA-Alexa Fluor™ 488 and imaging showed that the order is important as the passivation process affects HA immobilization: ineffective HA immobilization was observed when the passivation was performed as a first step (Fig. IV.S1).

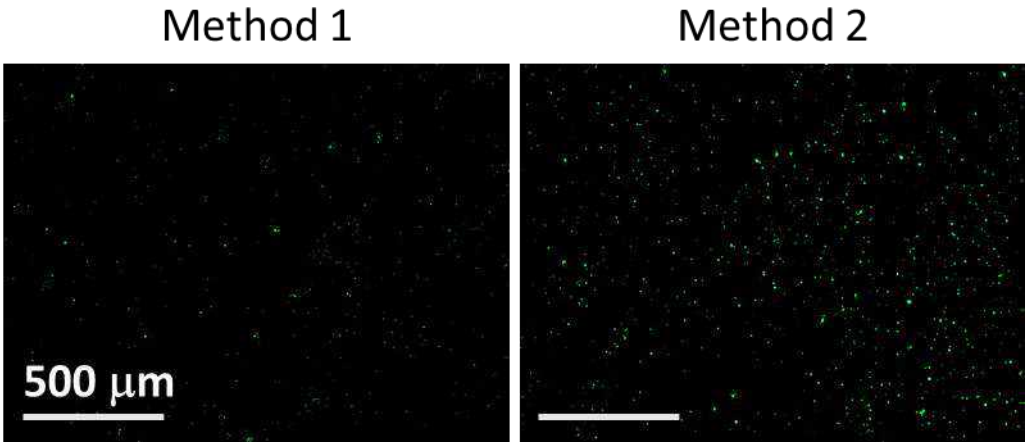

Figure IV.S1 Representative fluorescence microscopy images of hyaluronan immobilized on gold nanoparticles gradient and stained with with WGA-Alexa Fluor™ 488. Method 1: Aminated glass was first passivated with BSA, followed by incubation with thiolated HA. Method 2: Thiolated hyaluronan was first immobilized on gold nanoparticles gradient, and then passivation with BSA was carried. Both images were taken at position 10 of the gradient, *i.e.* high hyaluronan density.

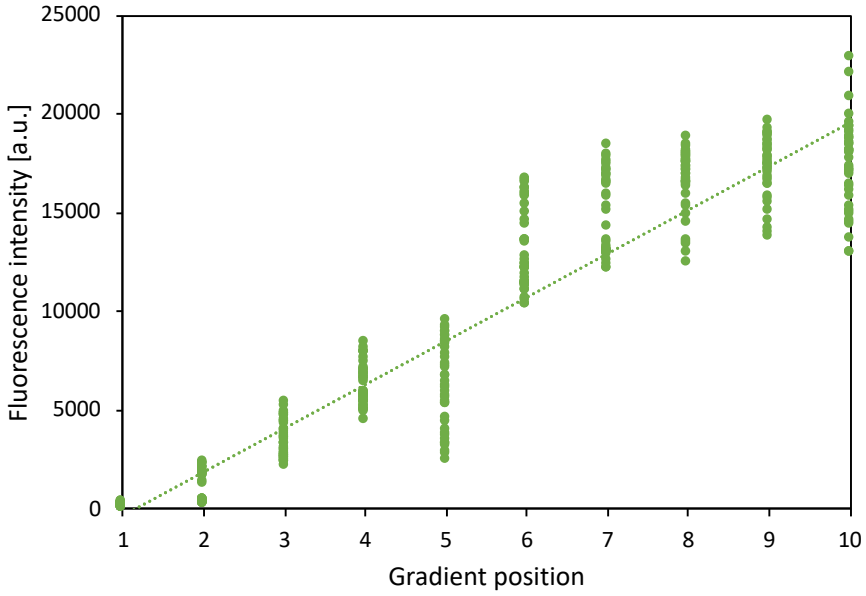

Figure IV.S2 Fluorescence intensity of HA gradient determined after labelling with Wheat germ agglutinin (WGA) Alexa Fluor® 488 conjugate.

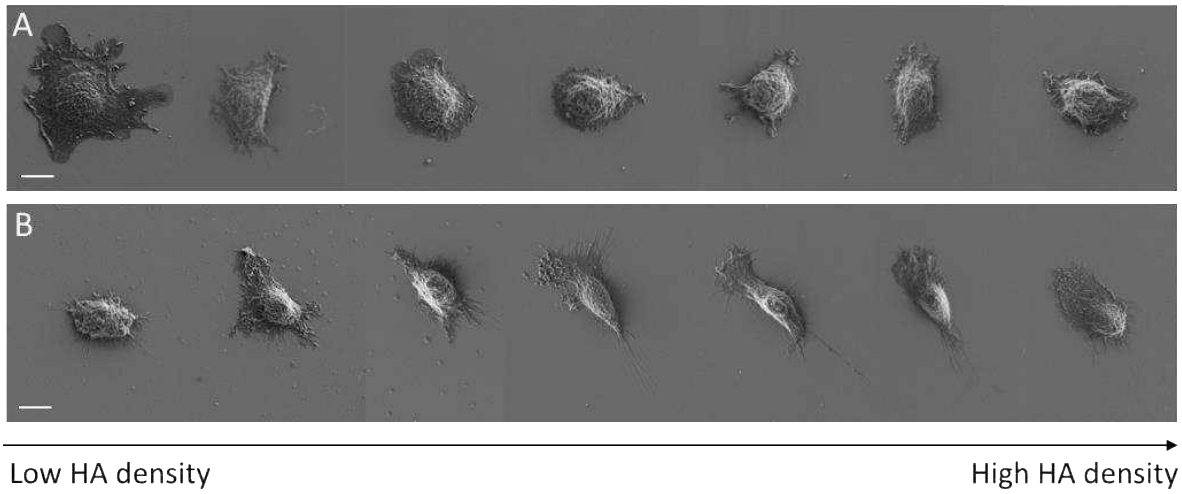

Figure IV.S3 Scanning electron microscopy (SEM) images of (A) Sk-Br-3 and (B) MDA-MB-231 cells on HA gradients. Scale bar = 10 μm.

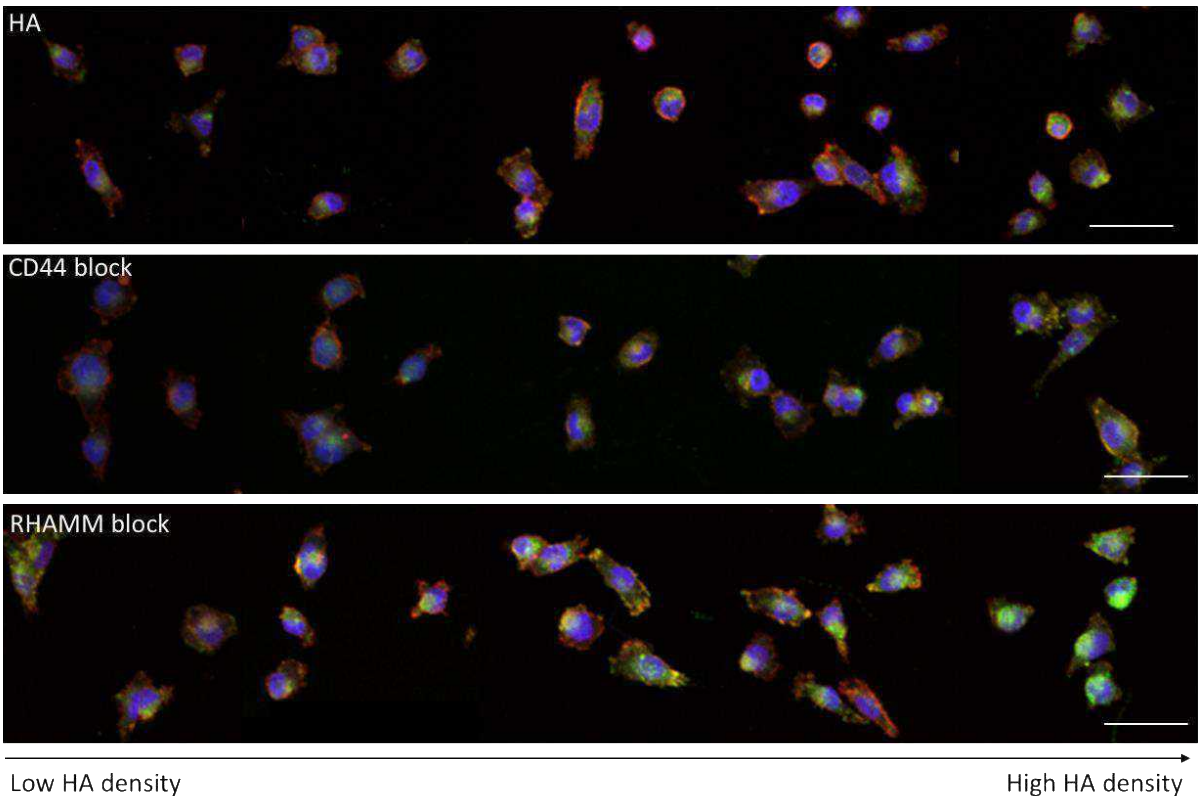

Figure IV.S4 Representative fluorescence microscopy images showing the expression of cortactin (green) by MDA-MB-231 cells seeded on HA gradients without (control) or with blocking of the HA receptors CD44 (CD44 block) and RHAMM (RHAMM block). Actin and nucleus were counterstained with phalloidin (red) and DAPI (blue), respectively, scale bar = 50 μm.

IV.6 REFERENCES

1. Caon, I., et al., *Revisiting the hallmarks of cancer: The role of hyaluronan.* Seminars in Cancer Biology, 2020. **62**: p. 9-19.
2. Li, Y., et al., *Silencing of hyaluronan synthase 2 suppresses the malignant phenotype of invasive breast cancer cells.* International Journal of Cancer, 2007. **120**(12): p. 2557-2567.
3. Bernert, B., H. Porsch, and P. Heldin, *Hyaluronan synthase 2 (HAS2) promotes breast cancer cell invasion by suppression of tissue metalloproteinase inhibitor 1 (TIMP-1).* Journal of Biological Chemistry, 2011. **286**(49): p. 42349-42359.
4. Koyama, H., et al., *Hyperproduction of hyaluronan in neu-induced mammary tumor accelerates angiogenesis through stromal cell recruitment: possible involvement of versican/PG-M.* The American journal of pathology, 2007. **170**(3): p. 1086-1099.
5. Carvalho, A.M., et al., *Co-localization and crosstalk between CD44 and RHAMM depend on hyaluronan presentation.* Acta Biomaterialia, 2021. **119**: p. 114-124.
6. Liu, S. and C.J.C.r. Cheng, *Akt signaling is sustained by a CD44 splice isoform–mediated positive feedback loop.* 2017. **77**(14): p. 3791-3801.
7. Cieply, B., C. Koontz, and S.M. Frisch, *CD44S-hyaluronan interactions protect cells resulting from EMT against anoikis.* Matrix Biology, 2015. **48**: p. 55-65.

8. Murai, T., *Lipid raft-mediated regulation of hyaluronan–CD44 interactions in inflammation and cancer.* Frontiers in immunology, 2015. **6**: p. 420.
9. Misra, S., S. Ghatak, and B.P. Toole, *Regulation of MDR1 expression and drug resistance by a positive feedback loop involving hyaluronan, phosphoinositide 3-kinase, and ErbB2.* Journal of Biological Chemistry, 2005. **280**(21): p. 20310-5.
10. Slomiany, M.G., et al., *Hyaluronan, CD44, and Emmprin Regulate Lactate Efflux and Membrane Localization of Monocarboxylate Transporters in Human Breast Carcinoma Cells.* Cancer Research, 2009. **69**(4): p. 1293-1301.
11. Bourguignon, L.Y., et al., *Hyaluronan-CD44 interaction promotes c-Src-mediated twist signaling, microRNA-10b expression, and RhoA/RhoC up-regulation, leading to Rho-kinase-associated cytoskeleton activation and breast tumor cell invasion.* Journal of Biological Chemistry, 2010. **285**(47): p. 36721-36735.
12. Banerji, S., et al., *Characterization of a functional hyaluronan-binding domain from the human CD44 molecule expressed in Escherichia coli.* Protein Expr Purif, 1998. **14**(3): p. 371-81.
13. Teriete, P., et al., *Structure of the regulatory hyaluronan binding domain in the inflammatory leukocyte homing receptor CD44.* Molecular Cell, 2004. **13**(4): p. 483-496.
14. Xu, H., et al., *CD44 correlates with clinicopathological characteristics and is upregulated by EGFR in breast cancer.* International Journal of Oncology, 2016. **49**(4): p. 1343-1350.
15. Han, S., et al., *Prognostic value of CD44 and its isoforms in advanced cancer: a systematic meta-analysis with trial sequential analysis.* Frontiers in oncology, 2019. **9**: p. 39.
16. Yang, B., et al., *Identification of a common hyaluronan binding motif in the hyaluronan binding proteins RHAMM, CD44 and link protein.* The EMBO Journal, 1994. **13**(2): p. 286-296.
17. Song, J.M., et al., *Hyaluronan-CD44/RHAMM interaction-dependent cell proliferation and survival in lung cancer cells.* 2019. **58**(3): p. 321-333.
18. Chen, F., et al., *RHAMM regulates the growth and migration of lung adenocarcinoma A549 cell line by regulating Cdc2/CyclinB1 and MMP9 genes Running title: RHAMM regulates the growth of lung adenocarcinoma cells.* Math Biosci Eng, 2020. **17**(3): p. 2150-2163.
19. Kouvidi, K., et al., *Receptor for hyaluronic acid- mediated motility (RHAMM) regulates HT1080 fibrosarcoma cell proliferation via a beta-catenin/c-myc signaling axis.* Biochimica Et Biophysica Acta-General Subjects, 2016. **1860**(4): p. 814-824.
20. Mele, V., et al., *The hyaluronan-mediated motility receptor RHAMM promotes growth, invasiveness and dissemination of colorectal cancer.* Oncotarget, 2017. **8**(41): p. 70617-70629.
21. Mascaro, M., et al., *Low molecular weight hyaluronan induces migration of human choriocarcinoma JEG-3 cells mediated by RHAMM as well as by PI3K and MAPK pathways.* Histochemistry and Cell Biology, 2017. **148**(2): p. 173-187.
22. Tolg, C., et al., *Hyaluronan and RHAMM in wound repair and the "cancerization" of stromal tissues.* BioMed Research International, 2014. **2014**.
23. Veiseh, M., et al., *Cellular heterogeneity profiling by hyaluronan probes reveals an invasive but slow-growing breast tumor subset.* Proceedings of the National Academy of Sciences, 2014. **111**(17): p. E1731-E1739.
24. Veiseh, M., et al., *Uncovering the dual role of RHAMM as an HA receptor and a regulator of CD44 expression in RHAMM-expressing mesenchymal progenitor cells.* Frontiers in cell developmental biology, 2015. **3**: p. 63.
25. Nedvetzki, S., et al., *RHAMM, a receptor for hyaluronan-mediated motility, compensates for CD44 in inflamed CD44-knockout mice: a different interpretation of redundancy.* Proceedings of the National Academy of Sciences 2004. **101**(52): p. 18081-18086.
26. Tolg, C., et al., *Rhamm−/− fibroblasts are defective in CD44-mediated ERK1, 2 motogenic signaling, leading to defective skin wound repair.* The Journal of cell biology, 2006. **175**(6): p. 1017-1028.
27. Carvalho, A.M., et al., *Redox-Responsive Micellar Nanoparticles from Glycosaminoglycans for CD44 Targeted Drug Delivery.* Biomacromolecules, 2018. **19**(7): p. 2991-2999.
28. Karrasch, S., et al., *Covalent binding of biological samples to solid supports for scanning probe microscopy in buffer solution.* Biophysical journal, 1993. **65**(6): p. 2437-2446.
29. Argekar, S.U., T.L. Kirley, and D.W.J.J.o.M.R. Schaefer, *Determination of structure-property relationships for 3-aminopropyltriethoxysilane films using x-ray reflectivity.* 2013. **28**(8): p. 1118-1128.
30. Kimling, J., et al., *Turkevich Method for Gold Nanoparticle Synthesis Revisited.* The Journal of Physical Chemistry B, 2006. **110**(32): p. 15700-15707.

31. Keenan, T.M. and A. Folch, *Biomolecular gradients in cell culture systems.* Lab on a chip, 2008. **8**(1): p. 34-57.
32. Kettunen, T., et al., *Peritumoral ADC values in breast cancer: region of interest selection, associations with hyaluronan intensity, and prognostic significance.* European radiology, 2020. **30**(1): p. 38-46.
33. Turley, E.A., D.K. Wood, and J.B. McCarthy, *Carcinoma Cell Hyaluronan as a "Portable" Cancerized Prometastatic Microenvironment.* Cancer Research, 2016. **76**(9): p. 2507-12.
34. Tzircotis, G., R.F. Thorne, and C.M. Isacke, *Chemotaxis towards hyaluronan is dependent on CD44 expression and modulated by cell type variation in CD44-hyaluronan binding.* Journal of Cell Science, 2005. **118**(21): p. 5119-5128.
35. Pogoda, K., et al., *Soft substrates containing hyaluronan mimic the effects of increased stiffness on morphology, motility, and proliferation of glioma cells.* Biomacromolecules, 2017. **18**(10): p. 3040-3051.
36. Rape, A.D., et al., *A synthetic hydrogel for the high-throughput study of cell–ECM interactions.* Nature Communications, 2015. **6**(1): p. 1-9.
37. Hachet, E., et al., *Design of biomimetic cell-interactive substrates using hyaluronic acid hydrogels with tunable mechanical properties.* Biomacromolecules, 2012. **13**(6): p. 1818-1827.
38. Carvalho, A.M., et al., *Influence of Hyaluronan Density on the Behavior of Breast Cancer Cells with Different CD44 Expression.* Advance Healthcare Materials: p. e2101309.
39. Ngo, B.K.D. and M.A. Grunlan, *Protein resistant polymeric biomaterials.* ACS Macro Letters, 2017.
40. Dickinson, L.E., et al., *Functional surfaces for high-resolution analysis of cancer cell interactions on exogenous hyaluronic acid.* Biomaterials, 2010. **31**(20): p. 5472-5478.
41. Hsu, Y.-P., X. Meng, and M. VanNieuwenhze, *Methods for visualization of peptidoglycan biosynthesis*, in *Methods in Microbiology*. 2016, Elsevier. p. 3-48.
42. Hamilton, S.R., et al., *The hyaluronan receptors CD44 and Rhamm (CD168) form complexes with ERK1, 2 that sustain high basal motility in breast cancer cells.* Journal of Biological Chemistry, 2007. **282**(22): p. 16667-16680.
43. Sørlie, T., et al., *Gene expression patterns of breast carcinomas distinguish tumor subclasses with clinical implications.* Proceedings of the National Academy of Sciences, 2001. **98**(19): p. 10869-10874.
44. Sorlie, T., et al., *Repeated observation of breast tumor subtypes in independent gene expression data sets.* Proceedings of the National Academy of Sciences of the United States of America, 2003. **100**(14): p. 8418-8423.
45. Li, W., et al., *Unraveling the roles of CD44/CD24 and ALDH1 as cancer stem cell markers in tumorigenesis and metastasis.* Scientific Reports, 2017. **7**(1): p. 1-15.
46. Witschen, P.M., et al., *Tumor Cell Associated Hyaluronan-CD44 Signaling Promotes Pro-Tumor Inflammation in Breast Cancer.* Cancers, 2020. **12**(5): p. 1325.
47. Reiprich, S., et al., *Adhesive Properties of the Hyaluronan Pericellular Coat in Hyaluronan Synthases Overexpressing Mesenchymal Stem Cells.* International Journal of Molecular Sciences, 2020. **21**(11): p. 3827.
48. Kyykallio, H., et al., *The Density and Length of Filopodia Associate with the Activity of Hyaluronan Synthesis in Tumor Cells.* Cancers 2020. **12**(7): p. 1908.
49. Winkler, J., et al., *Concepts of extracellular matrix remodelling in tumour progression and metastasis.* Nature communications, 2020. **11**(1): p. 1-19.
50. Wang, C., et al., *The overexpression of RHAMM, a hyaluronan-binding protein that regulates ras signaling, correlates with overexpression of mitogen-activated protein kinase and is a significant parameter in breast cancer progression.* Clinical cancer research, 1998. **4**(3): p. 567-576.
51. Koelzer, V.H., et al., *Expression of the hyaluronan-mediated motility receptor RHAMM in tumor budding cells identifies aggressive colorectal cancers.* Human Pathology, 2015. **46**(11): p. 1573-1581.
52. Misra, S., et al., *Interactions between hyaluronan and its receptors (CD44, RHAMM) regulate the activities of inflammation and cancer.* Frontiers in immunology, 2015. **6**: p. 201.
53. Takano, H., et al., *Involvement of CD44 in mast cell proliferation during terminal differentiation.* Laboratory investigation 2009. **89**(4): p. 446-455.
54. Xiao, W., et al., *Brain-mimetic 3D culture platforms allow investigation of cooperative effects of extracellular matrix features on therapeutic resistance in glioblastoma.* Cancer Research, 2018. **78**(5): p. 1358-1370.

55. Bourguignon, L.Y., et al., *Hyaluronan-CD44 interaction with IQGAP1 promotes Cdc42 and ERK signaling, leading to actin binding, Elk-1/estrogen receptor transcriptional activation, and ovarian cancer progression.* 2005. **280**(12): p. 11961-11972.
56. McFarlane, S., et al., *CD44-mediated activation of α5β1-integrin, cortactin and paxillin signaling underpins adhesion of basal-like breast cancer cells to endothelium and fibronectin-enriched matrices.* Oncotarget, 2015. **6**(34): p. 36762-36773.
57. Vigetti, D., et al., *Hyaluronan-CD44-ERK1/2 regulate human aortic smooth muscle cell motility during aging.* 2008. **283**(7): p. 4448-4458.
58. Zhang, S., et al., *The Hyaluronan Receptor RHAMM Regulates Extracellular-regulated Kinase.* Journal of Biological Chemistry, 1998. **273**(18): p. 11342-11348.
59. Hall, C.L., et al., *pp60(c-src) is required for cell locomotion regulated by the hyaluronanreceptor RHAMM.* Oncogene, 1996. **13**(10): p. 2213-2224.
60. Hall, C.L., et al., *Hyaluronan and the hyaluronan receptor RHAMM promote focal adhesion turnover and transient tyrosine kinase activity.* The Journal of cell biology, 1994. **126**(2): p. 575-588.
61. Wang, C., et al., *The overexpression of RHAMM, a hyaluronan-binding protein that regulates ras signaling, correlates with overexpression of mitogen-activated protein kinase and is a significant parameter in breast cancer progression.* 1998. **4**(3): p. 567-576.
62. Weaver, A.M., *Cortactin in tumor invasiveness.* Cancer letters, 2008. **265**(2): p. 157-166.
63. Bourguignon, L.W., et al., *CD44 interaction with c-Src kinase promotes cortactin-mediated cytoskeleton function and hyaluronic acid-dependent ovarian tumor cell migration.* Journal of Biological Chemistry, 2001. **276**(10): p. 7327-7336.
64. McFarlane, S., et al., *CD44-mediated activation of α5β1-integrin, cortactin and paxillin signaling underpins adhesion of basal-like breast cancer cells to endothelium and fibronectin-enriched matrices.* Oncotarget, 2015. **6**(34): p. 36762.
65. Song, G., et al., *HI44a, an anti-CD44 monoclonal antibody, induces differentiation and apoptosis of human acute myeloid leukemia cells.* Leukemia Research, 2004. **28**(10): p. 1089-96.
66. Jin, L., et al., *Targeting of CD44 eradicates human acute myeloid leukemic stem cells.* Nature Medicine, 2006. **12**(10): p. 1167-74.
67. Tremmel, M., et al., *A CD44v6 peptide reveals a role of CD44 in VEGFR-2 signaling and angiogenesis.* Blood, 2009. **114**(25): p. 5236-44.
68. Matzke, A., et al., *A Five-Amino-Acid Peptide Blocks Met- and Ron-Dependent Cell Migration.* Cancer Research, 2005. **65**(14): p. 6105-6110.
69. Peck, D. and C.M. Isacke, *Hyaluronan-dependent cell migration can be blocked by a CD44 cytoplasmic domain peptide containing a phosphoserine at position 325.* Journal of Cell Science, 1998. **111**(11): p. 1595-601.
70. Desai, B., et al., *Characterization of the expression of variant and standard CD44 in prostate cancer cells: Identification of the possible molecular mechanism of CD44/MMP9 complex formation on the cell surface.* Journal of Cellular Biochemistry, 2009. **108**(1): p. 272-284.
71. Piotrowicz, R.S., et al., *A6 Peptide Activates CD44 Adhesive Activity, Induces FAK and MEK Phosphorylation, and Inhibits the Migration and Metastasis of CD44-Expressing Cells.* Molecular Cancer Therapeutics, 2011. **10**(11): p. 2072-2082.
72. Boyd, D.D., et al., *A urokinase-derived peptide (A6) increases survival of mice bearing orthotopically grown prostate cancer and reduces lymph node metastasis.* The American journal of pathology, 2003. **162**(2): p. 619-626.
73. Mummert, M.E., et al., *Functional roles of hyaluronan in B16-F10 melanoma growth and experimental metastasis in mice.* Molecular Cancer Therapeutics, 2003. **2**(3): p. 295-300.
74. Paul, C.P., et al., *Effective expression of small interfering RNA in human cells.* Nature Biotechnology, 2002. **20**(5): p. 505-8.
75. Misra, S., et al., *Delivery of CD44 shRNA/nanoparticles within cancer cells: perturbation of hyaluronan/CD44v6 interactions and reduction in adenoma growth in Apc Min/+ MICE.* Journal of Biological Chemistry, 2009. **284**(18): p. 12432-46.
76. Carvalho, A.M., et al., *Redox-Responsive micellar nanoparticles from glycosaminoglycans for CD44 targeted drug delivery.* Biomacromolecules, 2018. **19**(7): p. 2991-2999.

77. Carvalho, A.M., et al., *Co-localization and crosstalk between CD44 and RHAMM depend on hyaluronan presentation.* Acta Biomaterialia, 2021. **119**: p. 114-124.
78. Kimling, J., et al., *Turkevich method for gold nanoparticle synthesis revisited.* Journal of Physical Chemistry B, 2006. **110**(32): p. 15700-15707.

CHAPTER V

INFLUENCE OF HYALURONAN DENSITY ON THE BEHAVIOR OF BREAST CANCER CELLS WITH DIFFERENT CD44 EXPRESSION

INFLUENCE OF HYALURONAN DENSITY ON THE BEHAVIOR OF BREAST CANCER CELLS WITH DIFFERENT CD44 EXPRESSION

Abstract

Molecular gradients are common in biosystems and play an essential role in physiological and pathological processes. During carcinogenesis, for example, hyaluronan (HA) homeostasis is hijacked by cancer cells, and the altered synthesis and degradation processes result in the formation of HA gradients within the tumor microenvironment. Herein, we developed a platform to study the biological role of HA gradient in breast cancer cells. We selected cells with different aggressiveness and expression of CD44 - the main HA receptor usually overexpressed in breast cancers and used as a marker of tumor aggressiveness. The developed platform is compatible with several imaging modalities and allows assessment of cell density, morphology, CD44 expression, and cell motility in a function of HA density. Using high-throughput analysis, we show that cells that do not express CD44 did not change along the gradient. In contrast, CD44 positive cells responded differently to the HA gradient depending on the level of CD44 expression and HA density. Furthermore, this different response was associated with the activation of different signaling pathways by the CD44-HA interactions.

This chapter is based on the publication:

Carvalho, Ana M.; Soares da Costa, Diana; Reis, Rui L.; Pashkuleva, Iva: "Influence of hyaluronan density on the behavior of breast cancer cells with different CD44 expression", Advanced Healthcare Materials, 2021, 2101309.

V.1. INTRODUCTION

Cancer development, progression, and recurrence rely on bidirectional communication between cancer cells and the extracellular matrix (ECM).[1, 2] This communication results in ECM remodeling and the formation of both physical and molecular gradients, contributing to a malignant interactome and disease progression.[3] Among different ECM components, hyaluronan (HA) - a linear non-sulfated glycosaminoglycan, is one of the main players in cancer initiation and progression.[1, 2, 4-6] HA synthesis and degradation are tightly regulated, but in most tumors, including breast ones, the resident cells hijack HA homeostasis, causing accumulation of HA oligosaccharides that interact with several cell surface receptors to activate pro-tumorigenic pathways.[2, 5, 7, 8] The main HA receptor is the cluster of differentiation 44 (CD44), a type I transmembrane adhesion glycoprotein commonly upregulated in cancer.[2, 6, 8-10] CD44/HA interactions are implicated in several signaling cascades towards pathological processes, including cell adhesion, proliferation, cell survival, motility, invasion, and multi-drug resistance.[2, 5, 6, 11, 12]

The experimental setups for elucidation of the HA role in cancer usually rely on supplementation of exogenous HA in solution. Such supplementation differs from the native HA presentation: HA is partially immobilized on the cell surface, where it is secreted by hyaluronan synthases, or in the ECM, where it interacts with other biomolecules.[5, 6] We and others have demonstrated that the presentation of HA affects its bioactivity and signaling.[13-16] Biomimicking partial immobilization of HA (*e.g.*, end-on immobilization, electrostatic deposition) allows for an increased local concentration without compromising the conformational freedom/flexibility needed for interactions with other biomolecules.[17, 18] Besides the increased concentration in the tumor microenvironment, HA turnover also results in the formation of molecular gradients, which might have a pivotal role in tumorigenesis.[3, 19, 20]

Herein, we developed a 2D platform by end-on immobilization of HA in a continuous gradient fashion. This platform allowed high-throughput screening of cells in contact with the gradients and was validated with three breast cancer cell lines that have different CD44 expressions, namely Sk-Br-3 (CD44–), MDA-MB-468 (CD44+), and MDA-MB-231 (CD44++). In addition, these cell lines

were characterized in terms of CD44 expression, cell adhesion, morphology, and motility along the HA gradients.

V.2. Materials and methods

V.2.1. End-on modification of hyaluronan.

Sodium hyaluronate (HA, average molecular weight 4.8 kDa, polydispersity of 1.18) was obtained from Lifecore (USA). HA was modified at the reducing end by oxime reaction with an alkanethiol as previously described.[13, 21] Briefly, HA (200 mg in 5 mL of acetate buffer, pH 4.5) was added to 11-(Aminooxy)-1-undecanethiol (3 mol excess to HA) dissolved in 5 mL of ethanol. Aniline (100 μL) was used as a catalyst and added to the reaction mixture. The reaction was performed under stirring at 45 °C for 24 h. The product was precipitated with ethanol and extensively dialyzed (cut-off 14 kDa, ethanol). Ethanol was evaporated (40 mBar, 50 °C), and the final product was obtained after freeze-drying. The degree of modification was determined by ^{1}H NMR (60 °C in D_2O, Bruker Avance 400 MHz) from the peaks corresponding to the aliphatic protons (δ 1.25 ppm) and the protons of the glucuronic acid unit (δ 3.4 ppm) and calculated to be 98 % (Fig. V.S1).

V.2.2. Synthesis of gold nanoparticles.

Gold nanoparticles were synthesized by the Turkevich method, as described elsewhere.[22] Briefly, gold (III) chloride trihydrate (95 mL) was heated to 95 °C, and sodium citrate dihydrate (5 mL, *i.e.,* a final concentration of 1 mM of gold and 3.8 mM of sodium citrate) was added under vigorous magnetic stirring for 15 min. The solution was cooled down to room temperature and stored at 4 °C (stock dispersion). The size of the nanoparticles was determined by atomic force microscopy (AFM, Fig. V.S2B).

V.2.3. Preparation of gradients.

Glass coverslips were cleaned with piranha solution and amino-functionalized with 3-(aminopropyl)triethoxysilane (APTES) (details in V.5). Gradients were generated on the aminated

coverslips using a two-step procedure. In the first step, a gradient of gold nanoparticles was obtained by diffusional deposition of colloidal nanoparticles. Aminated coverslips were vertically positioned in empty containers, and dispersion of gold nanoparticles (5 mL of the stock dispersion in 95 mL of Milli-Q water) was pumped (100 μL/min) at the bottom of the container until the coverslips were completely immersed (~2 h) (Fig. V.1A). The substrates were removed gently from the containers, washed with Milli-Q water, dried under nitrogen flow, and stored at room temperature. The generated gold gradients were characterized by scanning electron microscopy (SEM) and functionalized with HA before each assay. Immobilization of end-on-thiolated HA (500 μg/mL in Milli-Q water) was carried overnight in an orbital shaker (100 rpm) at room temperature. The functionalization of the gold gradients with HA and their bioactivity was confirmed by incubation with wheat germ agglutinin (WGA) Alexa Fluor® 488 conjugate (1.25 μg/mL in PBS 10 min) and microscopy imaging (inverted microscope Axio Observer, Zeiss). Before cell studies, surfaces were sterilized by UV light (30 min).

V.2.4. Culture and characterization of breast cancer cell lines.

Three breast cancer cell lines were selected for these studies, namely MDA-MB-231, MDA-MB-468, and Sk-Br-3. Cells (6 x 10^4 cells/cm2) were cultured on tissue culture polystyrene using Dulbecco Modified Eagle Medium (DMEM) high glucose with phenol red (Sigma-Aldrich, UK), supplemented with 10 % fetal bovine serum (FBS) (Invitrogen, Netherlands) and 1 % antibiotic/antimycotic (Invitrogen, Scotland). Upon 70 % of confluence, cells were detached by incubation with 4 mM ethylenediaminetetraacetic acid (EDTA, Sigma-Aldrich) in phosphate-buffered saline (PBS pH 8, Sigma-Aldrich) for 10 min at 37 °C in 5 % CO_2 humidified atmosphere. Cells were characterized by flow cytometry and immunocytochemistry using the following antibodies: human anti-CD44 PE (BD Pharmingen, USA), human anti-CD24 FITC (BD Biosciences, USA), a monoclonal antibody to CD44 – Ascites (Acris, Germany), AlexaFluor® 488 donkey anti-rabbit IgG (H+L) (Molecular Probes, USA). The expression of surface receptors CD44 and CD24 was quantified by flow cytometry analysis (BD FACSCalibur). Cells were incubated with the respective antibody (anti-CD44-PE or anti-CD24 FITC, 2 μg for 5 x 10^5 cells in 100 μL of PBS) for 30 min at room temperature, washed with PBS, centrifuged for 5 min at 300xg, and suspended in acquisition buffer (1 % formalin in PBS) for analysis. For immunocytochemical characterization, cells were fixed with 10 % formalin (4 °C, 1 h) and permeabilized with 0.2 % of Triton-X-100/PBS

(15 min, RT). Incubation with monoclonal antibody to CD44 (dilution 1:400 in 1 % BSA/PBS) was performed overnight at 4 °C. After thorough washing with PBS, secondary antibody donkey anti-mouse Alexa Fluor® 488 (dilution 1:1000) was added together with DAPI (1 μg/mL) and phalloidin (250 ng/mL) for nucleus and actin counterstaining (1 h, room temperature). Microscope slides were mounted with VectaShield mounting medium (Vector Laboratories) and observed by an inverted confocal microscope TCS SP8 (Leica Microsystems).

V.2.5. Interactions of breast cancer cell lines with the gradients.

Cells were seeded on the gradients at a density of 5 x 10^4 cells/cm2. For receptor blocking experiments, cells were pretreated with anti-CD44 antibody [KM201] (150 ng/mL for 1 x 10^5 cells) in a complete cell culture medium for 30 min at 37 °C in 5 % CO_2 humidified atmosphere and then seeded on the gradients. After 24 h of culture, cells were fixed and characterized by immunocytochemistry and scanning electron microscopy (SEM). Immunocytochemistry was performed following the above-described protocol. Tile images of the whole gradient were acquired using an inverted confocal microscope TCS SP8 (Leica Microsystems). Image analysis was performed using Fiji software.[23] To quantify CD44 expression, cells or groups of cells (region of interest) were selected in phalloidin signal (cell body), and the mean grey value of the CD44 channel of each image was determined. Morphometric parameters of individual cells were manually measured in phalloidin signal. The cell aspect ratio was determined with ImageJ, and the cell perimeter to area ratio was calculated from perimeter/area determined with ImageJ. The number of cells was determined by nucleus count.

V.2.6. Scanning Electron Microscopy (SEM).

Samples were thoroughly washed with PBS, fixed with 2.5 % glutaraldehyde (1 h, 4 °C), dehydrated by incubation in a series of ethanol solutions with increasing concentration (50 %, 70 %, 90 %, and 100 %), and dried at room temperature overnight. After mounting on the holders, samples were sputter-coated with gold (1 nm), and images were acquired by high-resolution field emission scanning electron microscope AIRIGA® (Zeiss).

V.2.7. Cells motility on the gradients.

Cells were cultured in the gradients for 6 h, the medium was removed, and the substrates were washed to remove the non-adherent cells. The adherent cells were followed for 16 h by an inverted optical microscope with incubation (37 °C, 5 % CO_2 humidified atmosphere) Axio Observer (Zeiss). Cell tracking was performed using the manual tracking of Fiji software.[23, 24] The distance between timepoints was summed (total distance traveled) and plotted against time.

V.2.8. Statistics and graphical presentation.

All experiments were performed in triplicate (n=3), analyzing at least 2 regions of interest (ROI) per gradient. Data about cellular characteristics as a function of gradient position are graphically presented with the correspondent regression line that shows the respective tendencies in cellular behavior. Data normality and homogeneity of variances were tested by the Shapiro-Wilk normality test and Levene's test for equality of variance, respectively, at $p<0.05$. Statistical differences among groups (non-treated and CD44 antibody-treated cells) were assessed by the non-parametric Mann–Whitney U test with a 95 % confidence. Data processing, graphical representation, and statistical analysis were performed using RStudio (Version 1.2.5042).

V.3. Results and Discussion

V.3.1. Preparation and characterization of the gradients.

Biomolecular gradients are essential for life and play an essential role in physiological and pathological events.[25, 26] As an example, gradients of chemotactic extracellular molecules control all fundamental cellular processes such as survival, signaling, migration, differentiation. Thus, methods that generate controlled biomolecular gradients present a significant research endeavor. While such bioinspired gradients have different applications (*e.g.*, mimics of the cellular habitat for studying cellular behavior, high-throughput platform for screening ligand expression, biosensing),[27-29] their development is challenging at different levels. From a biochemical perspective, the difficulties are associated with the demand for a stable immobilization that usually

requires biomolecule modification and can compromise its bioactivity.[30] The main obstacles from the fabrication point-of-view are related to the resolution and the gradient size, which must be compatible with the cell size and the targeted application. Usually, nanofabrication methods are applied to fabricate gradients with sufficient resolution (nanoscale), but generally, these methods apply to small substrates. Herein, we developed surface gradients in two steps (Fig. V.1). In the first step, gold nanoparticle gradients were achieved by diffusional deposition of negatively charged gold nanoparticles on positively charged aminated glass (Fig. V.1A and V.1C). In this method, a longer incubation time leads to a higher density of immobilized gold nanoparticles and allows the formation of continuous linear gradients with high reproducibility between batches (Fig. V.S3). In the second step, this gradient was functionalized with end-on thiolated HA (Fig. V.1B). The introduced modification at the reducing end of HA preserves the biofunctionality of this glycosaminoglycan, as demonstrated previously.[13, 17, 18, 21, 31] Moreover, such surface presentation of HA is biologically relevant: HA biosynthesis occurs at the cell membrane where hyaluronan synthetases add alternately UDP-glucuronic acid and UDP-N-acetyl glucosamine substrates at the reducing end of the elongating HA chain that is secreted in the pericellular space.[32] We developed a long gradient (2 cm) with a low gradient slope - properties that allow a high-throughput study of cells behavior in discrete sections (10 positions) and avoid the chemoattractive properties of HA, *i.e.*, a single cell can't sense (and respond to) the gradient but only to the local concentration of HA at the area on which the cell has adhered. Of note, after the HA functionalization, the substrates were not passivated, thus, allowing formation of a double gradient of HA and -NH_2 (Fig. V.1D) that mimics the competitive and complex cell-ECM interactions (HA-mediated *vs.* non-HA-mediated response).

We used a labeled lectin, namely wheat germ agglutinin (WGA) that is specific towards N-acetyl-D-glucosamine,[33] to confirm the biofunctionality and the resolution of the developed HA gradients (Fig. V.1D). The results showed that the developed gradients have enough resolution to screen the effect of HA density on cell behavior.

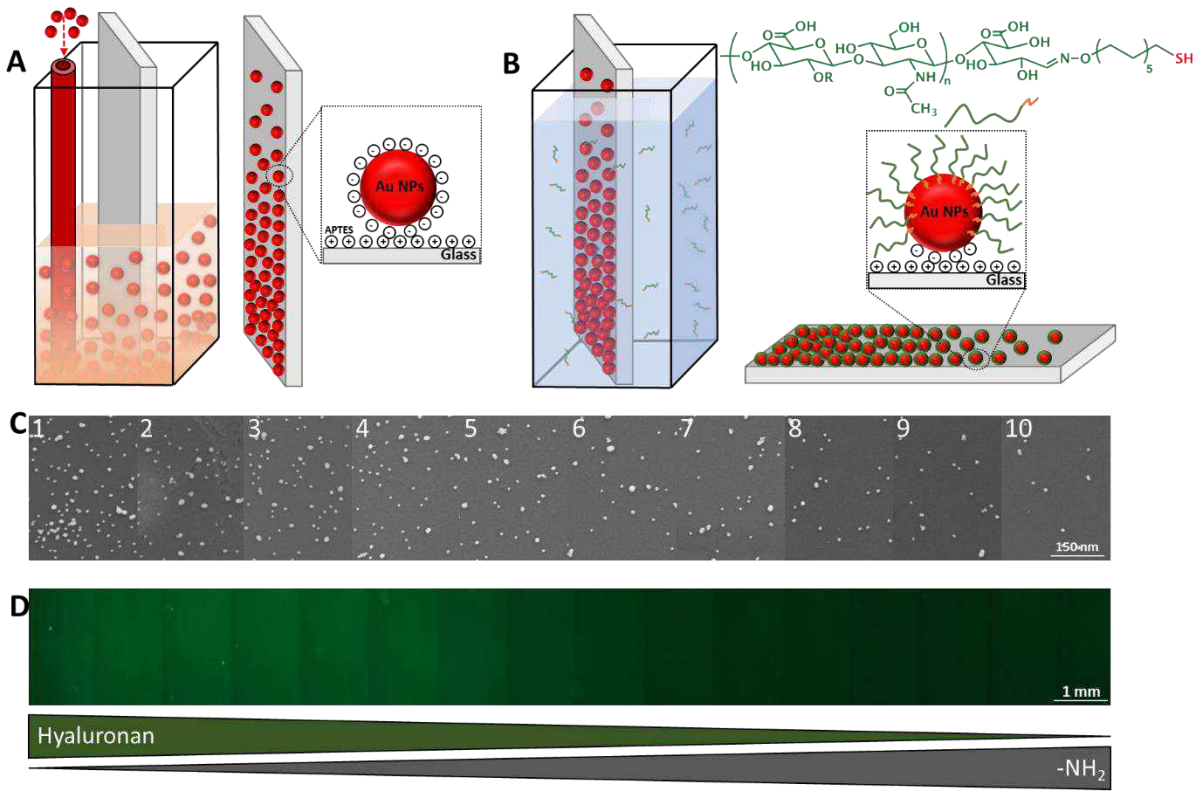

Figure V.1. Hyaluronan gradients. Schematic presentation of (A) diffusion deposition of gold nanoparticles on aminated glass and (B) functionalization of the developed gold nanoparticles gradients with end-on thiolated hyaluronan (HA) to generate the final gradient; (C) SEM images of diffusion deposited nanoparticles along the gradients at different equidistant positions; (D) Fluorescence tile image of hyaluronan stained with WGA-AlexaFluor 488 conjugate (green). For data analysis, gradients were sectioned in 10 areas, where area 1 corresponds to the bottom of the substrate, *i.e.,* longest contact with colloidal nanoparticles (highest density), and position 10 is at the top of the substrate.

V.3.2. Characterization of breast cancer cell lines.

MDA-MB-231, MDA-MB-468, and Sk-Br-3 breast cancer cell lines were chosen for this study based on previous data for their different CD44 expression and aggressiveness. Fluorescence microscopy and flow cytometry analysis (Fig. V.2) confirmed that MDA-MB-231 and MDA-MB-468 cells were CD44+, albeit mean fluorescence intensity (MFI) determined by flow cytometry showed different expression levels: MFI (MDA-MB-231) = 233 and MFI (MDA-MB-468) = 136. On the other hand, Sk-Br-3 cells were CD44– (Fig. V.2). The surface expression of CD44 is related to cancer aggressiveness and stemness: CD44+/CD24– cells are more aggressive than other phenotypes.[34, 35] In conformity with these previous reports, our flow cytometry data (Fig. V.2B)

showed that MDA-MB-231 and MDA-MB-468 cells have CD44+/CD24– phenotype (MFI CD44/CD24 was 11.41 ± 1.52 and 5.18 ± 0.11, respectively), while Sk-Br-3 cells are CD44–/CD24+ (MFI CD44/CD24 = 0.59 ± 0.12), confirming different degrees of aggressiveness.[35]

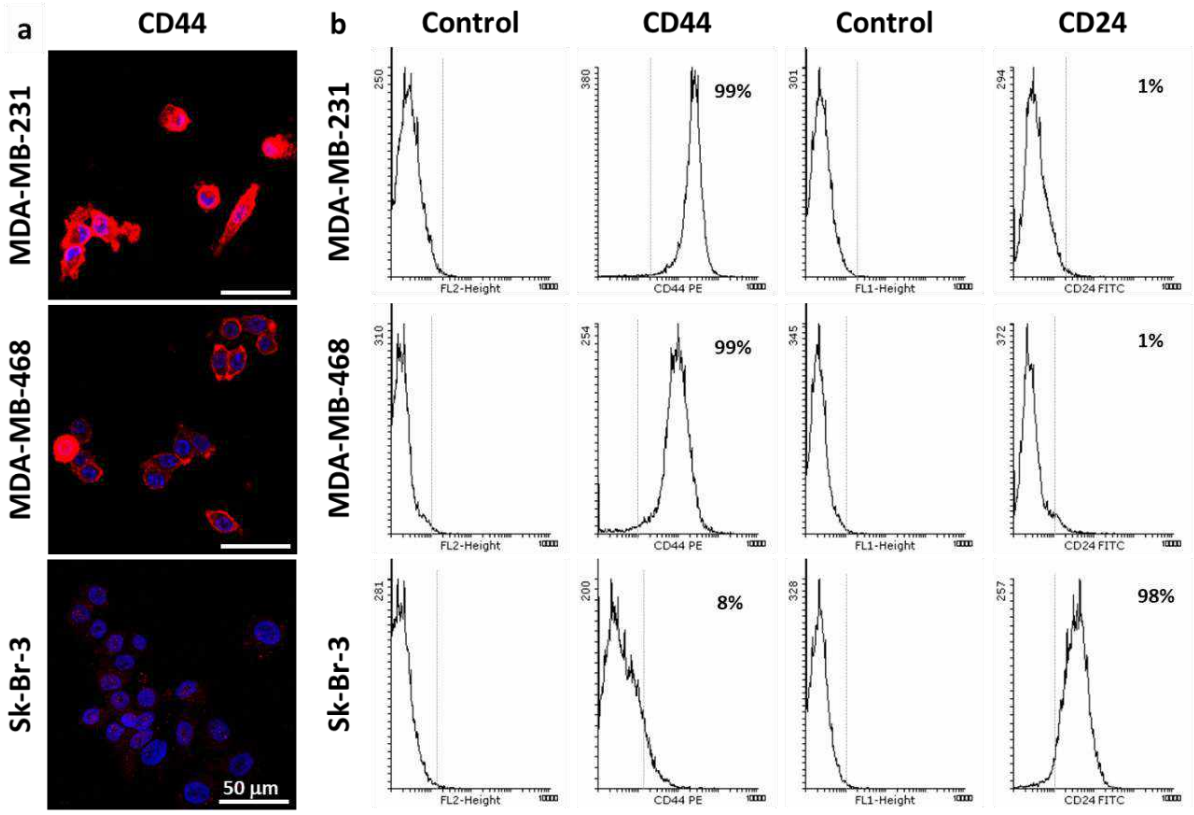

Figure V.2. Characterization of breast cancer cell lines MDA-MB-231, MDA-MB-468, and Sk-Br-3. (A) Confocal microscopy images of cells stained with DAPI (blue) for nucleus and immunostained for CD44 (red). (B) Flow cytometry results show the surface expression of CD44 and CD24 by the studied cells. Cells were cultured on tissue culture polystyrene for 72 hrs.

V.3.3. Cells response to HA density.

Cells' response to the developed gradients was analyzed in a high-throughput manner. We screened several parameters, namely cell adhesion, cell morphology, and expression of HA receptor CD44 along the gradients. We also investigated whether the observed responses were mediated by HA-CD44 recognition/interactions.

V.3.3.1. Cell adhesion on the gradients.

MDA-MB-231, MDA-MB-468, and Sk-Br-3 cells were differently distributed along the gradients (Fig. V.3). The influence of the HA density on the adhesion of MDA-MB-231 cells was evident: the number of adherent cells raised progressively along the gradient with increasing HA density, reaching maximum values at position 1, *i.e.,* at the highest HA density. In the case of Sk-Br-3 cells, the trend was opposite - fewer adherent cells were observed at high HA density (Fig. V.3B). An even distribution along the gradient was observed for MDA-MB-468 cells. To check whether this response is driven by the recognition of HA on the surface, we treated the cells with a function-blocking antibody for CD44 before seeding on the gradients.[14] This treatment changed the adhesion trend for the MDA-MB-231 cells: we observed homogeneously distributed cells along the gradient. CD44 blocking did not have such an effect on the other two cell lines that maintain their profile. These results indicated different adhesion mechanisms for the studied cell lines. The adhesion of MDA-MB-231 to the gradients is HA-dependent and mediated by CD44. Sk-Br-3 are CD44– and other receptors mediate their adhesion, most probably integrins, as the number of adherent cells increased with the augmentation of the $-NH_2$ density (opposite to HA density). Finally, the results obtained for MDA-MB-468 cells are not conclusive. While they are CD44+, the expression of this receptor on the cell surface is lower than for MDA-MB-231 cells, which might be associated with lower sensitivity to HA density, *i.e.*, CD44 mediates cell adhesion but the slope of HA gradient is not recognized by these cells.

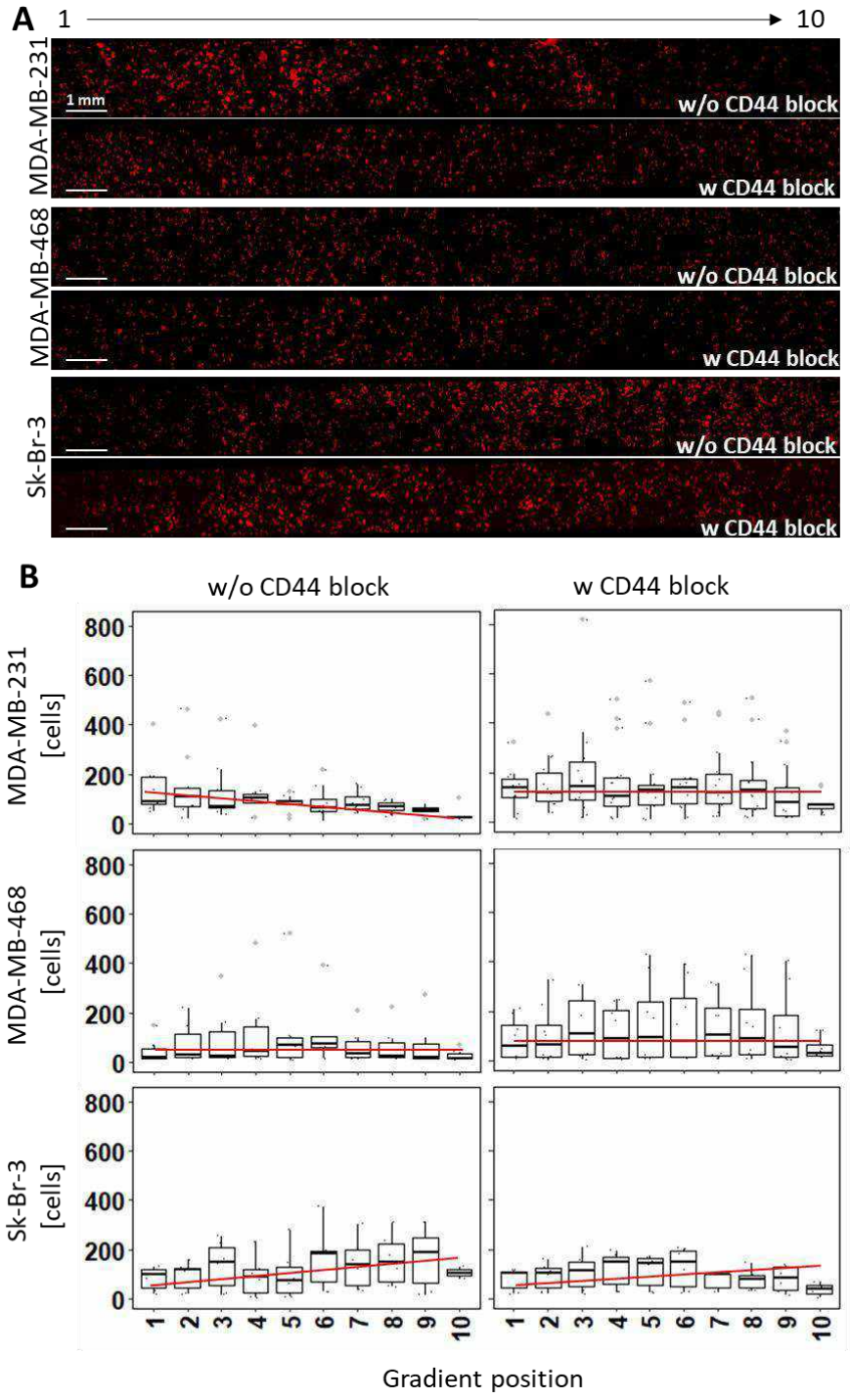

Figure V.3. Cell adhesion on gradients. (A) Representative tile images of MDA-MB-231, MDA-MB-468, and Sk-Br-3 cells cultured on HA gradients for 24 h and (B) Distribution of the adherent cells along the gradients (outliers are presented in grey). In the two experimental sets, we used cells without (w/o) and with (w) previous treatment with function-blocking antibody to CD44 (CD44 block). Cells' actin cytoskeleton was stained with phalloidin (red). In the graphs, HA density decreases from position 1 to position 10.

V.3.3.2. Expression of CD44 as a function of HA density.

In breast cancer, changes in HA metabolism are observed since the early stages: the high HA content in the pericellular space and ECM provides adhesion points and activates signaling cascades towards cell growth and proliferation, which are critical for tumorigenesis processes.[36, 37] CD44 is involved in most of these processes: it is commonly overexpressed in breast cancer, and thus, it is a therapeutic target.[8, 9] We assessed the CD44 expression by the adherent cells along the gradients (Fig. V.4). Similar CD44 expression (low and no differences along the gradient) was determined for the three studied cell lines on the control substrates - gradients without HA (Fig. V.S4). Functionalization of the gradients with HA changed dramatically the expression of CD44 by MDA-MB-231 and MDA-MB-468: a significant increase that was proportional to the HA density was observed for MDA-MB-468 cells (CD44+), while MDA-MB-231 cells (CD44++) presented similar (high) expression levels along the gradient. The response of Sk-Br-3 cells was consistent with their CD44– phenotype: they maintained a similar CD44 expression profile on the control and HA functionalized gradients. These results are consistent with previous studies reporting feedback response upon HA binding that regulates CD44 expression[12, 13] and show that this feedback depends on the HA density and cell phenotype. They also indicate aggressiveness: we observed that at high HA density (position 1 of the gradient), both MDA-MB-231 and MDA-MB-468 cells have similar high expression of CD44. This data suggests that the hijacking of the HA homeostasis at the early cancer stage and HA enrichment of the pericellular space is crucial for recruiting cells and activating regulatory genes during tumorigenesis.

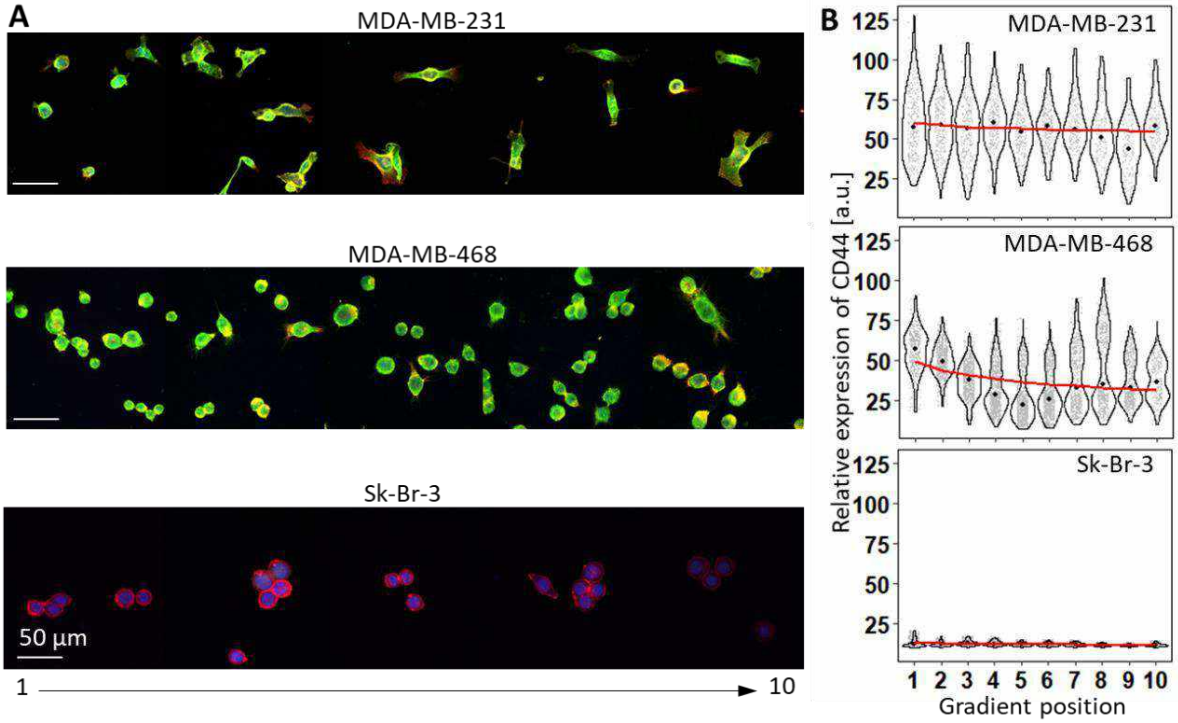

Figure V.4. Expression of CD44 by breast cancer cells adhered to the gradients. (A) Representative fluorescence images and (B) graphical presentation showing the expression of CD44 by MDA-MB-231, MDA-MB-468, and Sk-Br-3 cells along the gradient. Nuclei are represented in blue, the actin cytoskeleton in red, and CD44 in green. In the graphs, grey points represent each measurement of CD44 expression, and red dots represent the median value for each position. HA density decreases from 1 to 10. Data for control substrates (gradients without HA functionalization) are presented in Fig. V.S4.

V.3.3.3. Cell morphology.

Because CD44 is a cytoskeletal regulator that influences cell morphology upon interaction with HA[12], we also assessed morphological changes along the gradients. We determined the cell aspect ratio and cell perimeter to surface area ratio for the studied cell lines (Fig. V.5). We did not find any effect of HA density on the cells' aspect ratio (Fig. V.S4). Cell perimeter to surface area ratio can be used as an indicator for the formation of cellular protrusions, *e.g.,* lamellipodia and filopodia (Fig. V.5A).[38] This ratio was significantly different at high HA density for the studied cell lines and followed the order: MDA-MB-468 > MDA-MB-231 > Sk-Br-3 cells (Fig. V.5B).

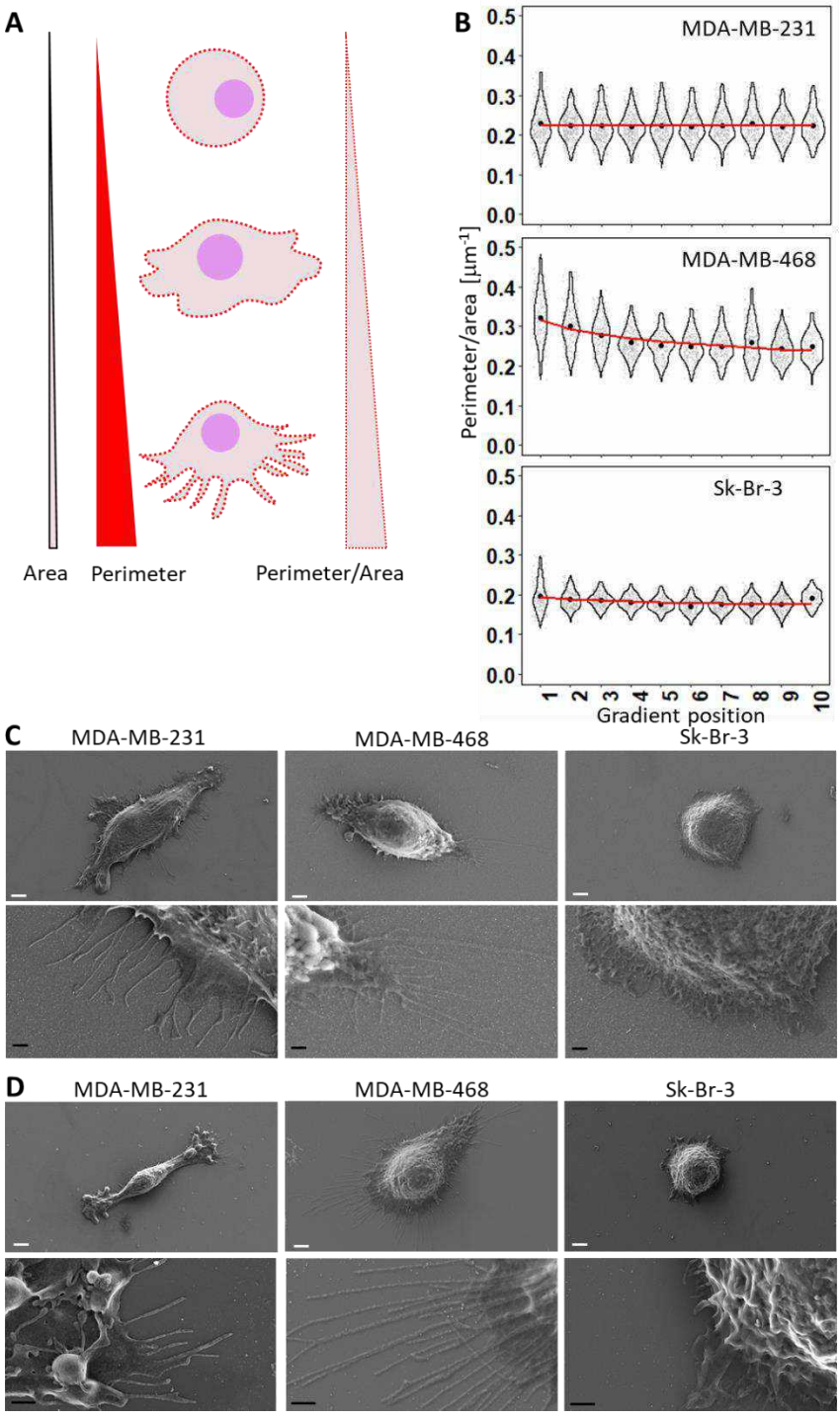

Figure V.5. Morphology of breast cancer cell lines interacting with the gradients. (A) Schematic presentation of the morphological parameters used for the analysis and (B) Cell perimeter to surface area ratio for MDA-MB-231, MDA-MB-468, and Sk-Br-3 cells cultured on the gradients for 24 h. (C, D) Representative scanning electron microscopy images of the studied cell lines at (C) the position 1 and (D) position 10 of the gradients (white scale bar = 4 μm and black scale bar = 1 μm). Data for cell aspect ratio (Fig. V.S5), cells on control substrates (Fig. V.S6), and additional SEM images (Figs. V.S7 and V.S8) are provided in V.5.

Moreover, we observed morphological changes for MDA-MB-468 cells along the HA gradient: a diminishing perimeter to surface area ratio was determined upon HA density decrease. Such a trend was not visible for MDA-MB-231 cells, despite confocal images of MDA-MB-231 showing an increase of cell spreading along HA gradient, consistent with the adhesive phenotype driven by CD44 expression. This different response of CD44+ cells to the gradients suggests that this receptor might be engaged in different signaling pathways in MDA-MB-231 and MDA-MB-468 cells. The different adhesion profiles observed for these two cell lines along the gradients confirm this hypothesis. The morphology of CD44– Sk-Br-3 cells did not change along the gradient, and the parameters were similar for HA-functionalized gradients and control (Fig. V.5B *vs.* Fig. V.S5B).

SEM images (Figs. V.5C, V.5D, and V.S8) corroborated the morphology differences between CD44+ and CD44– cells: filopodia are the main adhesion structures observed in MDA-MB-231 and MDA-MB-468 cells, while Sk-Br-3 cells interact with the surface mainly by lamellipodia and only a few short filopodia are present at the edge of the cells. Importantly, filopodia interact with HA-functionalized spots on the gradients (Fig. V.6): confocal orthogonal views of cell protrusions showed co-localization of CD44, actin, and gold for the filopodia of MDA-MB-231 and MDA-MB-468 cells. In the case of the Sk-Br-3 lamellipodia, we observed co-localization of actin and gold only. These results corroborate previous reports on the role of CD44-HA interactions in the formation and lengthening of filopodia processes, promoting cell migration.[39-42]

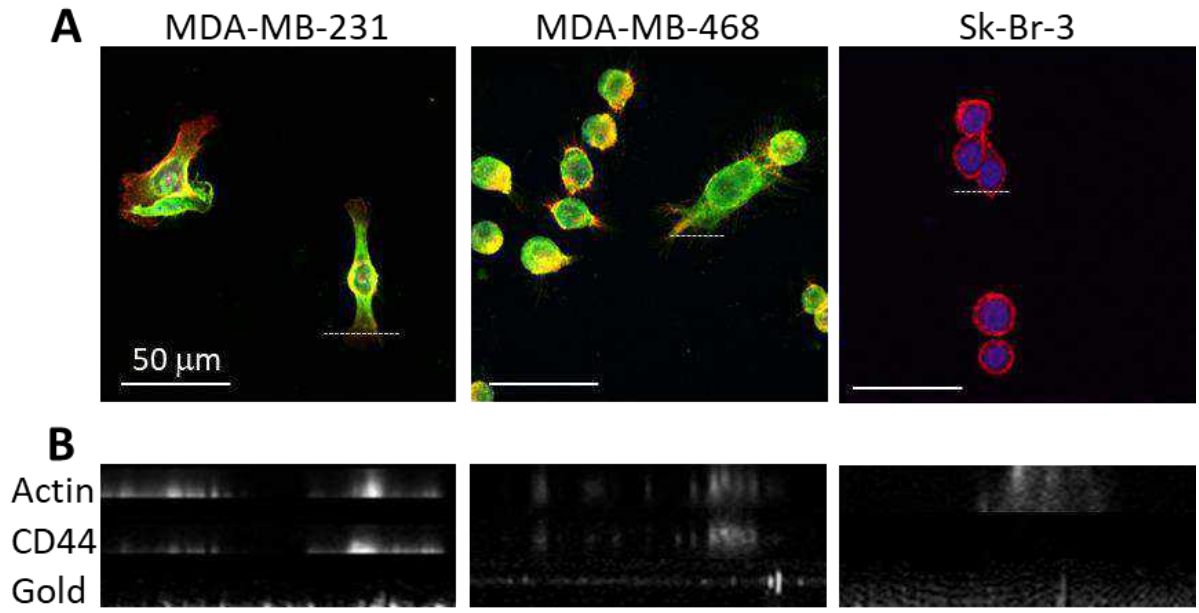

Figure V.6. Co-localization of actin (red), CD44 (green), and gold for the studied cell lines: (A) Maximum projections (z-stacks) and (B) orthogonal YZ confocal microscopy images of cell protrusions (filopodia of MDA-MB-231 and MDA-MB-468 cells, and lamellipodia of Sk-Br-3 cells). Dashed lines show analyzed sections.

V.3.3.4. Cells motility.

MDA-MB-231, MDA-MB-468, and Sk-Br-3 have different aggressive phenotypes, and thus, we have also studied the effect of HA density on cell motility (Fig. V.7). For these experiments, we cultured the cells on HA gradients for 6 h to allow cell adhesion. Then, live imaging was performed for the following 16 h to determine the total distance traveled, *i.e.*, to estimate the cell motility. We observed random cell migration for the studied cell lines, but their motility was different: significantly ($p < 0.001$) longer distance traveled was determined for MDA-MB-231 cells than for MDA-MB-468 and Sk-Br-3 cells (Fig. V.7A). Moreover, MDA-MB-231 cells showed increased motility at higher HA density, while similar values were observed for MDA-MB-468 and Sk-Br-3 cells along the HA gradient. These results agree with the performed characterization of the cell lines (Fig. V.2) and the literature that reports the following order of aggressiveness in MDA-MB-231 > MDA-MB-468 >> Sk-Br-3[13, 34, 35] and different metastatic potential for MDA-MB-231 and MDA-MB-468 (MDA-MB-231 > MDA-MB-468) upon their interaction with ECM components, including immobilized HA.[43] Moreover, CD44 blocking reduced the total traveled distance of

MDA-MB-231 cells on the gradients significantly (Fig. V.7B), confirming that CD44-HA interactions are involved in the signaling cascade of MDA-MB-231 motility. MDA-MB-468 and Sk-Br-3 cells traveled similar distances that were shorter than those measured for MDA-MB-231 and did not change along the gradients. When we blocked the CD44 in these cells, we observed no significant differences in cell motility for Sk-Br-3 cells, but in the case of MDA-MB-468, the total traveled distance shortened ($p < 0.05$) along the whole gradient (Fig. V.7B). These results showed that MDA-MB-468 cell motility is influenced by HA density, emphasizing the importance of the microenvironment and its potential influence on an aggressive phenotype.

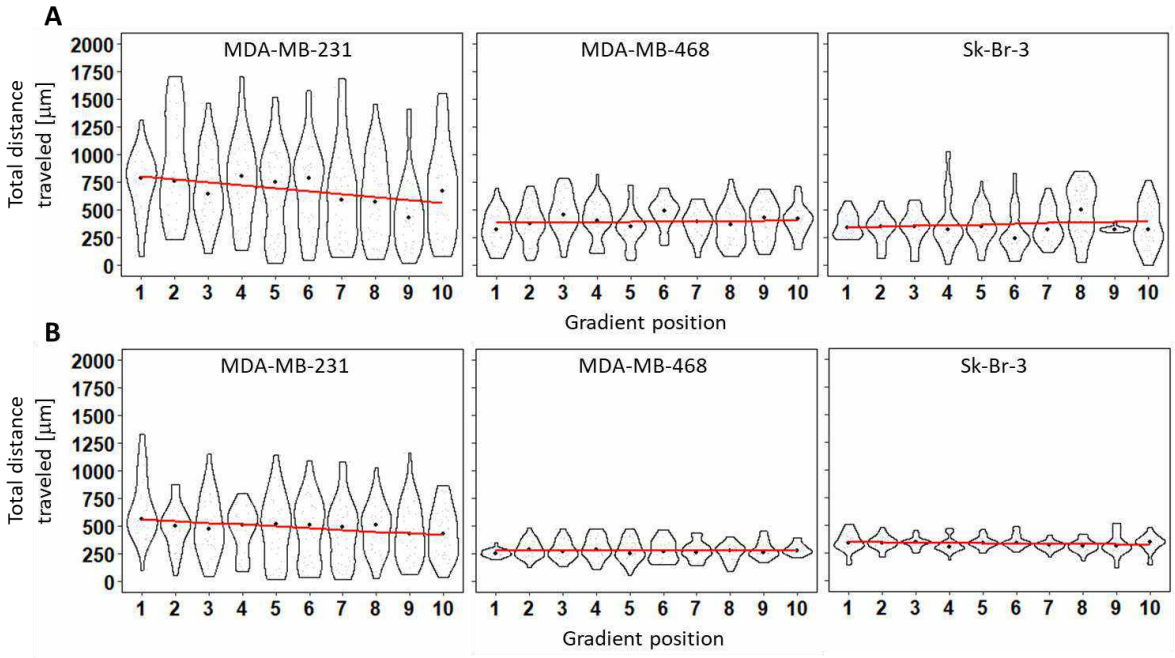

Figure V.7. Breast cancer cells motility on the gradients: (A) Total distance traveled of MDA-MB-231, MDA-MB-468, and Sk-Br-3 cells without and (B) with CD44 blocking.

V.4. Conclusions

We developed a platform that allows the presentation of HA in a biorelevant manner and in a gradient fashion and is also compatible with several high-throughput characterization methods. Our results demonstrated that this platform is a valuable tool for studying cell behavior in response to HA density. We showed that CD44-HA interactions result in different cell responses associated with cell phenotype and HA density, thus, highlighting the importance of bidirectional communication between cell traits and ECM. We observed increased cell density and motility for

MDA-MB-231 cells at higher HA density, while MDA-MB-468 cells increased their CD44 expression and changed the morphology (higher perimeter to surface area). These responses agree with the different aggressive phenotypes of these cells and suggest that HA-CD44 interactions have different roles and act as a multifunction signaling platform at different cancer stages. Treatment with function-blocking antibody to CD44 receptor inhibited the cells' response to HA density, showing the potential of the developed platform in screening possible blockers, competitors, and inhibitors of cell-HA interactions in diverse diseases.

V.5. SUPPORTING INFORMATION

Glass coverslips cleaning, modification and characterization.

Coverslips cleaning and silanization were performed as previously reported with some modifications.[44, 45] Glass coverslips (20 mm^2) were cleaned by immersion in piranha solution (3.5% H_2O_2 in 18M H_2SO_4) followed by several cycles of sonication in chloroform and Milli-Q water. The cleaned coverslips were finally dried under a nitrogen stream. Silanization of coverslips was achieved by overnight incubation in 1% APTES solution in acetone under orbital shaking. To remove unbounded APTES, the coverslips were sonicated in acetone. Curing was performed at 110 °C for 1 h under vacuum. Surfaces were characterized by atomic force microscopy (AFM) and contact angle measurements. AFM images were recorded using a NanoWizard 3 (JPK Instruments) in a non-contact mode in air and silicon probes ACTA (AFM) with a radius < 10 nm, spring constant of 40 N/m, and resonance frequency of 300 kHz, at a scan speed of 1 Hz with 256 x 256 pixels resolution. Water contact angles were measured on OCA15+ goniometer (Dataphysics) using the sessile drop method with Milli-Q water (3 μL). Measurements were performed in triplicate on 3 different substrates at room temperature.

Supplementary data

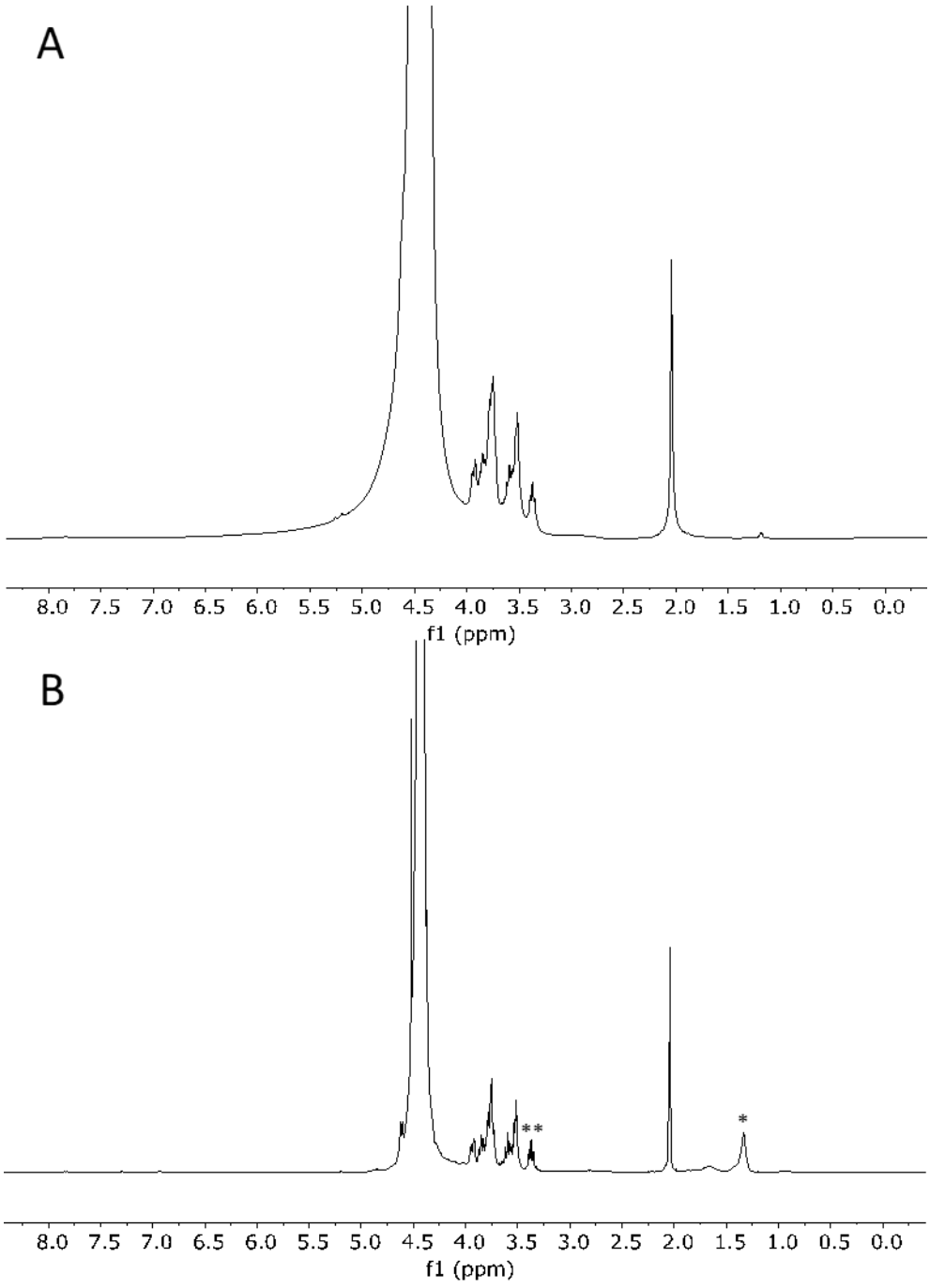

Figure V.S1. ^{1}H NMR spectra (60 ºC in D_2O) of (A) hyaluronan (HA) and (B) its thiolated derivative obtained by conjugation of alkanethiol at the reducing end ($HAC_{11}SH$). The degree of modification was calculated from the ratio of the peaks at δ 1.25 ppm (aliphatic protons) and δ 3.4 ppm (glucuronic acid protons) and was found to be 98 %.

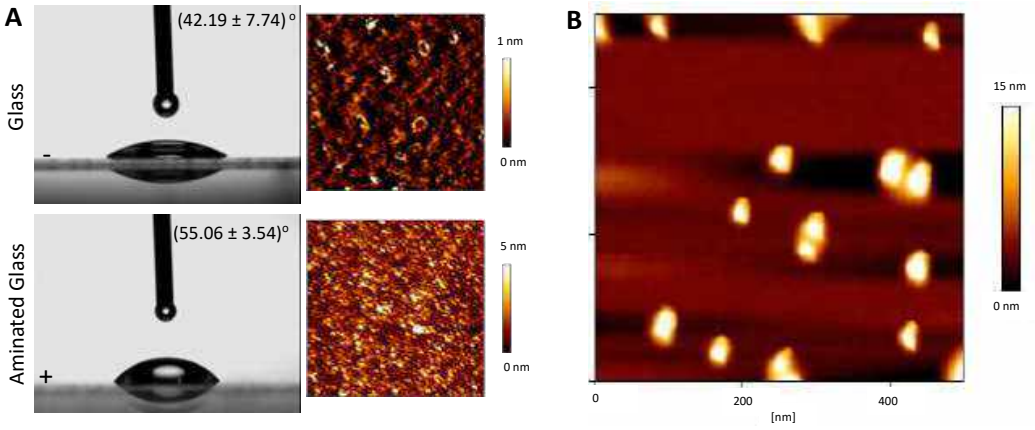

Figure V.S2. Characterization of the materials used for the preparation of gold nanoparticles gradients: (A) water contact angle and AFM images of unmodified and aminated glass substrates; (B) AFM images of gold nanoparticles synthesized by Turkevich method.

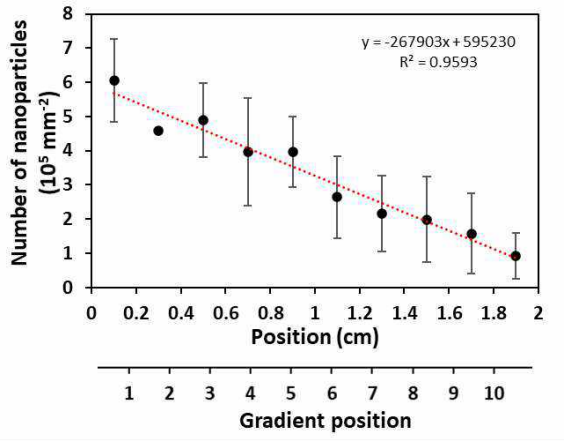

Figure V.S3. Quantification of gold nanoparticles density at equidistant positions in the surface. Average ± sd of several independent surfaces and different ROIs per each position.

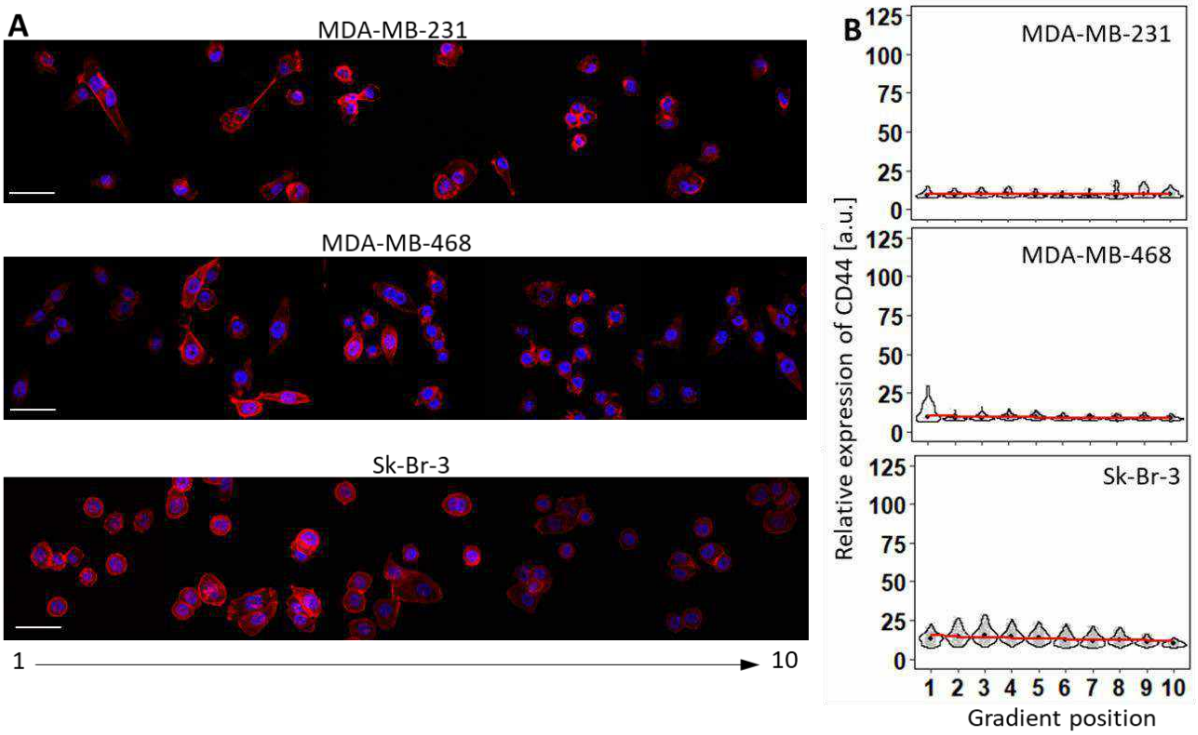

Figure V.S4. Expression of CD44 by breast cancer cells adhered to control gradients (without HA functionalization): (A) Representative fluorescence images (scale bar = 50 µm) and (B) Quantification of the expression of CD44 (green) by MDA-MB-231, MDA-MB-468, and Sk-Br-3 cells along the gradient. HA density decreases from 1 to 10. Nuclei were counterstained with DAPI (blue), and the actin cytoskeleton was counterstained with phalloidin (red).

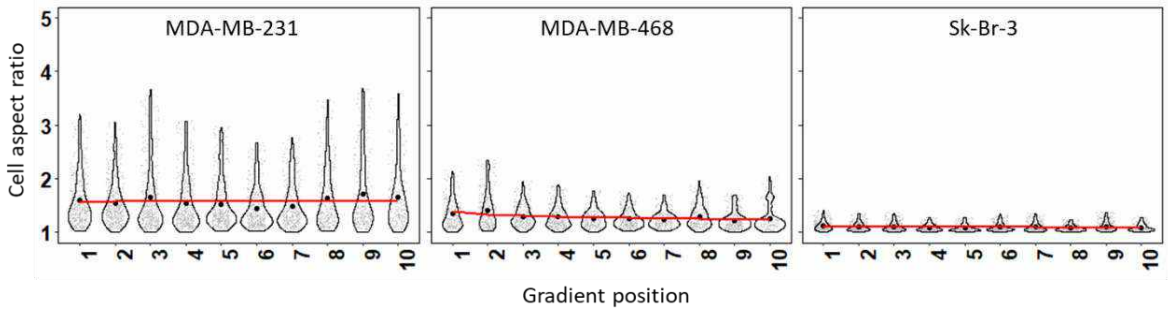

Figure V.S5. Cell aspect ratio of MDA-MB-231, MDA-MB-468, and Sk-Br-3 cells cultured on the gradients (with HA functionalization).

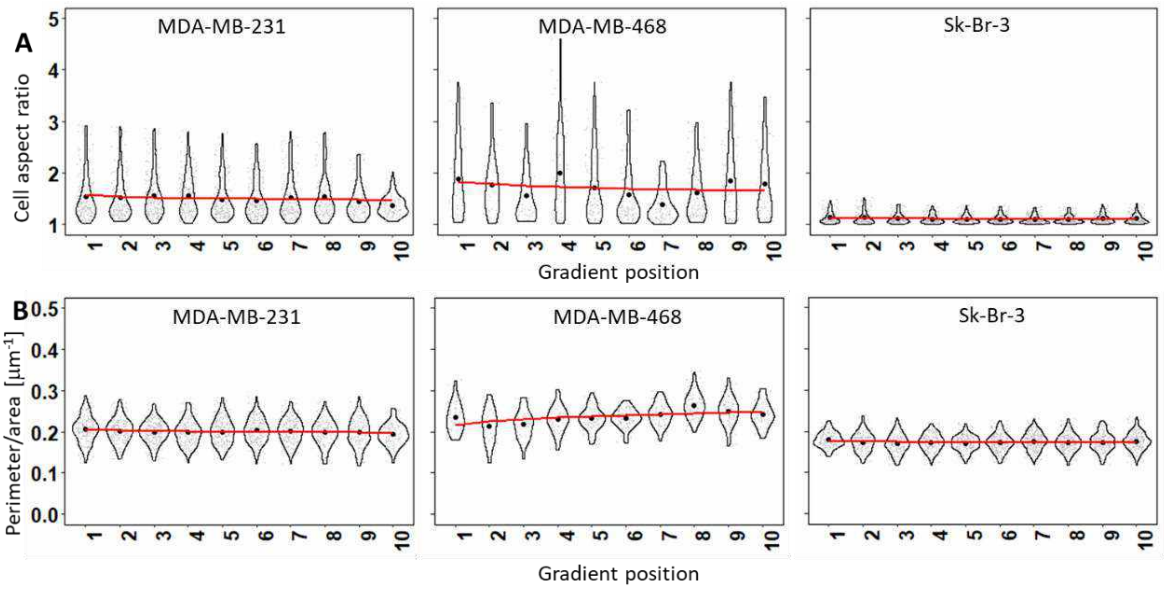

Figure V.S6. Morphometric data for MDA-MB-231, MDA-MB-468, and Sk-Br-3 cells cultured on control gradients (without HA functionalization): (A) Cell aspect ratio and (B) Perimeter to surface area ratio for these cells.

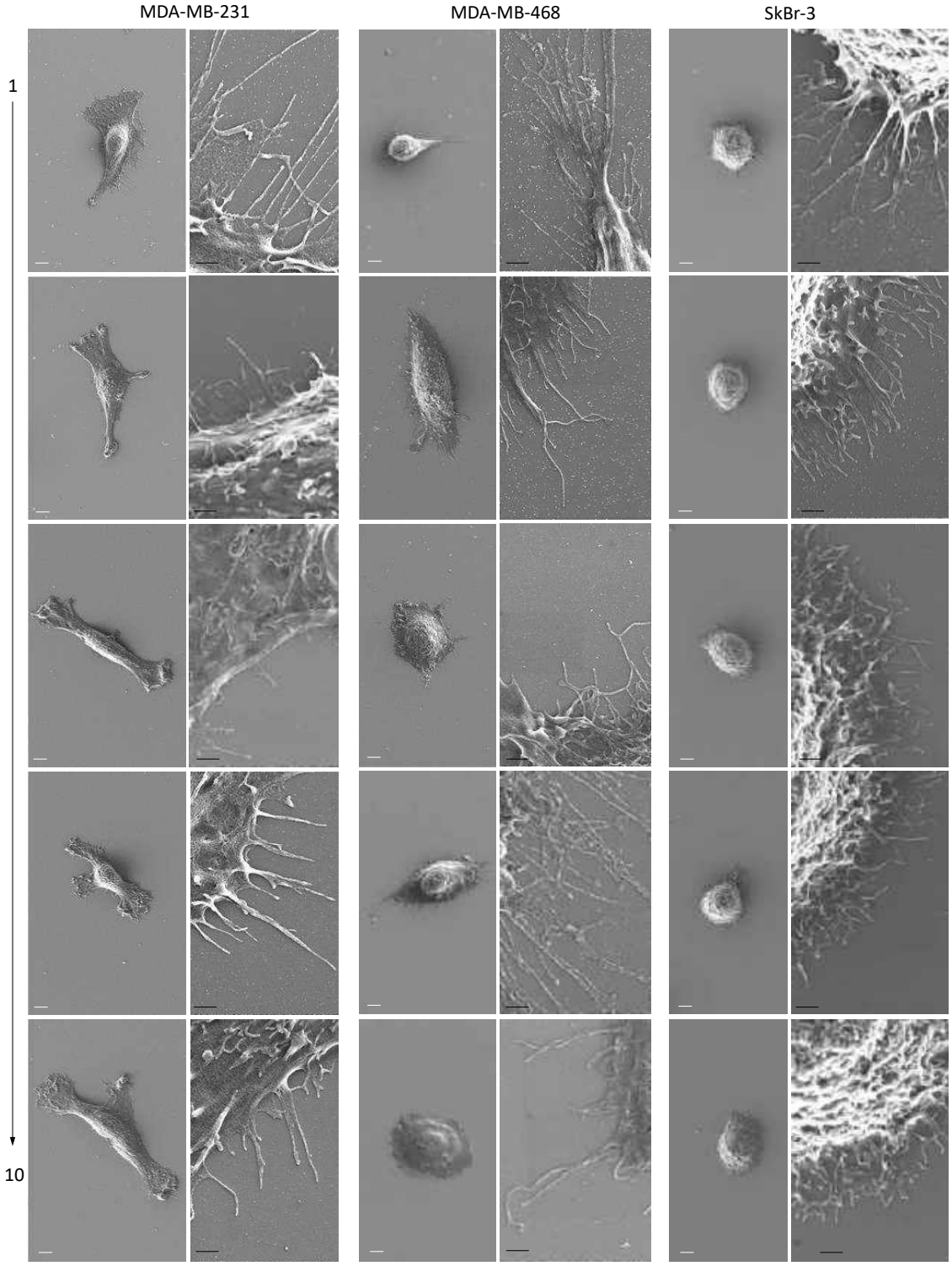

Figure V.S7. SEM images of MDA-MB-231, MDA-MB-468, and Sk-Br-3 cells adhered at different positions along with the control (without HA) gradient (white scale bar = 4 μm and black scale bar = 1 μm).

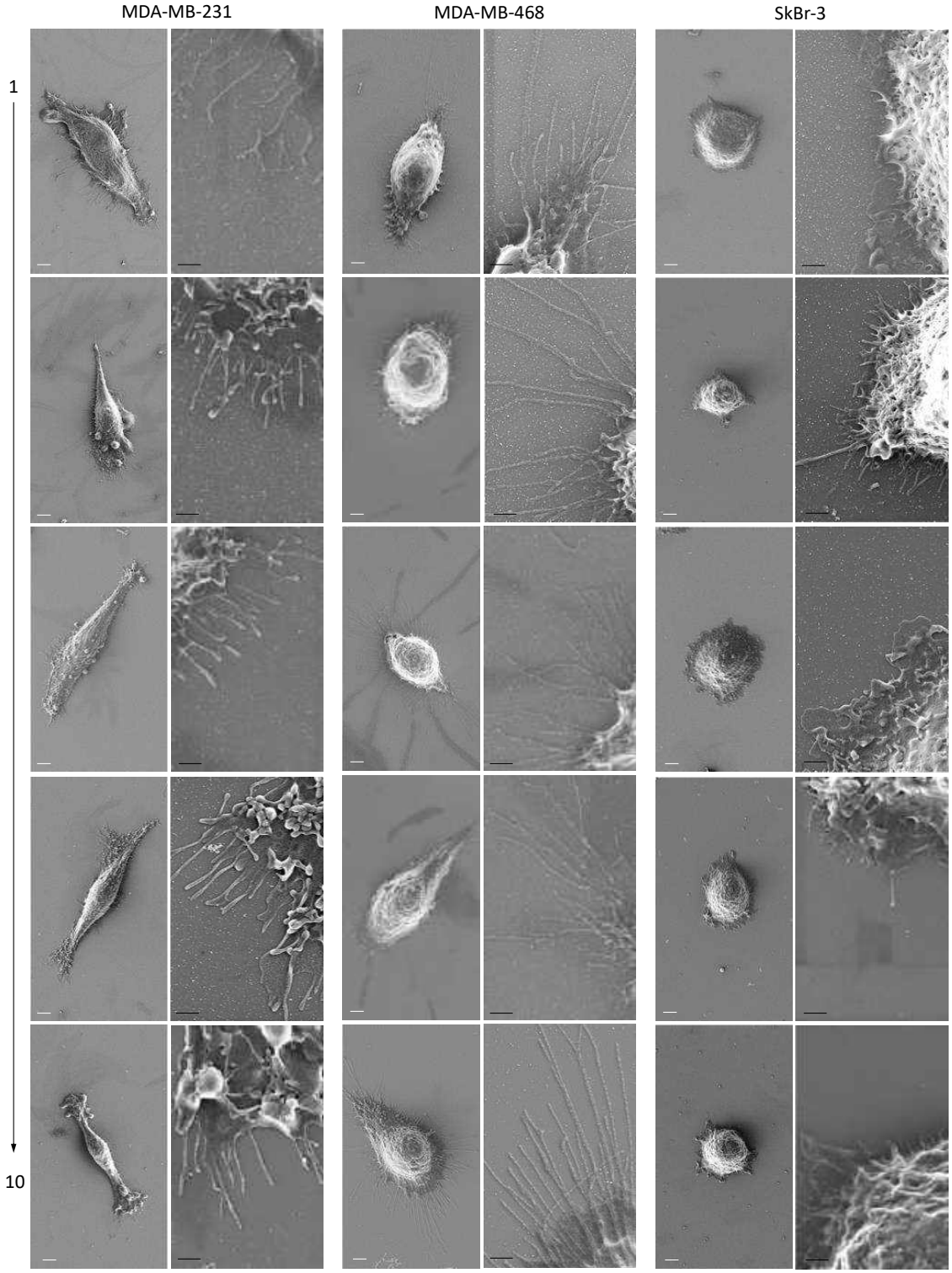

Figure V.S8. SEM images of MDA-MB-231, MDA-MB-468, and Sk-Br-3 cells adhered at different positions along the hyaluronan gradient (white scale bar = 4 μm and black scale bar = 1 μm).

V.6. REFERENCES

1. Cox, T.R., *The matrix in cancer.* Nature Reviews Cancer, 2021. **21**(4): p. 217-238.
2. Winkler, J., et al., *Concepts of extracellular matrix remodelling in tumour progression and metastasis.* Nature Communications, 2020. **11**(1).
3. Oudin, M.J. and V.M. Weaver, *Physical and Chemical Gradients in the Tumor Microenvironment Regulate Tumor Cell Invasion, Migration, and Metastasis.* Targeting Cancer, Vol 81, 2016, 2016. **81**: p. 189-205.
4. Caon, I., et al., *Revisiting the hallmarks of cancer: The role of hyaluronan.* Seminars in Cancer Biology, 2020. **62**: p. 9-19.
5. Toole, B.P., *Hyaluronan: From extracellular glue to pericellular cue.* Nature Reviews Cancer, 2004. **4**(7): p. 528-539.
6. Turley, E.A., D.K. Wood, and J.B. McCarthy, *Carcinoma cell hyaluronan as a "portable" cancerized prometastatic microenvironment.* Cancer research, 2016. **76**(9): p. 2507-2512.
7. Heldin, P., et al., *Deregulation of hyaluronan synthesis, degradation and binding promotes breast cancer.* Journal of Biochemistry, 2013. **154**(5): p. 395-408.
8. Auvinen, P., et al., *Hyaluronan in peritumoral stroma and malignant cells associates with breast cancer spreading and predicts survival.* American Journal of Pathology, 2000. **156**(2): p. 529-536.
9. Liu, X., et al., *Homophilic CD44 interactions mediate tumor cell aggregation and polyclonal metastasis in patient-derived breast cancer models.* Cancer discovery, 2019. **9**(1): p. 96-113.
10. Chen, C., et al., *The biology and role of CD44 in cancer progression: therapeutic implications.* Journal of hematology & oncology, 2018. **11**(1): p. 64.
11. Bourguignon, L.Y., M. Shiina, and J.-J. Li, *Hyaluronan–CD44 interaction promotes oncogenic signaling, microRNA functions, chemoresistance, and radiation resistance in cancer stem cells leading to tumor progression*, in *Advances in cancer research*. 2014, Elsevier. p. 255-275.
12. Zoller, M., *CD44: can a cancer-initiating cell profit from an abundantly expressed molecule?* Nature Reviews Cancer, 2011. **11**(4): p. 254-267.
13. Carvalho, A.M., et al., *Co-localization and crosstalk between CD44 and RHAMM depend on hyaluronan presentation.* Acta Biomaterialia, 2021. **119**: p. 114-124.
14. Amorim, S., et al., *Molecular weight of surface immobilized hyaluronic acid influences CD44-mediated binding of gastric cancer cells.* Scientific Reports, 2018. **8**.
15. Sapudom, J., et al., *Molecular weight specific impact of soluble and immobilized hyaluronan on CD44 expressing melanoma cells in 3D collagen matrices.* Acta Biomaterialia, 2017. **50**: p. 259-270.
16. Herrera-Gayol, A. and S. Jothy, *Effects of hyaluronan on the invasive properties of human breast cancer cells in vitro.* International journal of experimental pathology, 2001. **82**(3): p. 193-200.
17. Altgärde, N., et al., *Probing the biofunctionality of biotinylated hyaluronan and chondroitin sulfate by hyaluronidase degradation and aggrecan interaction.* Acta Biomaterialia, 2013. **9**(9): p. 8158-8166.
18. Wolny, P.M., et al., *Analysis of CD44-Hyaluronan Interactions in an Artificial Membrane System INSIGHTS INTO THE DISTINCT BINDING PROPERTIES OF HIGH AND LOW MOLECULAR WEIGHT HYALURONAN.* Journal of Biological Chemistry, 2010. **285**(39): p. 30170-30180.
19. Boehm, H., et al., *Mapping the mechanics and macromolecular organization of hyaluronan-rich cell coats.* Soft Matter, 2009. **5**(21): p. 4331-4337.
20. Tzircotis, G., R.F. Thorne, and C.M. Isacke, *Chemotaxis towards hyaluronan is dependent on CD44 expression and modulated by cell type variation in CD44-hyaluronan binding.* Journal of Cell Science, 2005. **118**(21): p. 5119.
21. Carvalho, A.M., et al., *Redox-Responsive micellar nanoparticles from glycosaminoglycans for CD44 targeted drug delivery.* Biomacromolecules, 2018. **19**(7): p. 2991-2999.
22. Kimling, J., et al., *Turkevich method for gold nanoparticle synthesis revisited.* Journal of Physical Chemistry B, 2006. **110**(32): p. 15700-15707.
23. Schindelin, J., et al., *Fiji: an open-source platform for biological-image analysis.* Nature Methods, 2012. **9**(7): p. 676-682.
24. Meijering, E., O. Dzyubachyk, and I. Smal, *Methods for cell and particle tracking*, in *Methods in enzymology*. 2012, Elsevier. p. 183-200.

25. Ellison, D., et al., *Cell–cell communication enhances the capacity of cell ensembles to sense shallow gradients during morphogenesis.* Proceedings of the National Academy of Sciences, 2016. **113**(6): p. E679-E688.
26. Gurdon, J., S. Dyson, and D. St Johnston, *Cells' perception of position in a concentration gradient.* Cell, 1998. **95**(2): p. 159-162.
27. Morgenthaler, S., C. Zink, and N.D. Spencer, *Surface-chemical and-morphological gradients.* Soft Matter, 2008. **4**(3): p. 419-434.
28. Riepl, M., et al., *Molecular gradients: an efficient approach for optimizing the surface properties of biomaterials and biochips.* Langmuir, 2005. **21**(3): p. 1042-1050.
29. Lagunas, A., E. Martínez, and J. Samitier, *Surface-bound molecular gradients for the high-throughput screening of cell responses.* Frontiers in bioengineering and biotechnology, 2015. **3**: p. 132.
30. Pashkuleva, I. and R.L. Reis, *Sugars: burden or biomaterials of the future?* Journal of Materials Chemistry, 2010. **20**(40): p. 8803-8818.
31. Tanaka, N., et al., *Self-assembly immobilization of hyaluronan thiosemicarbazone on a gold surface for cell culture applications.* Carbohydrate polymers, 2010. **82**(1): p. 100-105.
32. Tammi, R.H., et al., *Transcriptional and post-translational regulation of hyaluronan synthesis.* The FEBS journal, 2011. **278**(9): p. 1419-1428.
33. MONSIGNY, M., et al., *Sugar-lectin interactions: how does wheat-germ agglutinin bind sialoglycoconjugates?* European journal of biochemistry, 1980. **104**(1): p. 147-153.
34. Jaggupilli, A. and E. Elkord, *Significance of CD44 and CD24 as cancer stem cell markers: an enduring ambiguity.* Clinical and Developmental Immunology, 2012. **2012**.
35. Li, W., et al., *Unraveling the roles of CD44/CD24 and ALDH1 as cancer stem cell markers in tumorigenesis and metastasis.* Scientific reports, 2017. **7**(1): p. 1-15.
36. Caon, I., et al. *Revisiting the hallmarks of cancer: The role of hyaluronan*. in *Seminars in cancer biology*. 2020. Elsevier.
37. Liu, M., C. Tolg, and E. Turley, *Dissecting the dual nature of hyaluronan in the tumor microenvironment.* Frontiers in immunology, 2019. **10**.
38. Mejillano, M.R., et al., *Lamellipodial versus filopodial mode of the actin nanomachinery: pivotal role of the filament barbed end.* Cell, 2004. **118**(3): p. 363-373.
39. Pusch, A., et al., *CD44 and hyaluronan promote invasive growth of B35 neuroblastoma cells into the brain.* Biochimica et Biophysica Acta (BBA)-Molecular Cell Research, 2010. **1803**(2): p. 261-274.
40. Sugahara, K.N., et al., *Hyaluronan oligosaccharides induce CD44 cleavage and promote cell migration in CD44-expressing tumor cells.* Journal of Biological Chemistry, 2003. **278**(34): p. 32259-32265.
41. Härkönen, K., et al., *CD44s Assembles Hyaluronan Coat on Filopodia and Extracellular Vesicles and Induces Tumorigenicity of MKN74 Gastric Carcinoma Cells.* Cells, 2019. **8**(3): p. 276.
42. Twarock, S., et al., *Hyaluronan stabilizes focal adhesions, filopodia, and the proliferative phenotype in esophageal squamous carcinoma cells.* Journal of Biological Chemistry, 2010. **285**(30): p. 23276-23284.
43. Köwitsch, A., A. Chhalotre, and T.J.T.I.j.o.a.o. Groth, *Effect of thiolated glycosaminoglycans on the behavior of breast cancer cells: toward the development of in vitro models of cancer.* 2017. **40**(1): p. 31-39.
44. Karrasch, S., et al., *Covalent binding of biological samples to solid supports for scanning probe microscopy in buffer solution.* Biophysical journal, 1993. **65**(6): p. 2437-2446.
45. Labit, H., et al., *A simple and optimized method of producing silanized surfaces for FISH and replication mapping on combed DNA fibers.* BioTechniques, 2008. **45**(6): p. 649-658.

CHAPTER VI

HYALURONAN BRUSH-LIKE COPOLYMERS PROMOTE CD44 DECLUSTERING IN BREAST CANCER CELLS

HYALURONAN BRUSH-LIKE COPOLYMERS PROMOTE CD44 DECLUSTERING IN BREAST CANCER CELLS

Abstract

We report on the synthesis of hyaluronan (HA) brush-like copolymers and their application as antagonists of tumorigenic CD44-HA interactions. HA (5 kDa, *ca.* 24 saccharides) was grafted on 2-hydroxyethyl methacrylate (HEMA) by end-on oxime ligation. The obtained copolymers were compared with low and high molecular weight HA in terms of hydrolysis kinetics in the presence of hyaluronidase (isothermal titration calorimetry) and interactions with CD44 (surface plasmon resonance). The results evidenced that the high molecular weight HA and HA-g-HEMA have a much higher affinity to CD44 than low molecular weight HA. Additionally, slower enzymatic degradation was observed for the copolymer, which makes it an excellent candidate for active targeting tumorigenic CD44-HA interactions. We, therefore, investigated the effect of the copolymers on cancer cell lines with different expression of CD44 and observed an efficient declustering of CD44 that is usually associated with reduction of metastasis and drug resistance.

This chapter is based on the following publication:

Carvalho, Ana M.; Valcarcel, Jesus; Gomes, Marisa, Vásquez, José António; Reis, Rui L.; Novoa-Carballal; Pashkuleva, Iva: "Hyaluronan brush-like copolymers promote CD44 declustering in breast cancer cells"; submitted

VI.1. INTRODUCTION

Hyaluronan (HA) is a linear, non-sulfated glycosaminoglycan (GAG) composed of a repeating disaccharide β(1,4)-D-glucuronic acid-β(1,3)-N-acetyl-D-glucosamine (Fig. VI.1A).[1, 2] It is synthesized at the cell membrane by HA synthases and continually secreted in the pericellular and extracellular space as a high molecular weight polymer (HMW, above 1000 kDa, Fig. VI.1B (**1**)). These long chains are then fragmented to low molecular weight HA (LMW, 1 to 500 kDa, Fig. VI.1B (**2**)) by the action of hyaluronidases (Hases) and reactive oxygen and nitrogen species.[2, 3]

The wide variety of HA sizes is related to the diverse biological functions of this GAG.[1-4] In cancer, for example, HA metabolism and catabolism are commonly deregulated, leading to the accumulation of either HMW or LMW forms within the tumor microenvironment.[1, 2, 5-7] HMW HAs form a functional pericellular coat by organization and clustering of several extracellular and membrane proteins (including CD44, Fig. VI.1C), growth factors, and cytokines via multivalent interactions.[1, 2, 8, 9] This coat provides sustained activation of anti-apoptotic, pro-invasion, and migration signaling pathways that facilitate the intravasation, protection against anoikis during circulation, and contribute to ectopic tissue colonization.[1, 2, 9-12] It also promotes the translocation of proteins and monocarboxylate transporters to the cell membrane that increase multidrug resistance and cancer cell survival.[13-15] On the other hand, LMW HA fragments can attenuate the effects of HMW HA by competitive binding to the main HA receptor CD44: binding of LMW HA to CD44 disrupts the CD44 clusters that are formed in the presence of HMW HA (Fig. VI.1C). This process, known as CD44 declustering, leads to inhibition of pro-tumorigenic signaling responses.[1, 2, 16, 17]

HA oligosaccharides (6 to 15 saccharides) have been used to reduce the aggressiveness and metastatic potential of tumor cells and augment the responsiveness to the currently used chemotherapies.[18, 19] The therapeutic use of HA oligosaccharides, however, has some drawbacks: several studies have reported that these fragments can also activate pathways towards cell migration, inflammation, and proliferation-related with the metastasis, as well as challenging targeted delivery *in vivo* given the oligosaccharides susceptibility to degradation by the overexpressed Hases to shorter fragments that do not bind CD44.[20, 21]

Thus, several other strategies that target the interactions between HMW HA/CD44 and CD44 declustering have been explored, such as the addition of soluble CD44[22] or peptides with HA-binding motifs[23] to bind the endogenous HMW HA; blocking cancer-specific CD44 variants (CD44v) with antibodies[24, 25] or function inhibitory peptides;[26-30] and deletion of CD44v using siRNA/shRNA.[31] Herein, we propose an alternative simple and cost-effective strategy that uses a brush-like glycopolymer of HA (Fig. VI.1B, **3**). This copolymer has several LMW HA branches that bind CD44 in a multivalent fashion, thus, ensuring high affinity to this receptor (Fig. VI.1C). Its interactions with CD44 are, however, different from the HMW HA-CD44 binding as they do not induce CD44 clustering. Moreover, when used in a competitive assay with endogenous HA, the copolymer induced CD44 declustering.

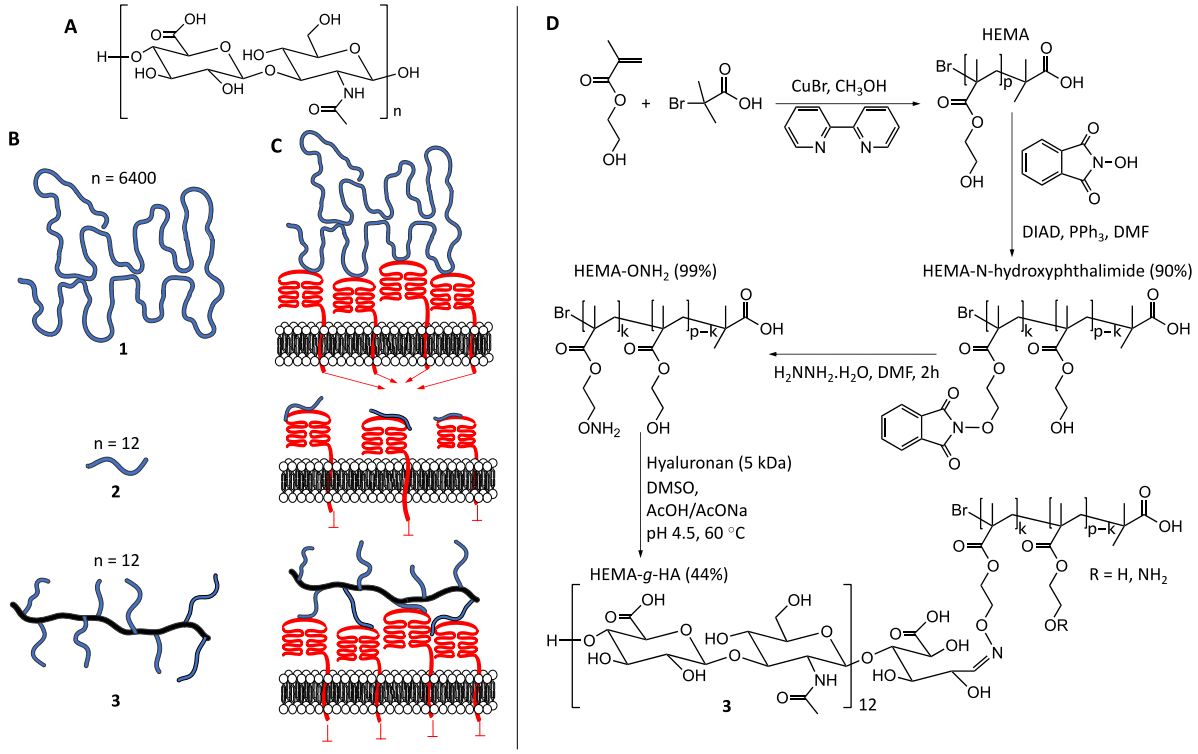

Figure VI.1. Schematic presentation of the polymers used in this study and their interactions with CD44 receptors: (A) Chemical structure of the repeating disaccharide unit of hyaluronan (HA); (B) Cartoon representation of high molecular weight HA (1, 1.35 MDa), low molecular weight HA (2, 4.8 kDa), and HA-brush like copolymers HEMA-g-HA (3, each HA branch is 4.8 kDa); (C) their mode of binding to CD44 receptors and (D) synthetic pathway used for the preparation of hyaluronan brush-like copolymers (3, HA-g-HEMA).

VI.2. MATERIALS AND METHODS

VI.2.1. Materials.

All reagents were purchased from Sigma-Aldrich if not specified. Aniline was purified by distillation under a vacuum. The other reagents were used without further purification. Sodium hyaluronate (HA, average molecular weight 1.35 MDa (**1**) and of 4.8 kDa (**2**)) was obtained from Lifecore Biomedical LLC (USA). The antibodies used in this study were monoclonal antibody to CD44 – Ascites (Acris), AlexaFluor® 594 donkey anti-mouse IgG1 (H+L). We used 4′,6-diamidino-2-phenylindole (DAPI, Biotium) and fluorescein isothiocyanate labeled phalloidin (phalloidin-FITC). Ultrafiltration membranes (Millipore) from regenerated cellulose with cut-offs of 3 and 30 kDa were used.

VI.2.2. Polymerization of 2-hydroxyethylmethacrylate (HEMA).

We used atom transfer radical polymerization with an alkyl bromoinitiator and CuBr/ 2,2´-bipyridine as a catalyst.[32] HEMA (99%, Aldrich) was passed through a plastic syringe filled with basic alumina to remove the inhibitor. A round bottom flask was charged with 2-bromo-2-methyl propionic acid (0.12 g, 1 eq.), HEMA (20 g, 220 eq.), 2,2´-bipyridine (1.1 g, 10 eq.), and 5 mL of methanol. The mixture was degassed with N_2 stream and CuBr (0.5 g, 5 eq.) was added into the reaction system under N_2. Next, the polymerization was performed at 40 °C for 24 h under magnetic stirring. The reaction flask was opened and bubbled with air to stop the polymerization. The crude reaction product was dissolved in methylene chloride, the solution passed through a column with neutral aluminum oxide to remove the copper catalyst, and dialyzed (Mw cut off 12 kDa, cellulose) against ethanol to remove the excess of the monomer. After 7 days of dialysis, water was added, ethanol evaporated under vacuum, and the polymer was recovered by lyophilization and analyzed by NMR (d-DMSO) and GPC.

VI.2.3. Synthesis of HEMA-ONH_2.

Poly-HEMA (1 eq.), N-hydroxyphthalimide (N-Pht, from 0.5 to 1.2 eq. in respect to OH of HEMA to obtain different degrees of substitution) and triphenylphosphine (same eq. as N-Pht) were mixed

in dried DMF (ca 20 g/L mL of HEMA) under N_2 atmosphere. To this mixture diisopropyl azodicarboxylate (same eq. as N-Pht) was added dropwise (color change to red). The reaction was stirred at room temperature (RT) for 24 h. The product was purified by ultrafiltration (cut off 5 kDa) in DMF. An excess of water was added and freeze-drying was performed. The obtained products were analyzed by NMR. The degree of substitution (DS) was determined by integrating the peaks corresponding to the phthalimide substituted -OH groups and was found to be 10, 25, 50, 60, 80, and 100 %. The phthalimide group was cleaved by adding hydrazine hydrate (3 eq. per phthalimide group) in DMF, leading to the deprotected aminooxy group. After 2 h, the product was diluted in water and freeze-dried under a vacuum. The cleavage was confirmed by NMR. The crude product was used in the next step without further purification or alternatively ultra-filtered in DMF (details below) with a cellulose membrane (cut off 5 kDa).

VI.2.4. Synthesis of HEMA-*g*-HA (3).

The reaction conditions (excess of HA, co-solvent ratio, reaction time, temperature, and catalyst) were optimized for the oxime condensation between HEMA-ONH_2 and LMW HA (**2**) (Table VI.S1 and VI.5). The crude HEMA-ONH_2 and the respective amount of HA were mixed in an acetate buffer (AcOH /AcONa (0.078 M AcOH/0.0625 AcONa; pH 4.5) and DMSO at different ratios. The reaction mixture was stirred at 45 or 60 °C. Then 10 to 80 eq. of aniline (with respect to the HA) were added to the mixture. Aliquots were taken every 24 h along 7 days and analyzed by GPC. The product from the reactions with the best yields was freeze-dried and ultra-filtered with a cellulose membrane (cut off 30 kDa).

VI.2.8. Isothermal titration calorimetry (ITC).

Single-injection ITC kinetics measurements were performed on MicroCal PEAQ-ITC (Malvern, UK). In a single injection ITC experiment, the total heat measured is proportional to the apparent enthalpy (ΔH_{app}) and the number of moles of generated product. The reaction rate can be related to the amount of heat generated over time. From the derived Michaelis–Menten plots, the affinity for the substrate (K_M), turnover rate (K_{CAT}), and catalytic efficiency (K_{EFF}) values can be obtained from Equation VI.1.

Equation VI.1: $$K_{EFF} = \frac{K_{CAT}}{K_M}$$

We used bovine testicular HYAL (Type I-S, Aldrich H3506, Batch SLBR736V, 451 units/mg) for these measurements because it catalyzes the hydrolysis of the β(1,4) bonds in HA similarly to human Hase.[33] All ITC experiments were performed at 37 °C in PBS. A HYAL solution in PBS was placed in the cell of the equipment, and the HA polymer solution in PBS was loaded in the syringe. All solutions were prepared before the experiments and used in the next 1 to 8 h. Initial experiments were performed at concentrations of HA polymers in the range of 0.5 to 3 g/L and HYAL solutions of 0.75 to 3 g/L, *i.e.*, in excess of the enzyme (molar ratio of HYAL to HA disaccharide 33 to 260) to rapidly convert the substrate into the product (HA tetrasaccharides). The best thermograms were obtained when HA of 1 g/L and Hase of 1.5 g/L were used (molar ratio of Hase to HA disaccharide 230). At these concentrations, single injection experiments were performed by injecting 10, 20, and 35 μL with a speed of 0.5 μL/s and a reference power of 20 μcal/s. The thermograms were recorded until an equilibrium was reached (15 min after the last injection). Control experiments were performed to compare the heat generated by the dilution of HA in PBS and the addition of PBS into HYAL to the heat generated by the enzymatic reaction (Fig. VI.S9). Apparent enthalpy of the reaction, heat rate (dQ/dt), and Michaelis–Menten plots were obtained using MicroCal PEAQ-ITC Analysis Software (Malvern). The molar concentrations to calculate K_M are expressed as a concentration of cleavable sites.[34] Such expression of K_M is appropriate for kinetic experiments that follow each cleavage event because in our case, cleaved HA polymers generated by HYAL are also HYAL substrates that contain cleavable sites.

VI.2.9. Surface plasmon resonance (SPR).

The SPR analysis was performed on a Biacore X100 instrument (GE Healthcare, Germany) using PBS containing 0.005 % Tween 20 (pH 7.4) as running buffer at 25 °C. The CD44 protein (human recombinant, Fc fusion, biotin-labeled, 50.6 kDa, BPS Bioscience, USA; 25 μg/mL) was immobilized onto streptavidin-functionalized chip (Cytiva) according to manufacturer recommendations (15 min, 5 μL/min). A blank immobilization, *e.g.*, without CD44 immobilization, was used as a reference. **1**, **2**, and **3** solutions were prepared at a range of concentrations (25 – 200 ng/mL) in the running buffer. Increasing concentrations of each HA polymer were successively injected (30 μL/min) for 180 s (association) followed by a 180 s

running buffer (dissociation). The regeneration was achieved with 100 mM glycine. HCl at pH 2.0 for 30 s in the case of 2 or with 1 M NaCl in 50 mM NaOH for 30 s, when 1 and 3 were tested as regeneration solutions. Preliminary results showed that around 50 % of CD44 could be regenerated after interaction with **3** and full recovery was observed for **1** and **2**. To overcome this technical issue, high CD44 immobilization levels were used to provide enough sensitivity (ng/mL range) and allow total CD44 regeneration.

Kinetic constants were determined by a two-state reaction model in BIAevaluation 2.0.2 software (Table VI.S3). The two-state binding model assumes 1:1 binding of analyte (HA or HEMA-*g*-HA; A) to an immobilized ligand (CD44, B) followed by a conformational change that stabilizes the complex (AB*) and is described by Equation VI.2.

Equation VI.2*:* $A + B \underset{k_{a1}}{\overset{k_{d1}}{\rightleftarrows}} AB \underset{k_{a2}}{\overset{k_{d2}}{\rightleftarrows}} AB^*$

where k_{a1} and k_{d1} are the association and dissociation constants of the binding of the analyte to the ligand and k_{a2} and k_{d2} are the association and dissociation constants of the conformational adjustment of the formed complex.

VI.2.10. Cell culture and transfection.

Breast cancer cells, MDA-MB-231 and Sk-Br-3, were seeded on tissue culture polystyrene (TCPS) at 37 °C in Dulbecco Modified Eagle Medium (DMEM) high glucose (4.5 g/L) with phenol red (Sigma-Aldrich) supplemented with 3.7 mg/mL sodium bicarbonate (Sigma-Aldrich), 10 % fetal bovine serum (FBS, Gibco) and 1 % antibiotic/antimycotic (10000 units/mL penicillin G sodium, 10000 μg/mL streptomycin sulfate, and 25 μg/mL amphotericin B in 0.85 % saline; Gibco). Upon confluence, the cells were detached with TrypLE Express™ (Gibco) and used in the following experiments at a cell density of $2x10^5$ cells/mL.

Sk-Br-3 cells were transfected with GFP-tagged CD44 (human, transcript variant 7, NM_001202556, Origene, 25 ng) using Lipofectamine 3000 (Invitrogen) according to manufacture instructions. After 48 h incubation, cells were selected and cultured in the above-described medium supplemented with 1 μg/mL of geneticin. Cells were used up to passage number 3 after transfection.

VI.2.11. Fröster resonance energy transfer (FRET) microscopy.

In this experiment, CD44-GFP was used as a donor and Rho-labeled HA polymers (VI.5) as acceptors. CD44-GFP transfected Sk-Br-3 cells were seeded in 8-well μ-slide polymer coverslip (ibidi), allowed to adhere for 24 h and then supplemented with a culture medium with dissolved Rho-labeled HA polymer (50 μg/mL) for 30 min at 4 °C. Cultures with medium alone were used as controls. Cells were fixed with 10 % formalin and washed with PBS. Sensitized FRET images were acquired on a confocal laser scanning microscope (TCS SP8, Leica) with a 63x water immersion objective with 512x512 px resolution for quantitative proposes and 2048x2048 px resolution and 3x virtual magnification for the acquisition of representative images. Fluorescence images were acquired sequentially through sensitized fluorescence emission (λ_{ex} = 488 nm and λ_{em} = [571;700] nm), Rho emission (λ_{ex} = 561 nm and λ_{em} = [571;700] nm) and GFP emission (λ_{ex} = 488 nm and λ_{em} = [498;563] nm. Acquired images were processed in ImageJ 1.53c software. Stacks were projected to a sum. Region of interest was defined at the cell membrane and it was used to measure CD44-GFP and FRET intensity. The ratio between FRET signal and CD44-GFP was used as an indicator of FRET efficiency.[35, 36]

VI.2.12. Internalization of 1-3 by MDA-MB-231 and Sk-Br-3.

MDA-MB-231 and Sk-Br-3 were cultured for 24 h as described above and then supplemented with Rho-labeled HA polymers (25 μg/mL, VI.5) for 2 h at 37 °C. Cells were then fixed with 10 % formalin and stained for actin with phalloidin-FITC (250 ng/mL) and for nuclei with DAPI (1 μg/mL). Fluorescence images were acquired using a confocal laser scanning microscope (TCS SP8, Leica) with a 63x water immersion objective with 512 x 512 px resolution. Images were processed and analyzed in ImageJ 1.53c software. Stack images were sum projected, cell boundaries (region of interest) were determined according to phalloidin signal and used for Rho fluorescence measurement. At least 40 cells per condition were analyzed.

VI.2.13. Digestion of endogenous HA.

MDA-MB-231 and Sk-Br-3 cells were seeded on tissue culture polystyrene (TCPS) coverslips for 24 h and then supplemented with Hase (type IV-S from bovine testes, 750-3000 units/mg) at a concentration of 250 μg/mL (2 μL; 1 h).

VI.2.14. Effect of 1-3 on CD44 expression.

MDA-MB-231 and Sk-Br-3 cells were seeded on TCPS for 24 h and then supplemented with **1**-**3** at different concentrations (25, 50, or 100 μg/mL) for 2 h. Cells were washed with PBS and fixed. Immunocytochemistry against CD44 was performed. Briefly, cells were permeated with 0.2% Triton-X-100 in PBS (15 min, RT), blocked with 3 % BSA in PBS (1 h at RT), followed by incubation with monoclonal antibody to CD44 (dilution 1:400) in 1 % BSA in PBS (overnight at 4 °C). After washing, cells were incubated with secondary antibody AlexaFluor® 594 donkey anti-mouse IgG (dilution 1:600), phalloidin-FITC (250 ng/mL), and DAPI (1 μg/mL) (1 h at RT). Microscope slides were mounted with VectaShield mounting medium (Vector Laboratories, USA) and stored at 4°C. Images were acquired using a confocal laser scanning microscope (TCS SP8, Leica). CD44 expression was analyzed by immunocytochemistry. At least 150 cells were analyzed per condition. Images were processed and analyzed in ImageJ 1.53c software. Stack images were sum projected, cell boundaries (region of interest) were determined according to phalloidin signal and used for CD44 fluorescence measurement. Cells pretreated with Hase were also used in these studies to evaluate the competition between endogenous and exogenous HA for CD44 binding.

V.2.15. Evaluation of CD44 clustering.

Cells were cultured and supplemented with **1**-**3** (100 μg/mL, 2 h) as described above. Cells were washed with PBS, detached from the TCPS with 4 mM EDTA in PBS (pH 8), and washed again with PBS. CD44 clusters were crosslinked by incubation with 2 mM bis(sulfosuccinimidyl) suberate (BS3) (Sigma) for 1 h at 4 °C followed by incubation with 20 mM Tris (pH 7.5) for 15 min at RT for quenching. Cells were washed with PBS twice and lysed with RIPA lysis buffer. Samples were then analyzed by Western blot.

V.2.16. CD44 quantification by Western blot.

Cells were harvested with 4 mM EDTA in PBS (pH 8) and homogenized in ice-cold RIPA lysis buffer supplemented with protease inhibitor cocktail and phosphatase inhibitor cocktail 1 and 2 (1:100, Sigma). The protein lysate was incubated over ice for 30 min with cycles on the vortex and centrifuged (13 000 g, 20 min, 4 °C). Protein concentration in the supernatant was determined by BCA protein assay according to manufacture instructions (ThermoFisher Scientific). Equal protein amounts were separated in Bolt™ 8 % Bis-Tris gel (Thermofisher Scientific) with Bolt™ MES SDS Running Buffer (Thermofisher Scientific) and transferred onto PVDF membrane. The membranes were blocked with 5 % BSA in Tris-buffered saline containing 0.1 % Tween-20 (TBS-T) for 30 min at RT and incubated with monoclonal antibody to CD44 [8E2F3] (diluted 1:5000, OriGene) and with anti-GAPDH antibody [EPR16891] (diluted 1:10000, abcam) at 4 °C overnight. Then membranes were washed with TBS-T and incubated with anti-rabbit and anti-mouse IRDye (diluted 1:10000, Li-Cor) in 1 % BSA/TBS-T for 1 h at RT. After washing with TBS-T and TBS, blots were visualized using Odyssey® Fc Imaging System (Li-Cor). Densitometry analysis was carried on ImageJ 1.53c software. CD44 signal was normalized to lane using the GAPDH as a loading control and the control condition, *i.e.*, cells in growth medium.

VI.2.17. Statistical analysis.

All experiments were repeated at least in duplicate in two independent experiments. The results are presented as mean ± standard deviation. Data failed homogeneity of variances; therefore, the Kruskal-Wallis test was used to test differences between groups with 95 % significance for multicomparison between conditions Benjamini and Hochberg *p*-adjusting method was used.

VI.3. Results and Discussion

VI.3.1 Synthesis of HA brush copolymers

There are different molecular designs of HA copolymers: most of them are based on the grafting of synthetic polymer chains at the -COOH groups of HA and only a few examples are reported in

which HA is end-on linked (*i.e.*, at the reducing end) to a synthetic core. These examples include diblock copolymers,[37-40] star-like copolymer with a relatively low Mw hyperbranched core,[41] and glycopolymers made of a synthetic core with short (up to tetrasaccharides) glycan branches.[42] The presented herein copolymers differ from these previous designs, as they contain longer HA branches with preserved structure/bioactivity whose density can be controlled. We have selected polyhydroxyethyl methacrylate (HEMA) as a linear core for the HA brush-like copolymers because of its wide use in the biomedical field and the free -OH groups whose functionalization allows to generate copolymers.[43, 44] We synthesized HEMA by a previously described atom transfer radical polymerization (with an alkyl bromoinitiator and CuBr/ 2,2´-bipyridine as a catalyst) that permits obtaining on-demand molecular weights (Fig. VI.1D).[32] Herein, we synthesized and used HEMA with the following characteristics: Mn 62.4 kDa, Mw 74.6 kDa, PDI 1.20 (Figs. VI.S1 and VI.S2).

To graft HA via its reducing end, we first obtained HEMA-N-hydroxyphthalimide by Mitsunobu reaction followed by hydrazine deprotection to generate aminooxy groups needed for an oxime ligation (Fig. VI.1D). Previously, we have used oxime coupling to prepare diblock and star-like copolymers of GAGs and have demonstrated that this coupling preserves the bioactivity of the grafted GAG.[41, 45] Of note, we initially used an excess of phthalimide for the Mitsunobu reaction aiming to generate maximum possible reactive sites. However, the copolymers obtained under these conditions had low solubility in the solvent system/conditions usually used for the next oxime couplings. We, therefore, performed an extensive optimization of the coupling conditions (temperature, solvent, catalysts, and polymers with varying degrees of aminooxy functionalization, Tables VI.S1 and VI.5, and Figs. VI.S3-8). The highest conversion rate (~ 44 % of HA into HA-*g*-HEMA) was obtained when we used HEMA-ONH_2 polymers with 25 % of -OH groups substituted by -ONH_2 groups in DMSO/acetate buffer at 60 °C. Under these conditions, we generated HA-*g*-HEMA copolymers with a different number of HA chains by tuning the HA stoichiometry (Table V.S5, and Figs. VI.S6-8).

The copolymers were characterized by nuclear magnetic resonance (NMR, Figs. VI.S6-8) and gel permeation chromatography (GPC, Figs. VI.S4-5) with viscosity and light scattering detectors. NMR shows the presence of oximes at the distinctive chemical shifts [41, 45] between 6.5 and 8 ppm, and was used to determine the degree of substitution (DS) of HEMA-ONH_2 and the number of HA chains linked to the HEMA core. Very high absolute molecular weight (abs Mn) and short

retention times, *i.e.*, high apparent molecular weight (app Mn), were obtained for HA-*g*-HEMA with low DS (as determined by NMR) (Table VI.S5). This behavior can be explained by the above-mentioned low solubility of HEMA-ONH_2 in water. The polymers with low DS are prompt to aggregate in water and aqueous media, *e.g.*, buffer solutions. On the other hand, the polymers with high DS have longer retention times associated with a lower app and abs Mn because they are dissolved, do not aggregate, and the determined abs Mn is similar to the Mn estimated by NMR (Table VI.S5). To confirm that the polymers with longer retention times have indeed higher DS, the oxime linkage was hydrolyzed in acid media and the released HA was quantified by GPC (Table VI.S5).

The GPC analysis with light scattering (at two angles) and viscosity detectors also allows determining the radius of gyration (R_g) and the hydrodynamic radius (R_h) of the polymers in solution (Table VI.S5), data for HA are included for comparison (Table VI.S4). HA-*g*-HEMA with low DS has R_g/R_h that is typical for polymer micelles (R_g/R_h=1.1), confirming the proposed aggregation.[46] For the copolymers with intermediate DS, we obtained R_g/R_h ratios similar to HA (R_g/R_h=1.9), corresponding to a semi-rigid structure.[47] The R_g/R_h determined for the HA-*g*-HEMA with the highest DS (R_g/Rh=2.3) agrees with a rigid structure found in densely modified copolymers with soluble grafts.[47] For the following experiments, we selected HA-*g*-HEMA with intermediated DS (3), *i.e.* DS of 1.6, which corresponds to 8 grafted HA chains.

VI.3.2 Degradation of HA polymers by Hyaluronidase

Because the fragmentation of HA is crucial for its biological activity, we studied the degradation of **1**, **2**, and **3** by HYAL. HYAL mechanism of action is complex: it acts in an endolithic random fashion and catalyzes the break of β(1,4) bonds in HA and chondroitin sulfates, but at final degradation stages, it also promotes the recombination of the generated dimers to form tetramers.[48-50] HYAL is a non-processive enzyme (*i.e.*, it releases the substrate before the next hydrolysis) that forms a complex with a tetrasaccharide and there are no reports about the simultaneous binding of several HYAL molecules to a long HA chain.[50] Despite its complex mechanism of action, HYAL kinetics follows the Michaelis-Menten law as shown by UV spectrometry,[48, 51] GPC,[52] or electrophoresis combined with UV or mass spectrometry.[53] Herein, we used single-injection experiments to determine the kinetics parameters for the

degradation of **1**, **2**, and **3** by HYAL. ITC is a relatively new method for studying enzyme kinetics - in 2001 was demonstrated for the first time that in situ determination of the reaction heat can be used for precise and fast acquisition of the Michaelis-Menten parameters.[54, 55] We could not find previous reports on the use of ITC for studying the HYAL action on HA. The concentrations of the substrates and the enzyme were optimized to obtain a full conversion within minutes and enough heat to avoid the dilution effects in the thermograms (VI.5 for details). This information was then expressed in terms of reaction rate and fitted to the Michaelis-Menten equation to obtain the main kinetic parameters (Table VI.1 and Figs. VI.S9 and VI.S10).

Table VI.1. Affinity for the substrate (K_M, Michaelis constant), turnover rate (K_{CAT}), and catalytic efficiency (K_{EFF}) of the degradation of substrates 1-3 by HYAL determined by isothermal titration calorimetry (ITC, n=3) and Michaelis-Menten equation.

Substrate	K_M [μM]	K_{CAT} [s^{-1}]	K_{EFF} [$\mu M^{-1}s^{-1}$]
HMW HA (1)	607±150	(69±10)x10-2	1150±108
LMW HA (2)	772±250	(80±14)x10-2	1007±169
HEMA-*g*-HA (3)	284±75	(22±6)x10-2	766±18

The obtained K_M agrees well with the data obtained by other methods and reported in the literature.[48, 51, 56, 57] The K_M determined for **3** is smaller (higher affinity) as compared to **1** and **2** (Table VI.1). This difference can be explained by a higher stoichiometry, *i.e.*, binding of more than one HYAL to the brush-like structure of **3**. The semi-rigid structure of **3** with different exposed and extended HA branches makes the multiple binding in the brush structures more probable than in native HA.[58] In fact, similar multiple binding of HYAL has been reported recently for nanoparticles with surface-exposed HA (also of *ca*. 5 kDa).[40] These nanoparticles inhibit the degradation of HMW HA by HYAL *via* competitive binding of the enzyme.[40]

The ITC also allows determining the hydrolysis rate (K_{CAT}). Besides the high affinity of HYAL to **3**, we observed lower K_{CAT} (slow hydrolysis) for the copolymer compared to **1** and **2**. Such a slower reaction rate can be explained by an inefficient enzyme release from the more crowded complex **3**/HYAL (*i.e.*, non-processive enzyme). The smaller K_{CAT} and K_M results in significantly lower K_{EFF},

showing that the hydrolysis takes longer for **3**, which might have important biological consequences.

V.3.3 Interaction of HA polymers with CD44

To further check the effect of the multivalent HA presentation, we have investigated the interactions of **1**-**3** with CD44 - the main HA receptor - by several characterization methods. A real-time interaction was followed by surface plasmon resonance (SPR, Fig. VI.2).

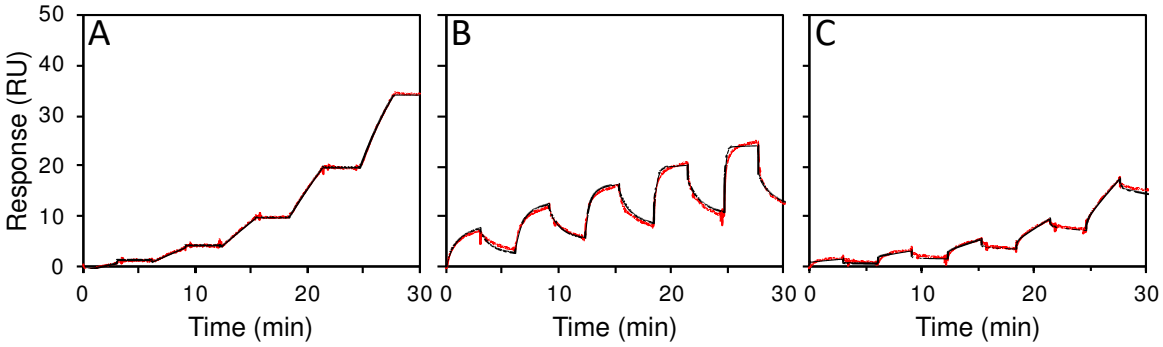

Figure VI.2. Representative SPR sensograms showing the kinetics of the CD44 interactions with (A) HMW HA (1), (B) LMW HA (2), and (C) HA-*g*-HEMA (3). Solutions with increasing concentrations of HA polymer (12.5 – 200 ng/mL) were injected stepwise over the chip with immobilized CD44. Each of these injections was followed by a dissociation step. The raw data are presented in red and the fitting in black. The respective constants are shown in Table 2.

The obtained sensograms for **1** and **2** (Figs. VI.2A and VI.B) agree with previously reported data for HA: **1** binds steady and remains attached to CD44 because of the multivalent interactions with the long HA chains, while **2** binds and detaches rapidly from the functionalized sensor surface.[39, 59] The sensogram of **3** (Fig. VI.3C) is different from **1** and **2**: at first sight, it shows binding kinetics similar to the observed for **2** and a dissociation similar to **1** - while there is some loosely bound **3** that is released at the beginning of the dissociation process, most of the polymer remains attached to the surface. To render quantitative information (Table VI.2), the sensograms were fitted (Fig. VI.2, black line) with a two-state reaction model. This model was chosen because of the reported CD44 conformational change upon HA binging.[60] It assumes a 1:1 binding

between ligand and protein with a subsequent conformational change of the ligand[61] and in the case of **1** and **3**, the affinity reflects the average association. The alternative heterogeneity model presumes 2-4 binding sites,[59] which does not reflect either the real stoichiometry (the binding domain of CD44 is a HA octasaccharide,[62] *i.e.*, 1 has *ca.* 800 possible binding sites). We also applied this model to the obtained SPR data, but the fitting was not as good as the one obtained with the two-state model. The binding kinetics depends on the surface density of active CD44 too.[63] Considering the Mw of CD44 and the R_g of **1**-**3**, we estimated the surface density of CD44 (details in the VI.5) and the respective number of CD44 molecules available at the surface per ligand (Table VI.S4): **1** can interact with 477 CD44 molecules; **2** has only 0.3 CD44 available, and therefore can bind only one CD44 under the tested SPR experimental conditions; and **3** has 25 available CD44 molecules to bind via HA octasaccharides.

Table VI.2. Quantitative data for the interactions between CD44 and 1-3 obtained from the surface plasmon resonance sensograms fitted to a two-state reaction model (n=3): equilibrium constants of the two states (K_1 and K_2), association constant of the binding (K_A).

Ligand	K_1 [M^{-1}][a]	K_2 [M^{-1}]	K_A [M^{-1}]
HMW HA (1)	$(4.1\pm3.8)\times10^{11}$	$(1.1\pm1.8)\times10^{3}$	$(3.3\pm5.7)\times10^{13}$
LMW HA (2)	$(2.9\pm1.8)\times10^{6}$	4.1 ± 0.3	$(1.49\pm0.9)\times10^{7}$
HEMA-*g*-HA (3)	$(7.8\pm10)\times10^{7}$	$(3.0\pm5.2)\times10^{3}$	$(4.03\pm6)\times10^{10}$

[a] Sensograms (triplicate) were fitted to obtain the kinetic constants, k_{a1}, k_{d1}, k_{a2}, and k_{d2} for the two-state reaction model. Then $K_1 = k_{a1}/k_{d1}$ and $K_2 = k_{a2}/k_{d2}$ were calculated; the association constant was calculated from the equation $K_A = K_1(1+K_2)$. All fitted parameters and equations are included in VI.5.

Despite the model differences, the K_A values obtained for **1** and **2** (K_A(**1**)>K_A(**2**)) are in good agreement with previously reported data obtained from SPR kinetic assay and from the binding of fluorescein-conjugated HA to CD44 expressing cells.[64, 65] The analysis of the K_1 and K_2 indicates adequate selection of the model: K_1(**1**)>>K_1(**2**) due to the binding of several CD44 to 1 and 1:1 binding stoichiometry for **2**:CD44. K_2(**1**)>>K_2(**2**) and shows greater conformational freedom/changes upon binding of CD44 to **1**. An intermediate K_A was determined for **3**. An increased avidity is observed for this copolymer: **3** has 8 HA branches with the size of **2** but has more than 2500-fold higher K_A than **2**. The K_2(**3**) is similar to K_2(**1**), showing that besides the

avidity, the interactions between **3** and CD44 benefit from conformational adjustments similar to those determined for **1**. These results indicate a zipper-like mechanism of interactions between the copolymer and CD44: once one of the branches interacts with CD44, the other LMW HA chains are brought in close proximity to the surface and their recognition/association with CD44 is promoted. In the brush structure of **3**, the 8 LMW HA chains are relatively separated (the degree of polymerization of HEMA is 480, *i.e.*, there is one HA branch for every 60 HEMA monomers), which allows conformational freedom as indicated by K_2(**3**) and is beneficial for the proposed mechanism.

VI.3.4 Effect of HA polymers on CD44 expression and clustering in vitro

We selected two breast cancer cell lines, MDA-MB-231 and Sk-Br-3, to demonstrate the effect of **3** in vitro. These cells differ by the expression of CD44 and HA:[12, 66-68] MDA-MB-231 cells have high CD44 expression (CD44+) and a considerable amount of endogenous HA at the pericellular space (Fig. VI.S12A). In contrast, Sk-Br-3 cells have low expression of HA and CD44 (CD44–), and HA is mainly located in the cytoplasm (Figs. VI.S13A and VI.S13B).

Forster resonance energy transfer (FRET) experiments were performed to assess the recognition and binding of the HA polymers **1**-**3** by CD44 in vitro (Fig. VI.3). For these experiments, we used Sk-Br-3 cells (low expression of CD44) that were transfected with green fluorescence protein-CD44 (CD44-GFP). CD44-GFP has an intense signal at 488 nm (Fig. VI.3A, CTRL CD44-GFP) and very low intensity at 561 nm (Fig. VI.3A, CTRL FRET), *i.e.*, small contribution (6 %) from signal bleed-through to the FRET, while Rho has a negligible contribution to FRET (Fig. VI.S14). We optimized the polymers binding to the receptors by incubating CD44-GFP expressing Sk-Br-3 cells with **1**-**3** at different temperatures (37 °C, room temperature, and 4 °C), and FRET signaling was only obtained in cells incubated at 4 °C.

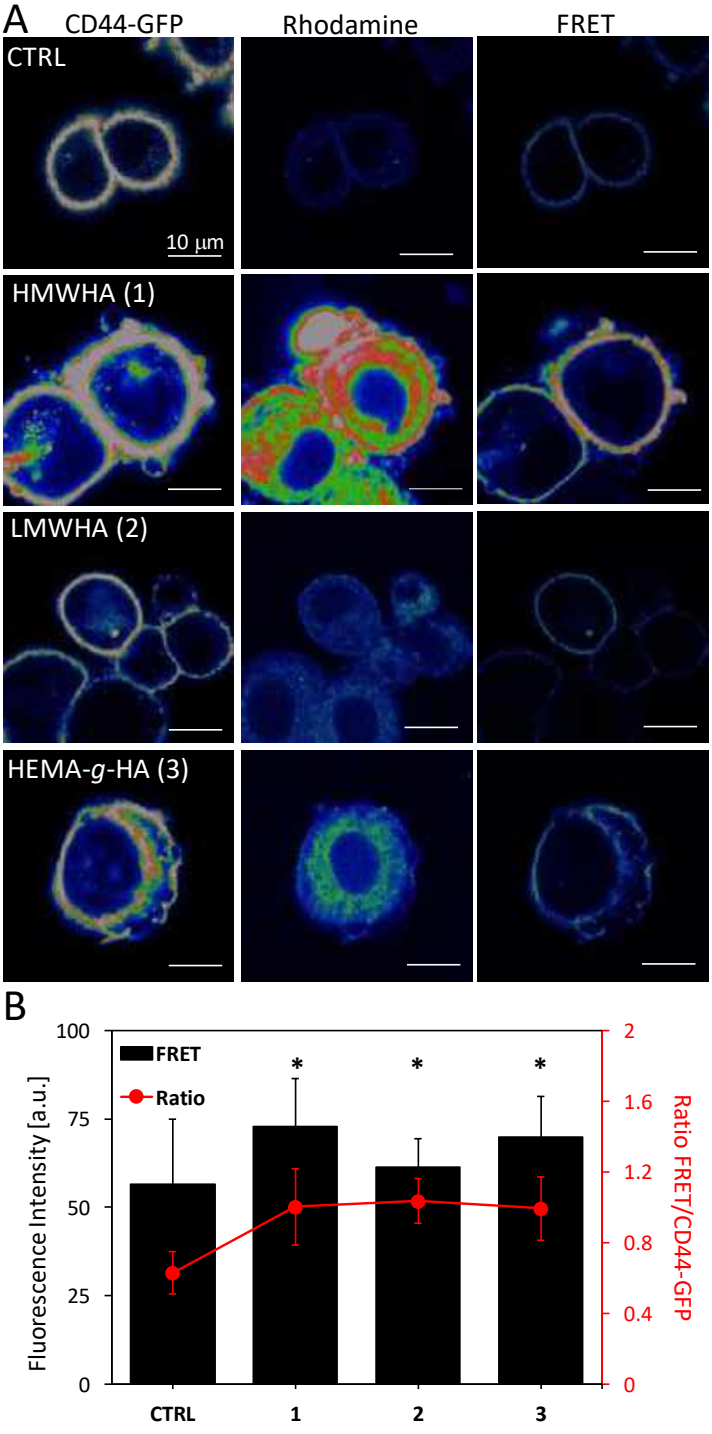

Figure VI.3. Effect of hyaluronan polymers 1-3 on the expression and binding of CD44 in Sk-Br-3 cells transfected with CD44-GFP. (A) Representative confocal images of Sk-Br-3 cells transfected with CD44-GFP (control, CTRL), cultures supplemented with Rhodamine-labeled 1-3, and Forster resonance transfer energy (FRET) for these cultures. (B) The ratio between fluorescence acquired for CD44-GFP and FRET, which indicates the energy transference efficiency of CD44-GFP to Rho. Statistically different from the control at *p< 0.001, n=3. Controls are presented in Fig. VI.S14.

Confocal microscopy analysis of the transfected cells showed expression of CD44-GFP mainly at the cell surface (Fig. VI.3A, CD44-GFP: CTRL). Cultures of these cells were then supplemented with Rhodamine (Rho)-labeled HA polymers (VI.5. for details on the synthesis and characterization of the labeled polymers). The supplementation increased the CD44-GFP expression, especially in the case of **1** and **3**, indicating possible recruitment of these receptors by the HA polymers (Fig. VI.3A, CD44-GFP: CTRL *vs.* **1**-**3**). FRET data confirmed that indeed the exogenous HA polymers **1**-**3** bind the CD44. We observed a significant increase of the FRET intensity compared to the control in the following order (Fig. VI.3B, black bars): FRET(**1**) > FRET(**3**) > FRET(**2**) > FRET(**CTRL**). This order indicates the relative amount of polymer that binds to CD44 and reflects the different K_A of **1**-**3** (Table VI.2). The ratio FRET/CD44-GFP (Fig. VI.3B, red) is indicative of the FRET efficiency. An increase of this ratio was observed upon supplementation with exogenous HA and FRET efficiency was similar (no difference at $p<0.05$) for all cultures supplemented with exogenous HA polymers, proving similar binding of **1**-**3** to CD44.

The effect of **1**-**3** on CD44 expression by non-transformed Sk-Br-3 and MDA-MB-231 cells was confirmed by immunocytochemistry and Western blot analysis. As stated above, the basal expression of CD44 in Sk-Br-3 cultures is very low and the Western blot data (Fig. VI.S15A) did not allow proper comparison between different culture conditions. Thus, we quantified the CD44 expression from the confocal microscopy data (Fig. VI.4B). We observed that supplementation of Sk-Br-3 cells with **1**-**3** induced different expression of CD44: a concentration-dependent increase of CD44 expression is observed for **1**, while **3** induces high CD44 expression even at a low concentration, and **1** has an effect only at the highest tested concentration. The Western blot analysis of MDA-MB-231 cells showed that cultures supplemented **3** have an increased CD44 expression in a concentration-dependent manner, the addition of **2** induced small (but not significant) decrease of CD44 expression, and the supplementation of **1** does not show any statistically significant effect (Fig. VI.S15B). The same trend was observed when the microscopy data were used for the quantification (Fig. VI.5B).

The immunocytochemistry for both MDA-MB-231 and Sk-Br-3 cell lines showed mainly cytoplasmic localization of CD44 in the cultures supplemented with **1** (Figs. VI.4A and VI.5A), indicating the binding of this polymer by CD44 followed by internalization.

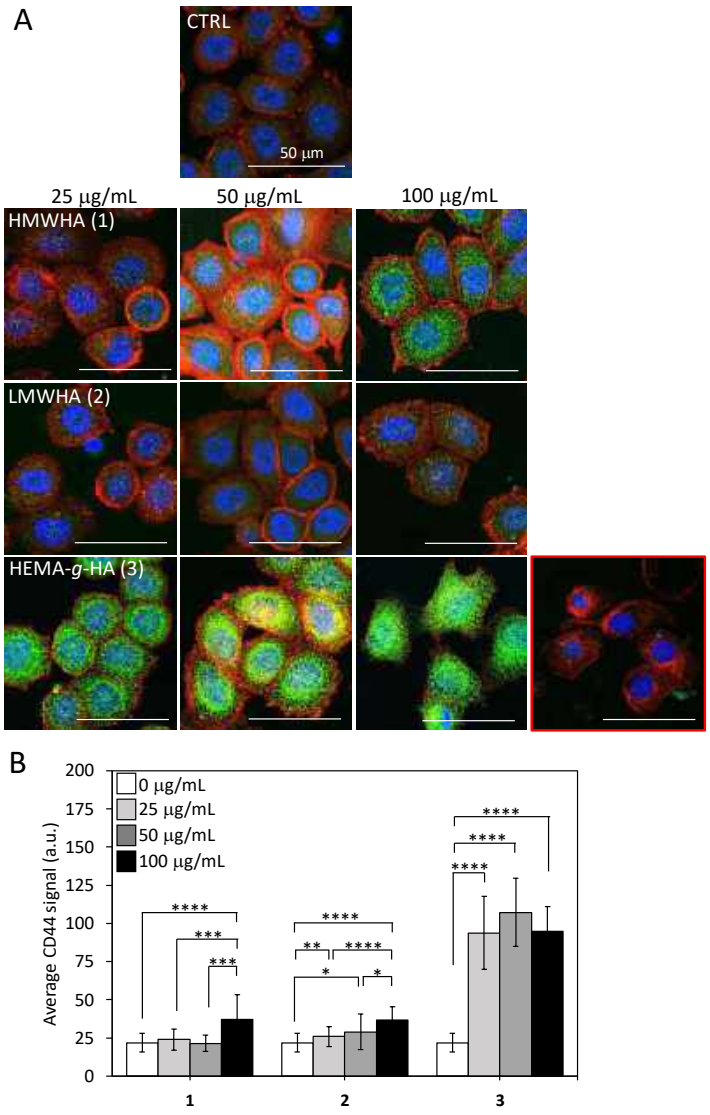

Figure VI.4. CD44 expression by Sk-Br-3 cultures supplemented with 1-3 at different concentrations for 2 h: (A) Representative confocal microscopy images showing Sk-Br-3 cells immunostained for CD44 (green), actin (red), and nuclei (blue); (B) Graphical presentation of the mean grey value of CD44 signal from confocal microscopy images of cells cultured in the presence of 1-3. The image featured in a red frame shows the appearance of the second cell population observed under these conditions. Statistical differences: *p<0.05, **p<0.01, ***p<0.001, ****p<0.0001; n=3.

A similar response was observed upon supplementation with **3**, suggesting that **1** and **3** might follow the same internalization pathway. Interestingly, the confocal imaging showed two populations of Sk-Br-3 cells for cultures supplemented with **3** at the highest concentration (100 μg/mL): one with high expression of CD44 and a faint actin staining and another that does

not express CD44 and has a compromised cytoskeleton, corresponding to around 50% of the cell culture (Fig. VI.4, featured in red frame image).

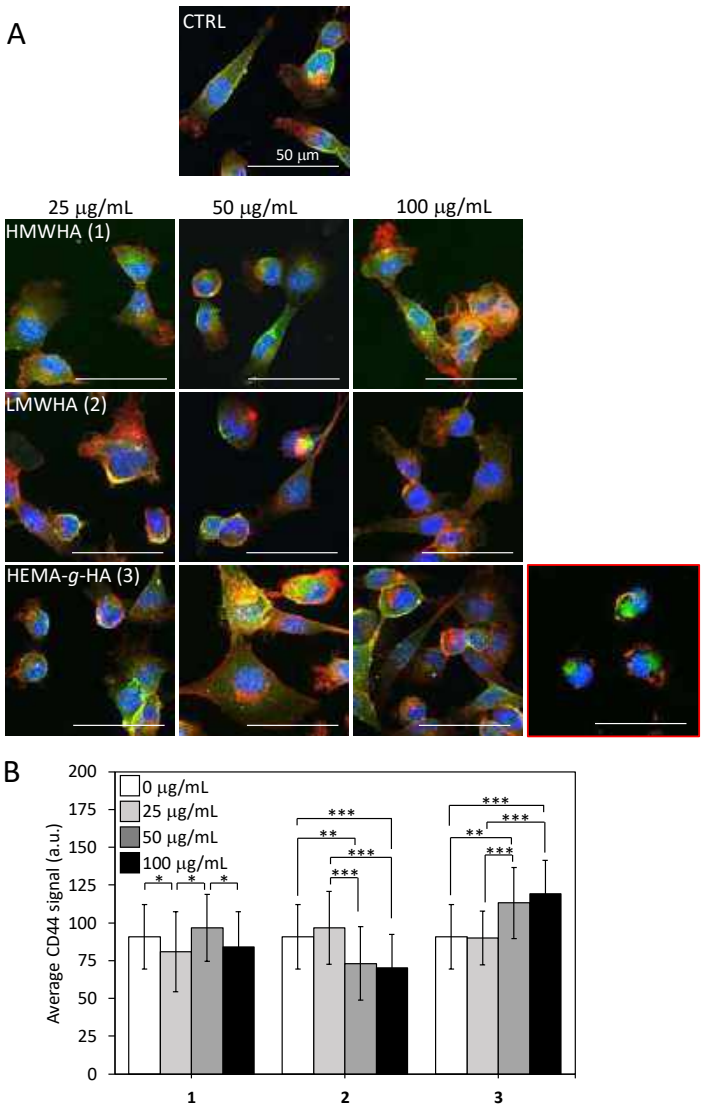

Figure VI.5. CD44 expression by MDA-MB-231 cultures supplemented with 1-3 at different concentrations for 2 h: (A) Representative confocal microscopy images showing MDA-MB-231 cells immunostained for CD44 (green), actin (red), and nuclei (blue); (B) Graphical presentation of the mean grey value of CD44 signal from confocal microscopy images of cells cultured in the presence of 1-3. The image featured in a red frame shows the appearance of the second cell population observed under these conditions. Statistical differences: *p<0.05, **p<0.001, ***p<0.0001; n=3.

We, therefore, studied the effect of the **1**-**3** on cell viability at the tested conditions (Fig. VI.S16). The results showed that MDA-MB-231 cells viability was not affected but the viability of Sk-Br-3 cells was compromised by the HA polymers in a concentration-dependent manner 2 h after the

supplementation with **1**-**3**. However, a recovery was observed 24 h after the supplementation with one exception - only 50 % of viability was observed for Sk-Br-3 cultures supplemented with **3** at a concentration of 100 μg/mL. This result indicated that the mechanism of action and bioactivity of **3** might be different from **1**.

To confirm the uptake of **1**-**3**, we used Rho-labeled HA polymers. The results showed clearly that **1** and **3** are internalized by the cells, whereas no internalization was visible upon supplementation of **2** (Fig. VI.6).

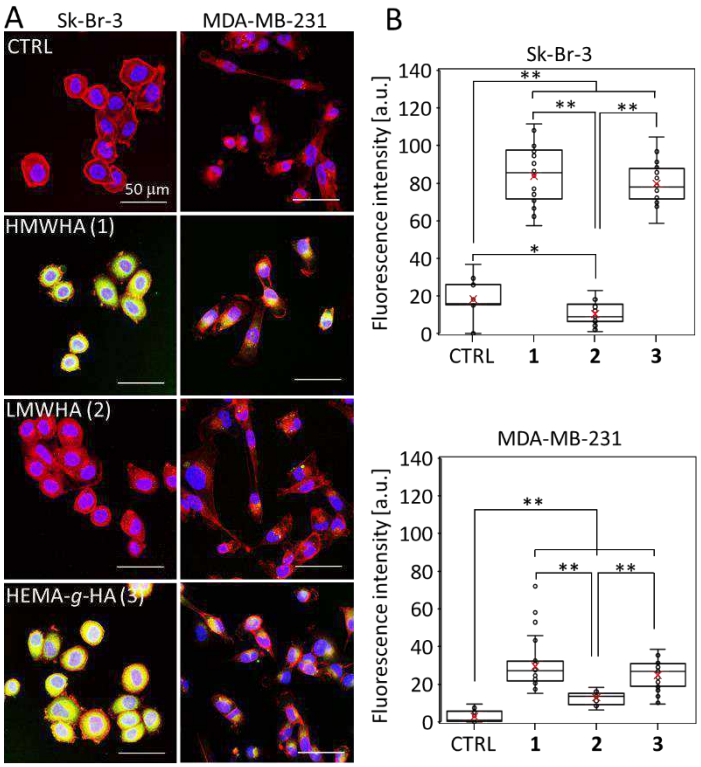

Figure VI.6. Internalization of 1-3 by MDA-MB-231 and Sk-Br-3 cells. (A) Representative confocal images of MDA-MB-231 and Sk-Br-3 cells incubated with Rhodamine-labeled polymers (green) and stained for actin (phalloidin, red) and nuclei (DAPI, blue). (B) Quantification of the Rhodamine fluorescence intensity for the studied conditions. Statistically significant data are marked with *$p < 0.05$ and **$p < 0.0001$, n=3.

Such different uptake is most probably due to the multiple binding sites in **1** and **3**, making possible the interactions of one molecule with several CD44 receptors, which favors endosome formation and further internalization.[1, 16] This process was evident for both cell lines, although a lower internalization was observed for MDA-MB-231 cells (Fig. VI.6). At first glance, these results seem contradictory, keeping in mind the high expression of CD44 in MDA-MB-231 cells. However,

these cells are also coated with a dense matrix of endogenous HA that competes with the exogenous HA for CD44 binding, thus, interfering with the internalization process. [16] On the other hand, Sk-Br-3 cells lack such pericellular HA coat, *i.e.*, the surface receptors are more exposed to the supplemented HA polymers.[10, 12]

To check if indeed the endogenous HA competes with the supplemented HA polymers toward CD44 binding, we treated MDA-MB-231 cells with HYAL. Of note, this treatment did not affect the high expression of CD44 at the cell surface (Fig. VI.S12). A tendency of an enhanced response of the HYAL-treated cells to the exogenous HA polymers was visible when compared to untreated MDA-MB-231 cells (Figs. VI.7 and VI.S12 *vs.* Fig. VI.5).

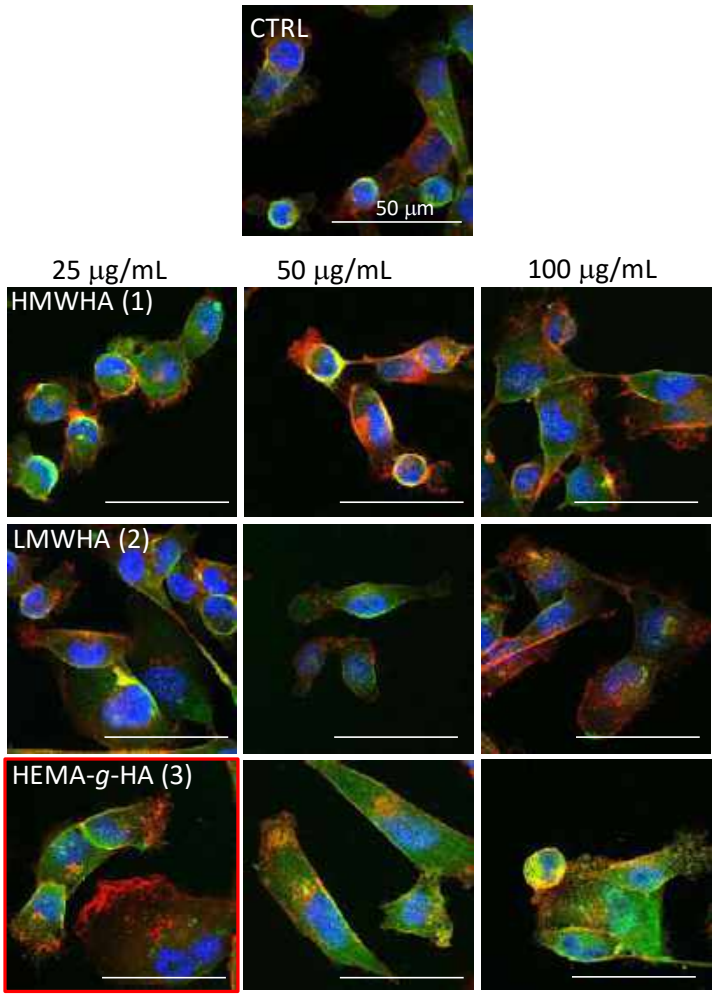

Figure VI.7. Expression of CD44 by MDA-MB-231 cells treated with HYAL (250 μg/mL, 1 h) and supplemented with 1-3 at different concentrations (25, 50 or 100 μg/mL) for 2 h. CD44 expression was visualized by immunocytochemistry (green). Actin was stained with phalloidin (red) and DNA with DAPI (blue). The image featured in a red frame shows compromised cytoskeleton organization (red staining). Controls (MDA-MB-231 without HYAL treatment) are presented in Fig. VI.5.

No significant changes in CD44 expression and location were observed between the control and the cultures supplemented with **1**, showing that **1** acts similarly to the endogenous HA.[1, 16] On the other hand, supplementation of HYAL-treated MDA-MB-231 cells with **3** led to an increased expression of CD44 regardless of the used concentration. Moreover, we observed structural changes of the cytoskeleton (Fig. VI.S17) similar to the ones described for Sk-Br-3 in around 90 % of the cultures, even at low concentrations of **3** (Fig. VI.7, image featured in red frame). Similar morphological changes were observed upon supplementation of **1** but only at the highest concentration and affected around 30 % of the cell population. These results suggested that **3** can compete with endogenous HA for CD44 binding and thus, might affect CD44 clustering. We, therefore, performed a chemical crosslink of the protein at the cell surface and quantified the crosslinked CD44 (Fig. VI.8).

Western blot analysis showed an additional band for the control samples after the applied crosslinking (Fig. VI.8A, the band nCD44), *i.e.*, the CD44 receptors in these cells are clustered. Supplementation with **1** did not significantly influence CD44 clustering, while **2** and **3** significantly decreased the CD44 clustering (p<0.0001). Moreover, more efficient CD44 declustering was observed in the presence of **3** when compared to **2**, which agrees with the higher binding affinity of **3** to CD44 as determined by SPR experiments.

The same procedure was applied to MDA-MB-231 cells after digestion of the endogenous HA (Fig. VI.8B). For these cells, all exogenous HA polymers disrupted the CD44 clustering but at different magnitude. The lowest declustering effect was observed in the presence of **1**. As discussed before, cells can degrade the supplemented HMW HA, *i.e.*, it provides a source of HA fragments that have attenuated the effect of LMW HA. The most pronounced effect on the CD44 clustering was observed for **3** followed by **2**.

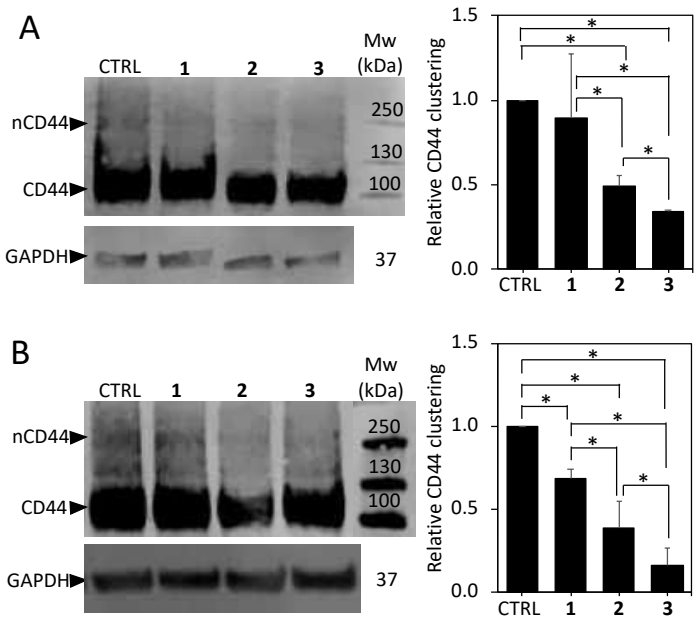

Figure VI.8. Western blot analysis and the respective densitometry quantification showing CD44 clustering in (A) MDA-MB-231 cells and (B) HYAL-treated MDA-MB-231 cells (cells were treated with 250 μg/mL of HYAL for 1 h) supplemented with 1-3 (100 μg/mL, 2 h). The densitometry quantification was normalized to loading control GAPDH and control sample (cells without supplemented HA polymers). Statistical differences are marked with * for $p<0.05$, n=3.

The disruption of CD44 clusters by LMW HA has already been studied in HK-2 and BT-549 cell lines, which have very high expression of CD44 and agree with our results: this previous study reports that LMW HA induced disruption of CD44 clustering in a concentration-dependent fashion and competes with endogenous HA for the same binding site on CD44.[16] A comparison of the data obtained for MDA-MB-231 cells with and without HYAL treatments supports that indeed the declustering activity of **2** and **3** results from the competition for CD44 binding with the endogenous HMW HA in the pericellular space and therefore is not observed for **1**. Therefore, HA-*g*-HEMA is an efficient platform to target CD44 clustering with a higher affinity than LMW HA.

VI.4. Conclusions

Oxime condensation is a feasible and versatile synthetic route to prepare hybrid glycosaminoglycan graft copolymers with different densities of the glycan chains. The grafted chains are in an extended conformation and, thus, optimally exposed to interact with cell surface CD44 in a multivalent fashion, ensuring specificity and high affinity of this interaction. Given its

peculiar structure, HA-*g*-HEMA shares some bioactivities with LMW HA (*e.g.*, competitive binding to CD44), while others with HMW HA (internalization by cells, effect on CD44 expression). The most promising bioactivity of the copolymer is the boost of CD44 declustering: its effect is stronger than the one caused by LMW HA. HA-*g*-HEMA also has the advantage of a higher affinity to CD44 and a slower HYAL degradation. Finally, the copolymer has an optimal size for tumor targeting (30 nm adequate for EPR effect).

VI.5 Supporting Information

Optimization of HEMA-*g*-HA (3) synthesis.

The reaction conditions (excess of HA, co-solvent ratio, reaction time, temperature, and catalyst) were optimized for the oxime condensation between HEMA-ONH_2 and LMW HA (**2**) (Table VI.S1).

Influence of the solvent: Initially, we used buffer:DMSO (1:1) but given the low solubility of the HEMA-ONH_2, we have also used 1:2, 1:3, 1:4, and 2:3 ratio. We found that 1:2 ratio is the optimal one.

Influence of the reaction time: The GPC analysis demonstrated an increased reaction conversion at 45 °C during the studied period (7 days). When the reaction was performed at 60 °C, the conversion was constant after 5 days. This is in good agreement with the results reported in the synthesis of HA star-copolymers by oxime condensation.[69]

Influence of the N-hydroxyphthalimide DS: Generally, the reactions performed with HEMA-N-hydroxyphthalimide with high DS (60, 80, and 100 %) led to relatively high conversion rates (up to 40 %), but the obtained products had a bimodal signal in the GPC and a low solubility in water (Table VI.S1). The compound whose peak appears closer to HA in the GPC was isolated by ultrafiltration (cut off 100 kDa) and showed to be HEMA (^{1}H NMR). On the other hand, when we used HEMA-N-hydroxyphthalimide with very low DS (10 %), we could not obtain any product. Therefore, we have selected HEMA-N-hydroxyphthalimide with DS of 25% as a good compromise between solubility and conversion of HA to HEMA-*g*-HA.

Influence of the temperature: The temperature was initially set to 45 °C previously reported as optimal for the synthesis of HA star copolymers obtained by oxime condensation, but an increase to 60 °C accelerated the reaction and led to better yields.

Influence of the HA excess: The maximum conversion was obtained when an intermediate excess of HA was used even at high temperatures and long reaction times (*e.g.,* 45 % conversion for HEMA with DS of 25 with an excess of 15 eq. leading to a copolymer with *ca.* 10 HA chains). The highest degree of HA substitution (*ca.* 20 HA chains) was obtained when a higher excess of HA (100 eq.) was used, but the achieved conversion was only 20 %.

Use of catalyst: We have previously demonstrated that adding aniline enhances the reaction rate of the oxime coupling dramatically.[69] Here, we have also tested p-phenylenediamine that is reported to be a stronger catalyst than aniline.[70] A better conversion was observed when 10 eq. of aniline or p-phenylenediamine were used as a catalyst. Nevertheless, the products became black rapidly when p-phenylenediamine was used due to its oxidation, and thus, we preferred the use of the aniline.

Influence of the HEMA-ONH_2 purification (ultrafiltration): Several reactions were performed with raw HEMA-ONH_2. This procedure speeds the reaction (given the lengthy ultrafiltration in DMF), but a higher amount of aniline is needed to achieve conversion rates that are similar to the conditions for which the purified HEMA-ONH_2 is used.

Table VI.S1. Reaction conditions tested during the optimization of the oxime condensation between hyaluronic acid (HA) and HEMA-ONH_2.

DS	HA:HEMA[1]	T [°C]	Catalyst. Eq.	Conv.[2] (%)	Acetate buffer:DMSO	Sol. reaction	Max shift in GPC[3], Homog.[4]	Solution prop.	n HA chains (NMR)
13	15	45	An. 10	0	1/2	Clear	–	–	–
28	15	45	An. 10	8	1/2	Clear	4.0, Mono	Turbid	n.d.
28	30	45	An. 10	8	1/2	Clear	2.9, Mono	Solube	n.d.
63	15	45	An. 10	1	1/2	Clear	4.6, bimod.	Turbid.	n.d.
63	30	45	An. 10	40	1/2	Clear	4.6, bimod.	Turbid.	n.d.
80	45	45	An. 10	4	1/1	Turbid	2.2, bimod.	Turbid	n.d.
80	45	45	An. 10	30	2/1	Turbid	3.0 bimod.	Turbid	n.d.
80	45	45	An. 10	5	3/1	Turbid	4.5, bimod.	Turbid	n.d.
80	85	45	An. 10	20	2/1	Turbid	3.3, bimod	Turbid	n.d.
80	15	45	An. 10	16	1/2	Clear	5, bimod.	Turbid	n.d.
80	30	45	An. 10	17	1/2	Clear	4.5 bimod	Turbid	n.d.
100	15	45	An. 10	20	1/4	Clear	4.6, bimod	Insoluble	n.d.
25	15	45	An. 40	8	1/2	Clear	5.5, Mono	Turbid	1.4
25	15	60	An .80	39	1/2	Clear	4.4, Mono	Soluble	7.0
25	15	60	An. 40	0	3/2	Clear	–	–	n.d.
25	15	60	An .40	28	1/2	Clear	4.4, Mono	Turbid	n.d.
25	15	60	An.40[5]	46	1/2	Clear	4.7, Mono	Soluble	6.5
25	15	60	An.10[5]	44	1/2	Clear	4.9, Mono	Soluble	8.0
25	15	60	An.80[5]	40	1/2	Clear	4.7, Mono	Soluble	7.9
25	15	60	An. 10	11	1/2	Clear	4.5, Mono	Soluble	8.4
25	15	60	PPD[6] 10	30	1/2	Clear	4.5, Mono	Soluble	7.5
25	100	60	An 10	21	1/2	Clear	3.5, Mono	Soluble	23

[1] Molar ratio of HA to the moles of the full HEMA chain; [2] % of HA transformed into HEMA-*g*-HA determined by the GPC (RI detector, freeze-dried aliquots before ultrafiltration) after 7 days of reaction; [3] Max shift observed in the GPC (RI detector; the LS detector always has a larger signal); [4] Copolymer profile in the GPC (RI detector). Mono or bimodal signal (RI or RI and LS after ultrafiltration); [5] The reaction was ultrafiltered with cellulose membrane YM3 in DMF after deprotection of ONH_2; 6 p-Phenylenediamine.

Synthesis of Rhodamine (Rho) labeled HA polymers (1-3)

HA polymer (15 mg of HMW HA (**1**) or 45 mg of LMW HA (**2**) or 10 mg of HA-*g*-HEMA with 8 HA chains, (**3**)) was dissolved in water (0.25 mL). A solution of Rhodamine isothiocyanate in DMSO (4 mol % to HA disaccharide, *i.e.*, 0.806 mg in 1mL for 1 and 2 or 0.19 mg for 3) was then added to the reaction and stirred for 24 h. The product was purified by ultrafiltration with a cellulose membrane (1 kDa cut off). The solution of the product was concentrated and then ultrafiltrated

against 200 mM NaCl (4x), water (4x), and then freeze-dried. All procedures were performed under light protection. The Rho-modified HA polymers were characterized by GPC, where no difference in retention time was observed compared to the unmodified polymers. The degree of modification was assessed by spectrophotometry and fluorescence spectroscopy. For spectrophotometry, standard solutions of Rhodamine B were prepared at concentrations between 4 μM and 300 μM in MilliQ water. Rho-labeled HA polymers were dissolved in MilliQ water (1 mg/mL), and an absorption spectrum was acquired at the wavelengths λ= 450 nm and 600 nm in Synergy HT microplate reader (Bio-Tek Instruments, USA). Rhodamine concentration was determined at the maximum absorbance peak (λ_{max} 562 nm). For fluorescence spectroscopy, standard solutions of Rhodamine B were prepared between 85 nM and 200 nM in MilliQ water, and Rho-labeled HA polymers were diluted to 50 μg/mL in MilliQ water. Rhodamine B was excited at λ_{ex} 520 nm and fluorescence spectrum acquired between 550 nm and 650 nm in FP-8500 Spectrofluorometer (Jasco Corporation, Japan). Rhodamine B concentration was determined according to the peak area. The degree of modification was determined by the molar ratio between Rhodamine B and HA disaccharides (Table VI.S2).

Table VI.S2. Degree of modification of 1-3 with rhodamine determined by spectrophotometry and fluorescence spectroscopy.

HA or HEMA-*g*-HA	Degree of modification (%)	
	Absorbance	Fluorescence
HMW HA (**1**)	1.42 ± 0.11	1.22 ± 0.24
LMW HA (**2**)	0.35 ± 0.01	0.24 ± 0.05
HEMA-*g*-HA (**3**)	2.39 ± 0.71	2.07 ± 0.09

Nuclear magnetic resonance (NMR) spectroscopy.

NMR spectra were recorded on Bruker AVANCE 400, and Varian Inova 750 spectrometers. D_2O, DMSO-d_4 or $CDCl_3$ were used as solvents. Chemical shifts are reported in ppm (δ units) downfield from internal tetramethylsilane when $CDCl_3$ was used as a solvent or 3-(trimethylsilyl)-propionic acid-d_4 when the spectra were taken in D_2O.

Gel permeation chromatography (GPC).

GPC characterization of HEMA homopolymer was performed on a LC system consisting of Agilent-SECcurity-Pump and an Agilent-SECcurity Autosampler connected to a refractive index (PSS-SECcurity DRI) and multi-angle static light scattering (PSS SLD 7100 MALLS) detectors. Samples separation was achieved using 4 columns (PSS, Mainz, Germany): PSS GRAM (Guard, 10 µm, 8x50mm), PSS GRAM (10 µm, 8x300mm, 100 Å), 2x PSS GRAM (10 µm, 8x300mm, 3000 Å). Column and detectors were kept at 70 °C. Samples were eluted with 57 mM LiBr in N,N-dimethylformamide at a constant rate of 1 mL/min. The light scattering detector was calibrated with a narrow polystyrene standard (PSS, Mainz, Germany) of Mw 87600 kDa and polydispersity index (PDI) 1.08. The dn/dc was set to 0.065 according to the literature.[71, 72] GPC characterization of HA and HA-g-HEMA was performed with a Malvern Viscotek TDA 305 with refractometer (RI-Detector 8110, Bischoff), right and low angle light scattering (RALS and LALS), and viscometer detectors on a set of four columns: pre-column Suprema, 5 µm, 8x50 mm, Suprema 30 Å, 5 µm, 8x300 mm, and 2x Suprema 1000 Å, 5 µm 8x300 mm. The system was kept at 30 °C. We have used phosphate-buffered saline (0.01 M phosphate buffer, 0.0027 M potassium chloride and 0.137 M sodium chloride, pH 7.4, at 25 °C) and 0.05% w/v NaN_3 as eluent that was pumped at a rate of 1 mL/min. The absolute molecular weight was determined by calibrating the RI, LS (90 and 7 °), and viscosity detectors using the software Omnisec 5.12 (ViskoteK) and pullulan (number-average molecular weight, Mn 48.8 kDa and PDI 1.07) as a standard. The dn/dc of HA (0.15 mL/g) was taken from the literature.[73] For HEMA-g-HA, the copolymers the dn/dc was determined on-line or estimated from the mass percentage of HA and HEMA calculated from NMR. The apparent (*i.e.*, relative) molecular weight was determined after a conventional calibration performed with a commercial polysaccharide set from Polymer Standard Sevive GmbH that contains 10 Pullulans with narrow polydispersity and Mp (molecular mass at the peak maximum) ranging from 180 Da to 708 kDa.

Table VI.S3. Associations (k_a) and dissociation (k_d) rates of ligand binding (1) and protein conformational change (2) fitted for sensograms obtained from 1, 2, and 3 interaction with CD44.

Ligand	k_{a1} [Ms^{-1}]	k_{d1} [s^{-1}]	k_{a1} [Ms^{-1}]	k_{d2}[s^{-1}]
HMW HA (**1**)	$(1.3\pm0.2)10^{7}$	$(2.4\pm0.7)10^{-5}$	$(4.6\pm3.0)10^{-2}$	$(1.3\pm1.8)10^{-2}$
LMW HA (**2**)	$(4.6\pm0.7)10^{4}$	$(2.5\pm2.3)10^{-2}$	$(3.4\pm0.4)\ 10^{-3}$	$(1.3\pm1.2)10^{-3}$
HEMA-g-HA (**3**)	$(2.6\pm0.7)10^{6}$	$(1.1\pm1.0)10^{-1}$	$(1.9\pm0.8)10^{-3}$	$(3.2\pm3.5)10^{-4}$

Calculation of the CD44 surface density and availability of HA: Given the molecular weight of CD44 (~200 kDa in dimer form) and the relation between response and protein density (1 RU = 1 pg/mm^2), we estimated a surface density of about 9 CD44 receptors per 1000 nm^2. The approximate projected area (A) for each polymer was calculated according to Equation VI.1

Equation VI.S1: $$A = \pi x R_g^2$$

where R_g is the radius of gyration of the respective polymer (Table VI.S4).

Table VI.S4. Surface density and availability of HA and octasaccharides per HA or HEMA-*g*-HA molecule.

HA polymer	R_g [nm]	Area [nm^2]	CD44:HA polymer	Octasaccharide per HA polymer
HMW HA (**1**)	130	53092	477	800
LMW HA (**2**)	3.3	35	0.31	2.8
HEMA-*g*-HA (**3**)	30	2827	25	22.4

According to Equation 1, **3** covers around 25 receptors, but we know from its structure (8 HA branches attached to a HEMA core) that each branch can only bind to one CD44 receptor.

Supplementary results

Characterization of poly-HEMA

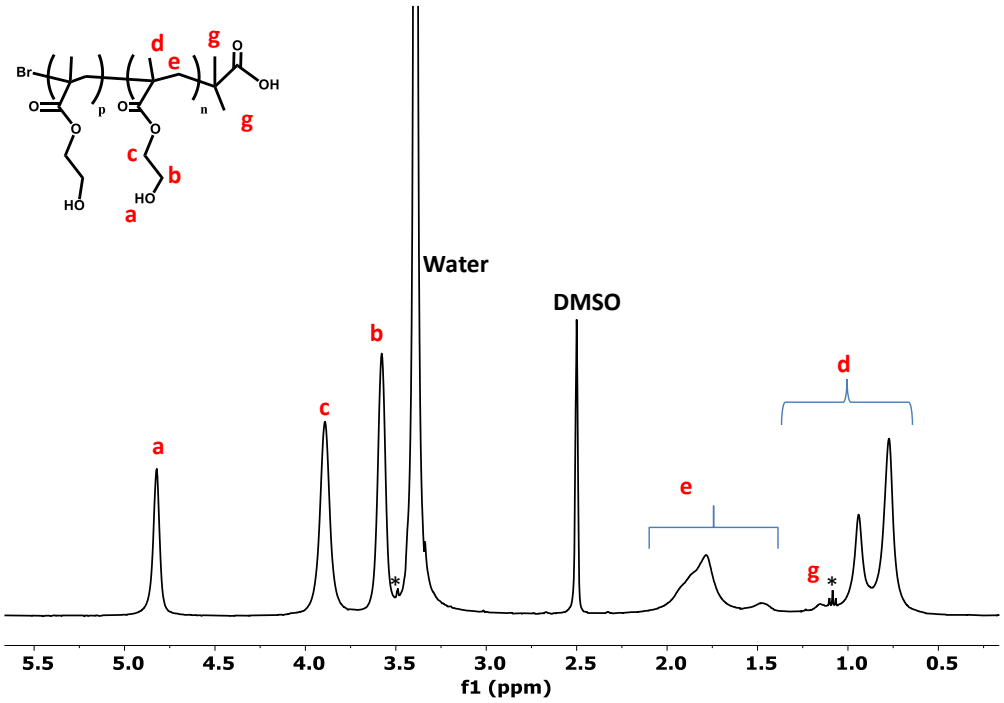

Figure VI.S1. Representative ^{1}H NMR (300 MHz, DMSO-d6, 298K) spectrum of poly-HEMA (Mn 62.4 Da, Mw 74.6 Da, PDI 1.20): δ 4.80 (br s, HEMA OH a); 3.90 (br s, c), G); 3.58 (br s, b); 2.00-1.40 (m, e); 1.20-0.80 (m, HEMA signals g+d).

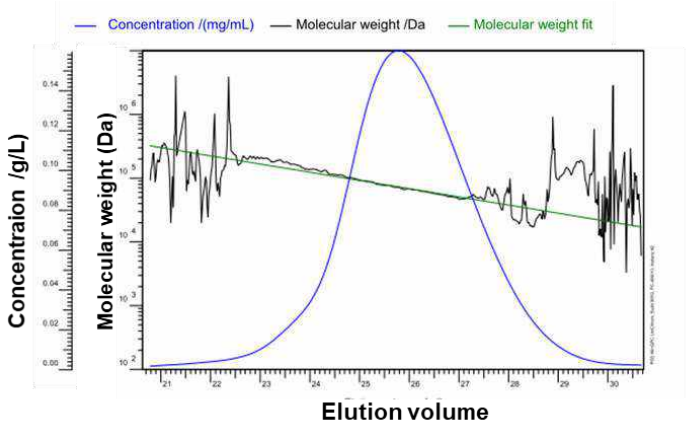

Figure VI.S2. GPC chromatogram of poly-HEMA (Mn 62.4 Da, Mw 74.6 Da, PDI 1.20) in DMF with 5 g/L LiBr. Blue line is the refractive index (concentrations detector) black signal is the Mw, and the green one is the molecular weight fit.

Characterization of HEMA-N-hydroxyphthalimide

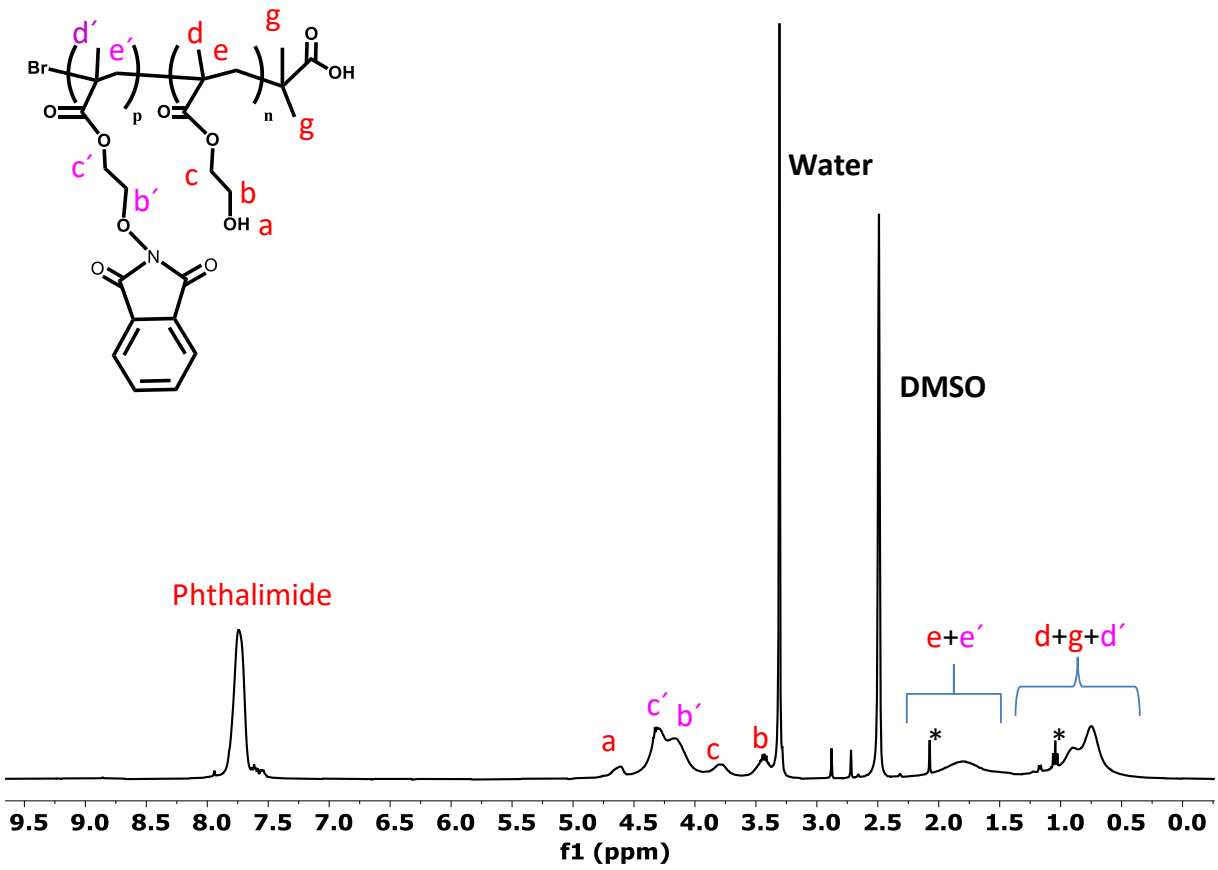

Figure VI.S3. Representative ^{1}H-NMR of the HEMA-phthalimide (300 MHz, DMSO-d6, 298 K) with 80 % of substitution with N-hydroxyphthalimide: δ 7.76 (br s, phthalimide), 4.65 (br s, a OH in HEMA), 4.30 (br s, c´); 4.20 (br s, b´); 3.85 (br s, c), 3.45 (br s, b); 2.2-1.40 (m, e+e´); 1.20-0.45 (m, HEMA signals d+g+ d´).

Characterization of HEMA-*g*-HA

GPC characterization

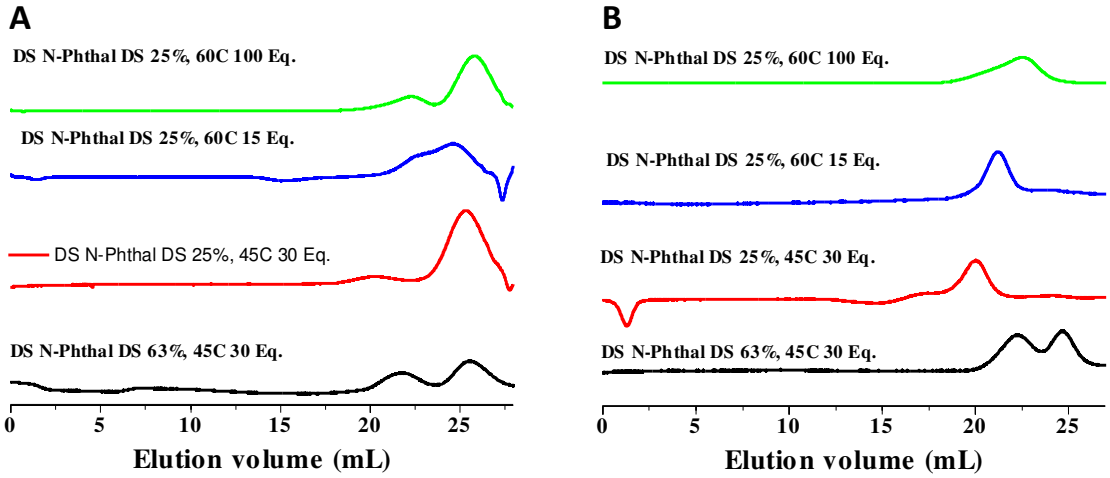

Figure VI.S4. Representative GPC chromatograms (RI detector) for HA-g-HEMA obtained at different reaction conditions (HEMA-N-hydroxyphthalimide with different degree of substitution (DS), temperature, and excess of HA) (A) before and (B) after ultrafiltration. Of note is the formation of bimodal products when N-hydroxyphthalimide with high DS is used.

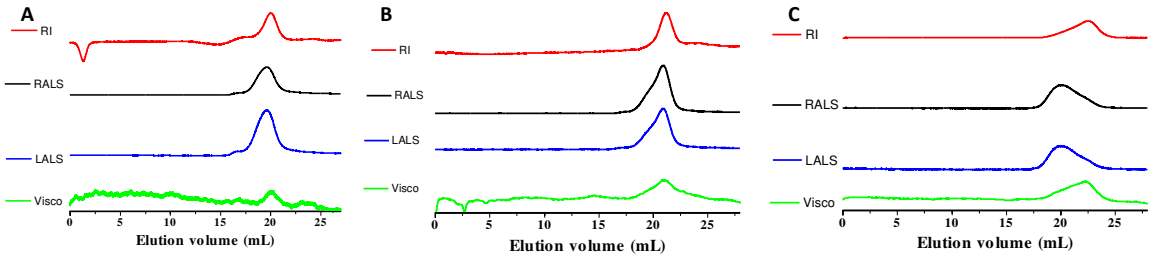

Figure VI.S5. GPC chromatograms of the HEMA-*g*-HA copolymer with (A) 1.4 HA chains, (B) 8.0 HA chains, and (C) 20 HA chains per HEMA core molecule. Color code: Refractive index detector (red), right-angle light scattering (90 degrees, black), low angle light scattering (7 degrees, blue), viscosimeter (green).

NMR characterization

The ^{1}H NMR spectra of the same HEMA-*g*-HA copolymers are shown below. We observed the appearance of a weak signal in the ^{1}H NMR spectra of the HEMA-*g*-HA copolymers (insets), which fit the oxime chemical shift and were assigned to the oxime NCH.[74] The spectra were recorded

in D_2O at several temperatures (25, 45, 60, 70, 80 °C) and in the D_2O:DMSO-d4 (1:1) mixtures at 60 and 70 °C to ensure that the aggregation of the polymer does not affect the DS calculated from these spectra.[75] For the calculation were: the 4.31 (br S, H2 of GlcNAc) signal was integrated versus 1.8-2.5 (m, Ac of GlcNAc and CH_2 of HEMA). The selection of the peaks is based on the strong overlap of all other peaks of HA and HEMA in the spectra. The analysis at different temperatures showed that the DS strongly decreases with a temperature increase from 25 to 60 °C and remains constant above this temperature. The sample with lower DS was turbid in water and was analyzed in DMSO/D2O at 60 and 70 °C where the determined DS was considerably lower. Samples with DS 8, *i.e.* HA polymer **3**, did not show difference in the determined DS between D_2O or DMSO/D_2O at 70 °C.

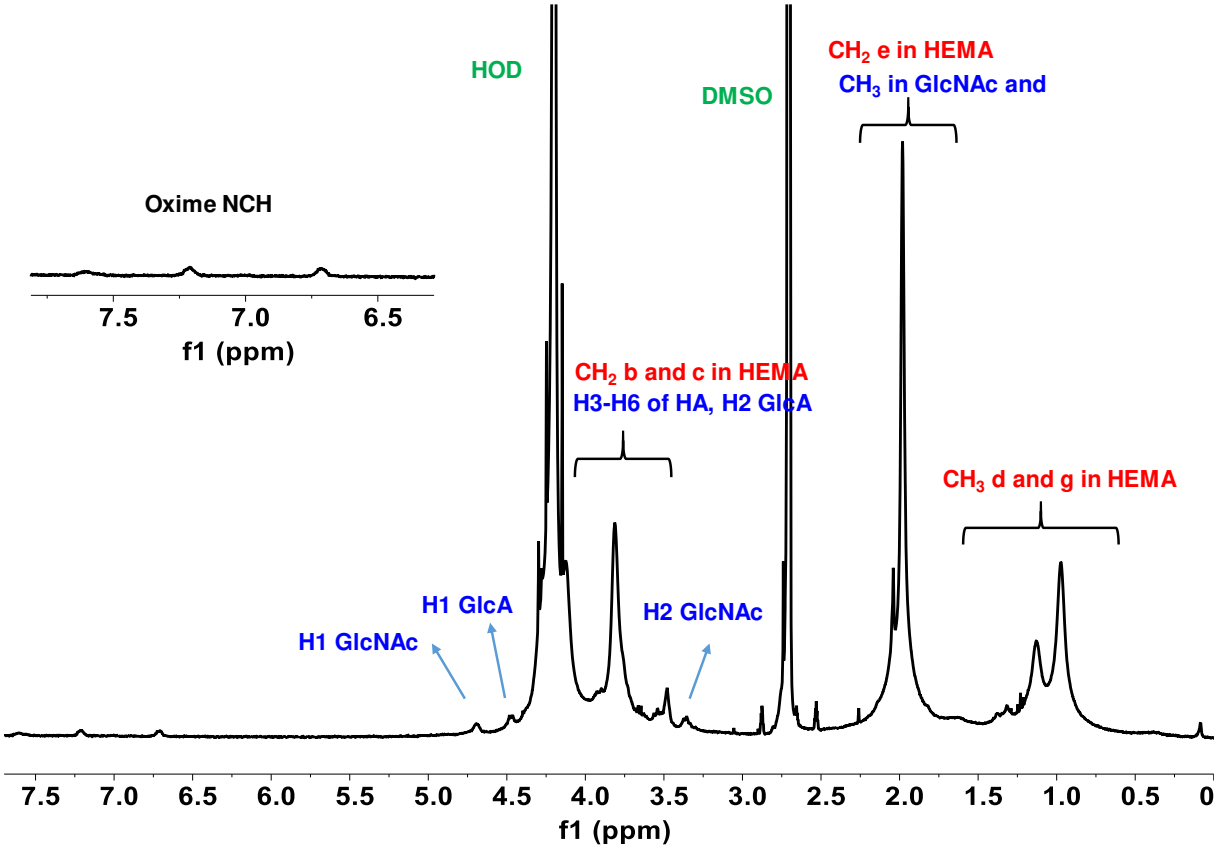

Figure VI.S6. ^{1}H-NMR spectrum (400 MHz, D_2O/DMSO 1/1, 343 K) of HEMA-*g*-HA (1.4 HA chains): δ 7.58 (br s, NHCH Oxime), 7.21 (br s, NHCH Oxime), 6.71 (br s, NHCH Oxime), 4.69 (br s, anomeric H1 of GlcNAc), 4.46 (br s, anomeric H1 of GlcNAc), 4.08 – 3.45 (m, H3-H6 of HA, H2 GlcA, CH2 b and c in HEMA), 3.35 (m, H2 of GlcNAc), 2.04 (s, CH_3 of GlcNAc), 1.98 (s, CH_2 e in HEMA), 1.5– 0.8 (m, CH_3 d in HEMA). The letters used for HEMA peaks identification are the same as in Figure VI.S3.

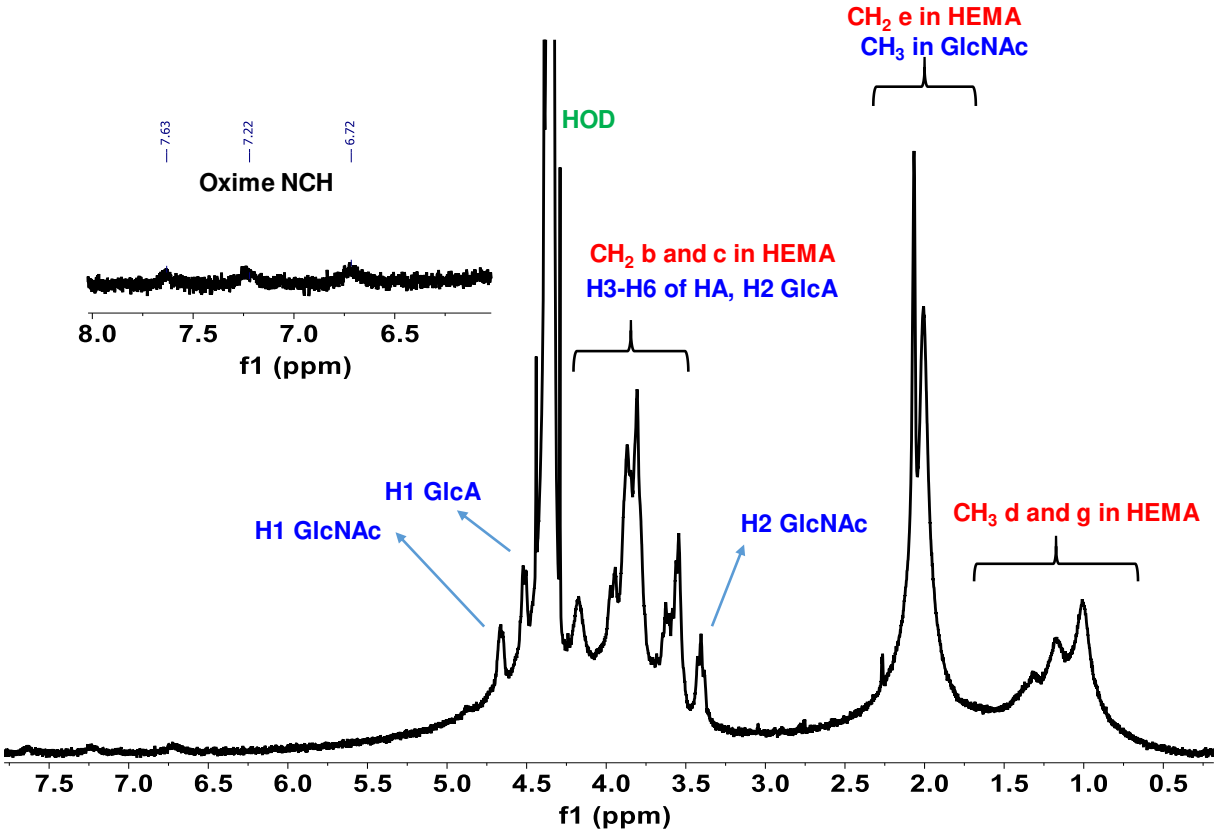

Figure VI.S7. ^{1}H-NMR spectrum (400 MHz, D_2O, 343 K) of HEMA-g-HA (8 HA chains, 3): δ 7.63 (br s, NHCH Oxime), 7.22 (br s, NHCH Oxime), 6.72 (br s, NHCH Oxime), 4.69 (br s, anomeric H1 of GlcNAc), 4.46 (br s, anomeric H1 of GlcNAc), 4.08 – 3.45 (m, H3-H6 of HA, H2 GlcA, CH2 b and c in HEMA), 3.40 (t, J 8.8 Hz, H2 of GlcNAc), 2.03 (s, CH3 of GlcNAc), 1.97 (s, CH_2 e in HEMA), 1.5– 0.8 (m, CH_3 d in HEMA).

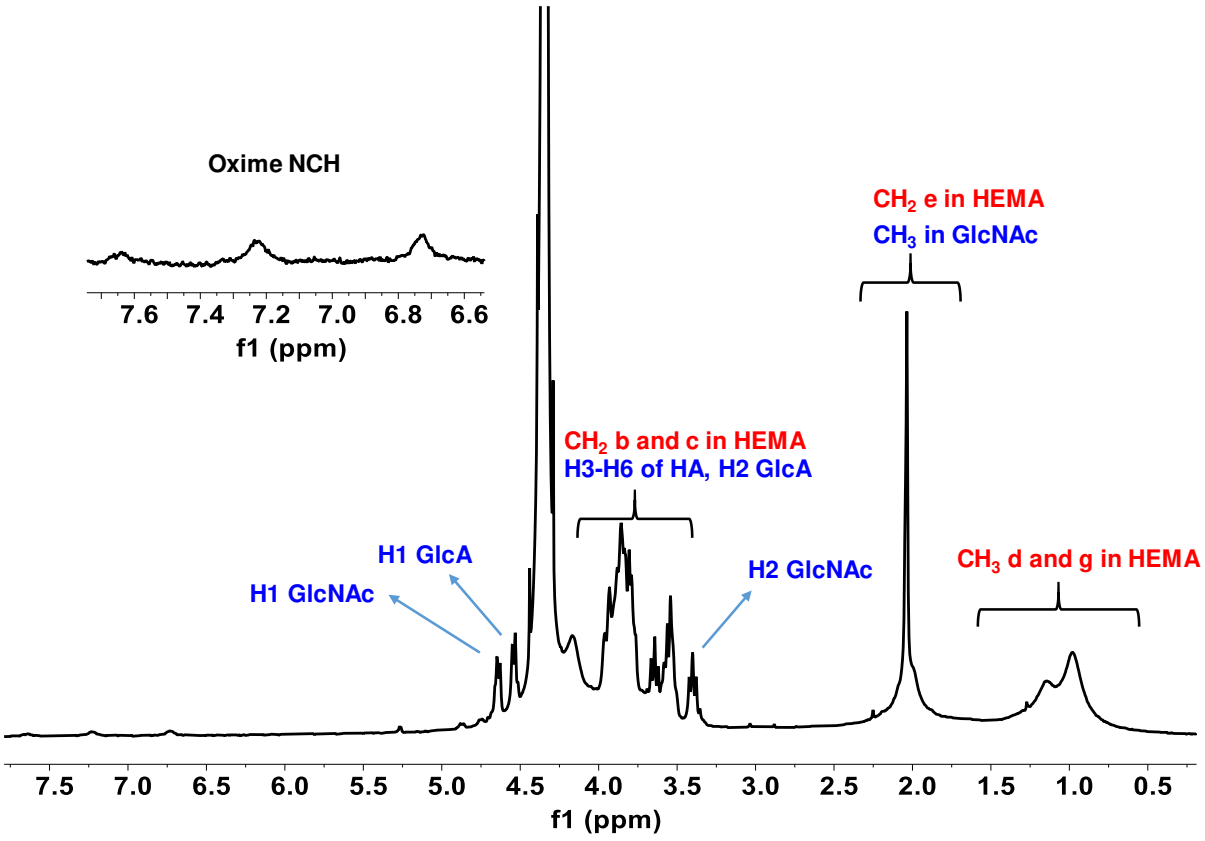

Figure VI.S8. ^{1}H-NMR spectrum (400 MHz, D_2O, 343 K) of HEMA-g-HA (20 HA chains): δ 7.64 (br s, NHCH oxime), 7.23 (br s, NHCH oxime), 6.73 (br s, NHCH oxime), 4.69 (br s, anomeric H1 of GlcNAc), 4.46 (br s, anomeric H1 of GlcNAc), 4.08 – 3.45 (m, H3-H6 of HA, H2 GlcA, CH2 b and c in HEMA), 3.40 (t, J 8.8 Hz, H2 of GlcNAc), 2.03 (s, CH_3 of GlcNAc), 1.97 (s, CH_2 e in HEMA), 1.5– 0.8 (m, CH_3 d in HEMA).

The apparent and the absolute molecular weight of the copolymers determined by GPC did not match the grafting degree determined by NMR (Table VI.S5). This difference can be explained by the used conventional calibration (made with homopolymer) that is not suitable for characterization of graft copolymers for which an additional detector is needed to determine the absolute molecular weight and the molar mass distribution.[76] Nevertheless, the absolute molecular weights were estimated by determining a mean dn/dc from the NMR composition, and the Mn fits relatively well for copolymers with high DS. In some cases, the copolymers with lower retention times, which in principle should have a higher molecular weight, showed a lower substitution degree by NMR (Table VI.S5). Since the product with shorter retention times is also slightly turbid in solution, we postulated that the incoherence between NMR and GPC is coming

from the aggregation behavior of the copolymer. To further confirm this hypothesis, we have hydrolyzed the oxime bond under acidic conditions (HCl 0.01 M, pH 2, 48 h) and the amount of the released HA was determined by GPC from the RI detector. It was previously confirmed that the selected acidic conditions do not hydrolyze HA. The data (Table VI.S5) show that after hydrolysis, more HA is released from the copolymers with higher DS and confirm the DS determined by NMR.

Table VI.S5. Characterization of HEMA-*g*-HA

HEMA-*g*-HA	App. Mn (kDa), PDI	Abs. Mn (kDa), PDI	NMR Mn (kDa)	Rg, Rh (nm) by SLS	Rg/Rh	Max shift in GPC	Number of HA chains (DS in %) by NMR	mass % of HA (NMR)	mass % of HA (GPC after hydrolysis)
Low DS	366, 1.44	6600, 1.28	69	35, 31	1.1	5.5	1.4 (0.29%)	10%	9%
Medium DS (**3**)	230, 1.43	2200, 1.44	105	30, 16	1.9	4.7	8 (1.6%)	39%	34%
High DS	116, 1.69	215, 2.01	180	26, 11	2.3	3.5	23 (4.6%)	64%	58%

Single-injection ITC kinetics measurements

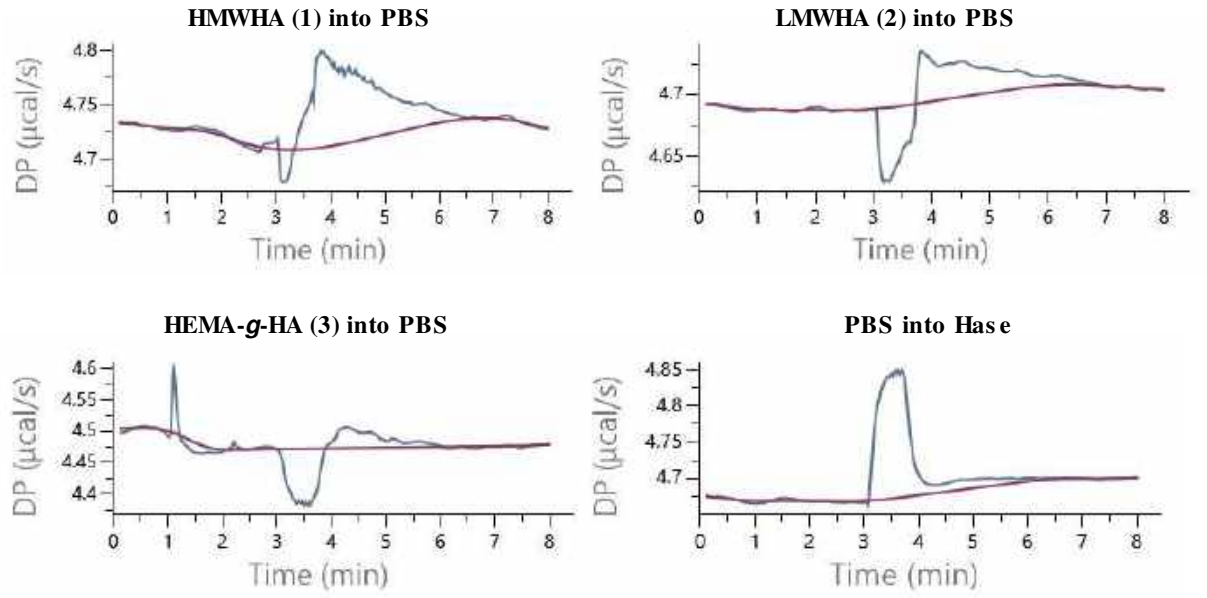

Figure VI.S9. Control titration experiments showing the changes in differential power (DP, µW) after injection of 1-3 (20 µL injection) into PBS or the PBS into the HYAL solution.

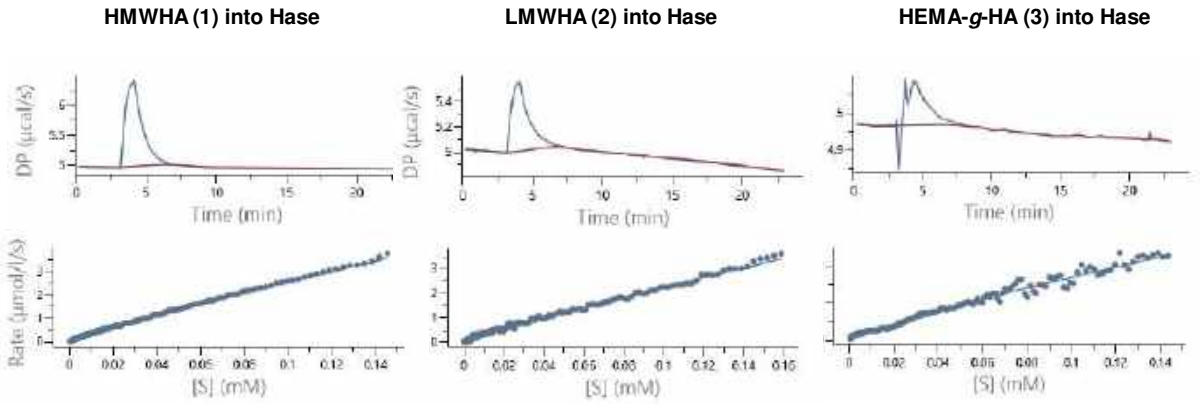

Figure VI.S10. Representative single-injection isotherms (top) and data fitting using the Michaelis–Menten model (bottom) for the HYAL mediated hydrolysis of 1-3.

Surface plasmon resonance (SPR)

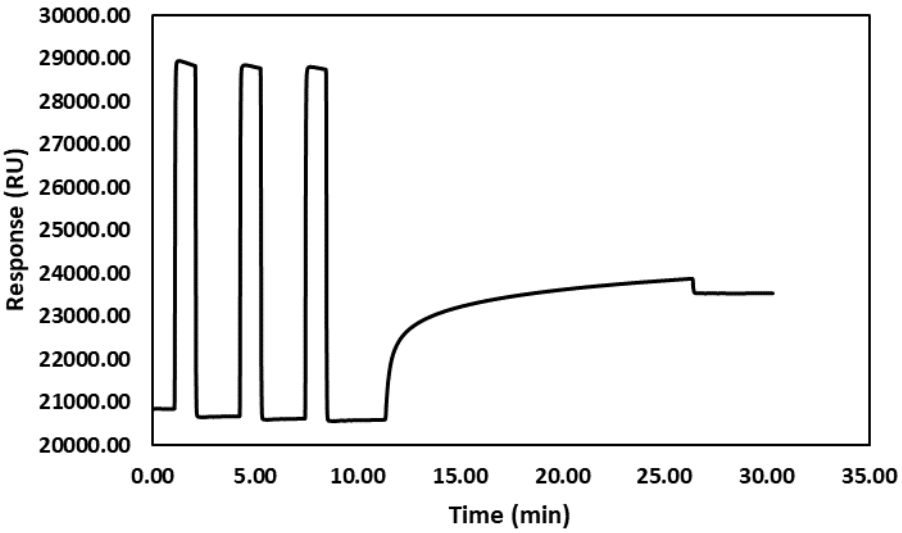

Figure VI.S11. Representative sensogram showing the immobilization of CD44 on the SPR chip: after chip conditioning with 1M NaCl in 50 mM NaOH (first 3 peaks) and equilibration (baseline), CD44-biotin was injected for 15 minutes (4th curve).

Cell culture and transfection

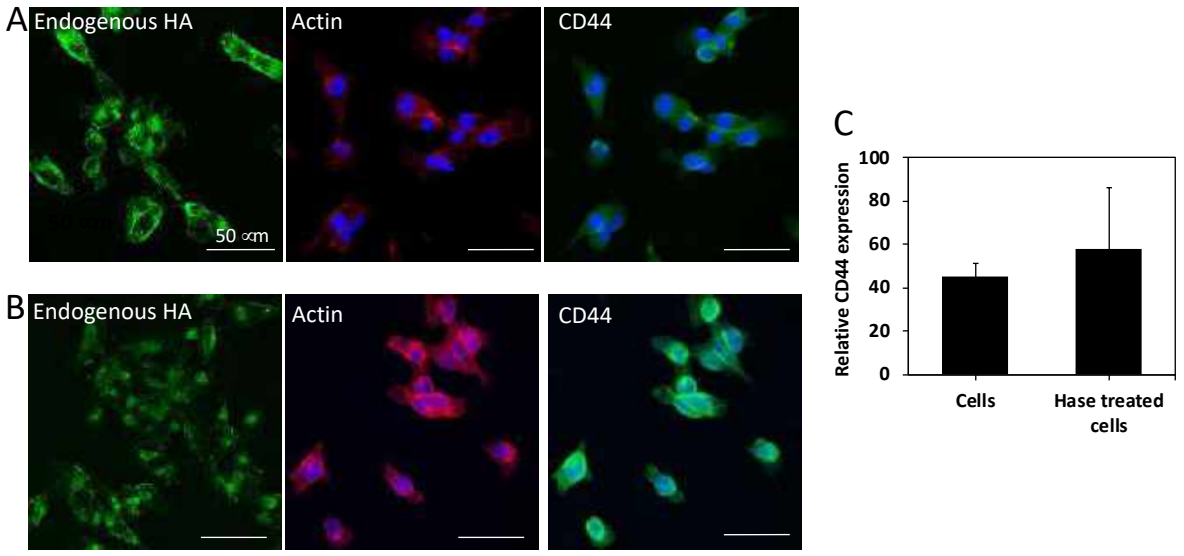

Figure VI.S12. Representative confocal microscopy images showing (A) MDA-MB-231 cells and (B) MDA-MB-231 cells treated with HYAL. Cells were stained with labeled-HA binding protein against endogenous hyaluronan (green, left images), with phalloidin (actin, red, center images) and DAPI (DNA, blue), and with labeled antibodies against CD44 (green, right images). (C) Relative CD44 expression on MDA-MB-231 cells and MDA-MB-231 cells treated with HYAL (signal intensity was determined from confocal images). No significant differences were found, n=3.

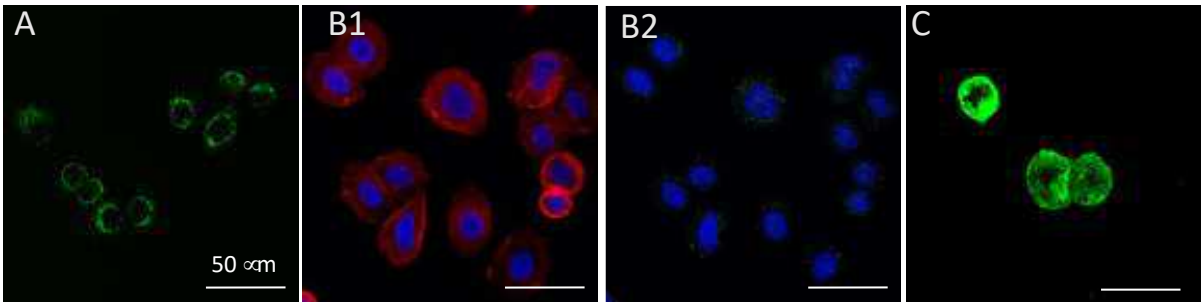

Figure VI.S13. Representative confocal microscopy images showing Sk-Br-3 cells stained with (A) labeled-HA binding protein (green), (B) phalloidin (actin, B1), and immunostained for CD44 (B2), and DAPI (nucleus, blue), (C) transfected with CD44-GFP.

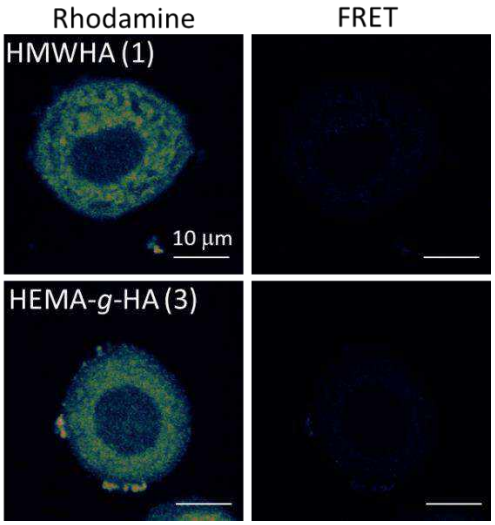

Figure VI.S14. Confocal microscopy images showing Sk-Br-3 treated with Rho-labelled HMW HA (1) and HEMA-*g*-HA (3) and corresponding crosstalk to FRET channel (right).

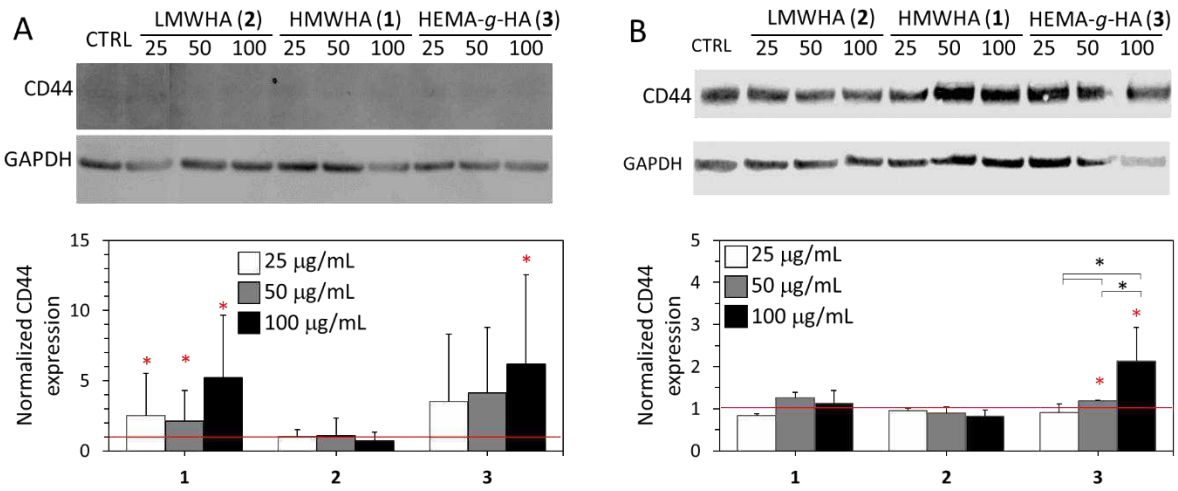

Figure VI.S15. Representative Western blot of CD44 (GAPDH was used as a loading control) and densitometry analysis, in which the CD44 expression was normalized to the loading control (GAPDH) and the control sample (cells treated with growth medium, red line) for (A) Sk-Br-3 cells and (B) MDA-MB-231 cells. Statistical differences to the control sample are shown in red and between treatments in black (*$p < 0.05$, n=3)

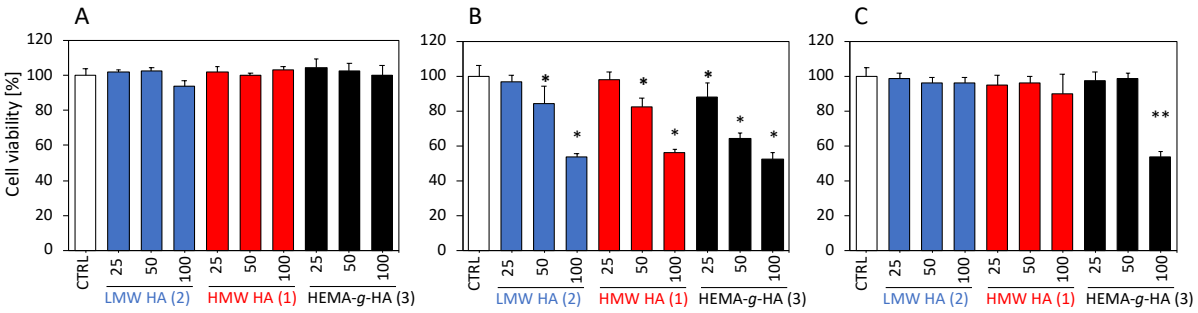

Figure VI.S16. Cell viability determined by MTS assay for cultures supplemented with 1-3 at different concentrations: (A) MDA-MB-231 cells, 2 h after the supplementation; (B) Sk-Br-3 cells, 2 h after the supplementation; and (C) Sk-Br-3 cells, 24 h after the supplementation. Significant differences to the control samples are marked *p< 0.05 and **p<0.01, n=3.

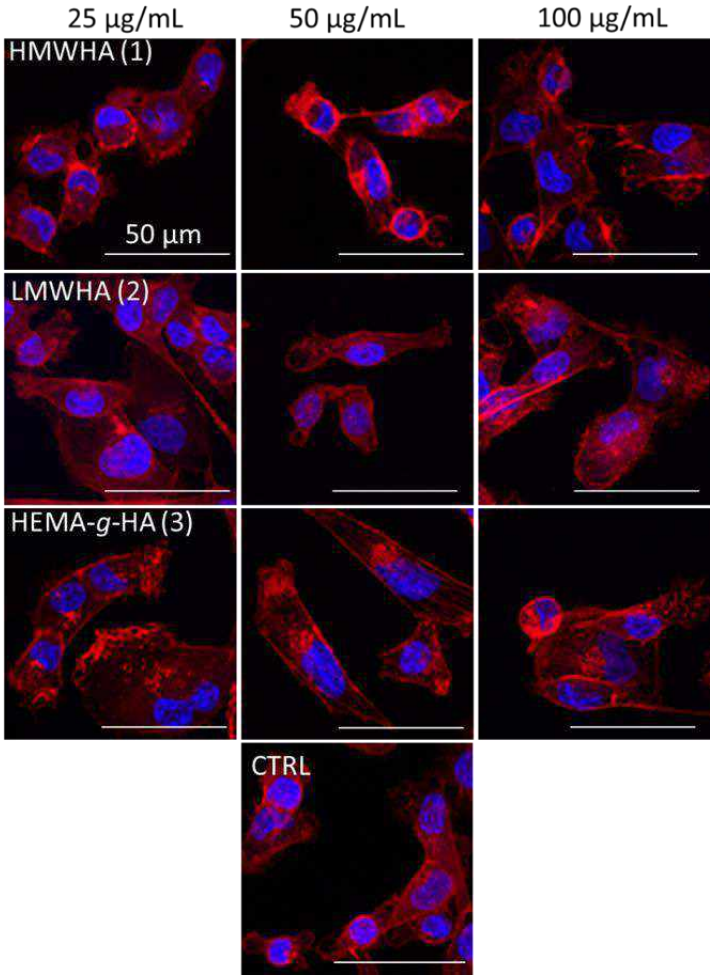

Figure VI.S17. MDA-MB-231 cells treated with HYAL (250 µg/mL, 1 h) and supplemented with 1-3 at different concentrations (25, 50 or 100 µg/mL) for 2 h. Actin was stained with phalloidin (red) and DNA with DAPI (blue).

VI.6. REFERENCES

1. Toole, B.P., *Hyaluronan: From extracellular glue to pericellular cue.* Nature Reviews Cancer, 2004. **4**(7): p. 528-539.
2. Liu, M.H., C. Tolg, and E. Turley, *Dissecting the Dual Nature of Hyaluronan in the Tumor Microenvironment.* Frontiers in Immunology, 2019. **10**.
3. Garantziotis, S. and R.C. Savani, *Hyaluronan biology: A complex balancing act of structure, function, location and context.* Matrix Biology, 2019. **78-79**: p. 1-10.
4. Amorim, S., et al., *Molecular weight of surface immobilized hyaluronic acid influences CD44-mediated binding of gastric cancer cells.* Scientific Reports, 2018. **8**.
5. Auvinen, P., et al., *Hyaluronan in peritumoral stroma and malignant cells associates with breast cancer spreading and predicts survival.* American Journal of Pathology, 2000. **156**(2): p. 529-536.
6. Heldin, P., et al., *Deregulation of hyaluronan synthesis, degradation and binding promotes breast cancer.* Journal of Biochemistry, 2013. **154**(5): p. 395-408.
7. Cox, T.R., *The matrix in cancer.* Nature Reviews Cancer, 2021. **21**(4): p. 217-238.
8. Vignal, P., et al., *Sonographic morphology of infiltrating breast carcinoma - Relationship with the shape of the hyaluronan extracellular matrix.* Journal of Ultrasound in Medicine, 2002. **21**(5): p. 531-538.
9. Simpson, M.A., et al., *Manipulation of hyaluronan synthase expression in prostate adenocarcinoma cells alters pericellular matrix retention and adhesion to bone marrow endothelial cells.* Journal of Biological Chemistry, 2002. **277**(12): p. 10050-10057.
10. Veiseh, M., et al., *Cellular heterogeneity profiling by hyaluronan probes reveals an invasive but slow-growing breast tumor subset.* Proceedings of the National Academy of Sciences of the United States of America, 2014. **111**(17): p. E1731-E1739.
11. Cieply, B., C. Koontz, and S.M. Frisch, *CD44S-hyaluronan interactions protect cells resulting from EMT against anoikis.* Matrix Biology, 2015. **48**: p. 55-65.
12. Carvalho, A.M., et al., *Co-localization and crosstalk between CD44 and RHAMM depend on hyaluronan presentation.* Acta Biomaterialia, 2021. **119**: p. 114-124.
13. Misra, S., S. Ghatak, and B.P. Toole, *Regulation of MDR1 expression and drug resistance by a positive feedback loop involving hyaluronan, phosphoinositide 3-kinase, and ErbB2.* Journal of Biological Chemistry, 2005. **280**(21): p. 20310-20315.
14. Lee, J.T., L.S. Steelman, and J.A. McCubrey, *Phosphatidylinositol 3 '-kinase activation leads to multidrug resistance protein-1 expression and subsequent chemoresistance in advanced prostate cancer cells.* Cancer Research, 2004. **64**(22): p. 8397-8404.
15. Slomiany, M.G., et al., *Hyaluronan, CD44, and Emmprin Regulate Lactate Efflux and Membrane Localization of Monocarboxylate Transporters in Human Breast Carcinoma Cells.* Cancer Research, 2009. **69**(4): p. 1293-1301.
16. Yang, C.X., et al., *The High and Low Molecular Weight Forms of Hyaluronan Have Distinct Effects on CD44 Clustering.* Journal of Biological Chemistry, 2012. **287**(51): p. 43094-43107.
17. Slomiany, M.G., et al., *Inhibition of Functional Hyaluronan-CD44 Interactions in CD133-positive Primary Human Ovarian Carcinoma Cells by Small Hyaluronan Oligosaccharides.* Clinical Cancer Research, 2009. **15**(24): p. 7593-7601.
18. Toole, B.P., S. Ghatak, and S. Misra, *Hyaluronan oligosaccharides as a potential anticancer therapeutic.* Current Pharmaceutical Biotechnology, 2008. **9**(4): p. 249-252.
19. Urakawa, H., et al., *Therapeutic potential of hyaluronan oligosaccharides for bone metastasis of breast cancer.* Journal of Orthopaedic Research, 2012. **30**(4): p. 662-672.
20. Tolg, C., et al., *Hyaluronan and RHAMM in Wound Repair and the "Cancerization" of Stromal Tissues.* Biomed Research International, 2014. **2014**.
21. Bourguignon, L.Y.W., et al., *Interaction of low molecular weight hyaluronan with CD44 and toll-like receptors promotes the actin filament-associated protein 110-actin binding and MyD88-NF kappa B signaling leading to proinflammatory cytokine/chemokine production and breast tumor invasion.* Cytoskeleton, 2011. **68**(12): p. 671-693.

22. Yu, Q. and I. Stamenkovic, *Localization of matrix metalloproteinase 9 to the cell surface provides a mechanism for CD44-mediated tumor invasion.* Genes & Development, 1999. **13**(1): p. 35-48.
23. Xu, X.M., et al., *A peptide with three hyaluronan binding motifs inhibits tumor growth and induces apoptosis.* Cancer Research, 2003. **63**(18): p. 5685-5690.
24. Song, G.L., et al., *HI44a, an anti-CD44 monoclonal antibody, induces differentiation and apoptosis of human acute myeloid leukemia cells.* Leukemia Research, 2004. **28**(10): p. 1089-1096.
25. Jin, L.Q., et al., *Targeting of CD44 eradicates human acute myeloid leukemic stem cells.* Nature Medicine, 2006. **12**(10): p. 1167-1174.
26. Tremmel, M., et al., *A CD44v6 peptide reveals a role of CD44 in VEGFR-2 signaling and angiogenesis.* Blood, 2009. **114**(25): p. 5236-5244.
27. Matzke, A., et al., *A five-amino-acid peptide blocks Met- and Ron-dependent cell migration.* Cancer Research, 2005. **65**(14): p. 6105-6110.
28. Khan, F., et al., *Identification of novel CD44v6-binding peptides that block CD44v6 and deliver a pro-apoptotic peptide to tumors to inhibit tumor growth and metastasis in mice.* Theranostics, 2021. **11**(3): p. 1326-1344.
29. Peck, D. and C.M. Isacke, *Hyaluronan-dependent cell migration can be blocked by a CD44 cytoplasmic domain peptide containing a phosphoserine at position 325.* Journal of Cell Science, 1998. **111**: p. 1595-1601.
30. Piotrowicz, R.S., et al., *A6 Peptide Activates CD44 Adhesive Activity, Induces FAK and MEK Phosphorylation, and Inhibits the Migration and Metastasis of CD44-Expressing Cells.* Molecular Cancer Therapeutics, 2011. **10**(11): p. 2072-2082.
31. Misra, S., et al., *Delivery of CD44 shRNA/Nanoparticles within Cancer Cells perturbation of hyaluronan/CD44v6 interactions and reduction in a adenoma growth in Apc Min/ plus MICE.* Journal of Biological Chemistry, 2009. **284**(18): p. 12432-12446.
32. Beers, K.L., et al., *Atom Transfer Radical Polymerization of 2-Hydroxyethyl Methacrylate.* Macromolecules, 1999. **32**(18): p. 5772-5776.
33. Stern, R. and M.J. Jedrzejas, *Hyaluronidases: Their Genomics, Structures, and Mechanisms of Action.* Chemical Reviews, 2006. **106**(3): p. 818-839.
34. Fang, S., A.-M.A. Hays Putnam, and M.J. LaBarre, *Kinetic investigation of recombinant human hyaluronidase PH20 on hyaluronic acid.* Analytical Biochemistry, 2015. **480**: p. 74-81.
35. Carvalho, A.M., et al., *Co-localization and crosstalk between CD44 and RHAMM depend on hyaluronan presentation.* Acta Biomaterialia, 2021. **119**: p. 114-124.
36. Yang, C., et al., *The high and low molecular weight forms of hyaluronan have distinct effects on CD44 clustering.* The Journal of biological chemistry, 2012. **287**(51): p. 43094-43107.
37. Schatz, C. and S. Lecommandoux, *Polysaccharide-Containing Block Copolymers: Synthesis, Properties and Applications of an Emerging Family of Glycoconjugates.* Macromolecular Rapid Communications, 2010. **31**(19): p. 1664-1684.
38. Bonduelle, C., et al., *Synthesis and self-assembly of "tree-like" amphiphilic glycopolypeptides.* Chemical Communications, 2012. **48**(67): p. 8353-8355.
39. Duan, H.H., et al., *Multivalent and multifunctional polysaccharide-based particles for controlled receptor recognition.* Scientific Reports, 2018. **8**.
40. Duan, H.H., et al., *Hyaluronic-Acid-Presenting Self-Assembled Nanoparticles Transform a Hyaluronidase HYAL1 Substrate into an Efficient and Selective Inhibitor.* Angewandte Chemie-International Edition, 2020. **59**(32): p. 13591-13596.
41. Novoa-Carballal, R., et al., *Star-Like Glycosaminoglycans with Superior Bioactivity Assemble with Proteins into Microfibers.* Chemistry-a European Journal, 2018. **24**(54): p. 14341-14345.
42. Kiessling, L.L. and J.C. Grim, *Glycopolymer probes of signal transduction.* Chemical Society Reviews, 2013. **42**(10): p. 4476-4491.
43. Montheard, J.P., M. Chatzopoulos, and D. Chappard, *2-Hydroxyethyl Methacrylate (HEMA) - Chemical properties and applications in biomedical fields.* Journal of Macromolecular Science-Reviews in Macromolecular Chemistry and Physics, 1992. **C32**(1): p. 1-34.
44. Zare, M., et al., *pHEMA: An Overview for Biomedical Applications.* International Journal of Molecular Sciences, 2021. **22**(12): p. 6376.
45. Silva, C., et al., *Design of protein delivery systems by mimicking extracellular mechanisms for protection of growth factors.* Acta Biomaterialia, 2017. **63**: p. 283-293.

46. Antonietti, M., et al., *Determination of the Micelle Architecture of Polystyrene Poly(4-Vinylpyridine) Block-Copolymers in Dilute-Solution.* Macromolecules, 1994. **27**(12): p. 3276-3281.
47. Esquenet, C. and E. Buhler, *Aggregation behavior in semidilute rigid and semirigid polysaccharide solutions.* Macromolecules, 2002. **35**(9): p. 3708-3716.
48. Nehme, R., et al., *Kinetic theory of hyaluronan cleavage by bovine testicular hyaluronidase in standard and crowded environments.* Biochimica Et Biophysica Acta-General Subjects, 2021. **1865**(3).
49. Silva, C., et al., *Following the enzymatic digestion of chondroitin sulfate by a simple GPC analysis.* Analytica Chimica Acta, 2015. **885**: p. 207-213.
50. Stern, R. and M.J. Jedrzejas, *Hyaluronidases: Their genomics, structures, and mechanisms of action.* Chemical Reviews, 2006. **106**(3): p. 818-839.
51. Deschrevel, B., F. Tranchepain, and J.C. Vincent, *Chain-length dependence of the kinetics of the hyaluronan hydrolysis catalyzed by bovine testicular hyaluronidase.* Matrix Biology, 2008. **27**(5): p. 475-486.
52. Vercruysse, K.P., A.R. Lauwers, and J.M. Demeester, *Kinetic investigation of the degradation of hyalurinan by hyaluronidase using gel-permeation chromatography.* Journal of Chromatography B-Biomedical Applications, 1994. **656**(1): p. 179-190.
53. Fayad, S., et al., *Hyaluronidase reaction kinetics evaluated by capillary electrophoresis with UV and high-resolution mass spectrometry (HRMS) detection.* Analytica Chimica Acta, 2017. **951**: p. 140-150.
54. Todd, M.J. and J. Gomez, *Enzyme kinetics determined using calorimetry: A general assay for enzyme activity?* Analytical Biochemistry, 2001. **296**(2): p. 179-187.
55. Wang, Y., et al., *Enzyme Kinetics by Isothermal Titration Calorimetry: Allostery, Inhibition, and Dynamics.* Frontiers in Molecular Biosciences, 2020. **7**.
56. Fang, S.P., A. Putnam, and M.J. LaBarre, *Kinetic investigation of recombinant human hyaluronidase PH20 on hyaluronic acid.* Analytical Biochemistry, 2015. **480**: p. 74-81.
57. Valcarcel, J., et al., *Hyaluronic acid of tailored molecular weight by enzymatic and acid depolymerization.* International Journal of Biological Macromolecules, 2020. **145**: p. 788-794.
58. Cowman, M.K. and S. Matsuoka, *Experimental approaches to hyaluronan structure.* Carbohydrate Research, 2005. **340**(5): p. 791-809.
59. Mizrahy, S., et al., *Hyaluronan-coated nanoparticles: The influence of the molecular weight on CD44-hyaluronan interactions and on the immune response.* Journal of Controlled Release, 2011. **156**(2): p. 231-238.
60. Ogino, S., et al., *Two-State Conformations in the Hyaluronan-Binding Domain Regulate CD44 Adhesiveness under Flow Condition.* Structure, 2010. **18**(5): p. 649-656.
61. Zwanzig, R., *Two-state models of protein folding kinetics.* Proceedings of the National Academy of Sciences of the United States of America, 1997. **94**(1): p. 148-150.
62. Banerji, S., et al., *Structures of the Cd44-hyaluronan complex provide insight into a fundamental carbohydrate-protein interaction.* Nature Structural & Molecular Biology, 2007. **14**(3): p. 234-239.
63. Wolny, P.M., et al., *Analysis of CD44-Hyaluronan Interactions in an artificial membrane system: Insights into the distinct binding properties of high and low molecular weight hyaluronan* Journal of Biological Chemistry, 2010. **285**(39): p. 30170-30180.
64. Lesley, J., et al., *Hyaluronan binding by cell surface CD44.* Journal of Biological Chemistry, 2000. **275**(35): p. 26967-26975.
65. Banerji, S., et al., *Distinctive Properties of the Hyaluronan-binding Domain in the Lymphatic Endothelial Receptor Lyve-1 and Their Implications for Receptor Function.* Journal of Biological Chemistry, 2010. **285**(14): p. 10724-10735.
66. Carvalho, A.M., et al., *Redox-Responsive Micellar Nanoparticles from Glycosaminoglycans for CD44 Targeted Drug Delivery.* Biomacromolecules, 2018. **19**(7): p. 2991-2999.
67. Sheridan, C., et al., *CD44(+)/CD24(-) breast cancer cells exhibit enhanced invasive properties: an early step necessary for metastasis.* Breast Cancer Research, 2006. **8**(5).
68. Li, W.Z., et al., *Unraveling the roles of CD44/CD24 and ALDH1 as cancer stem cell markers in tumorigenesis and metastasis.* Scientific Reports, 2017. **7**.
69. Novoa-Carballal, R., et al., *Star-Like Glycosaminoglycans with Superior Bioactivity Assemble with Proteins into Microfibers.* Chemistry – A European Journal, 2018. **24**: p. 14341-14345.
70. Wendeler, M., et al., *Enhanced Catalysis of Oxime-Based Bioconjugations by Substituted Anilines.* Bioconjugate Chemistry, 2014. **25**(1): p. 93-101.

71. Adharis, A., et al., *Synthesis and Self-Assembly of Double-Hydrophilic and Amphiphilic Block Glycopolymers.* Biomacromolecules, 2019. **20**(3): p. 1325-1333. Altohught the dn/dc is not included in the article the value was provided by the auhtors.
72. Gallow, K.C., et al., *Influence of gradient strength and composition profile on the onset of the cloud point transition in hydroxyethyl methacrylate/dimethylaminoethyl methacrylate gradient copolymers.* Polymer, 2012. **53**(5): p. 1131-1137.
73. Han, Y., et al., *Impact of refractive index increment on the determination of molecular weight of hyaluronic acid by muti-angle laser light-scattering technique.* Scientific Reports, 2020. **10**(1): p. 1858.
74. Novoa-Carballal, R. and A.H.E. Müller, *Synthesis of Polysaccharide-b-PEG Block Copolymers by Oxime Click.* Chemical Communications, 2012. **48**(31): p. 3781-3783.
75. Novoa-Carballal, R., R. Riguera, and E. Fernandez-Megia, *Disclosing an NMR-Invisible Fraction in Chitosan and PEGylated Copolymers and Its Role on the Determination of Degrees of Substitution.* Molecular Pharmaceutics, 2013. **10**(8): p. 3225–3231.
76. Pasch, H. and B. Trathnigg, *HPLC of Polymers*. 1999.

CHAPTER VII

REDOX-RESPONSIVE MICELLAR NANOPARTICLES FROM GLYCOSAMINOGLYCANS FOR CD44 TARGETED DRUG DELIVERY

REDOX-RESPONSIVE MICELLAR NANOPARTICLES FROM GLYCOSAMINOGLYCANS FOR CD44 TARGETED DRUG DELIVERY

Abstract

Cancer progression is associated with overexpression of various receptors at the cell surface. Among these, CD44 is known to recognize and bind specifically hyaluronan (HA) and interact with less affinity to other glycosaminoglycans (GAGs), such as chondroitin sulfate (CS). In this study, we describe a simple method to obtain micellar nanoparticles with GAGs shell (HA or CS) as potential drug delivery systems that target cancer cells overexpressing CD44. Alkane thiol was conjugated at the reducing end of the respective GAG using highly efficient oxime chemistry. The alkane moiety confers amphiphilic behavior to the obtained conjugates and triggers their self-assembly into micellar nanoparticles, while the thiol group adds redox-responsiveness to the system. The properties of the particles depend on the used GAG: HA amphiphiles form more dense, smaller assemblies that are redox-sensitive. Both systems allow encapsulation of either hydrophobic or hydrophilic cargos with high efficiency. We demonstrate that the GAGs exposed on the surface of the nanoparticles are with preserved bioactivity and recognized by the cellular receptors: the particles were internalized via CD44 dependent pathways.

This chapter is based on the following publication:

Carvalho, Ana M.; Teixeira, Raquel; Novoa-Carballal, Ramón; Pires, Ricardo A.; Rui L.; Pashkuleva, Iva: "Redox-responsive micellar nanoparticles from glycosaminoglycans for CD44 targeted drug delivery" Biomacromolecules, 2018, 19, 7, 2991-2999

VII.1. INTRODUCTION

Conventional cancer therapeutics aim at selective cancer cell death and rely on exhaustive screenings of bioactive molecules that target different predefined hallmarks.[1-3] Despite the undeniable success of this approach, numerous molecules that have shown great therapeutic potential in vitro are ineffective against tumors *in vivo* and cause several side effects.[4] Usually, such failure is not associated with the pharmacodynamics (interaction of the drug with the target), but with the drug pharmacokinetics, biodistribution, and bioaccumulation.[3, 5] Nanotechnology offers an opportunity to improve the efficacy of such molecules by enhancing their solubility and stability via encapsulation in biocompatible and non-toxic nanoparticles and also by modulation of the release process in terms of targeting, triggering, and kinetics using nanoparticles with precisely tailored composition.[5-7] In such strategies, the peculiar tumor microenvironment can be used as a target because it is abundant in various biomolecules with altered expression. It can also be used as a triggering stimulus because of the changed pH and redox status as compared to the microenvironment of healthy cells.[8-12]_ENREF_8

Glycosaminoglycans (GAGs) are used as a hallmark of different cancers: they are associated with cancer development, metastasis, and invasiveness and exercise their role via interactions with specific membrane receptors that are also overexpressed in cancer cells.[13-17] An example is CD44, the main hyaluronan (HA) receptor that also binds other GAGs although with less affinity.[18-22] In fact, HA-CD44 interactions are already used as targets in different anticancer strategies.[8, 23-26] The most common strategy involves using GAG (HA or chondroitin sulfate, CS) decorated carriers of different compositions, shapes, and sizes that have loaded bioactive molecules. Such carriers improve the therapeutic efficacy of the cargo because of their ability to deliver it at the target, *i.e.*, the cancer cells that are identified by the carriers via the CD44 overexpression. The incorporation of the GAG can be achieved by different approaches. Usually, the functionalization of the GAG is performed in a side-on fashion via the –COOH groups of the uronic acid units.[10, 22, 24, 27, 28] Such an approach can compromise the CD44 targeting as it alters dramatically the GAG flexibility, *i.e.,* its ability to reorganize, adapt and bind multivalent to CD44; as well as its charge and polarity – the main driving forces in recognition processes.[29-31] Alternative end-on functionalization at the GAG reducing end has been proposed recently to

overcome this problem.[32, 33] This approach involves modifying the HA by introducing an alkyne function at the reducing end that further participates in Huisgen cycloaddition with an azido functionalized counterpart. Block co-polymers of HA generated by this approach self-assemble into polymersomes whose internalization by the cells is dependent on CD44 expression.

Herein, we propose an alternative, simple strategy for the end-on functionalization of GAGs (HA and CS). We demonstrate that GAG amphiphiles can be obtained in one step from aminooxy alkanethiol and GAG at mild conditions via oxime ether formation. The generated amphiphiles self-assemble into micellar nanoparticles that can be loaded with either hydrophilic or hydrophobic cargos. The thiol groups confer redox-responsiveness of the assembled carriers. This feature of the nanoparticles is advantageous for cancer treatment because of the significantly higher concentration of glutathione (GSH) in the cytosol of tumor cells compared to healthy ones.[9, 10]

VII.2. Materials and Methods

VII.2.1 Materials.

Sodium hyaluronate (HA) from Lifecore (USA) and chondroitin sulfate (CS) from Kraeber (Germany) were used in this study. All other reagents (analytical grade) were purchased from Sigma-Aldrich and used as received.

VII.2.2 Synthesis of glycosaminoglycan amphiphiles.

11-(Aminooxy)-1-undecanethiol (3 mol excess to GAG) was dissolved in 5 mL ethanol (for the synthesis of HA amphiphile), or 5 mL dimethyl sulfoxide (in the case of CS amphiphile), followed by the addition of 200 mg of HA or CS dissolved in 5 mL acetate buffer (78 mM acetic acid and 62.5 mM sodium acetate, pH 4.5). The reaction mixture was magnetically stirred at 45 °C for 24 h. Unreacted reagents were removed by dialysis against ethanol (cut-off 14 kDa). The product was obtained by ethanol evaporation followed by freeze-drying.

VII.2.3 Nuclear Magnetic Resonance spectroscopy (NMR).

^{1}H NMR spectra were recorded on a Bruker Avance 400 MHz spectrometer at 25 °C or 60 °C in appropriated solvent (D_2O or DMSO-d_6). Chemical shifts are reported in ppm (δ units) downfield from 3-(trimethylsilyl)-propionic acid-d_4.

VII.2.4 Gel Permeation Chromatography (GPC).

GPC measurements were performed with a Malvern Viscotek TDA 305 with a refractometer (RI-Detector 8110, Bischoff), right-angle light scattering (LS), and viscometer detectors on a set of four columns: pre-column Suprema 5 µm 8x50 S/N 3111265, Suprema 30 Å 5 µm 8x300 S/N 3112751, Suprema 1000 Å 5 µm 8x300 S/N 3112851 PL and Aquagel-OH MIXED 8 µm 7.5x300 S/N 8M-AOHMIX-46-51.[34] The system was kept at 30 °C. We used 0.1 M NaN_3, 0.01 M NaH_2PO_4 (pH = 6.6) as an eluent at a flow rate of 1 mL/min. The molecular weight of the GAGs was determined with a conventional (RI *vs.* elution time) and multidetector calibration (RI+LS+Viscosity) using the software Omnisec 4.6.1 (ViskoteK). The conventional calibration was performed with a commercial polysaccharide set from Varian that contains 10 pullulans with narrow polydispersity and molecular mass at the peak maximum (MP) ranging from 180 Da to 708 kDa. The multidetector calibration was performed using the pullulan of this set with number-average molecular weight (Mn) 48.8 kDa and PDI 1.09.

VII.2.5 Determination of critical micelle concentration (CMC).

CMC of GAG amphiphiles was determined according to a previously described method using the hypsochromic shift of emission spectra of the Nile Red probe in the presence of the amphiphiles at different concentrations.[35] Briefly, solutions of GAG amphiphiles (ultrapure water) with different concentrations (0.02 – 15 mg/mL) were incubated with Nile Red (2 µM in ethanol) at 45 °C for 45 minutes. Fluorescence spectra of these solutions were recorded on fluorescence spectrometer FP-8500 (Jasco) after cooling (25 °C). Nile Red was excited at 565 nm and emission spectra were recorded between 590 and 750 nm. The slit width was set at 5 nm for both excitation and emission. The peak intensity at 615 nm was recorded as a function of the logarithm of GAG

amphiphile concentration. CMC was determined at the interception of the two logarithmic equations.

VII.2.6 Size and zeta-potential of micellar nanoparticles.

GAG amphiphiles were dissolved in ultrapure water at a concentration above the CMC and vortexed. Hydrodynamic diameter and zeta potential were determined by dynamic light scattering (DLS) and electrophoretic light scattering (ELS) using NANO ZS (Malvern Instruments Ltd) equipped with a 4 mW He-Ne laser operating at a wavelength of 633 nm. The scattered light was detected at a back-scatter angle (173°), which provides the sensitivity required for measuring particles at low concentrations. Measurements were carried using a polystyrene cell at 25 °C. The CONTIN algorithm (intensity weighted) was applied to obtain the size distribution. The average hydrodynamic diameter (Dh) and polydispersity index (PDI) were determined by fitting the correlation function with the cumulant method. Particles stability was evaluated by monitoring the polydispersity index and ζ-potential over time.

The diameter was also measured by Atomic Force Microscopy (AFM). A droplet of sample aqueous solution was deposited on an aminated freshly cleaved mica surface.[36] The surface was dried under nitrogen flux. Measurements were performed with NanoWizard 3 (JPK, Germany) in quantitative imaging mode using silicon cantilevers (ACSTA, AppNano, USA) with a typical resonance frequency of 150 kHz and a spring constant of about 7.8 N m^{-1}. Size distribution was obtained after analyzing at least 150 particles using the software Gwyddion.

VII.2.7 Redox-responsiveness of the micellar nanoparticles.

The redox-responsiveness was evaluated by fluorescence quenching of Nile Red in the presence of 1,4-dithiothreitol (DTT). Nanoparticles containing Nile Red were prepared as described above. Solutions of GAG amphiphiles at a concentration above CMC (2.4 mg/mL HA and 6 mg/mL CS) containing 5 μM of Nile Red were incubated with DTT of different concentrations (50 – 200 mM) at 37 °C. The fluorescence was measured by fluorescence spectrometer FP-8500 (Jasco) at 25 °C. The excitation at 565 nm was performed and emission spectra were recorded in the range

590 - 750 nm. The slit width was set at 5 nm for both excitation and emission. Stern Volmer constant was determined (K_{sv}) by fitting Equation VII.1 to the experimental data

Equation VII.1: $K_{app} = K_{SV} + K_D K_S[Q]$

where K_{app} is the apparent quenching constant, [Q] is DTT concentration, K_D and K_S are the dynamic and static components of the fluorescence quenching.

The stability of the micellar nanoparticles in the presence of DTT was evaluated by DLS. GAG amphiphiles (2.4 mg/mL HA and 6 mg/mL CS) were mixed with DTT of different concentrations (0 – 200 mM) and analyzed by DLS using NANO ZS (Malvern Instruments Ltd) with fixed position and attenuator.

VII.2.8 Encapsulation efficiency.

Fluorescein isothiocyanate-dextran (FITC:Glucose 1:250, MW 4 000 g/mol) and Nile Red were used as a model hydrophilic and hydrophobic drug, respectively. FITC:Glucose or Nile Red (2 mol%) was added to micellar nanoparticles and the samples were incubated at 45 °C for 45 minutes. The free (non-encapsulated) compounds were separated by centrifugation using ultracentrifuge units with a cut-off of 30 kDa in a centrifuge (Gyrospin scanspeed Mini)) at 6000 G for 20 minutes. The supernatants were quantified using a fluorescence spectrometer (Jasco FP-8500). Encapsulation efficiency (% EE) was determined according to Equation VII.2

Equation VII.2: $\% EE = \frac{[C_{total}] - [C_{free}]}{[C_{total}]} \times 100$

where C_{total} is the concentration of probe in solution and C_{free} is the concentration of the non-encapsulated probe.

VII.2.9 Internalization assay.

We used two human breast cancer cell lines, namely MDA-MB-468 and Sk-Br-3, for these experiments. The cells were seeded on tissue culture polystyrene at 37 °C in Dulbecco Modified Eagle Medium (DMEM) high glucose with phenol red (Sigma-Aldrich, St. Louis, UK) supplemented with sodium bicarbonate, 10% fetal bovine serum (FBS), and 1% antibiotic/antimycotic. Upon confluence, the cells were detached with TrypLE™ and cultured in a fresh medium at a cell density

of 205 cell/cm^2 overnight. Blocking of CD44 was performed by treatment of the cells with 150 ng/mL of anti-CD44 antibody [KM201] in DMEM without phenol red and FBS for 1h at 37 °C. In addition, non-specific blocking was carried out at the same conditions using 150 ng/mL mouse IgG1, kappa monoclonal antibody (MOPC-21).

The respective amphiphile (HA or CS) was dissolved in ultrapure water at 3 mg/mL. The assembled micellar nanoparticles were incubated with Nile Red (1 μM) at 45 °C with orbital shaking for 2h. After cooling down to room temperature, the nanoparticles were filtered (0.22 μm) and added to DMEM at a volume ratio of 1:10. Treated and untreated cells were supplemented with this medium and incubated for 4h at 37 °C in humidified 5% CO2 atmosphere. After this period, the cells were washed with phosphate buffer saline (PBS) and fixed with 10% formalin at 4 °C. The cell membrane was stained with wheat germ agglutinin Alexa Fluor® 488 conjugate in PBS (1 μg/mL) for 15 min at room temperature. After washing, cells were permeated with 0.2 % Triton X and nuclei were stained with DAPI (1 μg/mL) for 30 min. Coverslips with the fixed cells were mounted with vectashield mounting medium. Fluorescent images were acquired in an inverted confocal microscope TCS-SP8 (Leica, Germany).

VII.3. Results and Discussion

VII.3.1. Synthesis and characterization of amphiphilic GAGs.

The feasibility and versatility of oxime coupling for the synthesis of different glycoconjugates have already been demonstrated.[31, 37-39] Previous studies showed that this coupling preserves GAG bioactivity and specificity towards proteins, such as growth factors.[30, 39] Herein, we obtained amphiphilic GAG derivatives from 11-(Aminooxy)-1-undecanethiol (Scheme VII.S1) and the respective GAG (HA or CS) by oxime coupling at the GAG reducing end (Fig. VII.1). Of note, the aminooxy alkanethiol was generated in situ from its protected derivative (Schemes VII.S1 and VII.3) to avoid side reactions due to the observed high reactivity of the aminooxy group. The successful synthesis was confirmed by NMR (Fig. VII.1B and VII.S4) and GPC (Table VII.1 and Fig. VII.S5).

The degree of substitution was determined from ^{1}H NMR by the integral's ratio of the peaks corresponding to the aliphatic protons (δCH_2 1.25 ppm) and the ones assigned to the protons of

the glucuronic acid unit (δH 3.4 ppm). We obtained 99% substitution for HA amphiphile and 85% for CS derivative.

We expected that the modification of GAG would result in a very small shift towards higher molecular weight (the molecular weight of the amphiphiles differ from the respective GAG with *ca.* 219 g/mol). Indeed, the amphiphilic derivatives have a higher weight-average molecular weight (Mw) and Mn than the GAGs (Table VII.1 and Fig. VII.S5). Significantly different Mn was determined for the CS derivative. This difference is caused by the presence of assemblies that results in the appearance of an additional peak at lower retention times (Fig. VII.S5E, orange). The assemblies' fraction is very small as it is detectable only by the light scattering (RALS) detector but not by the refractive index (RI) one. This secondary peak is not present in the GPC elugram of the HA amphiphile either below or above its CMC. Two possible reasons can explain this result: most assemblies are broken in the GPC columns, or they are not formed at the conditions used for GPC characterization (different solvents were used for GPC and CMC determination).

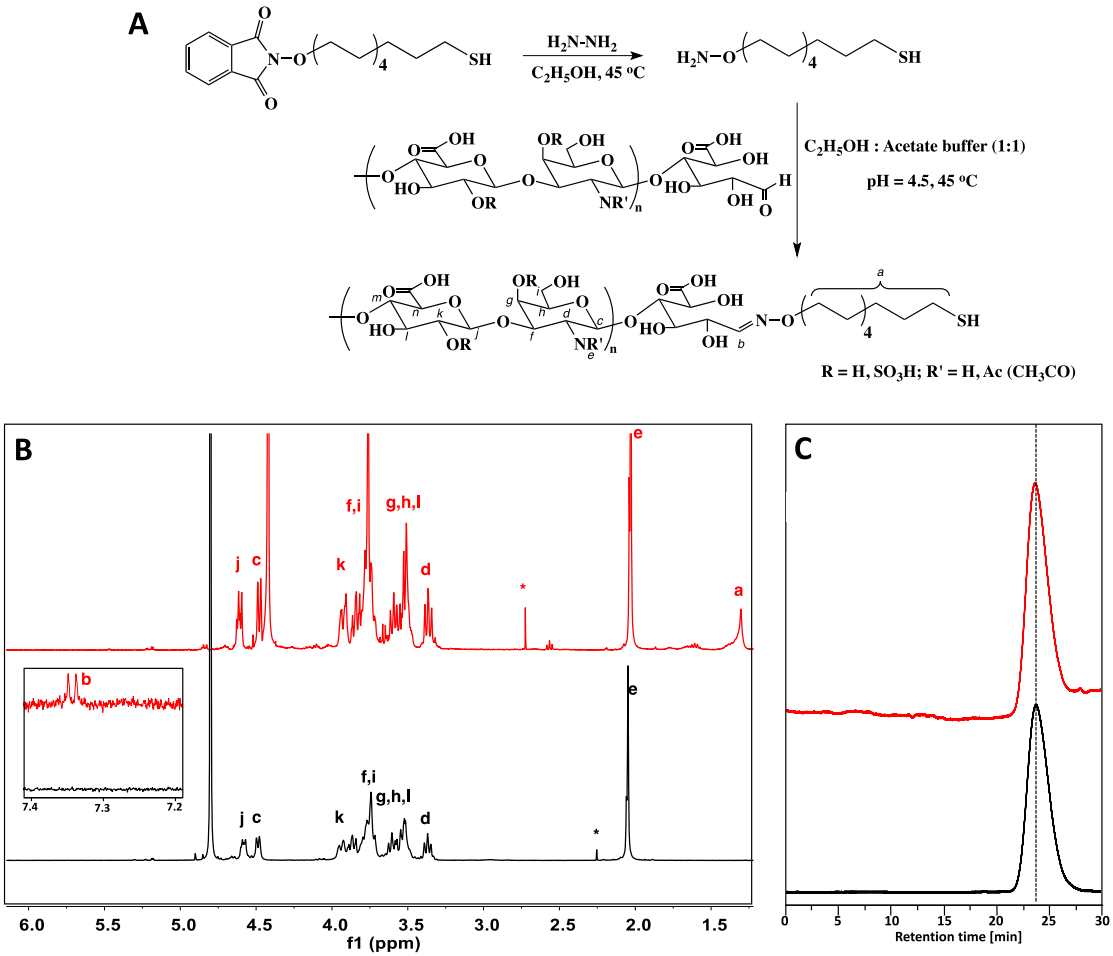

Figure VII.1. (A) Reaction scheme used for the synthesis of GAG amphiphiles and characterization of hyaluronan (black) and its derivative (red) by (B) ^{1}H NMR and (C) GPC chromatogram (refractive index signal). Signals marked with (*) correspond to impurities from the solvent. NMR and GPC data for chondroitin sulfate and its derivative are provided in SI.

Table VII.1. Number-average molecular weight (Mn) and weight-average molecular weight (Mw) of GAGs and their amphiphiles determined by gel permeation chromatography (GPC).

	Mn [kDa]	Mw [kDa]	PDI	Retention time [min]
HA	3.30	4.3	1.37	23.7
HA amphiphile	4.3	5.2	1.20	23.6
CS	12.3	19.2	1.56	22.2
CS amphiphile	18.5*	23.1*	1.25	22.2 (+18.8 LS)

*Increased values for Mn and Mw due to aggregation (see also Fig. VII.S5)

VII.3.2. Assembly of GAG amphiphiles.

Amphiphile molecules tend to self-organize in solution because of the thermodynamic incompatibility between their building blocks. As a result, different nanostructures (*e.g.*, micelles, vesicles, nanofibers, lamellae) can be generated. The size and the architecture of the assemblies depend on the molecular weight of the hydrophilic and the aliphatic portion, the ratio between them, and the environment (*e.g.*, solvent, temperature). The assembly of the obtained GAG amphiphiles was studied in water either at room temperature or at 37 °C. Atomic force microscopy (AFM) showed that these molecules self-organize in nanostructures with round shapes (Fig. VII.2C). The size of the assemblies is essential for drug intracellular delivery: sizes below 200 nm are associated with low reticuloendothelial uptake, minimal renal excretion, and effective enhanced permeation and retention (EPR) effect that favors passive tumor targeting.[5] Previous studies with side-on modified GAGs report different diameters ranging from 37 nm to 500 nm.[28, 40-44] DLS analysis of the assemblies of GAG amphiphiles obtained by us showed that they have Dh below 200 nm and low PDI (Table VII.2). The size depends on the GAG moiety in the amphiphile: HA amphiphiles form smaller assemblies whose size decreases with the temperature

increase. The assemblies generated from the CS amphiphile are bigger and their size does not depend on the temperature.

Table VII.2. Characterization of the formed assemblies in terms of size (DLS), charge (ELS), and critical micelle concertation (CMC, fluorescence spectroscopy of Nile Red).

	T [°C]	Dh [nm]*	PDI*	ζ-potential [mV]	CMC [μg/mL]
HA amphiphile	25	146 ± 7.4	0.20 ± 0.01	- 31.9 ± 1.7	310.17 ± 38.22
	37	99 ± 57.2	0.20 ± 0.01	- 34.9 ± 3.1	349.50 ± 107.22
	42				287.67 ± 5.86
CS amphiphile	25	193 ± 8.10	0.16 ± 0.02	- 25.1 ± 2.8	103.48 ± 17.24
	37	195 ± 10.99	0.14 ± 0.02	- 31.6 ± 0.1	80.50 ± 16.33
	42				96.47 ± 2.95

*Data reported as averaged values from at least three different measurements/batches; Used abbreviations: T temperature; Dh hydrodynamic diameter; PDI polydispersity index

There are two reasons behind the obtained results: (i) different solvation effects and Coulomb forces and (ii) different molecular weights of the used GAGs (Table VII.1). HA is a weak polyelectrolyte, whereas CS has a higher charge density/repulsion caused by the sulfate groups and longer chains.[17, 45] Consequently, HA derivatives form smaller and more compact assemblies than the CS ones. The temperature-dependent size of the HA assemblies can be explained by the ability of this GAG to form H-bonding with water molecules; higher temperature results in decreased hydration, enabling the formation of intermolecular H-bonding that lead to a decrease in the size of HA assemblies.

Previous reports about end-on functionalized HA describe the formation of polymersomes with a hydrodynamic diameter around 440 nm.[40] The structure of the amphiphiles obtained by us is different (large GAG portion and short aliphatic moiety) and the size that we have obtained is much smaller than the reported one. These differences are consistent with a micellar organization in which the GAG part is exposed on the surface, conferring colloidal stability and assuring targeted delivery, while the hydrophobic portion is hidden in the assembly interior (Fig. VII.2B). Indeed, the

negative ζ-potential confirm the presence of the GAG on the surface of the assemblies (Table VII.2). The formation of such structures has been observed in self-assembled HA with poly(DL-lactide-co-glycolide) (PLGA) co-polymers. [46] The end-on functionalization of HA (7.5 kDa) with PLGA (5 kDa) through disulfide linkage resulted in self-assembled micellar nanoparticles with a hydrodynamic diameter below 200 nm.

_ENREF_45

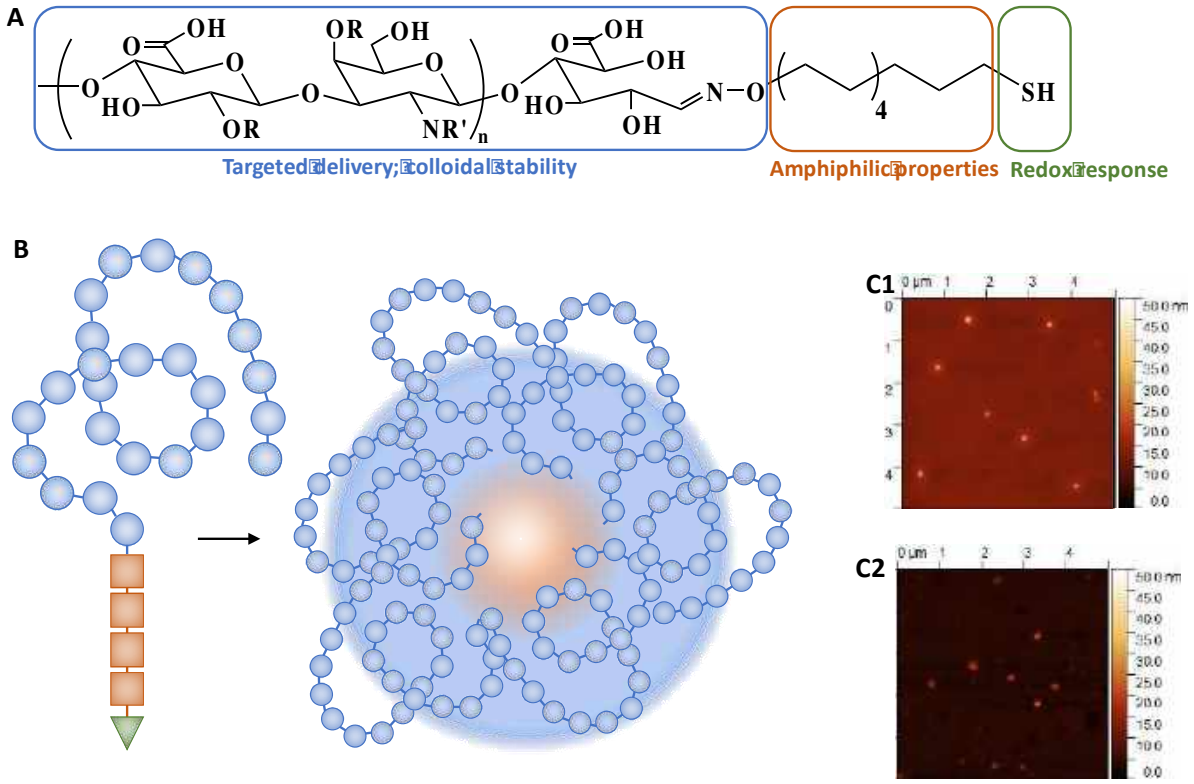

Figure VII.2. (A) Schematic presentation of the building blocks of GAG amphiphiles and their key role(s) in (B) the assembled micellar nanoparticles. (C) AFM images of the nanoparticles obtained from the (C1) hyaluronate and (C2) chondroitin sulfate amphiphiles.

Critical micelle concentration (CMC) is a key parameter related to the assembly and stability of the micellar nanoparticles. We used fluorescence spectroscopy of Nile Red to determine CMC (Table VII.2).[35, 47] Low fluorescence intensity of Nile Red was observed at lower concentrations of GAG amphiphiles consistent with free molecules in solution (Fig. VII.S6). When CMC was reached, we observed a sharp increase in the signal intensity because of the aggregate formation associated with Nile Red incorporation in the lipophilic compartment. CMC was determined at

different temperatures: we did not find significant differences in CMC for the studied range, which indicates the stability of the assemblies at physiological conditions, including hyperthermia (42 °C).

Previous studies with GAGs side-on modified with thiol reported CMC in the range 30 – 200 μg/mL, depending on the degree of modification and the molecular weight of GAG.[10, 28, 40, 41, 43] The values that we obtained are at the upper limit of this range or higher, most probably because of the ratio between the GAG and the aliphatic portion: side-on modification is associated with the introduction of several aliphatic moieties per GAG chain, while end-on functionalization results in the introduction of only one aliphatic tail per GAG.

Shelf stability of the micellar nanoparticles is another important property that was monitored by DLS, which is sensitive to small changes in the nanoparticles' surface composition (ζ-potential) and size (PDI). The obtained micellar nanoparticles have a strong negative charge associated with long shelf stability, low non-specific binding to plasma proteins, and long circulation half-time. Indeed, our results demonstrated no significant changes either for -potential or for the PDI for one month at 4 °C, *i.e.*, shelf conditions (Fig. VII.S7).

VII.3.3. Drug encapsulation.

Because the micellar nanoparticles have hydrophilic and hydrophobic compartments, we hypothesized that they could be used as carriers of either hydrophilic or lipophilic drugs. We, therefore, studied the encapsulation efficiency using the fluorescence probes Dextran-FITC (hydrophilic) and Nile Red (lipophilic) as model drugs. Our results demonstrated that Nile Red was encapsulated with 100 % efficiency in the nanoparticles assembled of either HA or CS amphiphile. Dextran-FITC was encapsulated with high efficiency (74.2%) in HA micellar nanoparticles but with a much lower yield (25.2%) in CS ones. These results are consistent with the characterization of the assemblies described above. The hydrophobic portion of both amphiphiles is the same and the cores of HA or CS nanoparticles are akin. Thus, we expected similar encapsulation efficiency for the lipophilic molecule. The bigger size of the CS nanoparticles is associated with the loose packing of the CS chains and the formation of a highly diffusive shell. As a result, the uncharged dextran cannot be encapsulated with high efficiency in this shell. On the other hand, the HA

amphiphile assembles in smaller nanoparticles in which the dextran can be efficiently encapsulated due to the establishment of H-bonding with the HA chains.

VII.3.4. Redox responsiveness of the micellar nanoparticles.

Functionalization of the amphiphile with a thiol group aimed to confer redox responsiveness to the assemblies generated from these amphiphiles. We expected that upon assembly the thiol groups would form disulfide bridges. In the tumor environment, these bridges can break upon the reductive action of the overexpressed GSH triggering the disassembly of the micellar nanoparticles and release of the encapsulated drug. We, therefore, evaluated the release of Nile Red from the amphiphiles assemblies in the presence of DTT with different concentrations (0 – 200 mM). We observed different effects for the HA and CS assemblies: increasing concentrations of DTT resulted in a decrease of fluorescence intensity of Nile Red for the HA assemblies, which demonstrates the release of the Nile Red and disassembly of the nanoparticles (Fig. VII.S8A, inset).[35] K_{app} of each point was determined and the linear fit of the experimental data as a function of DTT concentration (Fig. VII.S8A) allowed the determination of the Stern-Volmer (K_{sv}) constant (Table 3). The K_{sv} is temperature-dependent: temperature increase (from 25 to 37°C) resulted in higher values of K_{sv}, indicating that the HA assemblies are more sensitive to the reductive environment at physiologically relevant temperatures.

Table VII.3. Stern-Volmer constants (K_{sv}) for HA micellar nanoparticles obtained by Nile Red fluorescence quenching in the presence of increasing concentrations of DTT at different temperatures.

Temperature [°C]	K_{sv} [M^{-1}]
25	1.02 ± 0.40
37	11.80 ± 0.33
42	14.86 ± 0.17

CS assemblies behaved differently: no fluorescence quenching (*i.e.*, Nile Red release) was observed even at the highest concentration of DTT. This result demonstrated that the formation of disulfide bridges between CS amphiphiles is not favored. In fact, this agrees with the structural differences between the GAG assemblies discussed above: the CS amphiphiles are not packed enough close to allow the formation of bridges between the thiol groups.

Redox sensitivity was also evaluated by DLS. We analyze the size distribution of the micellar nanoparticles upon DTT addition (Fig. VII.S8B). The results are in good agreement with the fluorescence measurements: clear disassembly is visible for the HA nanoparticles. In the case of CS assemblies, we observed an effect upon the initial addition of DTT, but no further variations were detected upon increasing the DTT concentration.

VII.3.5. Internalization of the micellar nanoparticles.

We used two human breast cancer cell lines that differ by their CD44 expression: MDA-MB-468 overexpress CD44 while Sk-Br-3 do not express it (Fig. VII.S9). The HA moiety in the synthesized amphiphiles is longer than required for specific binding of CD44 (8 monosaccharides) and thus, we expected that the generated assemblies would be internalized by cells expressing this receptor.[48, 49] The data about the CS-CD44 dependent internalization are controversial; alternative internalization mechanisms are described in addition to CD44 dependent endocytosis.[22, 50] Our results demonstrated that MDA-MB-468 cells internalized both types of particles (Figs. VII.3A and VII.3D), although more intensive red staining was observed for the HA assemblies indicating a higher percent of internalization in this case (Fig. VII.3A2 *vs.* Fig. VII.4D2).

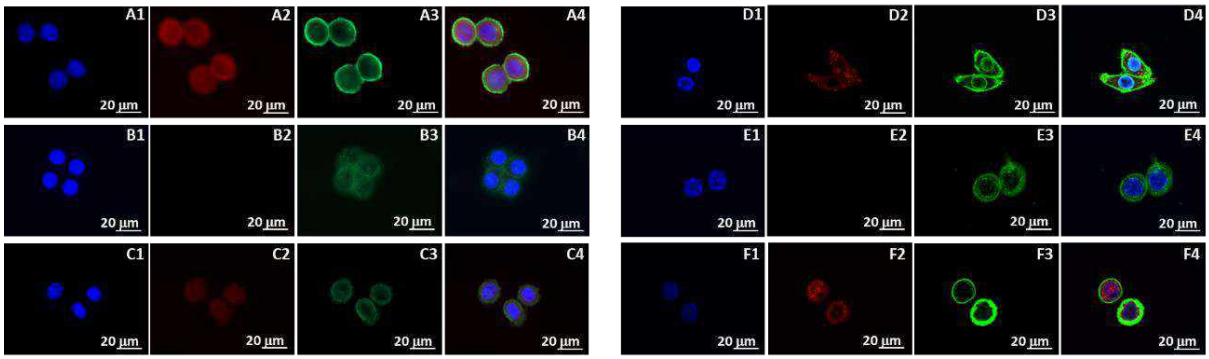

Figure VII.3. Internalization of HA (A-C) and CS (D-F) micellar nanoparticles loaded with Nile Red by MDA-MB-468 cells without blocking (A, D), after specific CD44 blocking (B, E) and after unspecific IgG1 blocking (C, F). Nuclei are represented in blue (1), nanoparticles in red (2), cell membrane in green (3), and merged images (4).

To ensure that this internalization is CD44 mediated, we blocked the CD44 receptors and performed the same assay (Figs. VII.3B and VII.3E). We did not detect any red staining at these conditions indicating no internalization. When using antibodies, however, the internalization could be impeded sterically but not specifically. We, therefore, performed an additional control experiment in which non-specific blocking was used (IgG1 antibody, Figs. VII.3C and VII.3F). The results demonstrated that although some steric obstruction may occur (lower intensity of Fig. VII.3C2 *vs.* Fig. VII.3A2), the non-specific blocking did not impede the uptake of the particles by the cells.

A different response was observed when cells that do not express CD44 were brought in contact with the nanoparticles (Fig. VII.4). Sk-Br-3 cells internalized neither HA nor CS assemblies. This result is very important as it shows the selectivity of the developed carriers.

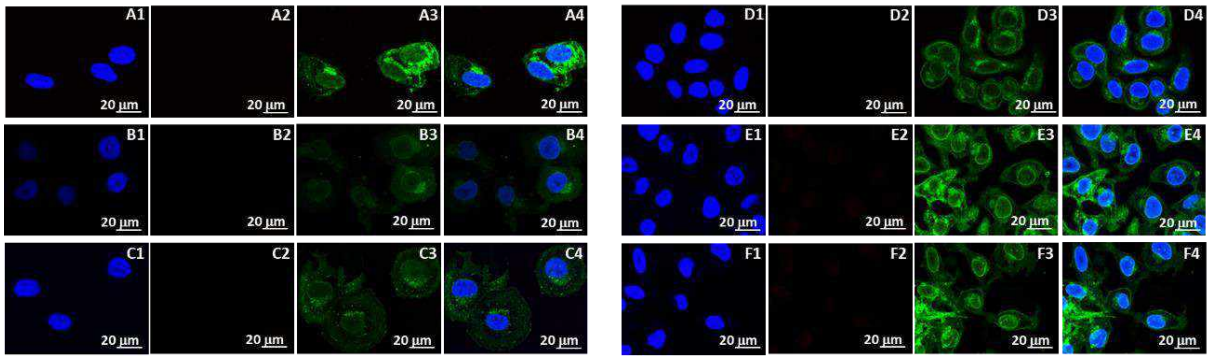

Figure VII.4. Internalization of HA (A-C) and CS (D-F) micellar nanoparticles loaded with Nile Red by Sk-Br-3 cells without blocking (A, D), after specific CD44 blocking (B, E) and after unspecific IgG1 blocking (C, F). Nuclei are represented in blue (1), nanoparticles in red (2), cell membrane in green (3), and merged images (4).

Altogether these data demonstrate that the GAG exposed on the surface of the assemblies is bioactive and interact specifically with the CD44 cell receptors, thus ensuring targeting delivery of the encapsulated cargo.

VII.4. CONCLUSIONS

We demonstrated that amphiphilic GAGs can be obtained by a simple end-on functionalization of different GAGs with aliphatic moiety. The obtained amphiphiles self-assemble in micellar nanoparticles that are stable either at storage or physiological conditions. The size and properties of the assemblies depend on the used GAG: greater encapsulation efficiency and physiological relevant redox responsiveness of the HA nanoparticles make them more suitable as tumor-targeting delivery systems. We further showed that the assemblies of HA amphiphiles are recognized by cells expressing CD44 and internalized via specific CD44 pathways. All these features make the HA assemblies very promising as specific nanotheranostic tools targeting CD44 overexpressing cancer cells.

VII.5. SUPPORTING INFORMATION

Synthesis of 11-(Aminooxy)-1-undecanethiol

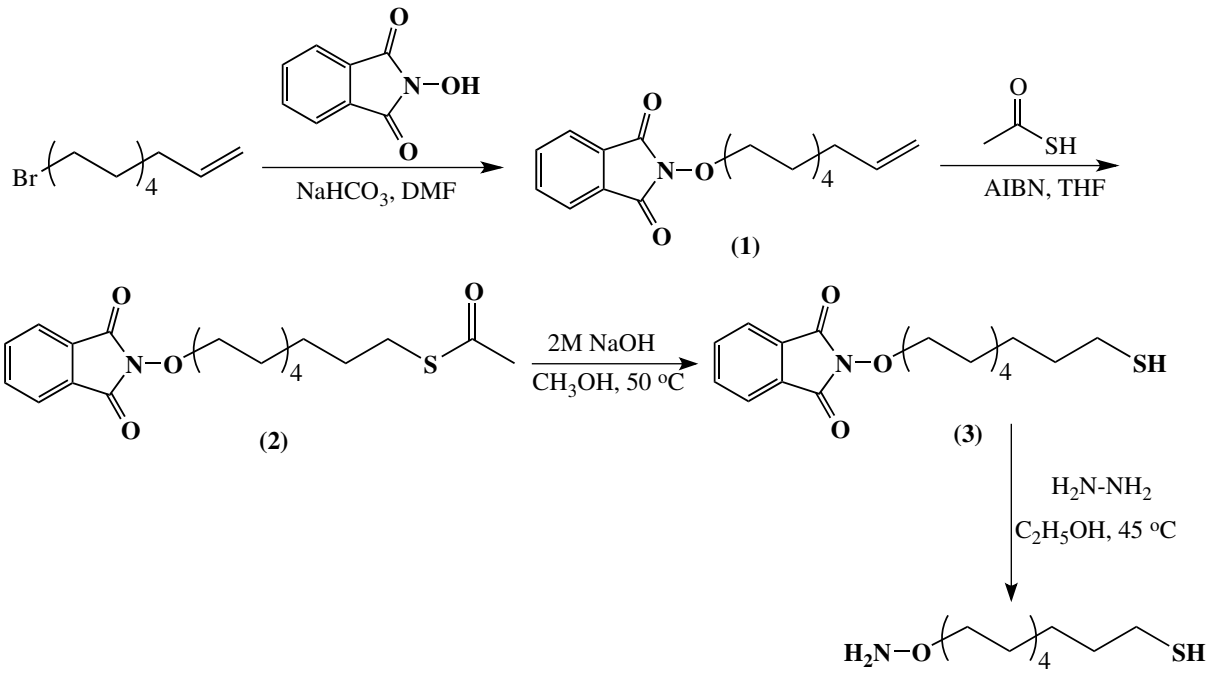

Scheme VII.S1. Schematic presentation of the synthetic route used to obtain 11-(Aminooxy)-1-undecanethiol

A solution of N-hydroxyphthalimide (2.44 g, 1.5 mol eq.) and sodium bicarbonate (1.388 g) in dimethylformamide (DMF, 50 mL) was stirred at 60 °C under argon for 1h. 11-bromo-1-undecene (2.3 mL, 1 mol eq.) was then added and the reaction was carried overnight: indicators for the successful synthesis of the product (1) are the colour change (from orange to dark orange) and the product precipitation. The product was isolated by liquid-liquid extraction (water and chloroform). ^{1}H NMR (400 MHz, Chloroform-*d*, Fig. VII.S1): δ 7.89 – 7.80 (m, 2H), 7.80 – 7.70 (m, 2H), 5.82 (ddt, J = 16.9, 10.2, 6.7 Hz, 1H), 5.00 (ddt, J = 17.1, 2.1, 1.6 Hz, 1H), 4.96 – 4.90 (m, 1H), 4.21 (t, J = 6.8 Hz, 2H), 2.05 (dtd, J = 8.0, 6.6, 6.0, 1.4 Hz, 2H), 1.85 – 1.73 (m, 2H), 1.49 (ddt, J = 9.4, 5.5, 3.5 Hz, 2H), 1.44 – 1.24 (m, 10H).

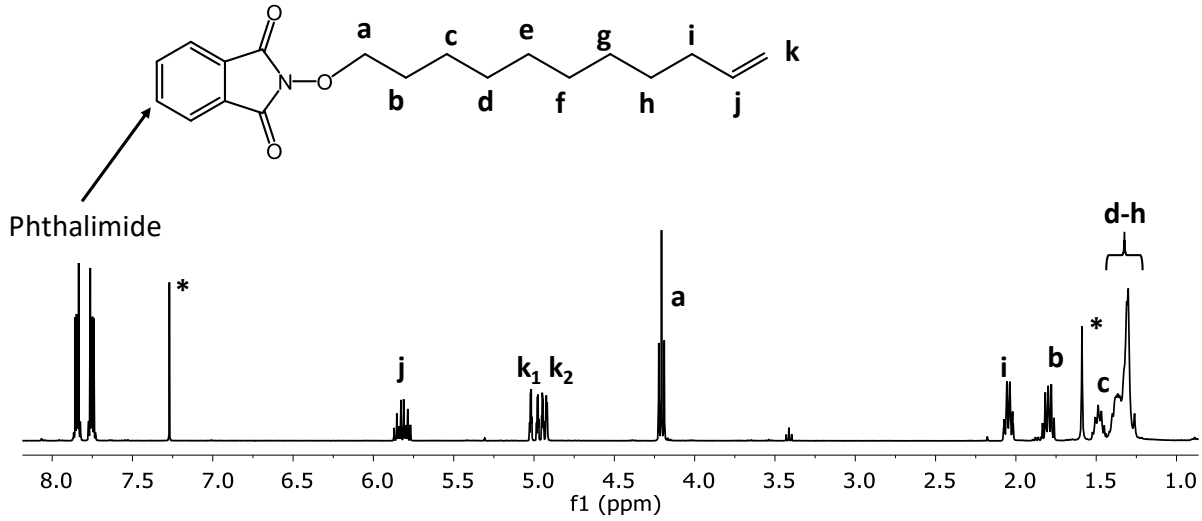

Figure VII.S1. ^{1}H NMR spectrum (400 MHz, $CDCl_3$) of compound (1).

2 g of (1) were dissolved in degassed tetrahydrofuran (THF, 80 mL). Azobisisobutyronitrile (AIBN, 100 mg) and thioacetic acid (2 mL) were added to this solution. The reaction mixture was stirred at room temperature under reflux for 3 days. After this period, toluene (50 mL) was added and the solvents were evaporated. This procedure was repeated (3x). Purification of the product (2) was performed by re-crystallization in chloroform/hexane mixture (1:30) at 4°C. The final product was freeze-dried. ^{1}H NMR (400 MHz, Chloroform-*d*, Fig. VII.S2): δ 7.88 – 7.81 (m, 2H), 7.79 – 7.72 (m, 2H), 4.20 (t, *J* = 6.8 Hz, 2H), 2.89 – 2.83 (t, *J* = 7.4 Hz, 2H), 2.33 (s, 3H), 1.86 – 1.73 (m, 2H), 1.59– 1.53 (m, 2H), 1.53 – 1.42 (m, 1H), 1.41 – 1.19 (m, 4H).

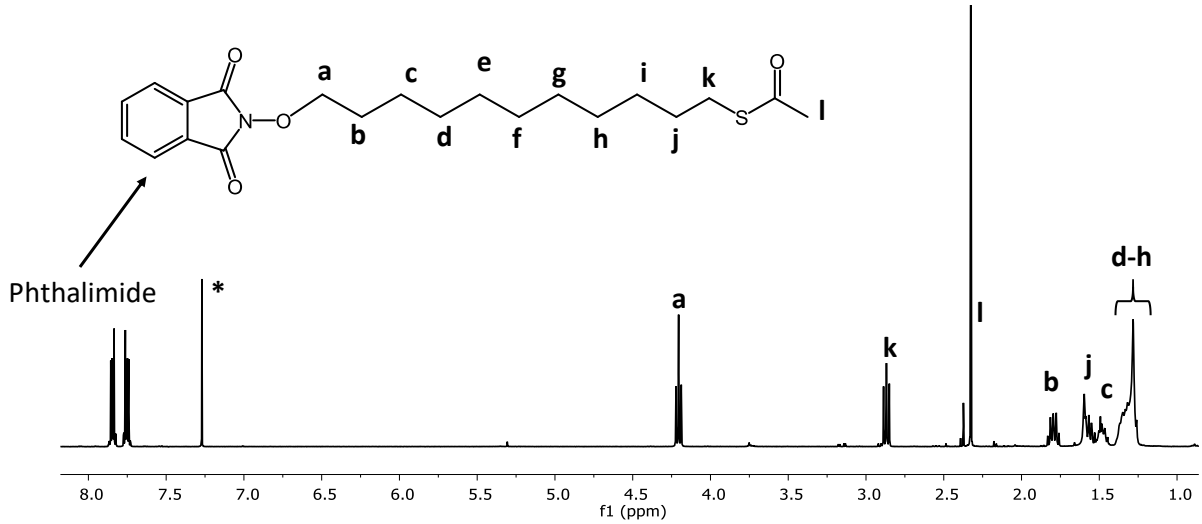

Figure VII.S2. ^{1}H NMR spectrum (400 MHz, $CDCl_3$) of compound (2).

Deprotection of (2) (950 mg; 2.43 mmol) was carried out in methanol (50 mL) at 50 °C by adding 2M NaOH (1.5 mL, 3 mol equivalent regarding 2). The reaction was carried for 3h under an inert atmosphere. The product (3) was isolated by precipitation with 2M HCl. Purification was carried out by dissolving the obtained powder in ethanol, filtering the solution, concentrating it, and finally, the pure product was obtained by freeze-drying with dioxane. 1H NMR (400 MHz, Chloroform-*d*, Fig. VII.S3) δ 7.88 – 7.81 (m, 2H), 7.79 – 7.72 (m, 2H), 4.21 (t, *J* = 6.8 Hz, 3H), 2.53 (qd, *J* = 7.6, 1.9 Hz, 4H), 1.79 (dq, *J* = 8.6, 6.8 Hz, 2H), 1.69 – 1.54 (m, 2H), 1.49 (s, 2H), 1.43 – 1.16 (m, 10H).

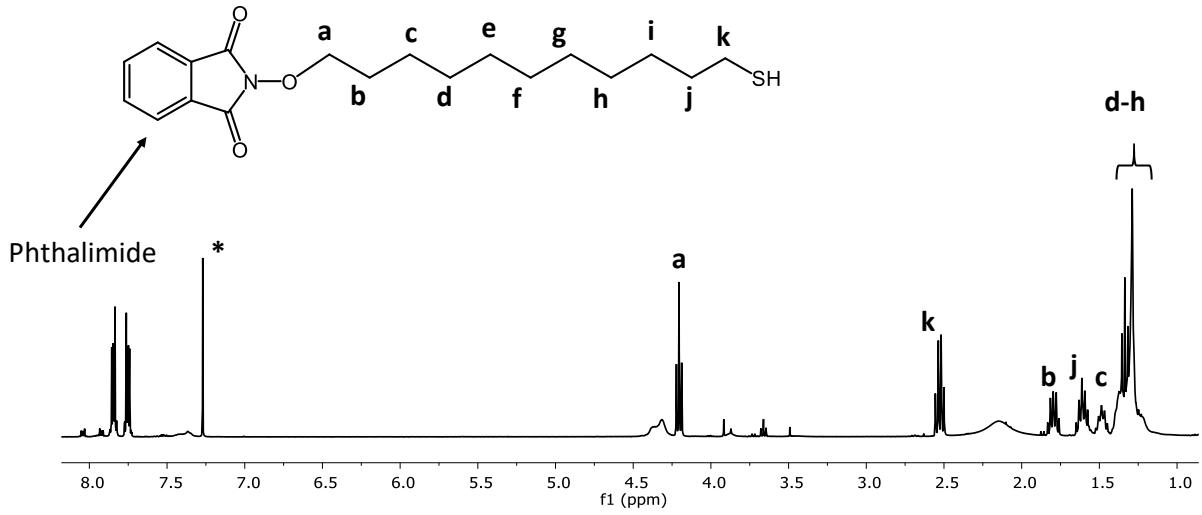

Figure VII.S3. ^{1}H NMR spectrum (400 MHz, $CDCl_3$) of compound (3).

3 was dissolved in ethanol (10 mL) and hydrazine (100 mL) was added to the solution. The reaction was carried at 45 °C for 1h. Unreacted hydrazine and solvent were removed by evaporation (30 mBar at 45 °C). The obtained 11-(Aminooxy)-1-undecanethiol was used immediately in the reaction with hyaluronan or chondroitin sulfate. Of note, storage or purification of the obtained product resulted in its hydrolysis.

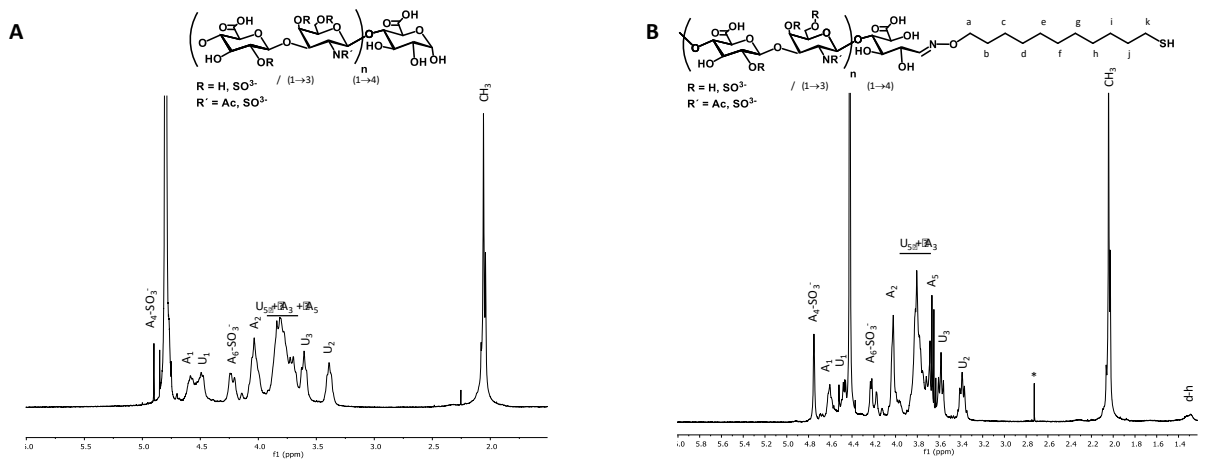

Figure VII.S4. ^{1}H NMR spectra (400 MHz, D_2O) of chondroitin sulfate (A) and its aliphatic derivative (B). Signals of GalNAc are labeled with A and GlcA ones with U. Peaks assigned with (*) correspond to contaminants from the solvent.

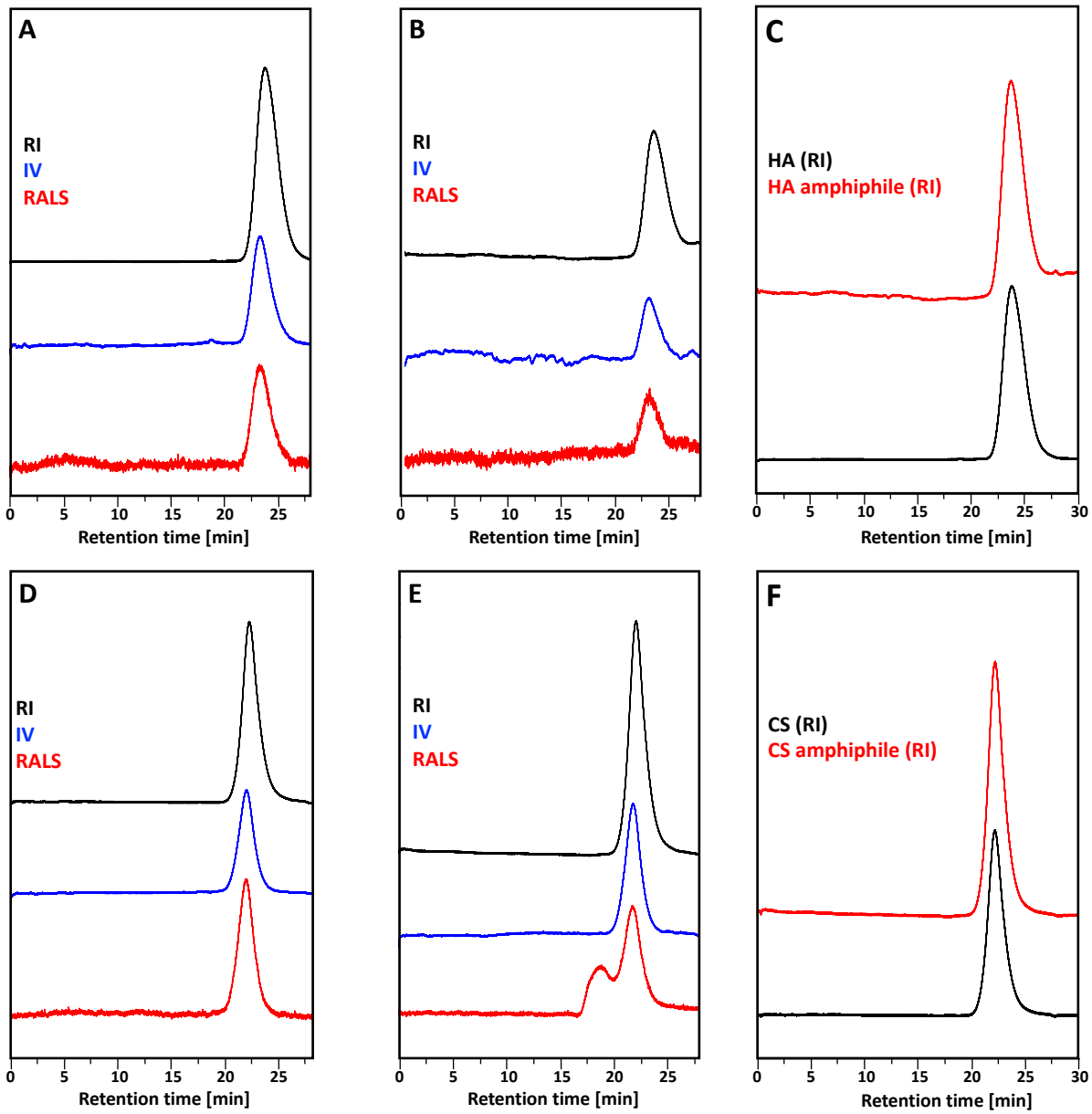

Figure VII.S5. GPC profiles of HA (A), HA amphiphile (B), CS (D) and CS amphiphiles (E) and comparison between unmodified and modified GAGs (C and F, RI signals).

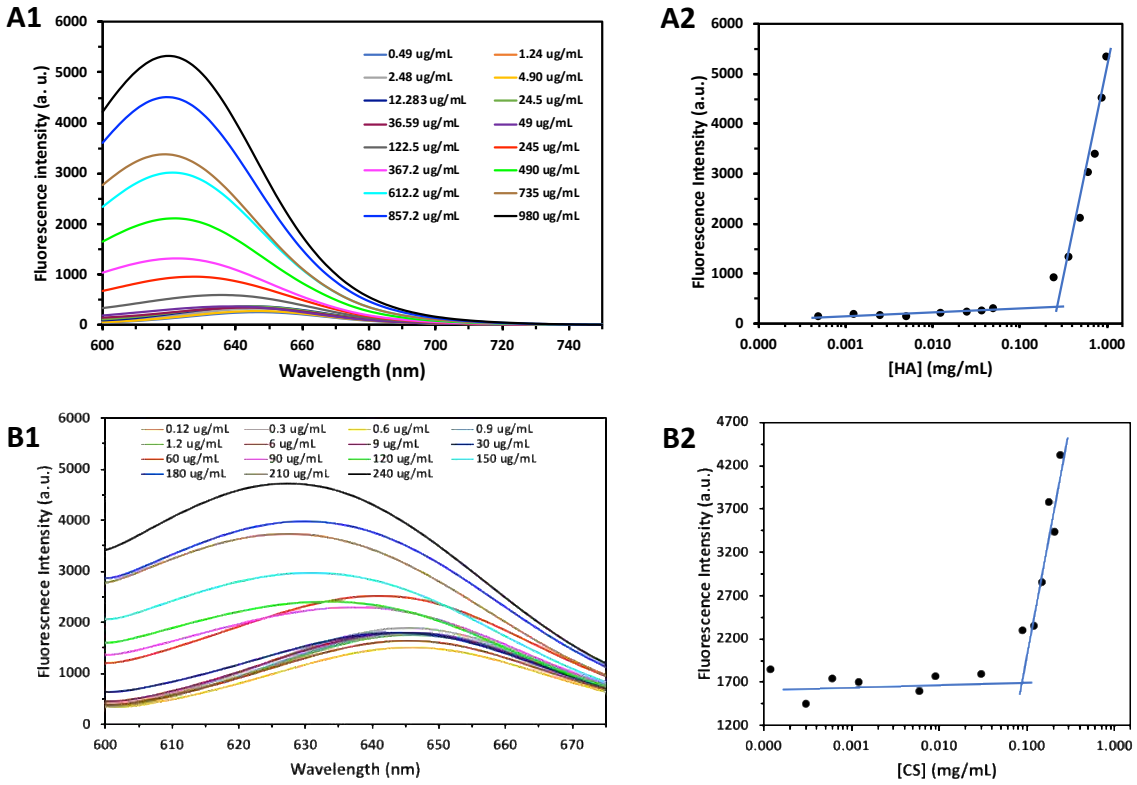

Figure VII.S6. Examples of CMC determination by fluorescence spectroscopy of Nile Red: Emission spectra of Nile Red in solutions of HA (A1) and CS (B1) amphiphile with different concentrations at 25 °C; Determination of CMC of HA (A2) and CS (B2) amphiphile at the cross-point between the two phases. The CMC results presented in Table VII.2 are averaged values of at least three independent measurements.

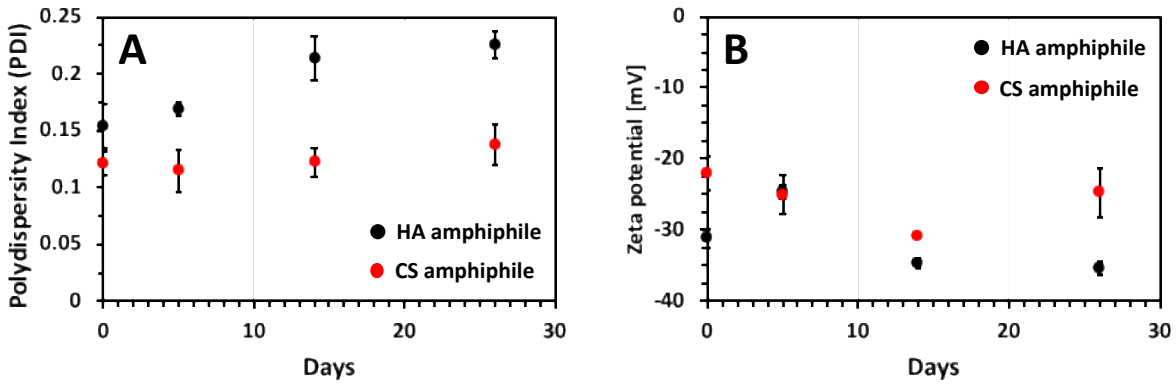

Figure VII.S7. Monitoring the stability of micellar nanoparticles from HA (black) and CS (red) amphiphiles by dynamic light scattering (DLS): polydispersity index (A) and ζ-potential (B).

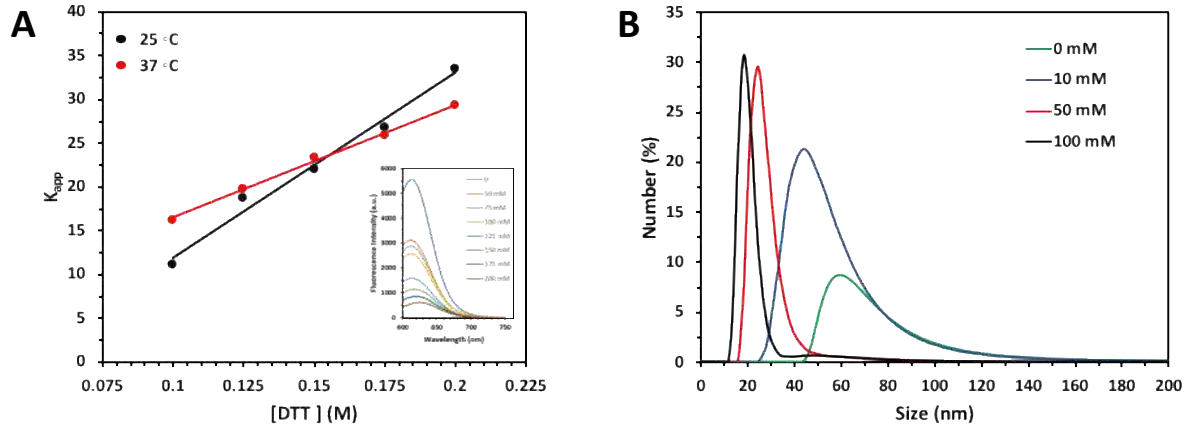

Figure VII.S8. Evaluation of redox-responsiveness of HA micellar nanoparticles by Nile Red fluorescence quenching (A) and dynamic light scattering (B). The inset (a) presents the experimental data for the fluorescence intensity of Nile Red upon adding different amounts of DTT. These data were used as inputs for the determination of K_{app}.

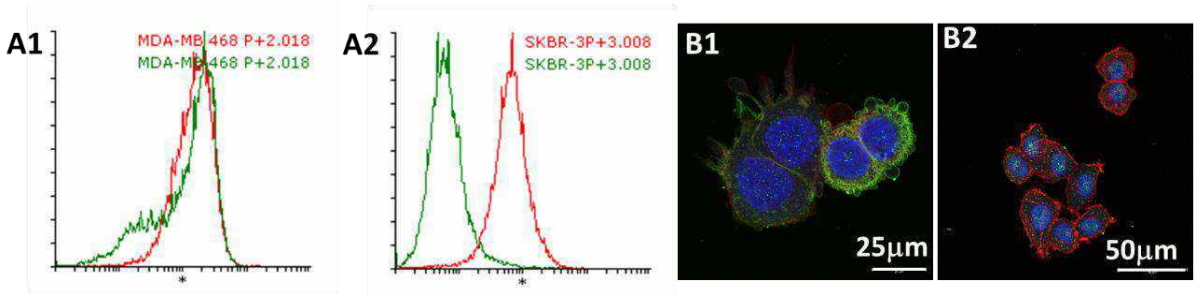

Figure VII.S9. Characterization of the used cell lines MDA-MB-468 (1) and Sk-Br-3 (2) by flow cytometry (A, CD44 in green and CD24 in red) and immunohistochemistry (B, nuclei in blue, CD44 in green and actin in red).

VII.6. REFERENCES

1. Hanahan, D. and R.A. Weinberg, *The hallmarks of cancer.* Cell, 2000. **100**(1): p. 57-70.
2. Hanahan, D. and R.A. Weinberg, *Hallmarks of Cancer: The Next Generation.* Cell, 2011. **144**(5): p. 646-674.
3. Burger, A.M. and H.H. Fiebig, *Preclinical screening for new anticancer agents*, in *Handbook of Anticancer Pharmacokinetics and Pharmacodynamics*. 2014, Springer. p. 23-38.
4. Begley, C.G. and L.M. Ellis, *Raise standards for preclinical cancer research.* Nature, 2012. **483**(7391): p. 531-533.
5. Blanco, E., H. Shen, and M. Ferrari, *Principles of nanoparticle design for overcoming biological barriers to drug delivery.* Nature Biotechnology, 2015. **33**(9): p. 941-951.
6. Chen, H.M., et al., *Rethinking cancer nanotheranostics.* Nature Reviews Materials, 2017. **2**(5).

7. Azevedo, H.S. and I. Pashkuleva, *Biomimetic supramolecular designs for the controlled release of growth factors in bone regeneration.* Advanced Drug Delivery Reviews, 2015. **94**: p. 63-76.
8. Gu, J., et al., *CD44-targeted hyaluronic acid-coated redox-responsive hyperbranched poly (amido amine)/plasmid DNA ternary nanoassemblies for efficient gene delivery.* Bioconjugate chemistry, 2016. **27**(7): p. 1723-1736.
9. Russo, A., et al., *Selective Modulation of Glutathione Levels in Human Normal Versus Tumor-Cells and Subsequent Differential Response to Chemotherapy Drugs.* Cancer Research, 1986. **46**(6): p. 2845-2848.
10. Li, J., et al., *Redox-sensitive micelles self-assembled from amphiphilic hyaluronic acid-deoxycholic acid conjugates for targeted intracellular delivery of paclitaxel.* Biomaterials, 2012. **33**(7): p. 2310-2320.
11. Yu, J., X. Chu, and Y.L. Hou, *Stimuli-responsive cancer therapy based on nanoparticles.* Chemical Communications, 2014. **50**(79): p. 11614-11630.
12. Lin, C.W., et al., *CD44-specific nanoparticles for redox-triggered reactive oxygen species production and doxorubicin release.* Acta Biomaterialia, 2016. **35**: p. 280-292.
13. Fuster, M.M. and J.D. Esko, *The sweet and sour of cancer: Glycans as novel therapeutic targets.* Nature Reviews Cancer, 2005. **5**(7): p. 526-542.
14. Rankin, K.S. and D. Frankel, *Hyaluronan in cancer - from the naked mole rat to nanoparticle therapy.* Soft Matter, 2016. **12**(17): p. 3841-3848.
15. Chanmee, T., P. Ontong, and N. Itano, *Hyaluronan: A modulator of the tumor microenvironment.* Cancer Letters, 2016. **375**(1): p. 20-30.
16. Wiranowska, M., et al., *Modulation of hyaluronan production by CD44 positive glioma cells.* International Journal of Cancer, 2010. **127**(3): p. 532-542.
17. da Costa, D.S., R.L. Reis, and I. Pashkuleva, *Sulfation of Glycosaminoglycans and Its Implications in Human Health and Disorders.* Annual Review of Biomedical Engineering, 2017. **19**: p. 1-26.
18. Bourguignon, L.Y.W., M. Shiina, and J.J. Li, *Hyaluronan-CD44 Interaction Promotes Oncogenic Signaling, microRNA Functions, Chemoresistance, and Radiation Resistance in Cancer Stem Cells Leading to Tumor Progression.* Hyaluronan Signaling and Turnover, 2014. **123**: p. 255-275.
19. Misra, S., et al., *Interactions between hyaluronan and its receptors (CD44, RHAMM) regulate the activities of inflammation and cancer.* Frontiers in Immunology, 2015. **6**.
20. Misra, S., et al., *Hyaluronan-CD44 interactions as potential targets for cancer therapy.* Febs Journal, 2011. **278**(9): p. 1429-1443.
21. Xin, Y., et al., *CD44V6 in gastric carcinoma: A marker of tumor progression.* Applied Immunohistochemistry & Molecular Morphology, 2001. **9**(2): p. 138-142.
22. Oommen, O.P., et al., *Multifunctional Hyaluronic Acid and Chondroitin Sulfate Nanoparticles: Impact of Glycosaminoglycan Presentation on Receptor Mediated Cellular Uptake and Immune Activation.* ACS Applied Materials & Interfaces, 2016. **8**(32): p. 20614-20624.
23. Toole, B.P., *Hyaluronan-CD44 Interactions in Cancer: Paradoxes and Possibilities.* Clinical Cancer Research, 2009. **15**(24): p. 7462-7468.
24. Song, S.S., et al., *Hyaluronan-Based Nanocarriers with CD44-Overexpressed Cancer Cell Targeting.* Pharmaceutical Research, 2014. **31**(11): p. 2988-3005.
25. Kang, B., et al., *Carbohydrate nanocarriers in biomedical applications: functionalization and construction.* Chemical Society Reviews, 2015. **44**(22): p. 8301-8325.
26. Mattheolabakis, G., et al., *Hyaluronic acid targeting of CD44 for cancer therapy: from receptor biology to nanomedicine.* Journal of Drug Targeting, 2015. **23**(7-8): p. 605-618.
27. Vafaei, S.Y., et al., *Self assembled hyaluronic acid nanoparticles as a potential carrier for targeting the inflamed intestinal mucosa.* Carbohydrate Polymers, 2016. **144**: p. 371-381.
28. Lin, T.S., et al., *Self-assembled tumor-targeting hyaluronic acid nanoparticles for photothermal ablation in orthotopic bladder cancer.* Acta Biomaterialia, 2017. **53**: p. 427-438.
29. Altgarde, N., et al., *Probing the biofunctionality of biotinylated hyaluronan and chondroitin sulfate by hyaluronidase degradation and aggrecan interaction.* Acta Biomaterialia, 2013. **9**(9): p. 8158-8166.
30. Silva, C., et al., *Design of protein delivery systems by mimicking extracellular mechanisms for protection of growth factors.* Acta Biomaterialia, 2017. **63**: p. 283-293.
31. Novoa-Carballal, R., et al., *Tunable nano-carriers from clicked glycosaminoglycan block copolymers.* Journal of Materials Chemistry B, 2014. **2**(26): p. 4177-4184.

32. Upadhyay, K.K., et al., *The intracellular drug delivery and anti tumor activity of doxorubicin loaded poly(gamma-benzyl L-glutamate)-b-hyaluronan polymersomes.* Biomaterials, 2010. **31**(10): p. 2882-2892.
33. Upadhyay, K.K., et al., *Biomimetic Doxorubicin Loaded Polymersomes from Hyaluronan-block-Poly(gamma-benzyl glutamate) Copolymers.* Biomacromolecules, 2009. **10**(10): p. 2802-2808.
34. Silva, C., et al., *Following the enzymatic digestion of chondroitin sulfate by a simple GPC analysis.* Analytica Chimica Acta, 2015. **885**: p. 207-213.
35. Kurniasih, I.N., et al., *Nile Red Dye in Aqueous Surfactant and Micellar Solution.* Langmuir, 2015. **31**(9): p. 2639-2648.
36. Shlyakhtenko, L.S., et al., *Silatrane-based surface chemistry for immobilization of DNA, protein-DNA complexes and other biological materials.* Ultramicroscopy, 2003. **97**(1-4): p. 279-287.
37. Peluso, S. and B. Imperiali, *Asparagine surrogates for the assembly of N-linked glycopeptide mimetics by chemoselective ligation.* Tetrahedron Letters, 2001. **42**(11): p. 2085-2087.
38. Novoa-Carballal, R. and A.H.E. Muller, *Synthesis of polysaccharide-b-PEG block copolymers by oxime click.* Chemical Communications, 2012. **48**(31): p. 3781-3783.
39. Thakar, D., et al., *A quartz crystal microbalance method to study the terminal functionalization of glycosaminoglycans.* Chemical Communications, 2014. **50**(96): p. 15148-15151.
40. Pitarresi, G., et al., *Self-assembled amphiphilic hyaluronic acid graft copolymers for targeted release of antitumoral drug.* Journal of Drug Targeting, 2010. **18**(4): p. 264-276.
41. Liu, H.X., et al., *Reduction-sensitive micelles self-assembled from amphiphilic chondroitin sulfate A-deoxycholic acid conjugate for triggered release of doxorubicin.* Materials Science & Engineering C-Materials for Biological Applications, 2017. **75**: p. 55-63.
42. Zhang, H., et al., *Self-assembled micelles based on Chondroitin sulfate/poly (D,L-lactideco-glycolide) block copolymers for doxorubicin delivery.* Journal of Colloid and Interface Science, 2017. **492**: p. 101-111.
43. Liu, Y.H., et al., *Dual targeting folate-conjugated hyaluronic acid polymeric micelles for paclitaxel delivery.* International Journal of Pharmaceutics, 2011. **421**(1): p. 160-169.
44. Wu, J.L., et al., *Preparation and characterization of nanoparticles based on histidine-hyaluronic acid conjugates as doxorubicin carriers.* Journal of Materials Science-Materials in Medicine, 2012. **23**(8): p. 1921-1929.
45. Teixeira, R., R.L. Reis, and I. Pashkuleva, *Influence of the sulfation degree of glycosaminoglycans on their multilayer assembly with poly-L-lysine.* Colloids and Surfaces B-Biointerfaces, 2016. **145**: p. 567-575.
46. Park, H.K., et al., *Smart Nanoparticles Based on Hyaluronic Acid for Redox-Responsive and CD44 Receptor-Mediated Targeting of Tumor.* Nanoscale Research Letters, 2015. **10**(1): p. 288.
47. Topel, O., et al., *Determination of critical micelle concentration of polybutadiene-block-poly(ethyleneoxide) diblock copolymer by fluorescence spectroscopy and dynamic light scattering.* Journal of Molecular Liquids, 2013. **177**: p. 40-43.
48. Louderbough, J.M.V. and J.A. Schroeder, *Understanding the Dual Nature of CD44 in Breast Cancer Progression.* Molecular Cancer Research, 2011. **9**(12): p. 1573-1586.
49. Sheridan, C., et al., *CD44(+)/CD24(-) breast cancer cells exhibit enhanced invasive properties: an early step necessary for metastasis.* Breast Cancer Research, 2006. **8**(5).
50. Pathak, A., et al., *Gene Expression, Biodistribution, and Pharmacoscintigraphic Evaluation of Chondroitin Sulfate-PEI Nanoconstructs Mediated Tumor Gene Therapy.* ACS Nano, 2009. **3**(6): p. 1493-1505.

SECTION 4

GENERAL CONCLUSIONS

CHAPTER VIII

GENERAL CONCLUSIONS AND FUTURE PERSPECTIVES

VIII.1. GENERAL CONCLUSIONS AND FUTURE PERSPECTIVES

In this thesis, we have developed glycotools that aid the mechanistic studies about GAGs interactions with cell receptors and modulate these interactions in cancer cells. Our results show that:

(i) Immobilization and modification of GAGs at their reducing end (end-on) is an appealing biomimicking strategy for the development of biofunctional glycotools;

End-on immobilization of GAGs mimics the native GAGs presentation: it does not compromise GAGs bioactivity as the binding epitopes and the conformational freedom are preserved;

(ii) GAGs presentation affects their recognition by the receptors and the following cell signaling, cell behavior, and ultimately pathology progression;

(iii) RHAMM and CD44 are involved in complex, cell-specific feedback loops signaling cascades (in-out cell signal translation) that are responsible for different GAGs bioactivities depending on the environment;

(iv) The screening platforms developed in this thesis can be used in the fundamental studies of pericellular HA dynamics and signaling, as well as for the identification of targets/mechanisms towards the design(s) of new therapeutics.

Besides these outputs, there are several challenges that remain:

(i) The developed screening platforms were validated with breast cancer cell lines as proof of concept. However, any pre-clinical application would involve further validation with patient cells derived from different types of cancers and with diverse phenotypes.

(ii) All experiments were performed under static conditions. Studies under dynamic conditions are essential for further validation and clinical translation of the platforms developed in Chapters VI and VII.

(iii) The platforms developed in Chapters III, IV, and V can be adapted to microfluidics that can be further used to analyze and sort circulating cancer cells and immune cells.

(iv) All designs and approaches described in the thesis are applicable to other GAGs (*e.g.*, heparin, heparan sulfate, chondroitin sulfate). Thus, they can be applied to screen and modulate molecular interactions and pathways that involve these glycans.

(v) All the experiments were design to study HA-cell interactions without considering the complexity introduced by cell-cell interactions and heterogeneous cell populations. This level of complexity must be considered in the further translation of the experimental design to 3D models.